

**Amorphous Oxide Transparent Thin Films:
Growth, Characterisation and Application to
Thin Film Transistors**

Thesis submitted to
COCHIN UNIVERSITY OF SCIENCE AND TECHNOLOGY
in partial fulfillment of the requirements
for the award of the degree of
DOCTOR OF PHILOSOPHY

Saji K. J.

Department of Physics
Cochin University of Science and Technology
Cochin - 682 022, Kerala, India

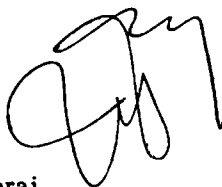
October 2008

Dr. M. K. Jayaraj
Reader
Department of Physics
Cochin University of Science and Technology
Cochin 682 022, India.

30th October 2008

Certificate

Certified that the work presented in this thesis entitled “Amorphous Oxide Transparent Thin Films: Growth, Characterisation and Application to Thin Film Transistors” is based on the authentic record of research carried out by Mr. Saji K. J. under my guidance in the Department of Physics, Cochin University of Science and Technology, Cochin 682 022 and has not been included in any other thesis submitted for the award of any degree.



Dr. M. K. Jayaraj
(Supervising Guide)

Declaration

Certified that the work presented in this thesis entitled “Amorphous Oxide Transparent Thin Films: Growth, Characterisation and Application to Thin Film Transistors” is based on the original research work done by me under the supervision and guidance of Dr. M. K. Jayaraj, Reader, Department of Physics, Cochin University of Science and Technology, Cochin-682 022 and has not been included in any other thesis submitted previously for the award of any degree.



Saji K. J.

Cochin-22
30th October 2008

Acknowledgments

I would like to express my sincere gratitude to my research guide, Dr. M. K. Jayaraj, for his unparalleled expertise shown in the guidance of my work and the unreserved willingness to share his knowledge and experience. It has been a pleasant experience to work with him because of the freedom extended to us in evolving ideas and his forbearance and willingness to hear and acknowledge sincere efforts. I express my heartfelt thanks towards him for making it possible for me the successful completion of this work. I especially thank him for his prompt reading and careful critique of my thesis. Throughout my life I will benefit from the experience and knowledge I gained working with Jayaraj sir.

I express my sincere thanks to Prof. Godfrey Louis, Head of the Department of Physics and all the former Heads of the Department - Prof. V. C. Kuriakose and Prof. Ramesh Babu Thayyullathil - for permitting me to use the research facilities in the department. I would like to thank my doctoral committee member Prof. K. P. Vijayakumar for his valuable suggestions and help. I gratefully acknowledge the help and inspiration from all my teachers at the Department of Physics who have contributed to my scholastic and personal development from the time that I have been studying for my M.Sc. Course.

I gratefully acknowledge the supports and helps received from Prof. Hideo Hosono, Prof. Toshiyo Kamiya and Dr. Kenji Nomura of Tokyo Institute of Technology, Japan, during my research period. I extend my thanks to Dr. G. S. Okram of IUC Indore for permitting me to take the low temperature conductivity measurements.

I am thankful to all the office and library staff of the Department of Physics and the technical staff at USIC for all the help and cooperation.

I thank University Grants Commission, Government of India for financially supporting me during this endeavour. I acknowledge the academic and financial support of SPIE - The international Society for Optical Engineering - during the period of my research work.

I gratefully acknowledge the helps and supports received from Joshy Sir throughout the period of my research work. It is my pleasure to acknowledge the helps received from my senior researchers in the lab, Dr. Aldrin Antony, Dr. Manoj, Dr. Nisha, Asha and Rahana. I would like to express my sincere appreciation to my colleagues in the optoelectronic devices laboratory Mr. Anoop Menon, Mr. Ajimsha, Mr. Ratheesh Kumar, Mini Krishna, Reshmi, Aneesh, Anila teacher and Vanaja Madam for all the help they had extended. I thank each of them for everything they have done for me. We had serious discussions about research topics and enjoyed parties and entertainments. It was very enjoyable in working with the younger generation of the lab - Arun, Krishna Prasad, Sanal, Sreeja and James Sir. I wish to express my love and regards to Anooja & Anjala for creating lively atmosphere in the evenings when they visit the lab.

I treasure my friendship with Prince sir, Sasanka Kumar, Vinitha, Ragitha, Sanjay, Anuraj, Sarathlal, Manu, Jafer, Saritha, Jem, Christie, Najla, Jobina and Shita whom I got acquainted with at optoelectronic devices laboratory.

I remember with gratitude the support and good will extended to me by my friends Narayanan, Sujith, Sarahu, Noushad, Vineeth, Manu and Sukesh.

I record my deep and utmost gratitude to my family for their selfless support, encouragement, patience and tolerance during the entire period of

my research work.

I thank the management of Fatima Mata National College, Kollam and the teachers of the Department of Physics, for all the support extended to me towards the end of my Ph.D. programme. Particularly I wish to thank Dr. P. J. Jojo for his selfless support to me during my service at Fatima College.

Above all, I bend my head in humble gratitude before the Omnipotent God Almighty for kindly allowing me to finish my work in time.

Saji K. J.

Contents

Preface	xix
1 Amorphous Semiconductors and Amorphous Oxide Thin Film Transistors	1
1.1 Amorphous materials: An introduction	1
1.2 Structure of amorphous materials	3
1.3 Electronic states	5
1.4 Effective mass concept	8
1.5 Band models	8
1.5.1 The Cohen-Fritzsche-Ovshinsky (CFO) model	11
1.5.2 The Davis-Mott model	12
1.5.3 Small-Polaron model	14
1.5.4 Weaire and Thorpe model	16
1.6 Optical absorption in amorphous semiconductors	18
1.6.1 Principle regions of optical absorption	22
1.6.2 Transition in tail states	26
1.6.3 Far infrared absorption	27
1.7 Electronic transport in amorphous materials	28

1.7.1	Carrier transport in a rigid lattice	28
1.7.2	Band conduction in non-degenerate state	29
1.7.3	Hopping conduction	29
1.7.4	Hall Effect	33
1.7.5	Doping in amorphous semiconductors	35
1.7.6	Advantages of amorphous materials over poly-crystalline materials	38
1.8	Transparent amorphous oxide semiconductors	40
1.8.1	Conductivity mechanism in transparent oxide semiconductors	40
1.8.2	Transparent amorphous oxide semiconductors	42
1.8.3	Electronic structure of amorphous oxide semiconductors	46
1.9	Amorphous thin film devices	47
1.10	Literature review on thin film transistors with transparent oxide semiconductor channels	48
1.10.1	Stability of oxide TFTs	61
1.10.2	Conduction mechanism in amorphous oxide TFTs	65
1.10.3	Device performance parameters	65
1.11	Relevance of present work	66
2	Experimental Techniques, Characterisation Tools and Thin Film Transistors	69
2.1	Experimental techniques	70
2.1.1	Sputtering	73
2.1.2	DC sputtering	77
2.1.3	Reactive sputtering	79

2.1.4	Radio frequency sputtering	80
2.1.5	Magnetron sputtering	81
2.1.6	Specifications of sputtering system	84
2.1.7	Pulsed laser deposition	86
2.2	Characterisation tools	90
2.2.1	Thin film thickness	90
2.2.2	Structural characterisation	91
2.2.3	Compositional analysis	96
2.2.4	Hall effect measurement	99
2.2.5	Optical characterisation	103
2.3	Thin film transistors (TFT)	105
2.3.1	Thin film transistor structures	106
2.3.2	Basic device operation	107
2.3.3	Modes of operation	110
2.3.4	Dielectrics	110
2.3.5	Amorphous oxide channel TFTs	113
2.3.6	Influence of channel layer thickness	115
2.3.7	Comparison of MOSFET and TFT	116
2.3.8	Thin film transistor characterisation	116
2.4	Conclusion	126
3	Characterisation of Zinc Tin Oxide Thin Films Prepared by Pulsed Laser Deposition	129
3.1	Introduction	129
3.2	Experimental conditions	131
3.3	Chemical composition	131
3.4	Structural characterisation	132

3.5	Optical properties	140
3.6	Electrical properties	144
3.7	Conclusion	146
4	Characterisation of Zinc Tin Oxide Thin Films Prepared by Co-sputtering	149
4.1	Introduction	149
4.2	Experimental setup	149
4.3	Deposition rate	151
4.4	Chemical composition	152
4.5	Structural characterisation	153
4.6	Optical properties	156
4.7	Electrical properties	158
4.8	Conclusion	160
4.9	Comparison of ZTO films prepared by PLD and co-sputtering	162
5	Characterisation of Amorphous Zinc Indium Tin Oxide Thin Films Prepared by Co-sputtering	165
5.1	Introduction	166
5.2	Effect of zinc content on the optical and electrical properties of ZITO thin films	167
5.2.1	Experimental details	167
5.2.2	Deposition rate	167
5.2.3	Compositional analysis	168
5.2.4	Structural characterisation	169
5.2.5	Optical characterisation	170
5.2.6	Electrical characterisation	177
5.2.7	Discussion	181

5.2.8	Effect of thermal annealing	184
5.3	Effect of oxygen partial pressure	187
5.3.1	Experimental setup	188
5.3.2	Deposition rate	189
5.3.3	Structural characterisation	190
5.3.4	Optical characterisation	192
5.3.5	Electrical characterisation	193
5.4	Analysis of carrier transport mechanism	197
5.5	Conclusion	199
6	Fabrication and Characterisation of Amorphous Zinc Tin Oxide and Amorphous Zinc Indium Tin Oxide Thin Film Transistors	201
6.1	Introduction	202
6.2	Fabrication of amorphous zinc tin oxide thin film transistors by PLD	204
6.2.1	Experimental details	204
6.2.2	Transistor performance	205
6.3	Amorphous zinc tin oxide thin film transistors by co-sputtering	208
6.3.1	Experimental details	208
6.3.2	Transistor performance	209
6.4	Amorphous zinc indium tin oxide thin film transistors	210
6.4.1	Experimental details	212
6.4.2	Transistor performance	214
6.4.3	Role of zinc in a-ZITO TFTs	221
6.5	Amorphous zinc indium tin oxide transparent thin film tran- sistors	223

6.5.1	Introduction	223
6.5.2	Experimental details	224
6.5.3	Channel properties	227
6.5.4	Transistor performance	228
6.6	Conclusion	230
7	Summary and Scope for further study	233
7.1	Summary of present study	233
7.2	Scope for further study	238
A	Symbols used in the thesis	239
B	Abbreviations used in the thesis	243
	Bibliography	246

Preface

Thin film transistor (TFT) is a special type of field effect transistor widely used in present day display applications. It consists of a thin film of a semiconducting material which forms the conducting channel between metallic source and drain electrodes. There will be a dielectric layer between the semiconducting material and gate electrode to prevent the current flow between the channel and gate. The most important field of TFT application is in liquid crystal displays (LCD) wherein TFTs are integrated to each of the sub pixels to modulate the amount of light reaching observer's eyes. In addition to this, TFTs are widely used in medical imaging equipments, organic light emitting diode displays, flat panel displays, field emission displays, imagers, scanners and various types of sensors etc.

Presently, all these applications make use of hydrogenated amorphous silicon (a-Si:H) as the semiconducting material for channel formation. Because of the disordered nature, the mobility of charge carriers is extremely low in this material. Hence, the field effect mobility of an a-Si:H channel TFT is around $1 \text{ cm}^2/Vs$. This mobility is not enough in certain applications like in video decoding electronics in which an active matrix LCD

requires microsecond switching speed, which is too fast for an a-Si:H TFT. In addition to this, these TFTs suffer from threshold voltage instabilities under bias stressing. Metallic capping is provided to these TFTs to avoid light induced carries generation in channel layer. Above all, these are opaque to light because of its very small band gap values. Hence when they are used in display applications, light is blocked from the regions occupied by the TFT. This severely affects the clarity and display resolution in active matrix LCD displays.

Scientists had been looking for an alternative material to overcome the drawbacks of a-Si:H TFTs. Eventhough poly-silicon TFTs show much better performance compared to a-Si:H TFTs, they are not feasible in large area applications. They also suffer from the grain boundary effects which affects the uniformity of device performance. Organic TFTs have been proposed as another possible candidate. These are very promising class of materials for low temperature fabrication to achieve light weight flexible displays that can be rolled up like a map. But, still after about twenty years form their invention, their performance is very poor and they also suffer from low field effect mobility. TFTs based on wide band gap oxide semiconductors were invented in the year 2003 by a group of scientists from U.S.A and Japan. Soon after that, many laboratories started the development of TFTs on different types of substrates using different types of wide bandgap oxide semiconducting materials. This led to the realisation of flexible transparent TFTs with field effect mobilities much higher than conventional a-Si:H TFTs. Eventually, amorphous ionic oxide materials were identified as most suitable for TFT applications owing to their high performance even in amorphous nature. In all aspects, these

amorphous oxide TFTs are superior to a-Si:H TFTs. Amorphous transparent conductors are much attractive because of low processing temperature requirement and the ability to grow on plastic substrates. TFTs using transparent oxide semiconductors (TOSs) as the channel layer have several merits compared with the conventional Si TFTs when applied to flat panel displays. These include the insensitivity of device performance to visible light illumination and efficient use of backlight in LCDs or emitted light in organic light-emitting diodes (OLEDs). In addition, oxide TFTs have potential advantages over the covalent semiconductor-based TFTs in terms of their high voltage, temperature, and radiation tolerances.

Most of these amorphous materials are multicomponent in nature and plenty of works remaining to be surveyed to improve active layer materials with new chemical compositions. It is not easy to vary the film chemical composition by a conventional sputtering technique because one needs to prepare a ceramic target for each chemical composition. The present work, studied the optical and electron transport properties of amorphous zinc tin oxide (ZTO) and zinc indium tin oxide (ZITO) system because there have been no systematic study on the effects of the chemical composition in TFT performance. In the present investigations, Pulsed laser deposition (PLD) and co-sputtering technique was used to develop thin films and TFTs. PLD is relatively a new technique in thin film deposition and allows the thin film deposition at higher oxygen pressures which helps to control the carrier density in the channel layer of a TFT. Co-sputtering is an effective technique for a multicomponent film to control the film chemical composition in a systematic and easy way. The optoelectronic properties of amorphous and transparent ZTO and ZITO films and the characteristics of ZITO TFTs were examined as a function of the chemical composition.

Chapter 1 presents a brief description about the fundamentals of amorphous semiconductors and a brief review of oxide thin film transistors. Different band models for amorphous semiconductor materials are described in this chapter. This includes the Cohen-Fritzsche-Ovshinsky (CFO), the Davis-Mott, the small-polaron and Weaire and Thorpe models. The optical absorption and electronic transport in amorphous materials are described. This chapter also provide the basic working hypothesis of transparent amorphous oxide semiconductors and their electronic structure. A literature review of thin film transistors using transparent oxide semiconductor material channel is given in the last part of this chapter.

Chapter 2 describes in detail the thin film growth techniques and characterization tools employed in the present work. Thin film growth was accomplished using pulsed laser deposition (PLD) and co-sputtering techniques. So this chapter describes the basic mechanism of DC & RF sputtering and PLD. Thickness of the films was measured using stylus profilometer. Structural characterization was performed by glancing angle x-ray diffraction method and atomic force microscopy (AFM). Compositional analysis was performed by x-ray fluorescence (XRF) studies. Band gap investigations were done by optical transmittance and reflectance studies using a UV-Vis-NIR spectrophotometer. The electrical properties of the films were carried out by a room temperature Hall Effect measurement system. The basic operation and specifications of all these characterisation tools are described in this chapter. A detailed description about TFT is given towards the end of this chapter. This section includes thin film transistor structures, the basic device operation, modes of operation, dielectrics, amorphous oxide channels, comparison between TFT and MOSFET, TFT characterisation etc.

Chapter 3 deals with the pulsed laser deposition and characterization of zinc tin oxide thin films. Zinc tin oxide films have the advantages of both ZnO (higher transparency and more stability in activated hydrogen environments than ITO and SnO₂) and SnO₂ (high stability in acidic and basic solutions and in oxidizing environments at higher temperatures). Structural, electronic and optical properties of amorphous and transparent zinc tin oxide films deposited on glass substrates by PLD were examined as a function of chemical composition and oxygen partial pressure (P_{O_2}). Two chemical compositions Zn:Sn = 1:1 and 2:1 were mainly investigated. The optical band gaps (Tauc' gaps) were 2.80 - 2.85 eV and almost independent of P_{O_2} , which are smaller than those of the corresponding crystals (3.35 - 3.89 eV). Films deposited at low P_{O_2} showed significant subgap absorptions, which were reduced by post thermal annealing. Hall mobility showed steep increases when carrier concentration exceeded threshold values and the threshold value depend on the film chemical composition. The films deposited at $P_{O_2} < 2 Pa$ had low carrier concentrations. It is thought that the low P_{O_2} produced high-density oxygen deficiencies and generated electrons, but these electrons were trapped in localized states which was observed as the subgap absorptions. Similar effects were observed for 600°C crystallized films and their resistivities were increased by formation of sub-gap states due to the reducing high-temperature condition. High carrier concentrations and large mobilities were obtained in an intermediate P_{O_2} region for the as-deposited films.

Chapter 4 deals with the deposition of zinc tin oxide (ZTO) thin films by co-sputtering technique and their optical and electrical characterisation. The ZTO thin films were deposited via a DC-RF co-sputtering method using high purity ZnO and SnO₂ powder targets. Chemical composition of

the films was shown systematic variation with proper control of sputtering power to the targets. The films were polycrystalline for low RF powers to SnO₂ target and became amorphous at high RF powers. All films were highly transparent in visible region. Amorphous films were shown better mobility compared to polycrystalline films which were explained as a consequence of grain boundaries. This chapter also gives a comparison of properties of ZTO films prepared by PLD and co-sputtering.

Chapter 5 describes the deposition of amorphous zinc indium tin oxide (a-ZITO) thin films by co-sputtering of ZnO and In₂Sn₂O₇ targets. This chapter is divided into two parts. First part gives the deposition and analysis of a-ZITO thin films as a function of chemical composition. Second part gives the effect of oxygen partial pressure on the optical and electrical properties of deposited films. Conductive transparent thin films of amorphous zinc indium tin oxide were prepared at room temperature. Film composition was varied by adjusting the power to the sputtering targets. Hall mobility was found to be strongly depending on the type of cationic contents in the films. The effect of thermal annealing (at 300°C in air) on the properties of the films was investigated. Annealing reduced the carrier concentration and carrier mobility in the films. The optical and electrical properties of co-sputtered a-ZITO films were also investigated as a function of oxygen partial pressure in the deposition chamber. There was a sharp change in optical band gap values between the films prepared with and without oxygen partial pressure owing to the effect of subgap states. Carrier concentration and Hall mobility decreased with the increases of oxygen partial pressure. Temperature dependent conductivity analysis showed the existence of non-localized tail states around conduction band bottom with potential barriers due to the random distributions of various cations.

Chapter 6 deals with the fabrication and analyses of TFTs using a-ZTO and a-ZITO semiconductors as channel layer. ZTO channel TFTs were fabricated by PLD and co-sputtering methods. Eventhough amorphous channel ZTO TFTs fabricated on silicon substrates showed typical transistor behaviour, its performance was very poor due to the presence of high density of subgap states. This caused very low mobility values and moderately high leakage currents. Amorphous ZITO TFTs with different chemical compositions were deposited on silicon substrates by co-sputtering from ZnO and $\text{In}_2\text{Sn}_2\text{O}_7$ targets. Effects of post annealing on ZITO TFT characteristics were analysed. The as-deposited films had high electron densities and did not produce operating TFTs. The thermal annealing at 300°C reduced the electron densities and produced operating TFTs. The TFT characteristics showed systematic variation with the chemical composition of the channels. The TFT having the largest Zn content (48 at%) showed a field effect mobility of $\sim 3.4 \text{ cm}^2/\text{Vs}$, a current on-off ratio $> 10^8$, and a positive threshold voltage of 12.1 V . The TFT having lowest Zn content (5 at%) showed a negative threshold voltage -19 V and a depletion mode operation. Co-sputtering has been demonstrated as an effective technique for multicomponent oxide channel layer deposition. Enhancement mode operation of transparent thin film transistors with amorphous ZITO as active channel layer has also demonstrated. Channel layer was deposited by a DC-RF co-sputtering method from ITO and ZnO targets. Resulting film was amorphous with Zn:In:Sn atomic ratio 0.37:0.57:0.06. Fabricated transistors showed $> 70\%$ transmission in the visible region. Room temperature fabricated transistor showed typical n-channel enhancement mode operation with a threshold voltage of 6 V and field effect mobility of $5.7 \text{ cm}^2/\text{Vs}$ and on-off ratio of 10^5 without any kind of thermal treatment.

Chapter 7 summarizes the main results in the thesis and recommends the scope for future works.

Part of the thesis has been published in the following internationally referred journals

1. Optical and carrier transport properties of cosputtered Zn-In-Sn-O films and their applications to TFTs, **K. J. Saji**, M. K. Jayaraj, K. Nomura, T. Kamiya and H. Hosono, *Journal of Electrochemical Society* 155(6), H390 (2008).
2. Optical and electrical properties of amorphous zinc tin oxide thin films examined for thin film transistor application, M.K. Jayaraj, **K. J. Saji**, K. Nomura, T. Kamiya and H. Hosono, *Journal of Vacuum Science and Technology B* 26(2), 495(2008).
3. Optical and electrical properties of co-sputtered amorphous transparent conducting zinc indium tin oxide thin films, **K. J. Saji** and M.K. Jayaraj, *Thin solid films*, 516(18), 6002 (2008).
4. Effect of oxygen partial pressure on optical and electrical properties of co-sputtered amorphous zinc indium tin oxide thin films, **K. J. Saji** and M.K. Jayaraj, *Physica Status Solidi A*, 205 (7), 1625 (2008).

Other publications to which author has contributed

1. Spatial and Temporal Studies of Laser Ablated ZnO Plasma, N. V. Joshy, **K. J. Saji**, and M. K. Jayaraj, *Journal of Applied Physics* 104, 053307 (2008).

2. Optical emission spectroscopic studies on laser ablated zinc oxide plasma, **K. J. Saji**, N. V. Joshy and M. K. Jayaraj, Journal of Applied Physics. 100, 043302 (2006).
3. Characterization of Radio Frequency plasma using Langmuir Probe and Optical Emission Spectroscopy, M. Nisha, **K. J. Saji**, R.S. Ajimsha, N.V. Joshy and M.K. Jayaraj, Journal of Applied Physics. 99, 033304 (2006).
4. Growth of zinc oxide thin films for optoelectronic application by pulsed laser deposition, **K. J. Saji**, R. Manoj, R. S. Ajimsha, and M. K. Jayaraj, Proc. SPIE Vol. 6286, 62860D (Aug. 28, 2006).

Conference Presentations

1. International conference on solar cells - January 2008, Zn-In-Sn-O Amorphous transparent conducting thin films for low temperature applications, **K. J. Saji** and M. K. Jayaraj.
2. International conference on solar cells - January 2008, Growth of transparent conducting oxides on flexible substrates, M. K. Jayaraj, **K. J. Saji** and M. Nisha.
3. Optics and Photonics 2006, San Diego, USA, August 2006, Growth of zinc oxide thin films for optoelectronic application by pulsed laser deposition, **K. J. Saji**, R. Manoj, R. S. Ajimsha, and M. K. Jayaraj.
4. DAE-BRNS 4th National Symposium on Pulsed Laser Deposition, Rajkot, Gujarat, 2007, Pulsed laser deposition of amorphous oxides for transparent electronics, M. K. Jayaraj and **K. J. Saji**.

5. National conference on New Horizons in Theoretical and Experimental Physics, Kochi, 2007, Enhancement mode thin film transistor with transparent amorphous zinc tin oxide channel layer, **K. J. Saji** and M. K. Jayaraj.
6. 20th National Symposium on Plasma and Technology, Kochi, 2005, Kinematics of plasma plume generated by Laser ablation of zinc oxide, **K. J. Saji**, N. V. Joshy, and M. K. Jayaraj.
7. 19th National Symposium on Plasma and Technology, Madhya Pradesh, 2004, Studies on RF plasma using optical emission spectroscopy, **K. J. Saji**, M. Nisha, R. S. Ajimsha, N. V. Joshy and M. K. Jayaraj.
8. National seminar on optoelectronic phenomena (NSOP-07), Kottayam, 2007, Transparent thin film transistors for flat panel displays, M. K. Jayaraj and **K. J. Saji**

Chapter 1

Amorphous Semiconductors and Amorphous Oxide Thin Film Transistors

First part of this chapter gives a broad introduction to amorphous semiconductors and their optical and electrical properties. Second part gives a review of thin film transistors limited to amorphous oxide channel devices.

1.1 Amorphous materials: An introduction

History of civilization is intimately connected with advances in material research. Materials science is an interdisciplinary area which comprehends the areas of physics and chemistry. Materials, in a broad sense, can be classified into crystalline and amorphous materials. A perfect crystalline material has a translational symmetry and a unit cell when extended in three dimensions give the structure of the material. Unlike the case of

crystalline materials, amorphous materials lack the long range periodicity. Until the end of last century, it was only the crystalline materials which got the attention of scientific community. It was believed that, due to the disordered nature of the amorphous materials, they will not find any technological applications.

In thermodynamic view point, an amorphous solid is in a non-equilibrium state; therefore its structure and bond configurations are not fixed but can be changed, sometimes reversibly, not only by thermal treatment but also by light irradiation. This is fundamentally different from the case of crystalline solids. Since amorphous phase is less thermodynamically stable (it possesses a greater free energy) than the corresponding crystalline form, the preparation of amorphous materials can be regarded as the addition of excess free energy to some manner into the crystalline polymorph. How this is done can vary widely, but it is a rule of thumb that the faster the rate of deposition or cooling, the further the amorphous solid lies from equilibrium.

The term “glass” and “amorphous” were widely used in the same sense in literature to describe the disordered materials. In a more precise form, usually the term “glass” is used for only those materials which can be quenched from the super-cooled melt and usually exhibit a glass transition and the term “amorphous” refers non-crystalline materials which can normally be prepared only in the form of thin films by deposition on substrates which are kept sufficiently cool to prevent crystallisation [1]. This convention will be followed when referring to “amorphous” materials throughout this thesis.

Randomness can occur in several forms, like topological, spin, substitutional, vibrational disorders etc (Figure 1.1) [2]. Disorder is not a unique

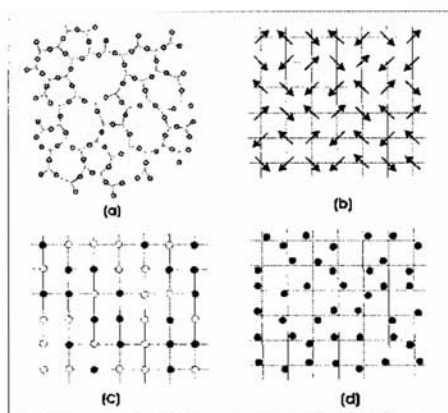


Figure 1.1: Types of disorder: (a) topological disorder (no long range order); (b) spin disorder on regular lattice; (c) substitutional disorder on regular lattice; (d) vibrational disorder about equilibrium positions of a regular lattice.

property, and must be compared to some standards, and that standard is the perfect crystal. A perfect crystal is that in which the atoms are arranged in a pattern that repeats periodically in three dimensions to an infinite extent.

1.2 Structure of amorphous materials

Knowledge of the structural arrangement of atoms of a crystalline or amorphous solid substance is an essential prerequisite to any detailed analysis of the physical or chemical properties of the solids. Crystalline solids are characterised by long range periodic order. The constraint of three-dimensional periodicity imposes the severe limitation of the existence of only seven crystal systems, 32 crystallographic point groups, and 230 space groups

resulting from the application of the translational symmetry operations of the crystal. Once the lattice vectors a_1, a_2, a_3 and the position of the atoms within the unit cell are known, the positions of all the atoms in the crystal can be described simply because of the periodicity in three dimensions.

The determination of structure of amorphous solids is an exceptionally difficult task, and no single experimental technique is wholly sufficient. Instead of the exact structural properties, a type of statistical description of the atomic arrangement is sought. We look the average coordination of the each atomic species in the material, the types, numbers and the average distance to the near neighbours etc.

The different methods for structure determination include *Radial Distribution Function (RDF)*, *Extended X-ray Absorption Fine Structure (EXAFS)*, *diffuse scattering of x-rays and neutrons*, etc.

RDFs give the distances and coordination numbers out to third or fourth neighbours and are useful for elemental amorphous materials. They are also extremely good for many oxide glasses and other systems where there are distinct distances that can be recognised, and where the structures of the amorphous materials are close to those of the crystalline. Under these circumstances, good models can be generated which fits the RDF. In many other polyatomic systems, the technique is far from good. In such cases, the A-A, A-B, and B-B neighbour distances are about the same, and all lead to one big broad first neighbour peak. As a result of that, one cannot obtain unique coordination numbers and unique structural interpretations of the RDFs.

EXAFS is atom specific since the x-ray absorption edge energy is characteristics of a given element and so the local structure around a particular type of element. In EXAFS, the scattering expression is a local function

and does not depend on translational periodicity; the technique is therefore equally applicable to crystalline and disordered materials. Structural information can be extracted by fitting the experimental amplitude to theoretical equations. EXAFS analysis yields information about the average atomic arrangement around a particular atomic species in the material. The draw back is that EXAFS provides information only about near neighbours in amorphous materials. EXAFS may even be misleading for near neighbours when there is a broad distribution of those neighbours.

1.3 Electronic states

The Hamiltonian describing a perfect crystal can be written as

$$H = \sum_i \frac{P_i^2}{2m_i} + \sum_j \frac{P_j^2}{2M_j} + \frac{1}{2} \sum_{j',j} \frac{Z_j Z_{j'} e^2}{4\pi\epsilon_0 |R_j - R_{j'}|} - \sum_{j,i} \frac{Z_j e^2}{4\pi\epsilon_0 |r_i - R_j|} + \frac{1}{2} \sum_{i,i'} \frac{e^2}{4\pi\epsilon_0 |r_i - r_{i'}|} \quad (1.1)$$

where r_i denotes the position of the i^{th} electron, R_j is the position of the j^{th} nucleus, Z_j is the atomic number of the nucleus, P_i and P_j are the momentum operators of the electrons and nuclei respectively. Prime over summation means that, summation is only over pairs of indices which are not identical. Such a many particle Hamiltonian is solved by large number of simplifications. The approximation is to separate electrons into two groups: valence electrons and core electrons (electrons in filled orbitals). Since core electrons are mostly localized around the nuclei, they can be lumped together with the nuclei to form the ion cores. So the indices j and j' in the above equation denotes the ion core while the electron indices

i and i' label the valence electrons. The next approximation is the Born-Oppenheimer or adiabatic approximation. The ions are much heavier than electrons, so they move much more slowly. The electrons can respond to ionic motion almost instantaneously. Or, in other words, to the electrons the ions are essentially stationary. On the other hand, ions cannot follow the motion of the electrons and they see only a time averaged adiabatic electronic potential. Mean field approximation assumes that every electron experiences the same average potential $V(r)$.

In almost all cases of crystalline solids, the one-electron approximation is applied to the Schrödinger equation, in which it is assumed that each electron moves in the average field due to all the others. This approximation neglects electronic correlations, i.e., the possibility that two electrons can correlate their motion in such a manner as to keep away from each other, and thereby minimise their repulsive interaction.

This formulation of solid state theory depends on the validity of both the adiabatic and one-electron approximations. In a wide class of materials, the effect of phonon coupling and electronic correlations are negligible, and theory and experiments are in good agreement. However, in some situation the electron-phonon interaction is large, and the adiabatic approximation becomes inaccurate. Similarly the one-electron approximation becomes erroneous in many cases. Electron-phonon interaction can be very strong in ionic solids. In order to correctly describe the transport in such materials, we have to consider the effects of polarons, small polarons etc.

The key element in the conventional approach to understanding the electronic structure of crystalline solids is the simplification of the problem by making use of the fact that the one-electron potential energy must exhibit the periodicity of the lattice. Theory can be applied to reduce the

problem to one involving the small number of electrons contained in a single primitive cell, from which the crystal can be generated. All electronic states are extended throughout the solid and have the same probability of finding in each of the primitive cells. The one electron density of states can be calculated by solving the one-electron problem in a single primitive cell and applying periodic boundary conditions. Because of the periodicity, the density of states (DOS) of any crystalline solid takes the form of alternating regions of energy with large densities, called bands separated from regions where no states are possible, called gaps.

Although conventional solid state theory has succeeded in explaining the behaviour of crystalline solids, it can be criticised on two major grounds [3].

1. This model completely neglects the short range order which reflects the chemistry of constituent atoms. For example, the symmetry of the primitive cells of covalently bonded c-Si is the exactly the same as that of metallic Ni and ionic NaCl, despite the very different local coordination.
2. The periodicity seems to be vital to the electronic behaviour of materials, which is inconsistent with experimental results. If periodicity were essential to the observed electronic transport in crystalline solids, we should expect large changes in conductivity upon melting, at which point the long range order spontaneously disappears. However, melting has only a very small effect on the conductivity of a large class of materials, including insulators, semiconductors, and metals. Thus, the basic DOS and mobility cannot be very sensitive to crystalline periodicity.

1.4 Effective mass concept

A charge carrier in any solid can only be made free by associating it with an effective mass through the effective mass approximation. As in the case of crystalline solids, theories have been developed by several authors for determining the effective mass of charge carriers in amorphous solids. As the wave vector \vec{k} is not a good quantum number in amorphous solids, the derivation of effective mass of charge carriers has been done in real coordinate space. It enables to determine effective masses in the extended and tail states separately. The effective mass of a charge is inversely proportional to the width of the corresponding energy states at a fixed concentration of atoms contributing to the tail states [4].

1.5 Band models

A model for electronic structure of the material is essential for the proper interpretation of experimental data of electrical transport properties. Making use of mathematical simplifications resulting from the periodicity, Bloch was able to derive some general properties of the electronic states in the crystal, from which Wilson developed the band theory of electronic transport. Since their pioneering work, it is known that the electronic structure of the crystal shows some universal characteristics. For semiconductors, the main features of the energy distribution of the density of electronic states $N(E)$ of crystalline solids are the sharp structure in the valence and conduction bands, and the abrupt terminations of $N(E)$ at the valence band maximum and the conduction band minimum (Figure 1.9). The sharp edges in the density of states produce a well-defined forbidden energy gap.

Within the band the states are extended, which means that the wave functions occupy the entire volume. The specific features of the band structure are consequences of the perfect short-range and long-range order of the crystal. In an amorphous solid, the long-range order is destroyed, whereas the short-range order, i.e., the interatomic distance and the bond angle, is only slightly changed. The concept of the density of states is equally applicable to non-crystalline solids. The DOS in the energy space can be written as [5]:

$$N(E) = \frac{V}{2\pi^2} \left(\frac{2m_e^*}{\hbar^2} \right)^{3/2} E^{1/2} \quad (1.2)$$

where, V is the volume of the sample, m_e^* is the electron effective mass and E the energy. This can be applied to both valence and conduction extended states using the respective effective masses of charge carriers. This form of DOS is not depend on the translational symmetry. The above form is obtained from the Schrödinger equation for a free electron by the boundary condition that, the Eigen functions must vanish at the sample boundaries and the normalisation condition that the electron is confined in a finite size sample. Above equation can, therefore, be applied to any solid, crystalline or non-crystalline, as long as it is a free electron system, because the above derivations are true only for free electron gas. If the electrons are not free, they can be made so by using the effective mass approach and then they will be free with that effective mass. Systems with different effective masses of their charge carriers will have different density of electron states. The DOS in amorphous solids is expected to be different since amorphous semiconductors have a different effective mass than compared to crystalline solids. For most of amorphous semiconductors, for energies, $E > E_C$, in the con-

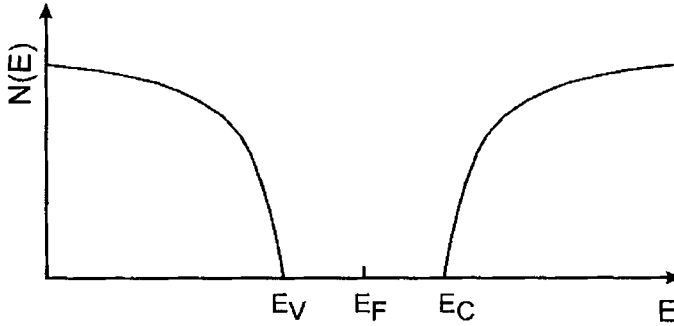


Figure 1.2: Schematic representation of DOS in crystalline semiconductors. Symbols: E_V is valence band maximum energy, E_C is conduction band minimum energy and E_F is the Fermi energy.

duction states, and $E < E_V$ in the valence states, the dependence of DOS in the equation 1.2 on the energy agrees with observed values. Replacing E by $(E - E_C)$ for conduction extended states and with $(E_V - E)$ for valence extended states in equation 1.2 suggest a sharp drop in the DOS at the mobility edges, which is against the observations in amorphous solids. This is because the derivation of DOS have only considered a fully coordinated network of atoms, which is usually not the case in any amorphous solid. There are also disorders present, which influence the DOS near the mobility edges.

Several models were proposed for the band structure of amorphous semiconductors, which were the same to the extent that they all used the concept of localized states in the band tails [6].

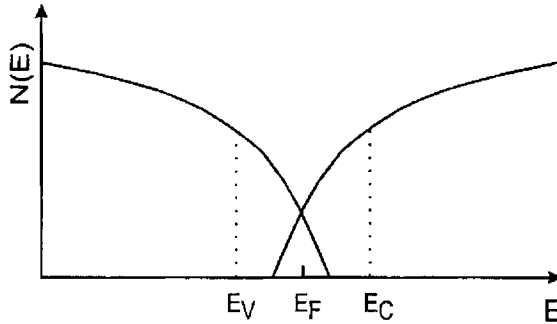


Figure 1.3: Schematic representation of DOS in CFO model. Symbols: E_V is valence band energy edge corresponding to crystalline case, E_C is conduction band energy edge corresponding to crystalline case and E_F is the Fermi energy.

1.5.1 The Cohen-Fritzsche-Ovshinsky (CFO) model

The CFO model was specifically proposed for the multicomponent chalcogenide glasses [7]. The authors suggested that in the chalcogenide alloys, the disorder is sufficiently great such that the tails of the conduction and valence bands overlap, leading to an appreciable density of states in the middle of the gap (Figure 1.3). A consequence of the band overlapping is that there are states in the valence band, ordinarily filled, that have higher energies than states in the conduction band that are ordinarily unfilled. As a result, a redistribution of the electrons must take place, forming filled states in the conduction band tail, which are negatively charged, and empty states in the valence band, which are positively charged. This model, therefore, ensures self-compensation, and pins the Fermi level close to the middle of the gap.

One of the major objections against the CFO model was the high transparency of the amorphous chalcogenides below a well-defined absorption

edge. It is now almost certain from different observations that the extent of tailing in chalcogenides is rather limited.

1.5.2 The Davis-Mott model

Based on Anderson's theory, Mott showed that spatial fluctuations in the potential caused by the configurational disorder in amorphous materials may lead to the formation of localized states, which do not occupy all the different energies in the band, but form a tail above and below the normal band [8]. According to Davis and Mott, the tails of localized states should be rather narrow and should extend a few tenths of an electron volt into the forbidden gap. Further, defects in the structure, such as dangling bonds, vacancies, etc leads to a distribution of electron states in the middle of the gap, near the Fermi energy E_F .

Figure 1.4 gives the Davis-Mott model; where, E_C and E_V represent the energies which separate the ranges where the states are localized and extended. The centre band may be split into a donor and an acceptor band, which will also pin the Fermi level (Figure 1.5). Mott suggested that at the transition from extended to localized states, the mobility drops by several orders of magnitude producing a mobility edge. The interval between the energies E_C and E_V acts as a pseudogap and is defined as the *mobility gap* [9]. Cohen proposed a slightly different picture for the energy dependence of the mobility [10]. He suggested that there should not be an abrupt but rather a continuous drop of the mobility occurring in the extended states just inside the mobility edge. In this intermediate range the mean free path of the carriers becomes of the order of the interatomic spacing, so that the ordinary transport theory based on the Boltzmann equation

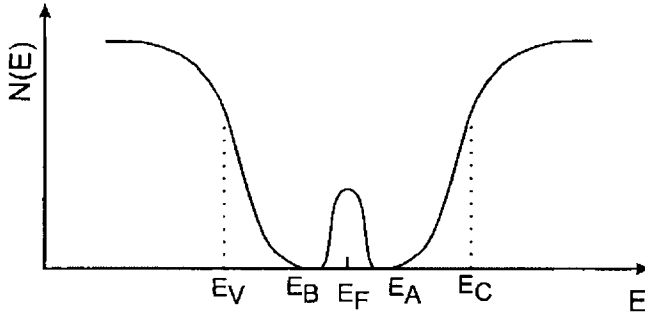


Figure 1.4: Schematic representation of DOS in Davis-Mott model. Symbols: E_V is valence band energy edge corresponding to crystalline case, E_C is conduction band energy edge corresponding to crystalline case, E_B and E_A are valence band and conduction band tailing edge and E_F is the Fermi energy.

cannot be used. Cohen described the transport as a Brownian motion in which the carriers are scattered continuously [10].

On the basis of the Davis-Mott model, there can be three processes leading to conduction in amorphous semiconductors. Their relative contribution to the total conductivity will predominate in different temperature regions (conduction mechanism in amorphous solids are discussed in section 1.7). At very low temperatures conduction can occur by thermally assisted tunnelling between states at the Fermi level. At higher temperatures charge carriers are excited into the localized states of the band tails; carriers in these localized states can take part in the electric charge transport only by hopping. At still higher temperatures carriers are excited across the mobility edge into the extended states. The mobility in the extended states is much higher than in the localized states. Hence it follows that electrical conductivity measurements over a wide temperature range are needed to study the electronic structure of amorphous semiconductors.

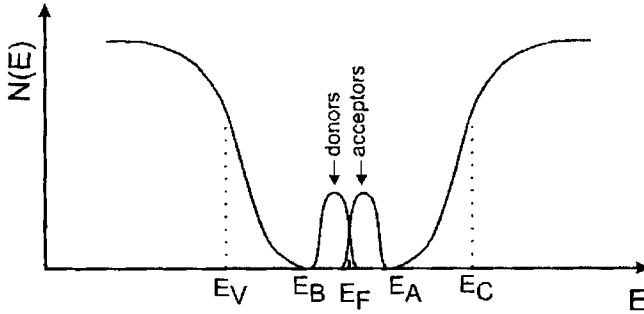


Figure 1.5: DOS in modified Davis-Mott model. Symbols: E_V is valence band energy edge corresponding to crystalline case, E_C is conduction band energy edge corresponding to crystalline case, E_B and E_A are valence band and conduction band tailing edge and E_F is the Fermi energy.

1.5.3 Small-Polaron model

It is a rival theory for electrical conduction in amorphous solids, particularly for the case of chalcogenides. The term polaron refers to the quasi-particle unit comprising the self trapped carrier and the associated atomic displacement pattern (Figure 1.6). If the spatial extend of carrier's wave function is severely localized on the scale of interatomic distances, the polaron is referred to as being small. If the wave function is of much large extend, it is said to be a large polaron. An important aspect of polaron formation in solids is that the size of the polaron that can be formed depends upon the range of the electron-lattice interaction. Small polaron band width is orders of magnitude smaller than that for non polaronic carriers. As a result, even rather modest disorder will produce Anderson localization in a system in which the carriers form the small polarons. Even in the absence of disorder, the energy uncertainty associated with the scattering of a small

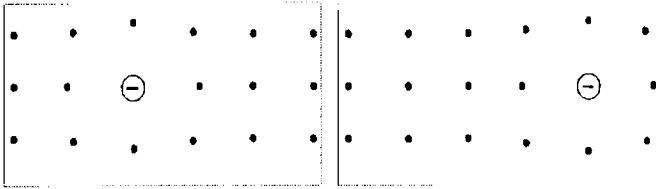


Figure 1.6: The atomic displacement pattern about a self trapped electron is illustrated for the charge occupying each of two adjacent sites.

polaron can be larger than the small polaron bandwidth. In such instances, which are equivalent to the mean free path being smaller than the intersite separation, the transport is best characterised by being phonon assisted hopping motion with rather low mobilities which increases with increasing temperature. Disorder may produce sufficient localization to enable self trapping and concomitant extreme localization to occur [11].

Experimental evidence, mainly coming from luminescence, photoconductivity and drift mobility measurements, has been found for the existence of various localized gap states, which are split off from the tail states and are located at well-defined energies in the gap [12]. These states are associated with defect centers, the nature of which is not always known. It is clear now that the density of states of a “real” amorphous semiconductor does not decrease monotonically into the gap but shows many peaks which can be well separated from each other (Figure 1.7). The position of the Fermi level is largely determined by the charge distribution in the gap states. There is no systematic theory developed for amorphous semiconductors to demonstrate that the DOS within the gap is like what is shown in the figure 1.7.

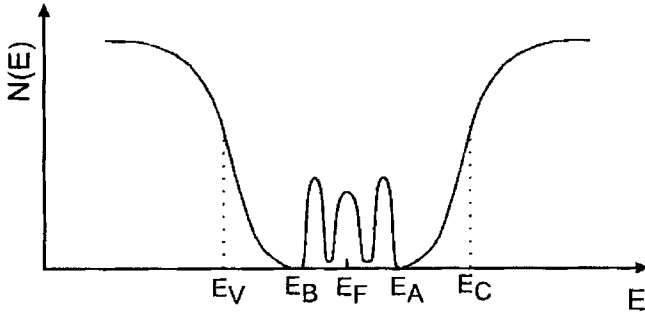


Figure 1.7: DOS model in amorphous semiconductors. Symbols: E_V is valence band energy edge corresponding to crystalline case, E_C is conduction band energy edge corresponding to crystalline case, E_B and E_A are valence band and conduction band tailing edge and E_F is the Fermi energy.

1.5.4 Weaire and Thorpe model

The first demonstration, that short range order alone can produce an energy gap in the density of states (DOS) of a semiconductor, was given by Weaire and Thorpe [13, 14]. For tetrahedrally coordinated amorphous structures, they considered a Hamiltonian of the form;

$$H = \sum_{i,j \neq j'} V_1 |\phi_{ij}\rangle \langle \phi_{ij'}| + \sum_{i \neq i',j} V_2 |\phi_{ij}\rangle \langle \phi_{i'j}| \quad (1.3)$$

where the atoms are denoted by the subscript i and the bonds by j , the states are localized sp^3 hybrid orbitals, and the matrix elements V_1 and V_2 represent the intra-atomic and interatomic interactions, respectively (Figure 1.8). This Hamiltonian makes it easy to separate the effects of quantitative disorder (i.e., bond angle variations), reflected in a spread of values of V_1 and V_2 , from topological disorder (i.e., variations in ring size). They showed that the bonds are essentially of bonding and anti-bonding charac-

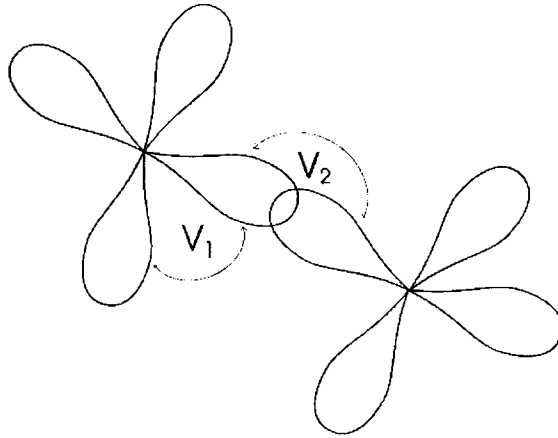


Figure 1.8: Wcaire-Thorp model showing intrasite (V_1) and intersite (V_2) interactions.

ter, split by the V_2 term and broadened by the V_1 term, and the broadening of bonds by V_1 term does not destroy the gap created by the V_2 term. There is always a band gap between two allowed bands, except for the one value $V_1/V_2 = 1/2$, at which they touch.

The importance of the work was that the electronic structure of a system with a Hamiltonian given by equation 1.3 is independent of the structure in which the atoms are distributed, provided only that the local coordination of four neighbours (of tetrahedral coordination) is maintained throughout the structure. The inclusion of the effects of the local deviations from perfect tetrahedral coordination, together with the interaction of more distant orbitals, generally results in a finite (though presumably small) density of states in the band gap. With a more generalised Hamiltonian, they were able to show the existence of band gap in amorphous compound semicon-

ductors [15].

Thus, the existence of a band gap for a non-crystalline solid can be understood in terms of chemical concepts.

Other methods in the calculation of DOS of amorphous materials include:

1. Empirical tight binding technique: in which the matrix elements and overlap integrals are treated as adjustable parameters to be fitted to known experimental results.
2. Orthogonalised linear combination of atomic orbitals (OLCAO): makes use of expansions of atomic orbitals in terms of Gaussians, with the potential constructed from all the atoms in a small cluster.
3. Pseudopotential techniques: in which the real potential is replaced by much smoother effective potential that yields high accuracy results for the outer electronic states but not the core. This give more accurate results than tight binding methods.
4. Generalised valence bond (GVB) method.
5. Self Consisted Field X_α Scattered Wave (SCF- X_α -SW) approach, and
6. Unrestricted Hartree-Fock (UHF) approach.

1.6 Optical absorption in amorphous semiconductors

The fluctuations in the atomic configurations away from the average are accompanied by the fluctuations acting on the electron. When the potential fluctuations are sufficiently deep or wide, the energies of the electronic

states are perturbed and results band broadening and band tailing [6]. The symmetry properties of the electrons and of fluctuations of the local order are both important in determining magnitude of the effect on the DOS. For example, the energies of the s states are less sensitive to fluctuations of the local coordination that have nearest neighbour distances fixed but vary the orientation of the nearest neighbour atoms than are the energies of p or d states. Thus the effect of disorder is expected to be different for the valence and conduction band edges of amorphous semiconductors. On the other hand, the probability of optical transitions between filled and empty tail states is limited in large extent by the disorder induced or Anderson localization of the electron states near the band edges. Transitions are therefore allowed only to the extent that there is spatial overlap of the localized wavefunctions. In contrast, transitions between localized and delocalized states beyond the mobility edges are strongly allowed.

The destruction of \vec{k} as a good quantum number in amorphous solids affects the optical properties, independent of the extend of band tails. In crystals, because of very small photon momentum, \vec{k} is conserved in all optical transitions which causes relatively weak optical absorption even above the energy gap in indirect band gap crystalline materials. Since \vec{k} is not a good quantum number in the absence of periodicity, this selection rule is inappropriate for the amorphous solids. In polycrystalline solids, each grain retains its periodicity, and \vec{k} conservation remains applicable even with a 50 Å grain size. The relative spread in \vec{k} , as estimated from the uncertainty principle, is of the order of [1]

$$\frac{\Delta k}{k_{BZ}} \sim \frac{a}{L} \quad (1.4)$$

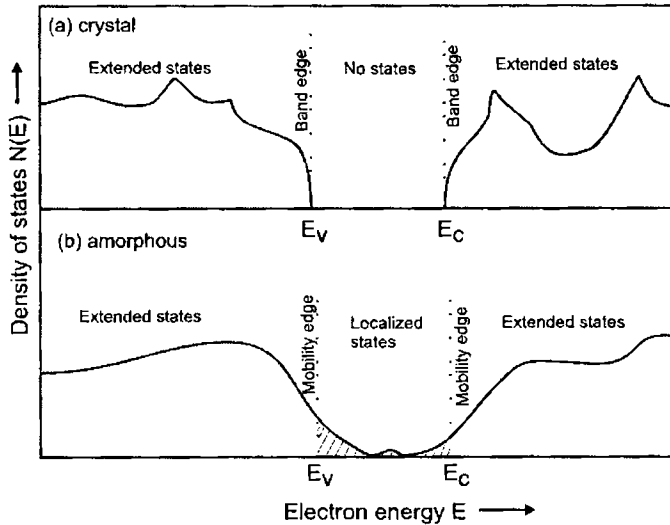


Figure 1.9: Schematic density of state diagram for a crystalline and an amorphous semiconductor in the vicinity of highest occupied and lowest empty states.

where k_{BZ} is the maximum crystal momentum in the first Brillouin zone, a is the size of the primitive cell, and L is the grain size. For a 50 \AA grain size, the spread in k is less than 10% and is relatively insignificant. However, for smaller grain sizes there is a large spread in k and presence of such deviations provide a more rigorous definition of an amorphous solid than does the range of the order. This is also a better criterion than one involving the existence of extensive band tails, since band tails can also arise from interface states at the grain boundaries of a polycrystalline solid.

The sharp features (discontinuities in the slope) in the DOS are the characteristics of crystalline solid (Figure 1.9). For a crystal, DOS function $N(E)$ is directly derived from the band structure $E(\vec{k})$ by simply counting

the states in \vec{k} space. The sharp structures in $N(E)$ arises from the presence of special places in \vec{k} space at which the gradient $\Delta_{\vec{k}}E(\vec{k})$ vanishes. This occurs whenever $E(\vec{k})$ has a local maximum or minimum. Since \vec{k} itself, as a quantum number labeling each electron eigenstate, depends for its validity upon translational periodicity, it follows that the sharp structure in $N(E)$ is a crystal property which requires long range order for its existence. In the absence of long-range order, these sharp features disappear.

As mentioned in the previous paragraph, the sharp structure in the electronic density of states $N(E)$ arises in a crystal as a band structure consequence of critical points in \vec{k} space at which the gradient $\Delta_{\vec{k}}E(\vec{k})$ vanishes. Since the first order allowed electronic transitions which dominate the ultraviolet region of the optical absorption spectrum of a crystalline semiconductor are \vec{k} conserving direct transitions, that spectrum mirrors the joint density of states ($N_{cv}(E)$). Since $N_{cv}(E)$ is determined by $E_{cv}(\vec{k}) \equiv E_c(\vec{k}) - E_v(\vec{k})$ and thus has structure at energies corresponding to \vec{k} values for which $\Delta_{\vec{k}}E_{cv} = 0$, the crystal band structure similarly gives rise to structure in the optical absorption spectrum. These critical point spectral singularities (*van Hove singularities*), which are especially sharp in the crystal spectrum at low temperatures, are specific consequences of translational periodicity (\vec{k} as a good quantum number). Hence, similar fine structure is absent in the amorphous spectrum.

In solids, the interactions between bonds broaden the bonding and anti-bonding levels into bands. The overall aspect of DOS is similar for both the crystalline and amorphous solid, since the overall electronic structure arises from the short-range order. E_{av} (the energy difference between the centres of CB and VB) reflects the bonding-antibonding splitting. The effect of long range disorder in amorphous form (such as tailing of a finite DOS into

the pseudogap region spanned by E_g) do not wash out the main features of the optical transitions. Amorphous solids, lacking any special directions associated with crystallographic axes, are optically isotropic.

In tetrahedral semiconductors (Si, Ge etc) the conduction band (CB) originates from the antibonding levels and valence band (VB) from the bonding levels. In chalcogenide semiconductors, while the CB originates from the antibonding levels the highest VB is not formed from bonding states but instead from nonbonding or lone pair state. This causes chalcogenides their characteristics double peak feature of their UV spectra.

In a crystal, a photon of energy $h\nu$ can induce a transition from a filled state of energy E to an empty state of energy $E + h\nu$ only if the initial and final states have the same wave vector (\vec{k}) and satisfy certain selection rules. Thus, among all the pairs of electron states separated by energy $h\nu$, only a very few contribute to optical absorption. But in a amorphous material, no such restrictions apply. Assuming that we are dealing with extended states, all such pairs of state (filled, at energy E , and empty, at energy $E + h\nu$) can contribute to optical processes.

1.6.1 Principle regions of optical absorption

Generally three distinct regions, A, B and C, are observed in the absorption coefficient of amorphous semiconductors near the electron mobility edge (schematically shown in figure 1.10). Above the mobility edge, in the region of strong absorption (region A in figure 1.10), the dependence of the absorption coefficient α on photon energy $h\nu$ can be described as [16, 17],

$$\alpha h\nu \propto (h\nu - E_0)^2 \quad (1.5)$$

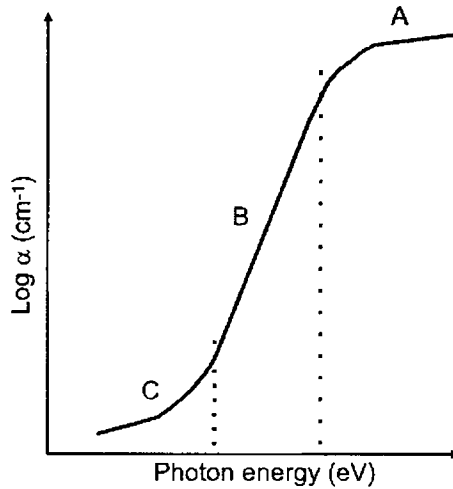


Figure 1.10: Three principal regions of optical absorption in amorphous semiconductors.

where E_0 is the optical gap. Usually equation 1.5 is written as

$$(\alpha h\nu)^{1/2} = C(h\nu - E_0) \quad (1.6)$$

where C is independent of the photon energy. A plot of $(\alpha h\nu)^{1/2}$ as a function of the photon energy $h\nu$ is called the Tauc plot, and the extrapolation of straight line region into the energy axis would give the optical gap E_0 (Tauc gap) [18–20]. Equation 1.6 is derived only for transitions from valence extended to conduction extended states, (without the involvement of any tail states) with the assumption that the matrix element is independent of the energies in the conduction and valence extended states. The optical gap thus obtained should correspond to the situation where there are no tail states, like in crystalline solids.

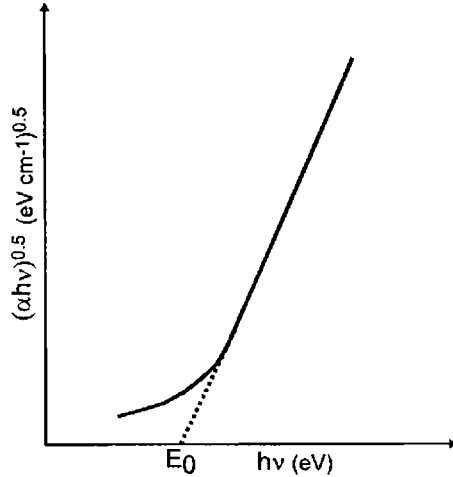


Figure 1.11: Schematic representation of the Tauc plot in amorphous semiconductors.

In the low absorption region (B region in figure 1.10), α increases exponentially with energy. In this region it can be written as

$$\alpha \propto \exp(h\nu/E_U) \quad (1.7)$$

where E_U is the width of the localized tail states and usually referred to as the Urbach tail. In the region C of figure 1.10, the absorption coefficient is written as another exponential function of the photon frequency

$$\alpha \propto \exp(h\nu/E_d) \quad (1.8)$$

where E_d is the width of the defect states, and usually it is found that E_d is larger than E_U . The region C is rather sensitive to the structural properties of materials [21].

While there seems to be a general consensus about the Tauc plot of the absorption coefficient from valence extended states to conduction extended states, there are some experimental data which fit much better to the following relation

$$(\alpha h\nu)^{1/3} = C_F(h\nu - E_0) \quad (1.9)$$

and have therefore used it to determine the optical gap E_0 . Here C_F is another constant [22]. The cubic dependence on photon energy can be obtained only when the DOS depends linearly on energy (instead of square root dependence as shown before), provided the assumption of constant transition matrix is valid for every amorphous solid.

In Cody's method of evaluating the matrix element [23], it is considered as a dependent function of energy, which leads to an expression like:

$$(\alpha h\nu) = (h\nu)^2[h\nu - E_0]^2 \quad (1.10)$$

Thus there are two different ways of evaluating the transition matrix element. Applying one approach it is found to be independent of the energy and momentum of the excited charge carriers, but the second approach shows that it depends on the photon energy and hence on energy of charge carriers. If one uses the first approach, then $(\alpha h\nu)^{1/2}$ is found to give the correct Tauc's plot (i.e. it is linear with the photon energy). However, if the second method was used, then $(\alpha/h\nu)^{1/2}$ would give the correct Tauc's plot. As the objective of Tauc's plot is to determine the optical gap, one may expect both approaches will produce the same value for the optical gap.

The DOS can be made to have parabolic dependence on energy (equation 1.2) for any particle by associating it with an appropriate effective mass. Then, the resulting absorption coefficient, obtained within the assumption of constant transition matrix element, will have the square root dependence on energy involving a different effective mass. In this view, a deviation from Tauc's plot cannot be explained by assuming the constant matrix element. However, using energy dependent matrix element, the RHS of equation 1.10 is a forth-order polynomial. Depending on which term on the polynomial may dominate, one can obtain a deviation from Tauc's plot. Therefore in a material in which a deviation from Tauc's plot is observed, the transition matrix element may not be constant.

In chalcogenides the situation is more complicated since the DOS in the valence and conduction states are expected to have different form. This can also lead to a deviation from Tauc's plot [4].

1.6.2 Transition in tail states

An exponential tail in the absorption coefficient of amorphous solids is usually observed for photon energies below the optical gap which is usually referred to as exponential tail or Urbach tail.

According to Abe and Toyozawa, the exponential densities of states in the tail region are caused by static disorder in amorphous solids [24]. The results also suggest that the effect of disorder plays role in the low energy region of the absorption, where the DOS also has exponential character, but the DOS itself is not the cause of Urbach tail.

Based on the experimental results, the current assumption is that the Urbach tails in amorphous semiconductors are caused by both thermal effects and static disorder [23]. Hence it can be concluded that, in the lower

temperature region, the occurrence of Urbach tail may be considered to be primarily from the structural disorders. As temperature increases, the thermal vibrations become active and the associated thermal disorders due to atomic vibrations also contribute to the exponential absorption. Once a sample is prepared and annealed, the structural disorders may not vary, however, as the temperature increases high enough the effect of structural disorders may be overtaken by that of thermal disorders. The temperature at which such an overtaking occurs is called the fictive temperature, above which the influence of structural disorders on the absorption spectrum becomes relatively negligibly small.

1.6.3 Far infrared absorption

In a crystalline solid, the lattice vibrational excitations are plane waves characterised by wave vector \vec{k} as well as frequency ν_{ph} . Each mode of excitation is termed a phonon, and the $\nu_{ph}(\vec{k})$ phonon dispersion relations provide an energy-versus-momentum representation of the vibrational modes which is analogous to the $E(\vec{k})$ band structure representation of the crystals electronic states. In an amorphous solid, the vibrational modes are no longer plane waves (and \vec{k} has no meaning), but continue to use phonons as a convenient abbreviation for the vibrational elementary excitations of the solid. While $\nu_{ph}(\vec{k})$ is not a valid concept in an amorphous solid, the concept of a vibrational density of states $N_v(\nu)$ retains its validity [25].

In the case of phonon excitations in crystalline solids, as a consequences of \vec{k} conservation, of the 10^{24} phonon modes that exists in a typical macroscopic sample, only a few posses the privilege of interacting with light. Whereas, in an amorphous solid, all phonons may participate in interactions with light [25].

1.7 Electronic transport in amorphous materials

1.7.1 Carrier transport in a rigid lattice

In a rigid network of atoms in an amorphous solid, electrons (holes) are assumed to move through the conduction extended-states (valence extended states) and/or through the localized states without being subjected to the lattice vibrations. Therefore, the electron-phonon coupling can be ignored in this case. The electronic configuration of individual atoms in a solid remains the same in both crystalline and amorphous solids. However the atomic configurations in amorphous solids are different from crystalline solids, because of the absence of long-range orders in the former. On the basis of the tight-binding approach, regardless of the lack of long-range orders, a fully coordinated atomic network of amorphous solids is expected to offer crystalline-like behavior to the transport of charge carriers [4]. An electron spends an equal amount of time on each of the two-bonded atoms. Thus such networks give rise to the extended states and therefore the transport of charge carriers in the conduction and valence extended states of amorphous solids is basically the same as that of charge carriers in the conduction and valence bands of crystalline solids. However, one can expect the effective mass of a charge carrier to be different in an amorphous solid from that in a crystalline solid. The density of states in the region of extended states deviates little from that in the band regions of crystalline solids and is given by the density of the free electron states. In which case it is proportional to the square root of the energy. It is the presence of tail states and dangling bond states in amorphous solids that makes them behave different from its crystalline form. Both tail states and dangling bond states are localized states and transport of charge carriers in these states at low temperatures

can only be described by quantum tunneling from one site to another. The border between the extended states and localized states is called the mobility edge. According to Mott, the zero-temperature electronic transport should vary discontinuously with energy at the mobility edge (leading to the famous term, *minimum metallic conductivity*) [26].

1.7.2 Band conduction in non-degenerate state

The nature of the transport of charge carriers gets altered when a charge carrier crosses the mobility edges E_C and E_V . The transport above E_C is the band conduction type for electrons and transport below E_V is band conduction type for holes. Transport through localized states is called the hopping conduction. The electronic transport at relatively high temperatures (near room temperature) in amorphous solid is believed to occur in the extended states. For electrons this yields an activation-type temperature dependence for the conductivity as

$$\sigma = \sigma_0 \exp(-\Delta E/kT) \quad (1.11)$$

where $\Delta E = E_C - E_F$ is called the activation energy and is the separation of E_F from the mobility edge E_C and σ_0 is the pre-exponential factor.

1.7.3 Hopping conduction

The term hopping conduction means that localized electrons jump (diffuse) quantum mechanically from site to site. The mechanism of hopping conduction was first discussed in doped semiconductors [27, 28] and was then extended to amorphous semiconductors [29]. The hopping may be

assisted by phonons and hence phonon-assisted hopping between sites will be treated in this section.

In Mott's formalism, the hopping process is simplified by assuming that the dominant contribution to the hopping current is through states within $k_B T$ of the chemical potential μ , thereby eliminating the exact occupation probabilities of the states in the description [29]. In this case the hopping probabilities (P_{ij}) are the probability of a carrier tunnelling from a localized state i with energy E_i to an empty state j with energy E_j :

$$P_{ij} \approx \begin{cases} \exp\left(-2\alpha R_{ij} - \frac{E_j - E_i}{k_B T}\right) & \text{if } E_j > E_i \\ \exp(-2\alpha R_{ij}) & \text{if } E_j \leq E_i \end{cases} \quad (1.12)$$

with R the physical distance separating the two localized states, and α the localization parameter of these states. In a one-dimensional system the α parameter corresponds with the exponential decay of a wave function in a potential barrier and is directly related to the height of the potential barrier. In systems of higher dimensions this relation is less obvious, and the α parameter is characterised by an integration of all possible tunnelling paths between two sites. That is, the α parameter reflects the 'potential landscape' surrounding the hopping sites.

In this description, the approximation $|E_i - E_j| \geq k_B T$ is used, although the validity of this approximation is questioned by several authors [30, 31].

Nearest-neighbour hopping (NNH)

Since the hopping probability depends on both the spatial and energetic separation of the hopping sites, it is usually described the hopping processes in a four-dimensional hopping space, with three spatial coordinates and one energy coordinate. In this hopping space a range R is defined as

$$R_{ij} = -\ln(P_{ij}) \quad (1.13)$$

This range, given by the magnitude of the exponent in equation 1.12, represents a distance in four-dimensional hopping space, indicating the hopping probability. In a system in which localized states are randomly distributed in both position and energy, the probability distribution function of all hops originating from one site is generally dominated by the hop to the nearest neighbouring site in the four-dimensional hopping space, due to the exponential character of the hopping probabilities. This site at closest *range* corresponds only with the spatially nearest neighbour if the first term on the right hand side of equation 1.12 is dominant. This is true if $\alpha R_0 \gg 1$, with R_0 the average spatial distance to the nearest neighbouring empty localized state. That is in cases of strong localization and/or low concentration of localized states, the hopping distance R is limited to the spatial nearest neighbouring hopping site at average distance R_0 , and the corresponding conduction mechanism is called *nearest neighbour hopping* (NNH, see figure 1.12).

Variable range hopping (VRH)

If αR_0 is in the order or less than unity, or in all cases at sufficiently low temperatures, the second term on the right hand side of equation 1.12 contributes significantly to the hopping probability and hops to sites that are further away in space but closer in energy might be preferable. This is the *variable range hopping* (VRH) process, introduced by Mott (Figure 1.13).

The DC hopping conductivity can be expressed as

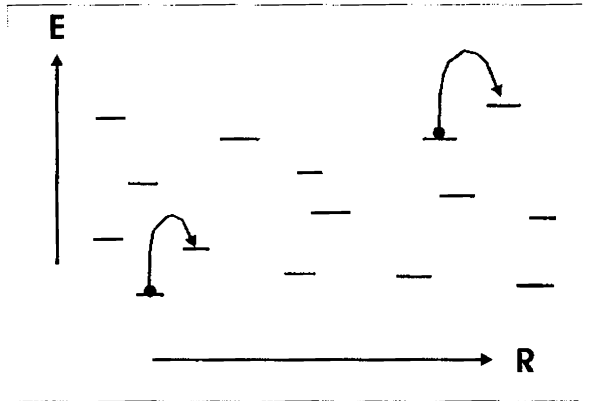


Figure 1.12: Schematic representation of nearest neighbour hopping.

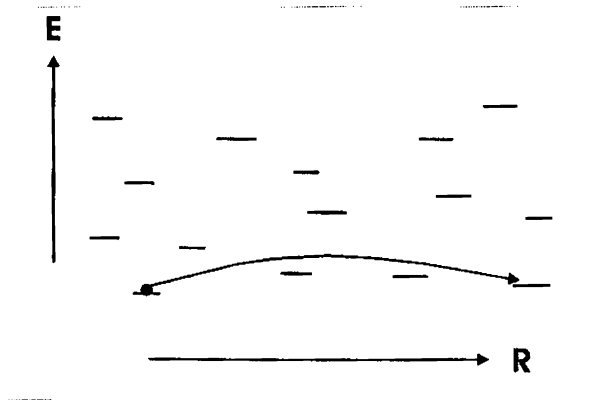


Figure 1.13: Schematic representation of variable range hopping.

$$\sigma = \sigma_0 \exp\left(\frac{T_0}{T}\right)^{\frac{1}{4}} \quad (1.14)$$

with

$$T_0 = C_T \frac{\alpha^3}{k_B N_F} \quad (1.15)$$

proportionality constant C_T is given by $C_T = \frac{24}{\pi}$ and

$$\sigma_0 = \nu_{ph} \left(\frac{N_F}{\pi \alpha k_B T} \right)^{\frac{1}{2}} \quad (1.16)$$

Large discrepancy is found between the experimental and theoretical values of pre-exponential factor σ_0 in most amorphous semiconductors [32, 33] and VRH theory is still considered incomplete [4]. Band conduction in degenerated state is described in section 1.8.2 while discussing the transparent amorphous semiconductors.

1.7.4 Hall Effect

The basic transport properties usually measured in crystalline semiconductors are the conductivity σ and Hall coefficient R_H . For n-type semiconductors the R_H is negative(positive for p-type) and is given by the general formula

$$R_H = -\frac{r}{nq} \quad (1.17)$$

where, r is the scattering factor, q is the electric charge and n is the electron density. From σ and R_H , we get the Hall mobility as $\mu_H = |R_H|\sigma$. This interpretation of hall coefficient is valid for materials in which the mean free path is large compared with the interatomic spacing [34].

The most anomalous behavior in the carrier transport in amorphous semiconductor is that the Hall effect has the opposite sign estimated from the thermoelectric power. It is called as *pn* anomaly; holes give a negative sign and electrons positive in the Hall voltage. However, there is no sign anomaly in degenerate amorphous semiconductors in which electronic transport occurs well above the mobility edge (discussed in section 1.8). When carrier transport occurs near mobility edge, the mean free path is expected to be very small and corresponds to the interatomic spacing. As a consequence, the standard transport theory based on the Boltzmann equation is not useful.

Applying the concept of hopping polarons developed by Friedman and Holstein [35], Friedman [36] has put forward a theory for the Hall effect for carriers moving in amorphous solids near the mobility edge. It produces interference between two scattering paths involving three atomic sites A, B and C. One path is from A to B direct and the other from A to B via C. The Hall mobility deduced in this way is found to be independent of temperature and in qualitative agreement with the observations, but the Hall coefficient is always found to be negative whether the carriers are electrons or holes. This has been interpreted as Friedman's theory being correct only in predicting the n-type Hall coefficient for p-type material but not the p-type Hall coefficient for n-type material.

For explaining the behavior of n-type a-Si:H, Emin has suggested a theory by considering that carriers form polarons located on Si-Si bonds [37]. Emin's theory requires that the odd order close loops must be predominant in the structure, because the orbital on each bond is antibonding so that the wavefunction changes sign at each hop. Although polarons are not formed in crystalline silicon, Emin has suggested that they can be formed

in amorphous silicon due to its softened structure. The observed activation energy in the mobility is then attributed to the polaron hopping. However, Emin's theory is not widely accepted, because it demands on the electron to move from one bond to an adjacent bond, around an odd numbered ring, which is not always possible in any amorphous structure.

Mott has suggested that the positive Hall coefficient for n-type silicon can be explained without any assumption of odd-numbered paths, if the centers which scatter electrons are considered to be the stretched Si-Si bonds [38]. Such stretched bonds have electron energies different from the majority of the bonds. Extending then Friedman's theory to such stretched bonds as scattering centers, the interference between two paths, AB and ACB, can lead to a change in the sign of the electronic wavefunction.

Applying a perturbative renormalization-group procedure, Okamoto *et al.* [39] have studied the behavior of weak field Hall conductivity near the mobility edge and found that the anomalous sign in the Hall coefficient can occur if the mean free path of carriers is shorter than a critical value. Accordingly, the microscopic Hall conductivity changes its sign near but above the mobility edge and hence the Hall coefficient also changes its sign. A quantum interference effect of electron transport near the mobility edge has been taken into consideration, which is also taken into account in a metallic conduction regime. The Hall mobility against the carrier mean free path is deduced. This is also consistent with the observation no sign anomaly in degenerate amorphous semiconductors [40].

1.7.5 Doping in amorphous semiconductors

Generally, transparent conductors show their highest conductivity in its crystalline phase. They are also very conductive in its amorphous state and

can achieve electron mobilities of 10 to 40 cm^2/Vs . Anderson suggested that disorder can cause a localization of electron states in the band structure [41]. Mott and Davis showed that disorder first localizes states at the band edges, and that the extended states and localized tail states were separated by an energy called the mobility edge. As the disorder increases, the mobility edge move further into the bands and eventually whole band becomes localized.

In pure amorphous silicon, there is large density of band gap states, which makes this material electronically dirty. The addition of hydrogen to this has the effect of cleaning out the undesirable band gap states. Hydrogen terminates (bonds to) the dangling bonds, removing the gap states associated with this native defect. Hydrogen opens up the weak reconstructed bonds associated with the voids and bonds to those Si atoms as well, replacing each such long Si-Si bond by two Si-H bonds. Since the Si-H bond is very strong and its bonding-antibonding splitting is larger than that of Si-Si, the states introduced by the Si-H bonds lie at energies which are outside of the band gap region of the a-Si host. In case of a-Si:H, bonds are sp^3 states, but states around its band gap are p states. The valence band maximum (VBM) consists of pure p states, whereas the conduction band minimum (CBM) consists of mixed s, p states. The Si-Si bond length is relatively fixed in a-Si:H, but the bond angle θ varies by 10° and the dihedral angle ϕ varies by 180° . The ϕ is a strong source of disorder in the valence band edge and causes a strong tailing of the valence band edge. Conduction band is less affected by dihedral angle disorder, but it is affected by bond angle disorder. This bond angle fluctuation gives quite strong tailing in conduction band edge, but less than for the valence band edge.

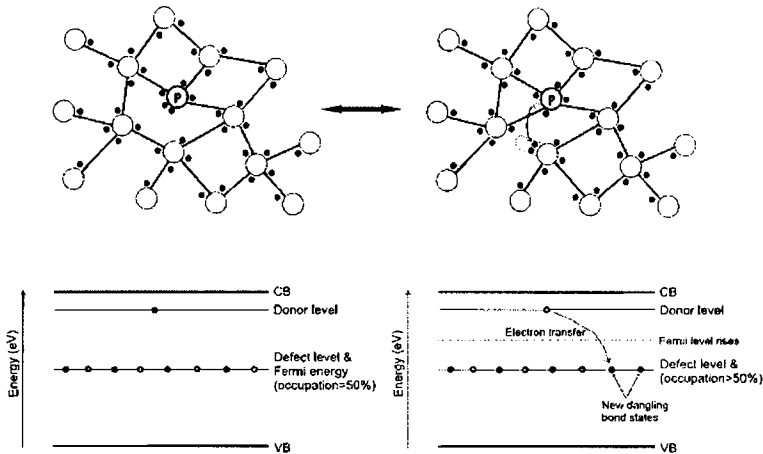


Figure 1.14: Doping of an amorphous network of Si atoms by a P atom. Band diagram of undoped and doped a-Si is also shown. The increased occupancy of the dangling bond level raises the Fermi energy.

Doping in a-Si:H is not quite the same as in crystalline Si. In crystalline materials, doping occurs by substituting impurity atoms. The surrounding semiconductor network imposes its bonding configuration upon the impurity atoms, which in the case of an acceptor is then one electron short of full valence or in the case of donor has one electron more than full valence. The former situation produces an acceptor electron energy level just above the valence band that is easily ionized to produce a free hole in the valence band, while the latter situation produces a donor level just below the conduction band that is easily ionized to produce a free electron in the conduction band [42].

If an impurity is added to an amorphous semiconductor, there is no constraint on the number of bonds that the impurity will form. For exam-

ple, if phosphorous were to be added to a-Si:H, the local Si network should adjust so that only the three bonds required by the phosphorous for perfect coordination would form. It might be expected, therefore, that amorphous semiconductors cannot be doped. However, Spear and LeComber demonstrated both p-type and n-type doping in a-Si:H by the so called “Street Mechanism” [43]. In this process, most of the dopant impurities will form the expected number of bonds according to their ideal coordination. For example, in the case of phosphorous, three bonds will be formed and the P will be neutrally charged (P_3^0 state). However, it requires only 0.5 eV for the P atom to form four bonds (P_4^0 state) (This doping site is always ionized so it is P_4^+). In the presence of a weak Si-Si bond, this energy may be recovered by breaking the weak bond to form a dangling bond. At the same time an electron is then transferred from the P atom to the dangling bond, which is then negatively charged (Si_3^- state). Thus doping is expressed by the equilibrium reaction, $P_3^0 + Si_4^0 = P_4^+ + Si_3^-$. As a result of this process, a higher proportion of the dangling bond defects in the mobility gap are negatively charged and the Fermi level rises to accommodate this change and the material is doped n-type [42]. Similarly in p-type doping, the dangling bonds becomes positively charged, and the Fermi level shifts towards the valence band. However, above equilibrium pins the Fermi energy E_F below the donor level, and thus doping in a-Si:H never moves E_F above the CB mobility edge.

1.7.6 Advantages of amorphous materials over poly-crystalline materials

Use of amorphous materials in devices helps to overcome the complexities and limitations of the use high substrate temperature during thin film depo-

sition. Since amorphous materials are not subjected to any selection rules, optical absorption is higher compared crystalline materials (see section 1.6). In solar cell applications, this property helps to reduce the thickness of the absorbing layer required to produce considerable light absorption compared to crystalline silicon. In other words, use of a-Si layer consumes less material to get the same absorption as that of a crystalline silicon device. Hence the product cost will be less in this case.

Materials with tunable energy gaps find a variety of applications in optoelectronic technologies. Crystalline $\text{Mg}_x\text{Zn}_{1-x}\text{O}$ alloy has a band gap tunability over the range 3.3 - 3.99 eV by adjusting the Mg content [44, 45]. However, crystal phase segregation between ZnO and MgO was observed for Mg concentrations $x \geq 36\%$, due to different crystal structures and large lattice mismatch between ZnO and MgO [46]. Similarly BeZnO alloys also have a large band gap tunability but still shows problems with lattice mismatch between ZnO and BeO [47, 48]. The problems of the crystal phase segregation between the components of a crystalline alloy and the lattice mismatch between film and substrate can be avoided by growing an amorphous structure of the considered alloy [49, 50].

Polycrystalline oxides like ZnO have columnar grain structures even at room temperature (RT) deposition. Thin film transistors (TFTs) with polycrystalline oxide channel suffer from problems associated with the grain boundaries [51, 52] such as the instability to the atmosphere by the gas absorption/desorption into the grain boundaries; higher film surface roughness because of facet formation etc. amorphous oxides have uniform structures and smoother surfaces which could yield smooth channel interfaces to the gate insulators.

1.8 Transparent amorphous oxide semiconductors

1.8.1 Conductivity mechanism in transparent oxide semiconductors

Today, optoelectronic materials research are mainly directed to oxide semiconductors as many of them are non-toxic and abundant in nature. This overcome serious resource and environmental issues which the modern industry are facing. In transparent oxide semiconductors (TOSs), a highly dispersed band at the bottom of the conduction band provides the high mobility electrons (due to their small effective masses) and low optical absorption due to a pronounced Burstein-Moss shift which helps to keep intense interband transitions out of the visible range. However, the interband transitions from the partially occupied band at the top of the conduction band prevents from achieving the 100% transparency in the visible range in the conventional TOSs.

Origin of conductivity in TOSs is generally related to the oxygen vacancies and cation interstitials. It has been postulated for a long time that the conductivity of transparent materials is related to the existence of shallow donor levels near the conduction band, formed by oxygen vacancies [53]. Medvedeva *et al.* [54] attributed the high conductivity of indium tin oxide (ITO) to the presence of shallow donor or impurity states located close to the host (In_2O_3) conduction band. This donor or impurity band is produced via chemical doping of Sn^{4+} for In^{3+} or by the presence of oxygen vacancy impurity states in $\text{In}_2\text{O}_{3-x}$. The excess or donor electron undergoes thermal ionization at room temperature into the host conduction band which ultimately leads to a degenerate gas of electrons in the conduction band. At the same time the fundamental host band gap is left intact, i.e.

the electrically conductive material remains optically transparent in the visible region.

In contrast, there are reports which show that oxygen vacancies form deep levels [55, 56]. First-principles calculations of formation energies and electrical (donor, acceptor) levels for various intrinsic defects (oxygen vacancy V_O , tin interstitial Sn_i , tin antisite Sn_O , tin vacancy V_{Sn} , oxygen interstitial O_i) in different charge states and under different chemical potential conditions in SnO_2 indicate that Sn_i plays a more prominent role than that of V_O . They inferred the following:

1. While oxygen vacancy produces a level inside the band gap, owing to its loosely bound outer electrons interstitial Sn produces a donor level inside the conduction band, leading to instant donor ionization and conductivity.
2. Sn_i has a very low formation energy.
3. The presence of Sn_i lowers the formation energy of V_O , explaining the natural oxygen deficiency and overall non-stoichiometry of SnO_2 .
4. The absence of inter-conduction band absorption is a consequence of a special feature of the band structure of SnO_2 , manifesting a large internal gap inside the conduction band that eliminates optical transitions in the visible range.

In addition to the general features of an oxygen vacancy model, these results reveal the important role of tin interstitial. They showed that Sn_i and V_O produce shallow donor levels which explains n-type conduction in undoped SnO_2 . The electrons released by Sn_i and V_O are not compensated owing to the absence of spontaneous formation of acceptor like intrinsic

defects (V_{Sn} and O_i), and do not make direct optical transitions in the visible range due to a large gap between the Fermi level and the energy level of first unoccupied states.

Similar studies on ZnO shows that [57]:

1. The zinc interstitial Zn_i form a shallow donor level, supplying electrons since its formation enthalpy is low for both Zn-rich and O-rich conditions and native compensating defects of Zn_i (i.e., O_i or V_{Zn}) have high formation enthalpies at the Zn-rich conditions so these electron killers are rare.
2. Since the defects that compensate p-type doping (V_O , Zn_i) have low formation enthalpies at both Zn rich and O-rich conditions, ZnO cannot be doped p type via native defects (O_i , V_{Zn}) (eventhough they form shallow acceptor levels).

In general, eventhough the contributions of metal interstitials are acknowledged, the oxygen vacancy model is still using to explain the observed conductivity behaviour in TOSs.

1.8.2 Transparent amorphous oxide semiconductors

Amorphous semiconductors have generally been classified in two categories: a tetrahedral system (represented by a-Si:H) and a chalcogenides system (such as $a - As_2S_3$). However neither system possesses both high transparency to visible radiation and high conductivity because of their small band gaps or small mobilities.

Low mobility in conventional amorphous materials causes great difficulty in obtaining transparent amorphous semiconductors. For instance,

the value of mobility in a-Si:H is of the order of $10^{-3} \text{ cm}^2/\text{Vs}$, which is smaller by ~ 3 orders of magnitude than that in polycrystalline Si. Although amorphous semiconductors based on transition metal oxides such as V_2O_5 have been extensively studied, low mobility ($\sim 10^{-4} \text{ cm}^2/\text{Vs}$) and intense colouring make them less interesting in transparent electronics.

Since the mobility is proportional to the width of the conduction bands, a large overlap between relevant orbitals is required to achieve high mobility in amorphous semiconductors. In addition, the magnitude of the overlap needs to be insensitive to the structural randomness which is intrinsic to the amorphous state. Metal oxides composed of heavy metal cations (HMCs) with an electronic configuration $(n-1)d^{10}ns^0$ (with $n \geq 4$) satisfy these requirements [58–60]. In amorphous oxide semiconductors, spatial spreading of the ns orbital is large and the overlap between these ns orbitals with spherical symmetry is large and insensitive to any angular variations in the M-O-M bonds (where M is a metal cation) compared with p-p or d-p orbitals having high anisotropy in geometry. Oxide systems have a large bandgap because of low energy of O 2p orbitals, which constitute the top of the valence band. The bottom part of the conduction band in these oxides is primarily composed of ns orbitals of HMCs. These are the major reasons for the large mobility and finite Hall voltage observed in these materials. Unlike the case of a-Si:H, these amorphous oxides do not show any anomaly in Hall voltages.

Double oxides are preferred over single oxides with respect to formation of an amorphous state. As the thickness of the active layers used to fabricate TFT is in general below 100 nm, the final device performances are highly dependent on the density of surface states and its morphology. So,

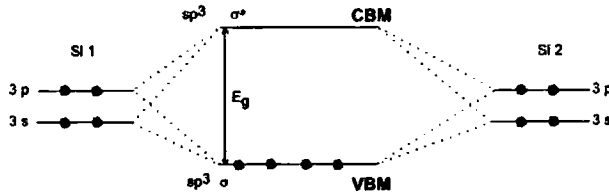


Figure 1.15: Formation of energy gap in covalent (for example, Si) semiconductors.

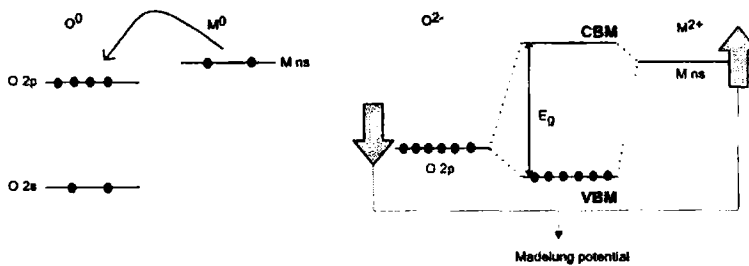


Figure 1.16: Formation of energy gap in ionic semiconductors.

highly smooth surfaces are easily obtained when the films are amorphous [61, 62].

In contrast to crystalline solids, oxides have strong ionicity and CBM and VBM are usually formed by different ionic species. When metal atoms and oxygen atoms come close, charge transfer occurs due to large differences in electron affinity and ionization potential, which ionizes these atoms. The ions form negative electrostatic potential at the cationic sites and positive potential at the anionic sites (Madelung potential), which consequently stabilizes the ionized states in the crystal structure (Figures 1.15 and 1.16). Therefore CBMs are mainly made of the metal cation and VBMs of oxygen 2p orbitals in typical oxides (these are not the cases for transition metals,

lanthanide and actinide as their d and f orbitals may locate near VBM or in the bandgap). Main group oxides have large bandgaps because the large Madelung potential increases the energy splitting. For TCOs such as SnO_2 and ITO, CBMs are mainly made of s orbitals with a large principle quantum number n (e.g., $n = 5$ for Sn and In). These s orbitals have large spatial size and form large hybridization even with second neighbor metal cations. This is the reason why TCOs have small electron effective masses. Such oxides can be good electrical conductors as long as high density carrier doping is possible [63].

In transparent amorphous oxide semiconductors (TAOSs), the conduction band minimum state is highly localized on the metal s states and its energy depends mainly on the interaction between second neighbour metal sites ($V(ss)$), and not much on the interaction between metal s and oxygen p states ($V(sp)$). The Slater-Koster interaction $V(l, m)$ between orbitals on atoms l and m would depend on their distance (r), the angles θ between the orbitals and separation vector r , and their dihedral angle ϕ [64],

$$V(l, m) = V(r, \theta, \phi) \quad (1.18)$$

Because of the spherical symmetry, the interaction between two s states reduces to,

$$V(ss) = V(r) \quad (1.19)$$

Hence the only source of disorder is the variation of the metal-metal distance, and any angular disorder has no effects on s states. In contrast to covalent bonded amorphous semiconductors, in TAOSs, the Fermi level

can be moved into the conduction band, creating large free carrier concentrations [60]. Since aliovalent dopants does not produce deep gap states in TAOSs, there are no localized states at the conduction band edge [57, 65]. Hence even in binary and ternary oxide systems, the conduction band edge is still delocalized and is not affected by compositional disorder. In case of simple oxides like ZnO, electrical conduction mechanism is controlled by oxygen vacancies and metal interstitial. Whereas for binary oxides, the the number of metal ions and their state of oxidation, together with oxygen vacancies and defects control the electrical conduction [66].

In a-Si:H, H acts as a key catalyst of bond breaking and rearrangement and hence it suffers from instabilities, called Staebler-Wronsky effects in solar cells and bias-stress instability in TFTs [67–70]. These instabilities can never really be removed in a-Si:H; their effects can be minimised by good design. In TCOs and TAOSs, hydrogen can exist, but it is present as ionized H^+ sites [71]. Atomic H lies next to an O^{2-} site and forms an OH^- ion releasing an electron. In this configuration, H is not able to catalyse bond rearrangements.

1.8.3 Electronic structure of amorphous oxide semiconductors

Structural disorder in amorphous semiconductors make it very difficult to study the electronic structure of amorphous semiconductors. Narushima *et al.* [72] performed ultraviolet photoelectron (PE) and ultraviolet inverse photoelectron (IPE) spectroscopic studies on amorphous cadmium germanate to observe the DOS of the valence band and conduction band, respectively . There was no substantial difference in the DOS with respect to the energy distribution at the conduction band bottom between the

amorphous and the crystalline states. The extended nature of the states at the conduction band bottom results comparable electron mobility and effective mass in the amorphous phase as those of the polycrystalline form. The magnitude of the overlap between neighboring Cd 5s orbitals was insensitive to the neighboring Cd-Cd distance which results large dispersion of the conduction band even in the amorphous state. The topological sequence of the ion arrangement did not show much influence on the electronic properties as the conduction band bottom is primarily composed of vacant s orbitals of the metal cations.

1.9 Amorphous thin film devices

The first major application of amorphous semiconductors was in the field of Xerography [73]. This process utilizes generally the photoconductivity of amorphous selenium films. Xerox Corporation has developed colour copier employing different layers of amorphous chalcogenides. Some of the earlier application of amorphous chalcogenide materials include the development of Ovonic threshold switch and Ovonic memory switch [3]. The switching refers to a rapid change in the electrical conductivity of the amorphous chalcogenide material when the applied field reaches of the order of 10^5 V/cm. In memory switching, high conductivity state is retained even after the applied voltage is removed. Rectifying junctions have been fabricated by sputtering amorphous silicon (a-Si) onto crystalline Si substrates [74]. TFTs have been constructed with vacuum deposited a-Si as the semiconductor on single crystalline silicon substrates with 3000 Å SiO₂ layer [75]. Because of large density of localized states in a-Si, these devices exhibit large threshold voltages (V_T) > 50 V.

First report on hydrogenated amorphous silicon (a-Si:H) appeared in 1969 [76]. Thereafter an amorphous $p - n$ junction has been fabricated by Spear *et al.* [77] and photovoltaic properties by Carlson *et al.* [78]. Zanzucchi *et al.* [79] constructed a photoconductivity cell using a-Si:H in 1977. Electroluminescence was detected in a forward biased a-Si:H diode [80]. Using the property of reversible, light induced conductivity changes in a-Si:H [81], the concept of optical storage was given by Staebler [82]. A field-effect type device was fabricated by Spear *et al.* [83] using a thick glass substrate as insulator to study the DOS in a-Si:H. In a later work, a thin film of amorphous Si_3N_4 was used as the insulating layer [84]. L. A. Goodman has successfully fabricated a-Si:H TFTs using a metal-oxide-semiconductor (MOS) structure with SiO_2 insulator [73].

1.10 Literature review on thin film transistors with transparent oxide semiconductor channels

Transparent amorphous semiconductor based TFTs have recently been investigated by several research groups. Devices fabricated from oxide semiconductor channel TFTs have relatively high mobilities despite their amorphous nature. This session gives a detailed review of TFTs using a wide bandgap oxide channel layer. The basic device structure, its working and characterisation is given in session 2.3 in the next chapter.

In 1996, Prins *et al.* [85] reported a field-effect transistor made of transparent oxide thin films, showing an intrinsic memory function due to the usage of a ferroelectric insulator. The device consists of a high mobility Sb-doped n-type SnO_2 semiconductor layer, $\text{PbZr}_{0.2}\text{Ti}_{0.8}\text{O}_3$ as a ferroelectric insulator, and SrRuO_3 as a gate electrode, each layer prepared by pulsed

laser deposition. This report focusses on the ferroelectric nature of the device and there was no mention about the electrical parameters of the TFT. Here the optical transparency of the TFT was limited by the gate electrode $SrRuO_3$. Following this, J.B. Giesbers *et al.* [86] of Philips research laboratory reported an all oxide transparent thin film memory transistor using a 10 nm n-type $SnO_2:Sb$ semiconductor channel with a 10 nm $BaZrO_3$ capping layer, $In_2O_3:Sn$ contact pads, a 250 nm $PbZr_{0.2}Ti_{0.8}O_3$ layer as a ferroelectric insulator, and conducting $SrRuO_3$ as gate electrode. This reports an on-off ratio greater than 10^3 . In 1998, Takatsuji *et al.* [87] reported the fabrication of sputter deposited amorphous indium zinc oxide (a-IZO) thin films on LCD grade glass substrate and their application to TFT.

Over the last few years, much interest has been shown in the development of TFTs with wide band gap semiconductor channel layers. Among the various types of channel layer materials, amorphous oxide semiconductors (AOSs) appear promising, especially when we consider the factors of large area deposition on flexible substrates and their mechanical stability. Present day large area LCD technology uses TFTs that have been fabricated on glass substrates. The fragile nature of glass impose a finite limit on the thickness reduction of the substrate. The substrates and their protecting bodies occupy the greater part of the electronics in volume and determine their total weight. Use of non-fragile soft substrates, like plastics and metal foils, in TFT fabrication helps to get rid of much of these problems. Such an approach limits the processing temperature because of their higher thermal expansion coefficients. Although organic TFTs (OTFTs) have been widely studied for years for this purpose, they are still facing the stability problems and facing much lower saturation mobility values.

In recent years, AOS TFTs emerged as an alternative to overcome much of these problems.

Several amorphous wide bandgap semiconductor materials like zinc oxide, indium gallium zinc oxide, zinc tin oxide, gallium nitride, and zinc indium oxide have been employed as TFT n-channel layers in recent years. The recent development in the area of TFTs using wide band gap semiconductors are summarized in the tables 1.1-1.6. Various parameters like mobility, threshold voltage, on-off ratio, subthreshold swing etc are shown in the tables. Table 1.1 shows the ZnO based thin film transistors using different types of source, drain, gate electrodes and gate insulators.

Following convention is used in the tables 1.1-1.6.

μ_{fe} : field effect mobility, μ_{sat} : saturation mobility

μ_I : Incremental mobility, μ_{PI} : Peak incremental mobility

V_{ON} : Turn on voltage, S-D: Source-Drain

Sub: Substrate, S: Subthreshold slope, Ref: Reference

Sub/annealing temp.: Substrate temperature or annealing temperature

RT: Room temperature, RTA: Rapid thermal annealing

RF: Radio frequency, PLD: Pulsed laser deposition

CBD: Chemical bath deposition

ALD: Atomic layer deposition

PECVD: Plasma enhanced chemical vapour deposition

RF-PERTE: RF plasma enhanced reactive thermal evaporation

Table 1.1: Properties of ZnO based thin film transistors: Performance parameters

Channel layer	S-D electrode	Gate electrode	Insulator	Sub	Mobility (cm^2/Vs)	On-Off ratio	Threshold voltage (V)	S (V/dec)	Ref
ZnO	-	Ta	a-SiN	-	$\mu_{fe}=7$	-	-	-	[88]
ZnO	GZO	ITO	ATO	Glass	$\mu_{sat}=27$	10^5	19	1.39	[89]
ZnO	ITO	ITO	ATO	Glass	$\mu_{eff}=2-5$	10^7	-	-	[90]
ZnO	Ti - Au	Ti - Au	SiO ₂	n-Si	$\mu_{fe}=2$	10^6	-	-	[91]
ZnO	In	Cr	SiO ₂ - SiN _x	Glass	$\mu_{fe}=0.031$	10^5	2.5	-	[92]
ZnO	ZnO:Ga	ITO	SiO ₂ N _y	Glass	$\mu_{fe}=70$	10^5	1.8	0.68	[93]
ZnO	-	-	-	SrTiO ₃	$\mu_{fe}=30$	10^6	3	-	[94]
ZnO	Ni	Mo	Ta ₂ O ₅	Glass	$\mu_{fe}=0.1$	10^5	-	-	[95]
ZnO	Al	Cr	BZN	Glass	$\mu_{fe}=1.13$	10^4	2.4	-	[96]
ZnO	ITO	ITO	SiO ₂	Glass	$\mu_{sat}=0.248$	10^5	-	-	[97]
a-ZnO	ITO	ITO	SiN	Glass	$\mu_{sat}=25$	10^7	4.53	1.24	
ZnO:N	-	-	Al ₂ O ₃	-	$\mu_{sat}=4$	10^6	2.63	1.82	[98]
ZnO	Ti - Pt	ITO	SiN	Glass	$\mu_{sat}=6.7$	10^7	4.1	0.67	[99]
- Au	-	-	-	-	$\mu_{fe}=0.5$	10^2	-	19	
					$\mu_{fe}=8$	10^6	-	0.9	[100]

Table 1.1:continued

Channel layer	S-D electrode	Gate electrode	Insulator	Sub	Mobility (cm^2/Vs)	On-Off ratio	Threshold voltage (V)	S (V/dec)	Ref
ZnO	ITO	Al	Al ₂ O ₃	Glass	$\mu_{fe}=0.8$	10 ⁷	8	1.5	[101]
ZnO	Ag	Ag	ZnMgO	p-Si	$\mu_{fe}=20$	10 ⁴	-	-	[102]
ZnO _x SnO _{2(1-x)}	Al	n ⁺ Si	SiO ₂	n ⁺ Si	$\mu_{sat}=2-12$	10 ⁷	-8 - 18	1.4	[103]
ZnO	GZO	GZO	a-HfO ₂	Glass	$\mu_{sat}=14.7$	10 ⁵	2	-	[104]

BZN: Bismuth zinc niobate

Table 1.2: Properties of ZnO based thin film transistors: Preparation technique

Channel deposition	Channel material	Sub/annealing temp. ($^{\circ}$ C)	Remarks	Ref
RF magnetron	ZnO	RT	$CaHfO_2$ buffer layer between channel and insulator, bottom gate staggered	[88]
Sputtering	ZnO	-	poly-crystalline channel, bottom gated, TTFT	[89]
Ion beam sputtering	ZnO	ZnO RTA at 600 - 800 $^{\circ}$ C	after ITO gate electrode deposition further RTA at 300 $^{\circ}$ C, bottom gated, TTFT	[90]
RF magnetron sputtering	ZnO	Near RT	poly-crystalline channel, bottom gated TFT	[91]
PLD	ZnO	450	poly-crystalline channel, double oxide bottom gated TFT	[92]
RF sputtering	ZnO		poly-crystalline channel, bottom gated, TTFT	[93]
PLD	ZnO			[94]
RF sputtering	ZnO	230	poly-crystalline channel, bottom gated TFT	[95]
RF sputtering	ZnO		Bismuth zinc niobate (BZN) insulator, bottom gated TFT	[96]
CBD	ZnO		bottom gated, transparent TFT	[97]
	a-ZnO	PECVD at 200 $^{\circ}$ C (for insulator)	bottom and top gated, amorphous ZnO by reduced channel thickness, amorphous channel, TTFT	[98]
ALD	ZnO:N	-	bottom gated TFT	[99]

Table 1.2:continued

Channel deposition	Channel material	Sub/annealing temp. ($^{\circ}$ C)	Remarks	Ref
RF sputtering	ZnO		two different refractive index SiN($n=2.45$ and $n=1.85$), PECVD (insulator), bottom gated TFT	[109]
	ZnO		dry etching method, top gated TFT	[101]
DC sputtering	ZnO	200 $^{\circ}$ C	poly-crystalline channel, bottom gated TFT	[102]
	(ZnO) $_x$	550-700 $^{\circ}$ C	Combinatorial study; annealing at 600 $^{\circ}$ C gave best performance, best performance composition $x=0.25$ and 0.8, bottom gated TFT	[103]
RF sputtering	ZnO	500 $^{\circ}$ C	RTA 200-500 $^{\circ}$ C for 1 min for enhancing transmittance	[104]

Table 1.3: Properties of zinc tin oxide (ZTO) and zinc indium oxide (ZIO) based thin film transistors: Performance parameters

Channel layer	S-D electrode	Gate electrode	Insulator	Sub	Mobility (cm^2/Vs)	On-Off ratio	Threshold voltage (V)	S	Ref
ZnO	IZO	ITO	ATO	Glass	$\mu_{sat}=26$	10^6	-	-	
a-IZO	- GZO				$\mu_{sat}=49.9$	10^8			[62]
In ₂ O ₃ (semicond.)	InO _x (cond.)	InO _x (cond.)	a-SiN _x	Glass	$\mu_{fe}=0.02$	10^4	2	-	[105]
a-CdInSbO	ITO	ITO	Al ₂ O ₃	PEN	$\mu_{fe}=0.45$	10^2	1.5	-	[106]
In ₂ O ₃	Ag	n ⁺ Si	SiO ₂	n ⁺ Si	$\mu_{fe}=27$	10^4	10.5	-	[107]
SnO ₂ - ZnO	ITO	ITO	ATO	Glass	$\mu_{PI}=5 - 15$	10^6	5 - 10	-	[108]
ZTO	AZO	ITO	ATO	Glass	$\mu_{fe}=11$	10^5	-	-	[109]
a-ZTO	ITO	ITO	ATO	Glass	$\mu_{fe}=5 - 15$	10^7	0 - 15	-	
					$\mu_{fe}=20 - 50$		-5 - +5	-	[110]
ZTO	ITO - Au	Al	SiON	Polyim.	$\mu_{fe}=14$	10^6	V _{ON} =-17	1.6	[111]
a-ZTO	Al	Al	SiO ₂	Si	$\mu_{fe}=16$	10^5	12		[112]
ZIO	ITO	ITO	ATO	Glass	$\mu_{I}=10 - 30$	10^6	0 - 10	0.3	
					$\mu_{J}=45 - 55$		-20 - -10	0.8	[113]
a-IZO	Al	Al	SiO ₂	Si	$\mu_{sat}=7.3$	10^7	2.5	1.47	[114]

Table 1.3:continued

Channel layer	S-D electrode	Gate electrode	Insulator	Sub	Mobility ($\text{cm}^2/\text{V}\cdot\text{s}$)	On-Off ratio	Threshold voltage (V)	S (V/dec)	Ref
SnO_2	ITO	ITO	ATO	Glass	$\mu_{fe}=0.8$ $\mu_{fe}=2$ (dep.)	10^5	10	-	[115]
P doped (Zn,Mg)O	ITO	Al	HfO_2	Glass	$\mu_{fe}=5.32$	10^3	2.8	-	
Sn doped Ga_2O_3	-	-	a- Al_2O_3	Al_2O_3	$\mu_{sat}=0.05$	-	-6.7	-	[116]
a-ZITO	Al	Ti - Au	SiO_2	Si	$\mu_I=5$	10^6	$V_{ON}=-4$	-	[117]
					$\mu_I=19$	10^6	$V_{ON}=-17$	-	[118]

semicond: semiconducting, cond: conducting, polyim: polyimide, dep: depletion mode

Table 1.4: Properties of zinc tin oxide (ZTO) and zinc indium oxide (ZIO) based thin film transistors: Preparation technique

Channel deposition	Channel material	Sub/annealing temp. ($^{\circ}C$)	Remarks	Ref
RF magnetron sputtering	ZnO & a-IZO		IZO-amorphous channel and ZnO-poly-crystalline, amorphous channel devices gave better performance than poly-crystalline channel, bottom gated, TTFT	[62]
RF-PERTE	InO _x	350	bottom gated,transparent TFT	[105]
Reactive evaporation	a-CdInSbO In ₂ O ₃	200, 300	flexible substrate, amorphous channel, top gated,TTFT annealing at 200 $^{\circ}$ C, annealing at 300 $^{\circ}$ C resulted high leakage current, poly-crystalline channel, bottom gated TFT	[106] [107]
RF sputtering	SnO ₂ - ZnO	600	sequential channel layer deposition and annealing, amorphous channel, bottom gated, transparent TFT	[108]
PLD	ZTO		Oxygen plasma assisted PLD, bottom gated,transparent TFT	[109]
RF sputtering	a-ZTO	175, 300	amorphous channel, bottom gated, transparent TFT, (ZnO) _x (SnO ₂) _{1-x} channel with x=1/2 and 2/3; little variation in device performance with stoichiometry variation	[110]
RF sputtering	ZTO	250	PECVD (insulator), bottom gated TFT	[111]
Spin coating	a-ZTO	600	bottom gated TFT; high off currents of the order of 10 ⁻⁸ A.	[112]

Table 1.4:continued

Channel deposition	Channel material	Sub/annealing temp. ($^{\circ}$ C)	Remarks	Ref
RF magnetron sputtering	ZiO	300, 600	amorphous (300° C) and poly-crystalline (600° C) channel, bottom gated, TTFT	[113]
Spin coating	a-IZO	500	solution processed, bottom gated TFT	[114]
RF magnetron sputtering	SnO ₂	600 (RTA)	poly-crystalline channel, bottom gated, TTFT, channel conductivity was reduced (hence enhancement mode) by reducing channel thickness to 10 - 20 nm	[115]
PLD	P doped (Zn,Mg)O	400, 600	poly-crystalline channel, top gated, TTFT	[116]
	Sn doped Ga ₂ O ₃		poly-crystalline channel	[117]
RF magnetron sputtering	a-ZiTO	100, 300	amorphous channel, bottom gated TFT	[118]

Table 1.5: Properties of indium gallium zinc oxide (IGZO) based thin film transistors: Performance parameters

Channel layer	S-D electrode	Gate electrode	Insulator	Sub	Mobility (cm^2/Vs)	On-Off ratio	Threshold voltage (V)	S (V/dec)	Ref
a-IGZO	Ti - Au	Ti - Au	Y_2O_3	Glass	$\mu_{fe}=12$	10^8	-	0.2	[119]
a-IGZO	Ti - Au	n^+ -Si	SiO_2	n^+ -Si	$\mu_{sat}=12$	10^7	3	-	[120]
a-IGZO	Ti - Pt	Mo	SiO_2	Si	-	-	-	-	[121]
a-IGZO	Ti - Au	Ti - Au	Y_2O_3	Glass	$\mu_{fe}=12$	10^8	1.4	0.2	[119]
a-IGZO	Ti - Au	Si	SiO_2	Si	$\mu_{sat}=14.55$	10^8	2.25	0.2	[122]
a-IGZO	MoW	MoW	SiN_x	Glass	$\mu_{fe}=35.8$	10^6	5.9	0.59	[123]
a-IGZO	Ti - Pt	MoW	SiN_x	Glass	$\mu_{fe}=3.3$	10^7	4.1	0.25	
					$\mu_{fe}=9.1$	10^6	1.6	0.19	[124]
a-IGZO	IZO	MoW	SiN_x	Glass	$\mu_{fe}=19.3$	10^7	0.59	0.35	[125]
a-IGZO	ITO	ITO	Y_2O_3	PET	$\mu_{sat}=6-9$	10^3	-	-	[126]
IGZO	-	-	a-HfO ₂	YSZ	$\mu_{fe}=80$	10^6	-	-	[127]
a-IGZO	IZO	IZO	HfO ₂	Glass	$\mu_{fe}=7.18$	10^5	0.44	0.25	[128]

PET: polyethylene terephthalate, YSZ: yttria stabilized zirconia

Table 1.6: Properties of indium gallium zinc oxide (IGZO) based thin film transistors: Preparation technique 8

Channel deposition	Channel material	Sub/annealing temp. ($^{\circ}$ C)	Remarks	Ref
RF sputtering	a-IGZO	RT	amorphous channel, top gated TFT	[119]
Combinatorial sputtering	a-IGZO		amorphous channel, bottom gated TFT, best performance for In:Ga:Zn=37:13:50	[120]
RF sputtering	a-IGZO		shift in V_T to less negative value w.r.t increase in O_2 pressure, amorphous channel, bottom gated TFT	[121]
RF sputtering	a-IGZO	RT	amorphous channel, top gated TFT	[119]
	a-IGZO	300	amorphous channel, bottom gated TFT	[122]
RF sputtering	a-IGZO	350	amorphous channel, bottom gated, In:Ga:Zn=2.2:2.2:1.	[123]
RF sputtering	a-IGZO		amorphous channel, bottom gated, mobility was increased after Ar plasma treatment	[124]
Co-sputtering	a-IGZO		PECVD at 330° C (insulator), amorphous channel, bottom gated, best composition In:Ga:Zn=0.65:0.23:0.12	[125]
PLD	a-IGZO	RT	amorphous channel, top gated, TTFT	[126]
PLD	InGaO ₃	1400	single crystalline channel, top gated, TTFT	[127]
RF sputtering	a-IGZO		bottom gated TTFT, saturation mobility remained almost stable while the threshold voltage showed small shift to higher positive values during 1000 hours of observation	[128]

1.10.1 Stability of oxide TFTs

Though there are many reports about AOS TFTs, studies on the TFT behaviour under bias stress is rather limited. In an application view point, it is necessary to understand how these devices behave under bias stress. Prolonged application of gate bias on the TFTs can result the deterioration of device performance. Two main mechanisms which are responsible for this instability are defect creation in the channel material and charge trapping in the gate insulator or at the insulator channel interface [129, 130]. Cross *et al.* [131] have studied the effect of bias stress on a ZnO channel TFT. ZnO was deposited on to a thermally oxidised p-type Si substrate by rf magnetron sputtering at room temperature. Thermally evaporated ITO was used as source and drain terminals. Application of positive and negative bias stress caused displacement of the transfer characteristics in the positive and negative directions respectively. Shift of threshold voltage indicates the charge trapping as the dominant instability mechanism. Unlike the case of a-Si:H TFTs, after both stress experiments, the device recovered their initial state after a period of relaxation of one hour. For low gate bias voltages, the subthreshold slope remained unchanged after both positive and negative stressing. However at large gate bias voltage, the subthreshold slope initially increased with time and then decreased. This is explained as some kind of defect creation/removal process taking place at high biases that becomes dominant over charge trapping.

Stability of transparent ZTO transistor was analysed by Görrn *et al.* [132]. ZTO channel layers were deposited on ATO/ITO coated glass substrates by oxygen plasma assisted PLD. PLD deposited ZnO:Al was used as source and drain. Stable device performance was observed for Zn:Sn atomic

ratio 36:64 in the channel. Both saturation mobility and threshold voltage was studied as a function of gate bias stress. In general, the change in mobility did not show a correlation to the threshold voltage shift. In this case, subthreshold voltage has not been shown any change with positive threshold voltage shift. Defects in the dielectric act as a charge trapping centre. However, devices with a negative threshold voltage shift have shown clear variations in subthreshold slope. This behavior has been explained due to the presence of traps in dielectric/semiconductor interface or in the semiconductor bulk material.

Suresh *et al.* [133] have reported the results of bias stress measurements on amorphous IGZO channel TFTs. The TFT consists of an ALD grown ATO insulator and ITO gate electrode on glass substrate. The IGZO channel and ITO source and drain were deposited by PLD at room temperature. Gate bias stress was carried out at $V_{DS} = 1\text{ V}$ instead of the saturation regime where the effect of bias stress on the threshold voltage shift is small. They observed a positive shift in threshold voltage with a positive gate bias stress. This voltage instability has been attributed to the charge trapping in the channel/dielectric interface or in dielectric due to bias stressing. However, no change in subthreshold slope was observed after bias stressing, which shows that no additional defect states are created at the channel/dielectric interface after the device was stressed. It is also reported that with a negative gate bias stress, the transistor channel is depleted of electrons at the channel/dielectric interface and there was no charge trapping.

In a practical point of view, in addition to the stability under bias stress, the light sensitivity of the TFTs is of critical importance. In a-Si TFTs, they are shielded from light source. In transparent TFTs, it is not

possible to use shielding layers to reduce the light sensitivity. In display applications wavelengths below 430 nm are not relevant and can be blocked by suitable filters without compromising the overall appearance. Owing to the wide band gap of oxide semiconductors, the fundamental band to band absorption of wavelengths in the visible region can be neglected. However, the amorphous nature of the channel layer may create defect states in the band gap region and produces band tailing. Hence, even below the band gap energy, a significant contribution of defect states to the light absorption can be expected. In a study of the influence of visible light on transparent zinc tin oxide TFTs, Görrn *et al.* [134] found that all light induced changes are totally reversible. Due to the lower density of defects in the materials, the TFTs processed with higher substrate temperatures showed less sensitivity to the light and profound saturation behaviour in V_T .

Park *et al.* [135] have studied the effect of water adsorption on the performance of a-IGZO transistors grown by rf sputtering on SiN_x /glass substrates. The TFTs were dipped and kept in distilled water for 12 hours and then the electrical characteristics were measured in a vacuum chamber coupled with a semiconductor parameter analyzer. The adsorbed water molecules induced the formation of an accumulation layer of extra electron carriers. It can act as either electron donor or deep level acceptor like traps depending on the channel thickness. When the channel thickness is larger than the screening length λ (the length over which the band bends to screen the applied gate field from the bulk of the semiconductor), the created traps did not respond to the applied gate voltage and hence thicker devices showed lesser degradation to subthreshold swing. For thinner devices (channel thickness $< \lambda$), the change in gate voltage resulted

band bending and simultaneous Fermi level shifting which led to the deterioration in subthreshold swing. Further, the acceptor like trap formation promotes a positive shift in V_T , which compensate for the negative V_T shift due to the donor effect of some of the adsorbed H_2O molecules. Hence thinner channel TFTs showed smaller V_T shift compared to thicker channels TFTs.

The effect of long term gate bias stress on the performance of nanocrystalline indium oxide channel TFTs were reported by Vygranenko *et al.* [136]. Silicon dioxide layer, deposited on a heavily doped p-type single crystalline silicon wafers by PECVD at 200 °C, was used as the gate dielectric. Indium oxide channel layers were deposited by reactive ion beam assisted evaporation. Mo was used as source/drain contacts and aluminium as gate electrode. Threshold voltage showed a positive shift initially, when a positive constant bias voltage is applied to the gate. After a stress time of around 3000 s, V_T showed a slow decrease while the subthreshold slope did not show significant change during the course of stressing. When relaxed, TFT showed fast recovery of threshold voltage without annealing. The threshold voltage shift was ascribed to the charge trapping at the channel insulator interface and/or charge injection into silicon dioxide gate dielectric. Because of the absence of covalent bonds, the defect state creation, which is responsible for instabilities in a-Si TFTs, is overruled in oxide TFTs.

Rameshan *et al.* [137] observed the improved performance in terms of off current and on-off current ratio on rapid thermal annealing (RTA) and subsequent N_2O plasma treated ZnO TFTs. The XPS analysis of the TFT samples showed that the RTA treated ZnO surface had more oxygen vacancies as compared to as deposited samples. These oxygen vacancies

were reduced by subsequent N_2O plasma treatment which caused a better off current and on-off current ratio.

1.10.2 Conduction mechanism in amorphous oxide TFTs

There are limited resources which deals with the conduction mechanism in amorphous oxide channel TFTs. Chung *et al.* [138] investigated the current conduction mechanism in rf-sputtered a-IGZO thin films using model devices designed to mimic the carrier injection from an electrode to an a-IGZO channel in TFTs. They showed that the large contact resistance is originated from the bulk a-IGZO itself rather than from the interface between the source/drain electrodes. Interface limited mechanisms, such as thermionic emission and Fowler-Nordheim tunnelling, failed to fit the measured current-voltage curves. Instead, the conduction is governed by the space charge limited (SCL) mechanism at low electric field. At high field ($> 0.1 \text{ MV/cm}$), thermionic injection of the charge carriers from the traps becomes important, leading to the enhancement of current flow by the SCL + Frenkel effect and Poole-Frenkel mechanisms.

1.10.3 Device performance parameters

Eventhough there are many possible applications to oxide TFTs, little efforts have been taken by the researchers to understand the various performance parameters. The DC and RF device performance of an IZO TFT has been reported by Wang *et al.* [139]. An SiN_x gate insulator was deposited by PECVD. The device showed a threshold voltage of -2.5 V , on-off current ratio $> 10^5$, and saturation mobility $14.5 \text{ cm}^2/\text{Vs}$. Device also showed a

unity gain cut off frequency of 180 *MHz* and maximum oscillation frequency of 155 *MHz*.

1.11 Relevance of present work

Transparent electronics is an emerging technology which are expected to find numerous applications like invisible electronic circuites, transparent displays, smart windows etc [140, 141]. The volume of work being carried out in the filed of transparent electronic materials and transparent electronic devices by various research labs and industry shows the importance of this technology. As in all new technologies, a deep understanding of various parameters of these devices both in basic physics and in applied level is necessary before realising the final product. Several oxide materials and their compounds show properties suitable to transparent electronics and all such materials were not fully explored for this purpose. This work mainly concentrate to understand the optical and electrical properties of amorphous zinc tin oxide and amorphous zinc indium tin oxide thin films for TFT applications. Amorphous materials are promising in achieving better device performance on temperature sensitive substrates compared to polycrystalline materials. Most of these amorphous oxides are multi-component and as such there exists the need for an optimized chemical composition. For this we have to make individual targets with required chemical composition to use it in conventional thin film deposition techniques like PLD and sputtering. Instead, if we use separate targets for each of the cationic element and if separately control the power during the simultaneous sputtering process, then we can change the chemical composition by simply adjusting the sputtering power. This is what is done in

co-sputtering technique. Eventhough there had some reports about thin film deposition using this technique, there was no reports about the use of this technique in TFT fabrication until very recent time. Hence in this work, co-sputtering has performed as a major technique for thin film deposition and TFT fabrication. PLD were also performed as it is a relatively new technique and allows the use high oxygen pressure during deposition. This helps to control the carrier density in the channel and also favours the smooth film surface. Both these properties are crucial in TFT.

Zinc tin oxide material is interesting in the sense that it does not contain costly indium. Eventhough some works were already reported in ZTO based TFTs, there was no systematic study about ZTO thin film's various optoelectronic properties from a TFT manufacturing perspective. Attempts have made to analyse the ZTO films prepared by PLD and co-sputtering. As more type of cations present in the film, chances are high to form an amorphous phase. Zinc indium tin oxide is studied as a multicomponent oxide material suitable for TFT fabrication.

Chapter 2

Experimental Techniques, Characterisation Tools and Thin Film Transistors

Various techniques that were used in the process of thin film deposition is briefed in this chapter. RF magnetron sputtering and pulsed laser deposition have been elaborated since these techniques were used for the growth of thin films and fabrication of TFTs described in this thesis. Various thin film characterisation methods, that were used to optimise film properties, are also discussed. This include stylus profiler, glancing angle x-ray diffraction, atomic force microscopy, energy dispersive x-ray spectroscopy, x-ray fluorescence, Hall effect measurements and UV-Vis-NIR spectrophotometer. Last section of this chapter gives the working principle of thin film transistors, especially an amorphous channel device. Method of deriving the various device performance parameters like threshold voltage, mobility, subthreshold voltage swing, on-off ratio etc are also discussed.

2.1 Experimental techniques

A thin film is defined as a low-dimensional material created by condensing, one-by-one, atomic/molecular/ionic species of matter. The thickness is typically less than a few micrometers. Thin films differ from thick films. A thick film is defined as a low-dimensional material created by thinning a three-dimensional material or assembling large clusters/aggregates/ grains of atomic/molecular/ionic species [142]. Thin film technology is one of the oldest arts and one of the newest sciences. Thin films have been used for more than a half century in making electronic devices, optical coatings, hard coatings, and decorative parts.

The birth of thin films of all materials created by any deposition technique starts with a random nucleation process followed by nucleation and growth stages. Nucleation and growth stages are dependent upon various deposition conditions, such as growth temperature, growth rate, and substrate chemistry. The nucleation stage can be modified significantly by external agencies, such as electron or ion bombardment. Film microstructure, associated defect structure, and film stress depend on the deposition conditions at the nucleation stage. The basic properties of film, such as film composition, crystal phase and orientation, film thickness, and microstructure, are controlled by the deposition conditions.

The chemical composition of deposited films is governed by the substrate temperature and/or the deposition atmosphere. Under low substrate temperatures, the chemical composition of deposited films coincides with that of the source materials. Under high substrate temperatures, the chemical composition of deposited films differs from the source materials due to

the re-evaporation of high vapour pressure materials from the films during the deposition.

Thin films exhibit unique properties that cannot be observed in bulk materials: unique material properties resulting from the atomic growth process like size effects, including quantum size effects, characterised by the thickness, crystalline orientation, and multi-layer aspects.

The properties of thin films are governed by the deposition method. Almost all thin-film deposition and processing method employed to characterise and measure the properties of films requires either a vacuum or some sort of reduced-pressure ambient. Different techniques like evaporation, sputtering, laser assisted deposition, chemical vapour deposition etc are widely used for thin film fabrication. The decision of whether to evaporate, sputter, or chemically deposit thin films for particular applications is not always obvious and has fostered a lively competition among these alternative technologies.

Vacuum thermal evaporation controllably transfer atoms from a heated source to a substrate located a distance away, where film formation and growth proceed atomistically. Thermal energy is imparted to atoms in a liquid or solid source such that their temperature is raised to the point where they either efficiently evaporate or sublime. Whereas metals essentially evaporate as atoms and occasionally as clusters of atoms, the same is not true of compounds. Very few inorganic compounds evaporate without molecular change and, therefore, the vapor composition is usually different from that of the original solid or liquid source. As a consequence the stoichiometry of the film deposit will generally differ from that of the source [143, 144].

Disadvantages of resistively heated evaporation sources include contamination by crucibles, heaters, and support materials and the limitation of relatively low input power levels. This makes it difficult to deposit pure films or evaporate high-melting-point materials at appreciable rates. Electron beam (e-beam) heating eliminates these disadvantages and has, therefore, become the preferred vacuum evaporation technique for depositing films. In principle, this type of source enables evaporation of virtually all materials over a wide range of practical deposition rates. The evaporant is placed in either a water-cooled crucible or in the depression of a water-cooled copper hearth. The purity of the evaporant is assured because only a small amount of material melts or sublimates so that the effective crucible is the unmelted skull material next to the cooled hearth. For this reason there is no contamination of the evaporant by Cu. Multiple source units are available for either sequential or parallel deposition of more than one material.

Chemical vapor deposition (CVD) is the process of chemically reacting a volatile compound of a material to be deposited, with other gases, to produce a nonvolatile solid that deposits on a suitably placed substrate [144]. It differs from physical vapor deposition (PVD), which relies on material transfer from condensed-phase evaporant or sputter target sources. Because CVD processes do not require vacuum or unusual levels of electric power, they were practiced commercially prior to PVD. Because they are subject to thermodynamic and kinetic limitations and constrained by the flow of gaseous reactants and products, CVD processes are generally more complex than those involving PVD.

Plasma-enhanced chemical vapor deposition (PECVD) is one of the modifications of the conventional CVD process. In the PECVD system,

electric power is supplied to the reactor to generate the plasma. The power is supplied by an induction coil from outside the chamber, or directly by diode glow-discharge electrodes. In the plasma, the degree of ionization is typically only 10^{-4} , so the gas in the reactor consists mostly of neutrals. Ions and electrons travel through the neutrals and get energy from the electric field in the plasma.

2.1.1 Sputtering

Sputtering is a process where atoms are knocked out from a solid target by the bombardment of energetic ions. Sputtering has become a common manufacturing process for a variety of industries. First and foremost is the semiconductor industry, where sputtering technology is used in the metallization process in the production of virtually every integrated circuit [142].

Mechanism of sputtering

Upon bombarding a surface, incoming ions may be reflected back, stick or adsorb, scatter, eject or sputter surface atoms, or get buried in subsurface layers (ion implantation). Surface heating, chemical reactions, atom mixing, and alteration of surface topography are other manifestations of ion bombardment.

In single knock-on process, ion-surface collisions set target atoms in motion and if enough energy is transferred to target atoms, they overcome forces that bind them and sputter. The minimum energy required to do this is called the threshold energy, E_t . Typical values for E_t range from 5 to 40 eV and depend on the nature of the incident ion, and on the mass

and atomic number of the target atoms, the binding energy of atoms to the surface (U_s). Typically, U_s may be assumed to be the heat of sublimation or vaporization and ranges between 2 and 5 eV [144].

At higher ion energies, one or more linear collision cascades are initiated. When this happens the density of recoils is sufficiently low so that most collisions involve one moving and one stationary particle, instead of two moving particles. The result of such processes is sputtering, i.e., the ejection of target atoms. Sputtering in the linear collision-cascade regime has been theoretically modeled by many investigators [145].

The sputter yield S , varies with the incident ion energy E . In the low-energy region near the threshold, S obeys the relation $S \propto E^2$. At the energy region in the order of 100 eV, $S \propto E$. In this energy region, the incident ions collide with the surface atoms of the target, and the number of displaced atoms due to the collision will be proportional to the incident energy. At higher ion energies of 10 to 100 keV, the incident ions travel beneath the surface and the sputter yields are not governed by surface scattering, but by the scattering inside the target. Above 10 keV, the sputter yields will decrease due to energy dissipation of the incident ions deep in the target. Maximum sputter yields are seen in the ion energy region of about 10 keV [142].

Sputtering of alloys

The primary reason for the widespread use of sputtering to deposit metal alloy films is its ability to form stoichiometric thin films. In contrast to the fractionation of alloy melts during evaporation, with subsequent loss of deposit stoichiometry, sputtering allows the deposition of films having the same composition as the target source [144]. This suggests that sputtering

is not governed by thermal processes, but by a momentum transfer process. However, at very high target temperature, thermal diffusion may change the composition of the alloy target, and result non-stoichiometric films. Also under higher substrate temperature, the resultant films show different chemical compositions because of the re-evaporation of the deposited films [142].

The sputtering yield and angular distribution of the sputtered particles are affected by the crystal structure of the target surface. The angular distribution may be either under cosine law or over cosine law when the target is composed of polycrystalline materials. Nonuniform angular distribution is often observed from the single-crystal target. Studies of ion-bombarded single crystals reveal that atom emission reflects the lattice symmetry. In FCC metals it has been demonstrated that atoms are preferentially ejected along the [110] direction, but ejection in [100] and [111] directions also occurs to lesser extents [143]. For BCC metals [111] is the usual direction for atom ejection. These results are consistent with the idea that whenever a beam sees a low density of projected lattice points the ions penetrate more deeply, thus reducing S . Such observations on single crystals confirmed momentum transfer as the mechanism for atomic ejection; the notion of ion-induced melting and evaporation of atoms was dispelled because preferred directions for sublimation of atoms are not observed [144].

The energy of the sputtered atoms is dependent on both the incident ion species and incident bombardment angles. The average energy distribution of the sputtered atoms peaks in between typical energies 2 to 10 eV. In the case of sputtered ions, their average energy is higher than that of sputtered neutral atoms. [142, 144]. Sputtered atoms may have sufficient energy to penetrate one to two atomic layers into the substrate surfaces which is

believed to be the reason for superior adhesion of sputtered film compared with films deposited by other methods. High energy of sputtered atoms plays a significant role in the lowering of epitaxial temperature through enhanced substrate cleaning [143].

Single crystal targets normally sputter preferentially along crystalline directions at elevated temperatures, but when the targets are cooled sputtering is isotropic. Apparently, at lower temperatures the ion bombardment and radiation damage create sufficient structural defects to amorphize surface layers. At higher temperatures, amorphous regions do not form because the defects anneal out; the target remains crystalline and sputters accordingly. Wide variations in S may arise from deep ion penetration or channeling along certain crystallographic directions and a complex damage distribution as a function of ion energy and flux.

The sputter yield S also depends on the incidence angle defined between the directions of ion incidence and the target normal. The yield increases with the incident angle and shows a maximum between angles 60° and 80° , while it decreases rapidly for larger angles. The influence of the angle is also governed by the surface structure of the target [142].

Angular distribution of sputtered atoms from polycrystalline or amorphous targets at normal ion incidence is governed by Knudsen's cosine law, which was observed in a thermal evaporation process [143]. Slight deviations from this law have been observed depending on ion energy, metal, and degree of crystallographic texture in the target.

Sputtering can develop a substantial *floating potential* at the substrate which may cause the ions to accelerate out of the plasma and can cause considerable resputtering [143]. The mechanism through which substrate temperature may influence the sputtered film properties is quite different

from evaporated films. Films deposited through sputtering are subjected to bombardment by ions and/or energetic neutrals which cause damage to the films through the introduction of point defects. For a growing film, low substrate temperatures will suffice to anneal out these defects.

The fraction of impurity species trapped in a sputtered film is expected to be higher than that of the other deposition techniques mainly because of the higher effective sticking coefficient of impurities. However, this fraction can be reduced by techniques like getter sputtering and biased sputtering. In biased sputtering, substrate is deliberately given a negative potential with respect to the plasma to enhance the resputtering from the film where most of the impurities are preferentially removed relative to the atoms of the main film. The possibility of trapping of argon atoms occur only if they arrive at the film surface at energies approximately of the order of 100 eV or more. Hence this possibility can be avoided by carrying out sputtering at high pressures which attenuates the energy of the argon atoms [143].

2.1.2 DC sputtering

In DC sputtering, the sputtering target become the cathode of an electrical circuit, and has a high negative voltage applied to it. The substrate is placed on an electrically grounded anode. These electrodes are housed in a vacuum chamber into which argon gas is introduced to some specified pressure. The electric field accelerates the electrons, which in turn collide with argon atoms, breaking some of them up into argon ions and more electrons to produce the glow discharge. The charged particles thus produced are accelerated by the field, the electrons tending towards the anode (causing more ionization on the way) and the ions towards the cathode, so that a current I flows. When the ions strike the cathode, they may sputter

some of the target atoms off. They may also liberate secondary electrons from the target which are responsible for maintaining the electron supply to sustaining glow discharge. The sputtered atoms from the target fly off in random directions, and some of them land on the substrate, condense there, and form a thin film [142, 143].

In sputtering, the relative film deposition-rate depends on sputtering pressure and current. At low pressures, the cathode sheath is wide, ions are produced far from the target, and their chances of being lost to the walls is great. The mean free electron path between collisions is large, and electrons collected by the anode are not replenished by ion-impact-induced secondary-electron emission at the cathode. Therefore, ionization efficiencies are low and self sustained discharges cannot be maintained below about 10 *mtorr*. As the pressure is increased at a fixed voltage, the electron mean free path is decreased, more ions are generated, and larger currents flow. But if the pressure is too high, the sputtered atoms undergo increased collisional scattering and are not efficiently deposited [143].

Despite the simplicity in technique, simple DC sputtering is no longer employed in production environments because of low deposition rates. These rates cannot be appreciably raised at higher operating pressures, because in addition to more gas scattering, increased contaminant levels of O₂ and H₂O in chamber gases can oxidize cathodes [142]. Thin insulating layers that form on the target further reduce the current and deposition rates. Even at optimum operating conditions, secondary electrons emitted from the cathode have an appreciable probability of reaching the anode or chamber walls without making ionizing collisions with the sputtering gas.

One of the several variants of DC sputtering that have been proposed to enhance the efficiency of the process is triode sputtering. A filament

cathode and anode assembly is installed close to the target, parallel to the plane of the target-substrate electrodes. When the filament is heated to high temperatures, thermionic emission and injection of electrons into the plasma increase the gas-ionization probability. The resulting ions are then extracted by the negative target potential. A disadvantage of triode sputtering is the nonuniform plasma density over target surfaces, which leads to uneven erosion of metal.

2.1.3 Reactive sputtering

In reactive sputtering, thin films of compounds are deposited on substrates by sputtering from metallic targets in the presence of a reactive gas usually mixed with an inert working gas (Ar). Since the drift velocity of the electrons moving through dark space is reduced by the presence of oxygen atoms which temporarily attach electrons and form negative ions, the addition of oxygen gas to a glow discharge in argon result in contraction of dark space and decrease in glow impedance. The most common compounds reactively sputtered are oxides, nitrides, carbides, sulfides, oxycarbides and oxynitrides. In practice, sputter rates of metals drop dramatically when compounds form on the targets. Corresponding decreases in deposition rate occur because of the lower sputter yield of compounds relative to metals. The effect is very much dependent on reactive gas pressure. Sputtering effectively halts at high gas pressures in DC discharges, but the limits are also influenced by the applied power. Conditioning of the target in pure Ar is essential to restore the pure-metal surface and desired deposition rates. Considerable variation in the composition and properties of reactively sputtered films is possible depending on operating conditions [142, 143].

2.1.4 Radio frequency sputtering

If we apply sufficient DC voltage to two metal electrodes of equal area facing one another, a dark space develops at the cathode. Instead of DC, if a low frequency alternating voltage is applied, the system behaves as though it had two cathodes since a dark space is seen at both electrodes since there is ample time for a DC discharge to become fully established within each cycle. At very high frequency of the applied voltage, electrons oscillate in the RF field and pick up sufficient energy from the field to cause ionization in the body of the gas. Thus the minimum pressure required to sustain the discharge gradually decreases with the increase of the frequency of applied field. The electron gains energy from the field if it undergoes collisions with gas atoms while it is oscillating so that its ordered simple harmonic motion is changed to a random motion. The electron can increase the random component of its velocity with each collision until it builds up sufficient energy to make an ionizing collision with a gas atom. Since the energy absorbed is proportional to the square of the electric field, electron can continue to gain energy in the field even though it may be moving either with or against it [142, 143].

Since the applied RF field appears mainly between the two electrodes, an electron which escapes from the inter electrode space as a result of a random collision will no longer oscillate in the RF field and will therefore not acquire sufficient energy to cause ionization. This will be lost to the glow. A magnetic field, applied parallel to the RF field, will constraint the electron motion and reduce their chance of being lost. Thus magnetic field is considerably more important for enhancing the RF discharge than it is for the DC case.

The net result is that there is no need to rely on secondary electrons emitted from the cathode to sustain the discharge. Secondly, at radio frequencies, voltage can be coupled through any kind of impedance so that the electrodes need not be conductors. This makes it possible to sputter any material irrespective of its resistivity.

RF sputtering essentially works because the target self-biases to a negative potential (where the electrode areas are unequal). Once this happens, it behaves like a DC target where positive ion-bombardment sputters away atoms for subsequent deposition. Negative target bias is a consequence of the fact that electrons are considerably more mobile than ions and have little difficulty in following the periodic change in the electric field. The disparity in electron and ion mobilities means that isolated positively charged electrodes draw more electron current than comparably isolated negatively charged electrodes draw positive ion current. For this reason the discharge current-voltage characteristics are asymmetric.

Because the plasma discharge has capacitive as well as resistive characteristics, efficient coupling of the RF power supply to the target requires an impedance-matching network consisting of some combination of variable and fixed capacitors and inductors to ensure maximum power delivery.

2.1.5 Magnetron sputtering

Magnetron sputtering is the most widely used variant of DC sputtering. One to two orders of magnitude more current is typically drawn in magnetron than simple DC discharges for the same applied voltage. Important implications of this are higher deposition rates or alternatively, lower voltage operation than for simple DC sputtering. Another important advantage is reduced operating pressures. At typical magnetron-sputtering

pressures of a few millitorr, sputtered atoms fly off in ballistic fashion to impinge on substrates. Hence we can avoid the gas phase collisions and scattering at high pressures which randomise the directional character of the sputtered-atom flux and lower the deposition rate. Here, for the same electrode spacing and minimum target voltage a stable discharge can be maintained at lower pressures [142].

In planar magnetron sputtering, targets erode preferentially in the race-track region where the plasma is most intense. This leaves a kind of race-track ditch or depression that progressively deepens, surrounded by a much larger target area that suffers less loss of metal. Such target erosion has a number of undesirable consequences such as:

1. Low process efficiency (only 10-30% of the target surface area is utilized)
2. Inhomogeneous metal loss during reactive sputtering is such that the racetrack remains metallic while the surrounding target area becomes covered with insulator films, enhancing the probability of arcing.
3. The uniformity of deposited films is adversely affected.
4. Nonuniform plasma erosion tends to reduce target life
5. Elastic distortion of the target may result in loss of contact to the water-cooled backing plate and a corresponding drop in cooling efficiency.

A remedy for many of these interrelated problems is to maintain uniform target erosion during sputtering. This is practically accomplished by mechanically moving the array of permanent magnets over the back face of planar targets [146].

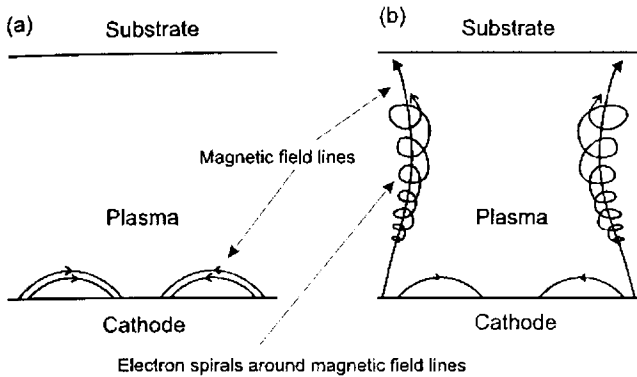


Figure 2.1: Principle of magnetic plasma confinement in a (a) conventional and (b) unbalanced magnetron

Unbalanced magnetron sputtering

The plasma in a conventional magnetron discharge is well confined in a torroidal magnetron magnetic field and so it is localized in a very close vicinity of sputtering target (Figure 2.1).

An unbalanced magnetron (UBM) has a proper magnetic field configuration in which a finite degree of the field lines from the outer magnetic pole diverge to the substrate, although the rest of the lines finish on the inner pole behind the target. Sufficient plasma density and a positive ion current on a metallic substrate even at a large distance from the target can be achieved in the UBM as compared with the conventional balanced magnetron (BM). Thin film deposition by physical sputtering in a UBM follows considerable positive ion impact on the surface during the process. The ion impact on the surface has a direct influence on the films morphological, compositional and crystallization properties. In particular, the surface

bombardment of high energy ions causes defects in the crystal structure, while the low-energy ions enhance crystallization. Therefore, it is of prime importance to control both the quality and the quantity of the ion bombardment in the magnetron in order to produce a thin film with satisfactory properties [142, 146].

2.1.6 Specifications of sputtering system

The sputtering system, which is used to carry out the work presented in this thesis, is a planar magnetron sputtering system. It consists of a box type steel vacuum chamber which houses two 2" magnetron guns (Sierra Applied Sciences, USA) and a substrate holder. There are provisions for supplying the working gas argon and reactive gas oxygen. Gas flow to the chamber is controlled by separate gas flow meters (GFC 17, Aalborg, USA). A circular substrate holder is attached to a programmable stepper motor to rotate it during the deposition.

Required base vacuum is created in the chamber using an oil diffusion pump backed by an oil rotary pump. Cold water is circulated through the diffusion pump and magnetron guns. For the deposition of channel layers in TFTs, co-sputtering method is employed. In this technique, two targets are simultaneously sputtered so that an alloy of the materials are formed at the substrate. During co-sputtering, either two separate RF generators or one RF generator and one DC power source are used to energize the magnetron guns. We have two RF generators: one 300 W (PFG 300 RF, Huttinger, Germany) maximum capacity and another one with 150 W capacity (Digilog Instruments, India). Huttinger RF generator is optically coupled to an automatic matching network. Digilog RF generator is coupled to plasma chamber through a matching network which is manually

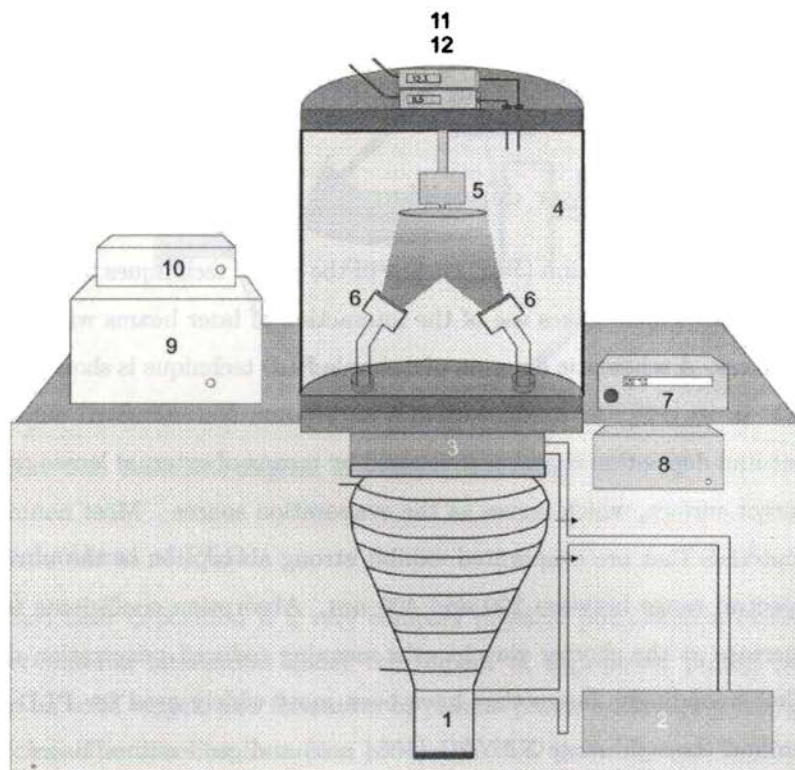


Figure 2.2: Schematic diagram of co-sputtering setup used in the study. (1) diffusion pump, (2) rotary pump, (3) baffle valve, (4) box-type vacuum chamber, (5) stepper motor with substrate holder, (6) magnetron guns, (7) RF generator, (8) matching network, (9) DC power supply, (10) stepper motor controller, (11&12) gas flow controllers

tuned to transfer maximum power to the plasma. DC power sources is a current controlled high voltage source (1000 V, 500 mA) manufactured by Digilog instruments. Throughout this study, deposition is carried out at room temperature without any intentional substrate heating.

2.1.7 Pulsed laser deposition

Pulsed laser deposition (PLD) is one of the newer techniques for depositing thin films which makes use of the interaction of laser beams with material surfaces. A schematic diagram of a simple PLD technique is shown in figure 2.3. In its simplest configuration, a high-power laser situated outside the vacuum deposition chamber is focused by means of external lenses onto the target surface, which serves as the evaporation source. Most nonmetallic materials that are evaporated exhibit strong absorption in the ultraviolet spectral range between 200 and 400 nm. Absorption coefficients tend to increase at the shorter wavelengths meaning reduced penetration depths. Correspondingly, lasers that have been most widely used for PLD center around the solid state Nd:YAG (1064 nm) and gas excimer lasers. In the case of the former, the 1064 nm radiation is frequency doubled twice so that outputs of 355 and 266 nm are produced. Although attenuated in power relative to the fundamental output, they are sufficiently intense for laser ablation. Other popular gas excimer lasers are the ArF (193 nm), KrF (248 nm), and XeCl (308 nm) lasers. Commercial versions of these deliver outputs of ~ 500 mJ/pulse at pulse repetition rates of several hundred Hz at ns pulse width.

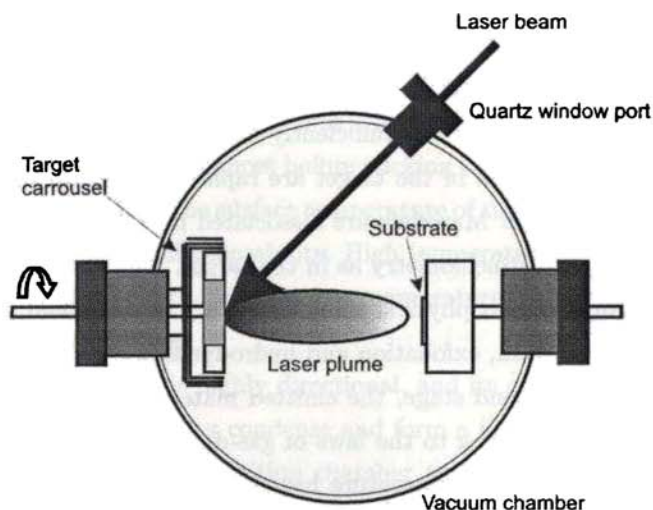


Figure 2.3: Schematic diagram of a simple PLD setup.

Mechanisms of PLD

Pulsed laser deposition is a very complex physical phenomenon involving laser-material interaction under the impact of high-power pulsed radiation on solid target, and formation of plasma plume with highly energetic species. The thin film formation process in PLD generally can be divided into the following four stages.

1. Interaction of laser radiation with the target material.
2. Dynamics of the ablated materials.
3. Deposition of the ablation materials on the substrate.
4. Nucleation and growth of a thin film on the substrate surface.

Various properties of deposited thin film strongly depends on each of the stages specified above. In the first stage, the laser beam is focused onto the surface of the target. At sufficiently high flux densities and short pulse duration, all elements in the target are rapidly heated up to their evaporation temperature. Materials are dissociated from the target surface and ablated out with stoichiometry as in the target. The ablation mechanisms involve many complex physical phenomena such as collisional, thermal, and electronic excitation, exfoliation and hydrodynamics.

During the second stage, the emitted materials tend to move towards the substrate according to the laws of gas-dynamics. The spot size of the laser and the plasma temperature has significant effects on the deposited film uniformity. The target-to-substrate distance is another parameter that governs the angular spread of the ablated materials.

The third stage is important to determine the quality of the thin film. The ejected high-energy species impinge onto the substrate surface and may induce various type of damage to the substrate. These energetic species sputter some of the surface atoms from the growing film and a collision region is formed between the incident flow and the sputtered atoms. Film grows after a thermalized region is formed. The region serves as a source for condensation of particles. When the condensation rate is higher than the rate of particles ejected by the sputtering from the substrate, thermal equilibrium condition can be reached quickly and film grows on the substrate surface. Ions in the plasma are accelerated to as much as 100 to 1000 eV [147].

Nucleation-and-growth of films depends on many factors such as the density, energy, ionization degree, and the type of the condensing material, as well as the temperature and the physico-chemical properties of the

substrate. The critical size of the nucleus depends on the deposition rate and the substrate temperature. The film growth depends on the surface mobility of the adatom (vapour atoms). Normally, the adatom will diffuse through several atomic distances before sticking to a stable position within the newly formed film. The surface temperature of the substrate determines the adatom's surface diffusion ability. High temperature favours rapid and defect free crystal growth, whereas low temperature deposition may result in amorphous structures.

In PLD, the plume is highly directional, and its contents are propelled to the substrate where they condense and form a film. Gases (O_2 , N_2) are often introduced in the deposition chamber to promote surface reactions or maintain film stoichiometry. Precautions are usually taken to minimise the number of gross particulates ejected as a result of splashing from being incorporated into the depositing film. Splashing of macroscopic particles during laser-induced evaporation is a significant drawback of PLD. High directionality of the plume is another major drawback, which makes it difficult to uniformly deposit films over large area.

The generation of particulates during splashing is believed to have several origins. These include the rapid expansion of gas trapped beneath the target surface, a rough target surface morphology whose mechanically weak projections are prone to fracturing during pulsed thermal shocks, and superheating of subsurface layers before surface atoms vaporize. A common strategy for dealing with splashing effects is to interpose a rapidly spinning pinwheel-like shutter between the target and substrate. The slower moving particulates can be batted back, allowing the more mobile atoms, ions, and molecules to penetrate this mechanical mass filter. Window materials, an important component in PLD systems, must generally satisfy

the dual requirement of optical transparency to both visible and ultraviolet light. Relatively few materials are suitable for this demanding role, but MgF_2 , sapphire, CaF_2 , and UV-grade quartz have served as suitable window materials.

2.2 Characterisation tools

2.2.1 Thin film thickness

Thickness is one of the most important thin film parameter to be characterised since it plays an important role in the film properties unlike a bulk material. Microelectronic applications generally require the maintenance of precise and reproducible film metrology (i.e., thickness as well as lateral dimensions). Various techniques are available to characterise the film thickness which are basically divided into optical and mechanical methods, and are usually nondestructive but sometimes destructive in nature. Film thickness may be measured either by in-situ monitoring of the rate of deposition or after the film deposition.

The stylus profiler takes measurements electromechanically by moving the sample beneath a diamond tipped stylus. The high precision stage moves the sample according to a user defined scan length, speed and stylus force. The stylus is mechanically coupled to the core of a linear variable differential transformer (LVDT). The stylus moves over the sample surface. Surface variations cause the stylus to be translated vertically. Electrical signals corresponding to the stylus movement are produced as the core position of the LVDT changes. The LVDT scales an ac reference signal proportional to the position change, which in turn is conditioned and converted to a digital format through a high precision, integrating, analog-to-digital

converter [148]. The film whose thickness has to be measured is deposited with a region masked. This creates a step on the sample surface. Then the thickness of the sample can be measured accurately by measuring the vertical motion of the stylus over the step.

The thicknesses of the thin films prepared for the work presented in this thesis were measured by a stylus profiler (Dektak 6M). Several factors which limit the accuracy of stylus measurements are [144]:

1. Stylus penetration and scratching of films (makes problem in very soft films)
2. Substrate roughness. Excessive noise is introduced into the measurement as a result of substrate roughness and this creates uncertainty in the position of the step.
3. Vibration of the equipment. Proper shock mounting and rigid supports are essential to minimise background vibrations.

In modern instruments the leveling and measurement functions are computer controlled. The vertical stylus movement is digitized and data can be processed to magnify areas of interest and yield best-profile fits. Calibration profiles are available for standardization of measurements.

2.2.2 Structural characterisation

Glancing angle x-ray diffraction (GXRd)

Glancing angle x-ray diffraction (GXRd) is a nondestructive, surface sensitive technique used to record the diffraction pattern of thin films with minimum contribution from the substrate. In the conventional XRD patterns of thin films deposited on a substrate, the contribution from the

substrate to the diffraction can overshadow the contribution from the thin film. Conventional x-ray diffraction reveals information about a top layer of a thickness of the order of 5-10 μm . By increasing the path length of the incident x-ray beam through the film, the intensity from the film can be increased. Thin films as thin as 100 \AA can be analysed by using a grazing incidence angle arrangement combined with a parallel beam geometry. This technique is based on the fact that, for high energy x-rays, the refractive index of material is slightly less than unity, as a result of which material is less refractive (for x-rays) than it is for vacuum. One can therefore have total external reflection from a surface if the incident angle is small enough (typically 1-25 milliradians or 0.05 - 1.5°), depending on the substrate electron density and the x-ray energy. At this point the substrate is not entirely invisible to x-rays, but only an evanescent wave penetrates into and scatters from it. The x-ray intensity is therefore highest at the surface [149].

In the conventional $\theta/2\theta$ geometry, a parafocusing arrangement is used where the x-ray source and the detector slit are at the focal points of the incident and diffracted beams, respectively. For GXRD, the incident and diffracted beams are made nearly parallel by means of a narrow slit on the incident beam and a long Soller slit on the detector side. In addition, the stationary incident beam makes a very small angle with the sample surface, which increases the path length of the x-ray beam through the film. This helps to increase the diffracted intensity, while at the same time, reduces the diffracted intensity from the substrate. Overall, there is a dramatic increase in the film signal to the background ratio. Since the path length increases when the grazing incidence angle is used, the diffracting volume increases proportionally which subsequently gives increased signal strength. During

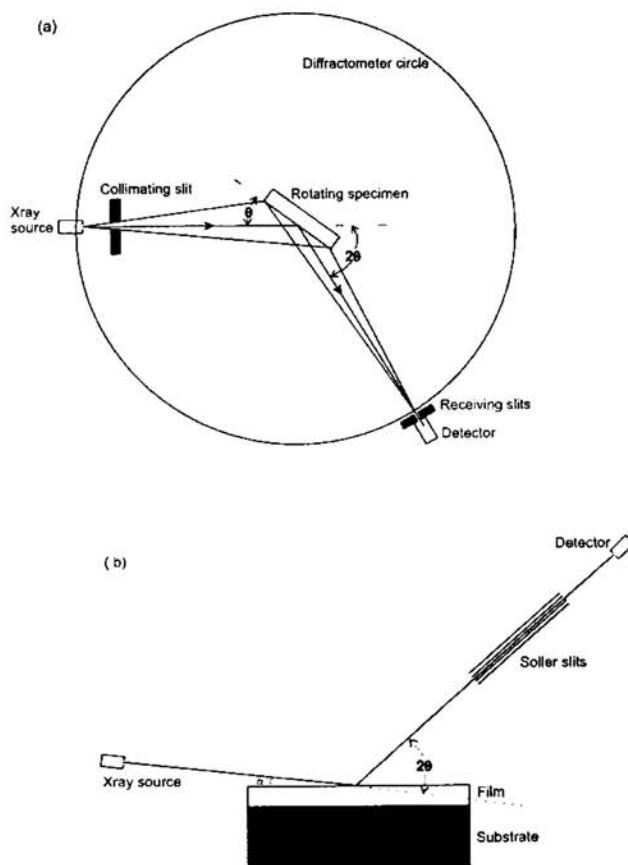


Figure 2.4: Geometries of (a) conventional and (b) glancing angle XRD.

the collection of the diffraction spectrum, only the detector rotates through the angular range, thus keeping the incident angle, the beam path length, and the irradiated area constant. The long Soller slit on the receiving side allows only those beams that are nearly parallel to arrive at the detector. This has an added advantage of reducing sensitivity to sample displacement from the rotation axis.

In the present study a Rigaku RINT-2000 GXRD with Cu $K\alpha$ radiation was used to analyse the deposited thin films.

Atomic force microscopy (AFM)

Scanning probe microscopy (SPM) is a fundamentally simple technology that is capable of imaging and measuring surfaces on a fine scale and of altering surfaces at the atomic level. There are three elements common to all probe microscopes.

1. A small, sharp probe. The interactions between the surface and the probe are used to interrogate the surface.
2. A detection system which monitors the product of the probe-surface interaction (e.g., a force, tunneling current, change in capacitance, etc.).
3. Scanning technique: Either the probe or sample is raster-scanned with nanoscale precision. By monitoring the interaction intensity, any surface variation translates to topographical information from the surface and generates a three-dimensional image of the surface.

The most commonly used SPMs are atomic force microscopy (AFM) and scanning tunneling microscopy (STM). AFM is the most widely used

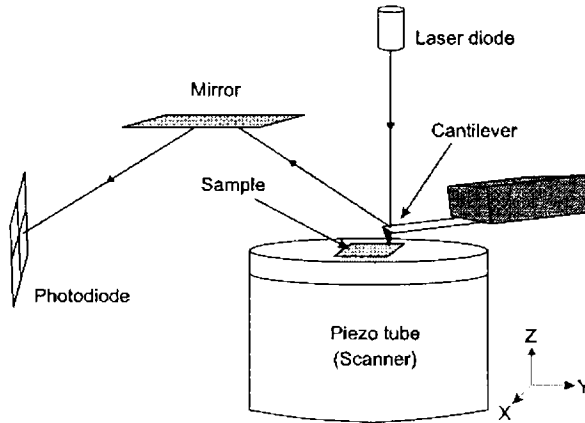


Figure 2.5: Schematic diagram of atomic force microscope.

local probe devices. It gives quick access to a wide range of surface properties, including mechanical, electrical, magnetic, and other properties, with good spatial resolution. In AFM, the probe tip is affixed to a cantilevered beam. The probe interacts with the surface and the resulting force deflects the beam in a repulsive manner, as described by Hooke's Law. In the same manner that a spring changes dimensions under the influence of forces, the attractive and repulsive forces between atoms of the probe and the surface can also be monitored when brought extremely close to each other. Hence, the net forces acting on the probe tip deflect the cantilever, and the tip displacement is proportional to the force between the surface and the tip. As the probe tip is scanned across the surface, a laser beam reflects off the cantilever. By monitoring the net (x , y , and z) deflection of the cantilever, a three-dimensional image of the surface is constructed (Figure 2.5).

The AFM typically operates in either of two principal modes: constant-force mode (with feedback control) and constant-height mode (without feedback control). Once the AFM has detected the cantilever deflection, it can generate the topographic data set by operating in one of the two modes-constant-height or constant-force mode. In constant-height mode, the spatial variation of the cantilever deflection can be used directly to generate the topographic data set because the height of the scanner is fixed as it scans. In constant-force mode, the deflection of the cantilever can be used as input to a feedback circuit that moves the scanner up and down in the z-axis, responding to the topography by keeping the cantilever deflection constant. In this case, the image is generated from the scanner's motion. With the cantilever deflection held constant, the total force applied to the sample is constant. The biggest advantage of AFM is that most samples can be investigated in their natural state, including biological samples (even in an aqueous environment), which is otherwise impossible by electron microscopy methods.

A SPI - 3800N, S.I.I AFM was used for roughness analysis in the present study.

2.2.3 Compositional analysis

In order to check the stoichiometry of the deposited films, compositional analysis is essential and the characterisation tools used in the present investigation is described below.

Energy dispersive x-ray spectroscopy (EDAX)

EDAX (or EDX) is a technique used for identifying the elemental composition of the specimen, on an area of interest. The EDAX analysis system works as an integrated feature of a SEM, and can not operate on its own without the latter [34, 150].

During EDAX analysis, the specimen is bombarded with an electron beam inside the SEM chamber. The bombarding electrons collide with the specimen atom's own electrons, knocking some of them off in the process. A position vacated by an ejected inner shell electron is eventually occupied by a higher-energy electron from an outer shell. In this process, the transferring outer electron must give up some of its energy by emitting an x-ray. The amount of energy released by the transferring electron depends on which shell it is transferring from, as well as which shell it is transferring to. Furthermore, the atom of every element releases x-rays with unique amount of energy during the transferring process. Thus, by measuring the energy of the x-rays emitted by a specimen during electron beam bombardment, the identity of the atom from which the x-ray was emitted can be established.

The output of an EDAX analysis is a spectrum, which is a plot of how frequently an x-ray is received for each energy level. An EDAX spectrum normally displays peaks corresponding to the energy levels for which the most x-rays had been received. Each of these peaks are unique to an atom, and therefore corresponds to a single element. The higher a peak in a spectrum, the more concentrated the element is in the specimen. An EDAX spectrum plot not only identifies the element corresponding to each of its peaks, but the type of x-ray to which it corresponds as well. For example,

a peak corresponding to the amount of energy possessed by x-rays emitted by an electron in the L-shell going down to the K-shell is identified as a K_{α} peak. The peak corresponding to x-rays emitted by M-shell electrons going to the K-shell is identified as a K_{β} peak.

X-ray fluorescence spectroscopy (XRF)

XRF is a nondestructive, rapid, precise, and potentially very accurate method used for elemental analysis of materials (solids, liquids and powders) [151]. A x-ray source is used to irradiate the specimen and to cause the elements in the specimen to emit (or fluoresce) their characteristic x-rays. The detector system is used to measure the positions of the fluorescent x-ray peaks for qualitative identification of the elements present, and to measure the intensities of the peaks for quantitative determination of the composition. All elements, except H, He, and Li, can be analyzed by XRF.

When an x-ray photon strikes an atom and knocks out an inner shell electron, a readjustment occurs in the atom by filling the inner shell vacancy with one of the outer electrons and simultaneously emitting an x-ray photon. The emitted photon (or fluorescent radiation) has the characteristic energy of the difference between the binding energies of the inner and the outer shells.

The instrumentation part includes a primary x-ray source, a crystal spectrometer, and a detection system. A schematic x-ray experiment is shown in figure 2.6. Fluorescent x-rays emitted from the specimen are caused by high-energy (or short-wavelength) incident x-rays generated by the x-ray tube. The fluorescent x-rays from the specimen travel in a certain direction, pass through the primary collimator. The analyzing crystal, oriented to reflect from a set of crystal planes reflects one x-ray wavelength

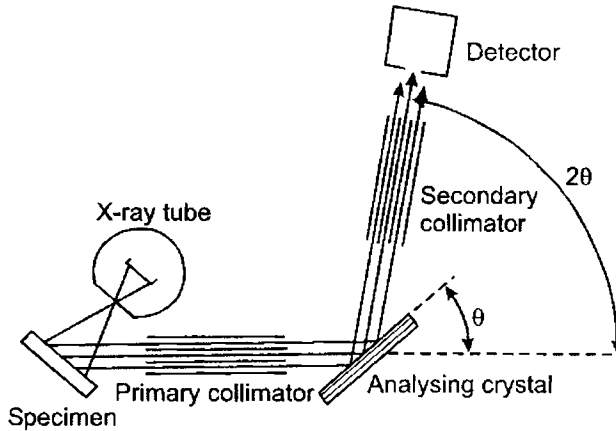


Figure 2.6: Schematic diagram of x-ray fluorescence spectrometer.

(λ) at a given angle (θ) in accordance with Bragg's law: $n\lambda = 2d \sin\theta$, where n is a small positive integer giving the order of reflection. By rotating the analysing crystal at one-half the angular speed of the detector, the various wavelengths from the fluorescent x-rays are reflected one by one as the analysing crystal makes the proper angle θ for each wavelength. The intensity of at each wavelength is then recorded by the detector. This procedure is known also as the wavelength-dispersive method.

Rigaku ZSX100E XRF was used in the present study to analyse chemical composition of the deposited films.

2.2.4 Hall effect measurement

The Hall effect measurement technique is widely applied in the characterisation of semiconductor materials as it gives the resistivity, the carrier density, type of carriers and the mobility of carriers. When a magnetic field

is applied to a conductor perpendicular to the current flow direction, an electric field will be developed at perpendicular to the direction of magnetic field and the current. This phenomenon is known as Hall effect and the developed voltage is called Hall voltage.

The force acting on a charge (q) moving with a velocity v in the presence of an electric (E) and magnetic (B) fields is given by the vector expression

$$\vec{F} = q(\vec{E} + \vec{v} \times \vec{B}) \quad (2.1)$$

For n-type and p-type samples, the electrons and holes respectively deflect to the same side of the sample for the same current direction because electrons flow in the opposite direction to holes and have opposite charge.

The Hall coefficient R_H is defined as

$$R_H = \frac{V_H d}{BI} \quad (2.2)$$

where d is the sample dimension in the direction of magnetic field B , V_H is the Hall voltage and I is the current through the sample [34]. Hall coefficient is related to hole (p) and electron (n) densities by the equation:

$$p = \frac{1}{qR_H}; \text{ and } n = -\frac{1}{qR_H} \quad (2.3)$$

Equation 2.3 is derived under the assumption of energy independent scattering mechanisms. With this assumption relaxed, the expressions for the hole and electron densities become

$$p = \frac{r}{qR_H}; \text{ and } n = -\frac{r}{qR_H} \quad (2.4)$$

where r is the Hall scattering factor, defined by $r = \langle \tau^2 \rangle / \langle \tau \rangle^2$, with τ being the mean time between carrier collisions. The scattering factor depends on

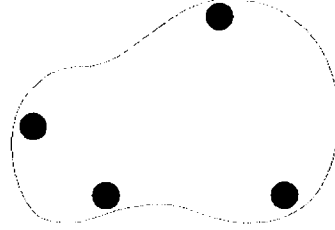


Figure 2.7: Lamella-type van der Pauw Hall sample.

the type of scattering mechanism in the semiconductor and generally lies between 1 and 2. For lattice scattering, $r = 1.18$, for impurity scattering $r = 1.93$, and for neutral impurity scattering $r = 1$. The scattering factor is also a function of magnetic field and temperature and can be determined by measuring R_H in the high magnetic field limit, i.e.,

$$r = \frac{R_H(B)}{R_H(B = \infty)} \quad (2.5)$$

In the high field limit $r \rightarrow 1$.

The Hall mobility μ_H is defined by

$$\mu_H = \frac{|R_H|}{\rho} = |R_H|\sigma \quad (2.6)$$

substituting the value of σ for hole and electron, the equation 2.6 becomes

$$\mu_H = r\mu_p; \mu_H = r\mu_n \quad (2.7)$$

for extrinsic p- and n-type semiconductors, respectively. Hall mobilities can differ significantly from conductivity mobilities since r is generally larger than unity. For most Hall-determined mobilities, r is taken as unity.

A more general geometry is the irregularly shaped sample in figure 2.7. The theoretical foundation of Hall measurement evaluation for irregularly

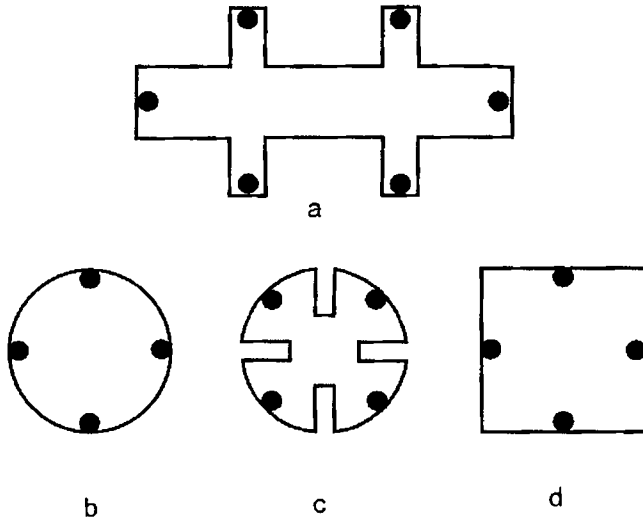


Figure 2.8: Bridge-type (a) and lamella-type (b-d) Hall configuration.

shaped samples is based on conformal mapping developed by van der Pauw. He showed how the resistivity, carrier density, and mobility of a flat sample of arbitrary shape can be determined without knowing the current pattern if the following conditions are met: contacts should be point contacts located symmetrically on the periphery of the sample, the sample is uniformly thick, and does not contain isolated holes. This is not achievable in practice, and some error is introduced thereby. Some common lamella or van der Pauw shapes are shown in figure 2.8.

For semiconducting films on insulating substrates, the mobility is frequently observed to decrease toward the substrate. Surface depletion forces the current to flow in the low-mobility portion of the film, giving apparent mobilities lower than true mobilities.

Hall effect measurements are simple to interpret for uniformly doped samples. Non-uniformly doped layer measurements are more difficult to interpret. If the doping density varies with film thickness, then its resistivity and mobility also vary with thickness. A Hall effect measurement gives the average resistivity, carrier density, and mobility.

Electrical resistivity and Hall coefficients of the films described in this thesis were measured by four probe van der Pauw configuration with AC modulation of magnetic field at room temperature using RESITEST 8300 (Toyo Corporation, Japan) Hall effect measurement setup.

2.2.5 Optical characterisation

Optical absorption coefficients of thin films can be determined from optical transmission or absorption measurements. During transmission measurements light is incident on the sample and the transmitted light is measured as a function of wavelength. The sample is characterised by reflection coefficient R , absorption coefficient α , complex refractive index $(n_1 - ik_1)$, and thickness t [34]. The absorption coefficient is related to the extinction coefficient k_1 by the equation

$$\alpha = \frac{4\pi k_1}{\lambda} \quad (2.8)$$

The transmitted light I_t can be measured absolutely or as the ratio of transmitted to incident light. The transmittance T of a sample with identical front and back reflection coefficient and light incident normal to the sample surface is

$$T = \frac{(1 - R)^2 e^{-\alpha t}}{1 + R^2 e^{-2\alpha t} - 2R e^{-\alpha t} \cos\phi} \quad (2.9)$$

where $\phi = 4\pi n_1 t/\lambda$ and the reflectance R is given by

$$R = \frac{(n_0 - n_1)^2 + k_1^2}{(n_0 + n_1)^2 + k_1^2} \quad (2.10)$$

where n_0 is the refractive index of the surrounding medium.

Semiconductors are generally transparent ($\alpha \approx 0$) for photon energies less than the band gap energy (E_g) and the transmittance becomes

$$T = \frac{(1 - R)^2}{1 + R^2 - 2R\cos\phi} \quad (2.11)$$

If the resolution of the instrument is insufficient to resolve the fine-structure oscillations, then above equation becomes

$$T = \frac{(1 - R)^2}{1 + R^2} = \frac{1 - R}{1 + R} \quad (2.12)$$

Optical bandgap of the films, presented in the thesis, are determined from the transmission (T) and reflection (R) data. Actual optical transmission is calculated as $T^* = T/(1 - R)$. Then, the absorption coefficient (α) of the film is given by the equation:

$$\alpha = \frac{1}{t} \ln \left(\frac{1}{T^*} \right) \quad (2.13)$$

where t is the thickness of the film.

As per equation 1.5, the optical bandgap (Tauc gap) of amorphous films presented in this thesis are determined by plotting $(\alpha h\nu)^{0.5}$ versus $h\nu$ and taking the intercept to energy axis. For, direct bandgap crystalline films, bandgap can be estimated from a plot of $(\alpha h\nu)^2$ versus $h\nu$.

For the measurement of T and R data, Hitachi U-4000 UV-VIS-NIR spectrophotometer was used in this study.

2.3 Thin film transistors (TFT)

Eventhough the basic principle of the field-effect transistor (a junction filed effect transistor, JFET) was proposed by Julius Edgar Lilienfeld as early as 1925 it got much attention in late 1970s only. Whilst several device structures and several semiconductor materials like CdSe, Te, InSb and Ge were investigated, the competition from the metal oxide semiconductor field effect transistor (MOSFET), based on the crystalline silicon technology, led the TFT technology to backcloth. Towards 1970, the requirement of low cost electronics for large area applications, like in displays, persuaded the scientists to think about alternatives for crystalline silicon. This helped TFT technology to become a forerunner in this scenario. In 1979, LeComber, Spear and Ghaith described a TFT using a-Si:H as the active semiconductor material. After that, technology underwent several modifications in the use of active channel layer material to achieve considerable carrier mobility and switching ratio. Since the mid-1980s, the silicon-based TFTs become the most important devices for active matrix liquid crystal displays (AMLCDs) and have successfully dominated the large area liquid crystal display (LCD) product market. Meanwhile, TFTs based on organic semiconductor channel layers were introduced in 1990 with electron mobilities similar to that of a-Si:H. Eventhough this new class of TFTs are very promising candidates for integration onto flexible substrates they also suffer from the reduced carrier mobility which limits its applications in circuits requiring high current and high speed operations. More recently, the TFT concept was fused with transparent semiconducting oxides to create the transparent thin-film transistor (TTFT).

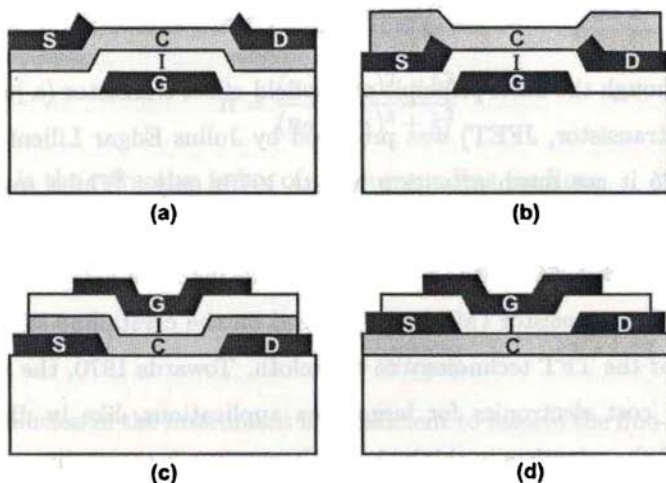


Figure 2.9: Different types of TFT structures. (a) staggered bottom gate, (b) coplanar bottom gate, (c) staggered top gate and (d) coplanar top gate. Symbols: S: source, D: drain, G: gate, I: insulator, and C: channel.

2.3.1 Thin film transistor structures

According to the position of the electrodes, there are four basic TFT structures: co-planar top-gate, co-planar bottom gate, staggered top-gate, and staggered bottom-gate, as shown in the figure 2.9. In a coplanar configuration, the source and drain contacts and the insulator are on the same side of the channel whereas, in a staggered configuration, the source and drain contacts are on opposite sides of the channel from the insulator. Both the staggered and the coplanar configurations are further categorized as bottom-gate and top-gate structures.

Different steps adopted for the TFT fabrication typically determines the selection of a particular structure. Generally, insulator layer deposition

requires the use of a higher power for evaporation or sputtering as compared to deposition of other layers. In the coplanar top-gate structure, the semiconductor channel layer is deposited first. Here the maximum semiconductor processing temperature is limited only by the semiconductor and the substrate. However, the high power deposition of insulator layer may damage the channel-insulator interface which ultimately limits the device performance. In bottom-gate structures, the insulator is deposited first. If the insulator is deposited using a plasma-process, such as RF sputtering or plasma-enhanced chemical vapor deposition, the plasma-induced damage to the channel layer can be reduced using this structure.

In a-Si:H TFTs, the co-planar structure is difficult to realize. a-Si:H TFTs utilise ion implantation to form an ohmic contact to the semiconductor. To avoid the damage from implantation, the channel must be protected during the implantation process. If the insulator is used as an implant-block, there is no source/drain-to-gate overlap. Without this overlap, the series resistance increases and retards carrier injection [152]. In addition, the co-planar structure has increased parasitic resistance as compared to the staggered structure due to a smaller effective contact area.

While staggered structures are commonly used in amorphous silicon TFTs, the coplanar structure is popular in polycrystalline silicon TFTs [130].

2.3.2 Basic device operation

Field effect is the phenomenon where the conductivity of a semiconductor is modulated by an electric field applied normal to the surface of the semiconductor. In a junction field effect transistor (JFET), the depletion region

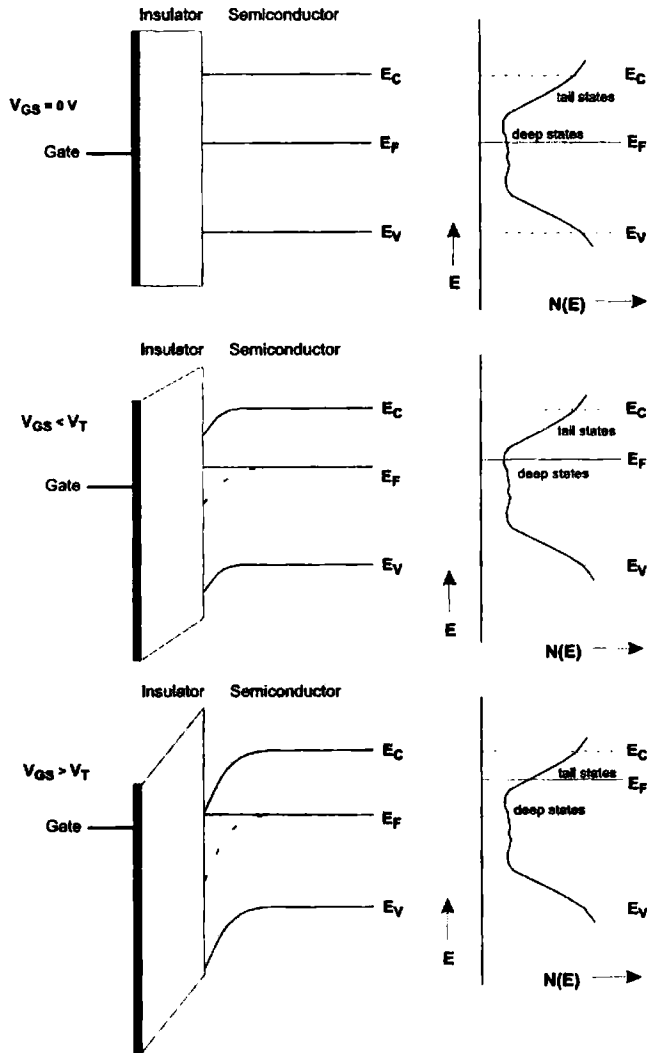


Figure 2.10: Schematic illustration of the basic operation of an amorphous channel TFT showing energy band bending for different biasing conditions.

associated with the pn junctions directly modulates the semiconductor conductivity between the source and drain contacts. The operation of a TFT can be understood on the basis of the working of a MOSFET. Figure 2.10 shows the structure and energy band diagrams of an n-channel, TFT [130].

At zero gate voltages the energy bands are close to the flatband condition. For negative gate voltage ($V_{GS} < 0$), the electric field across the insulator acts in such way that it repels mobile electrons in the semiconductor layer and pushes them deeper into the semiconductor. This creates a depletion layer near the insulator-semiconductor interface and relates to upward band bending in the insulator and the semiconductor (near the interface).

For positive gate voltages, less than the threshold voltage, electrons in the semiconductor are attracted towards the interface, creating an accumulation layer (or channel) near the insulator-semiconductor interface and a depletion region in the bulk. Biasing in this “subthreshold” regime causes downward band bending in the the insulator and the semiconductor (near the interface), and the Fermi level moves through the tail states, which are then occupied. Further increase in the gate voltage modulates the conductivity of the surface layer and causes increased degree of band bending (Figure 2.10). The gate voltage at which there is an appreciable electron carrier density present at the interface establishes the threshold voltage (i.e. $V_{GS} = V_T$). Now that channel formation has been established, application of a positive voltage on the drain attracts electrons towards the drain and accounts for the drain current, I_D (Figures 2.11 a & b). Initially, the drain current increases linearly with drain-source voltage V_{DS} (Figures 2.11 c & f). As the drain voltage increases, the width of the depletion region near the drain also increases. The voltage at which the channel region near the

drain is depleted of carriers, negating the effect of the surface accumulation layer, is the pinch-off voltage V_P or the saturation voltage V_{sat} (Figures 2.11 d & g). Further increase in V_{GS} confines the channel more towards the source side and drain current remains constant if the change in channel length is small compared to the channel length (Figures 2.11 e & h).

2.3.3 Modes of operation

TFTs can be operated in enhancement mode or depletion mode depending on whether it require a gate voltage to induce the channel conduction. In an enhanced mode of operation, the channel conductance is low in the absence of an applied gate voltage. Hence a low carrier density in the channel is essential to achieve this mode. Most conventional a-Si:H TFT devices use an undoped amorphous Si:H layer as the channel and operate in the enhancement mode. In contrast, if a gate bias voltage is required to deplete the channel of carriers, then it is called as depletion mode. Hence a depletion mode TFT consumes power even in its off state. For low power displays, the primary interest is in TFT devices that operate in enhancement mode exhibiting a normally off channel state.

2.3.4 Dielectrics

Development of transparent TFTs (TTFTs) demands the use of high band gap dielectric materials, higher than the semiconductor, with preferable conduction band offset, to avoid high leakage current. Also a good interface formation with the semiconductor layer is crucial for the electron transport through the channel. Although traps present anywhere in the semiconductor affect TFT operation, traps at the insulator-semiconductor

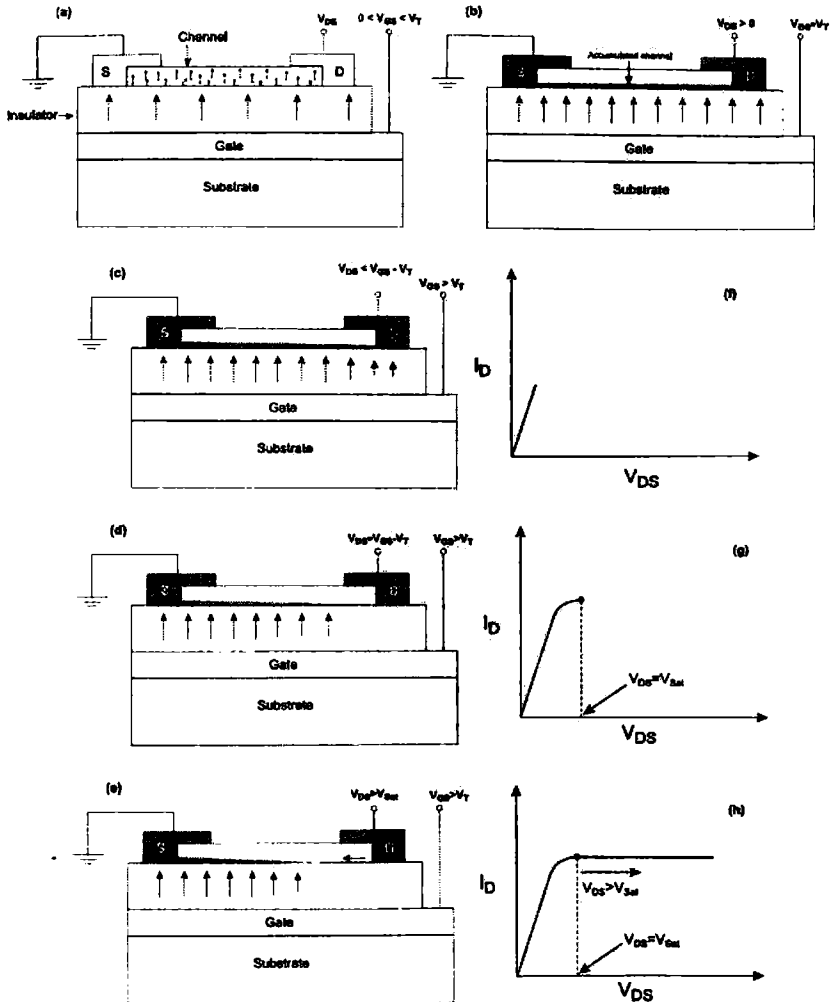


Figure 2.11: Schematic illustration of working of an n-channel TFT. (a) Electrons are attracted by the applied electric field when $0 < V_{GS} < V_T$. (b) Channel formation at $V_{GS} = V_T$. Figures (c-e) show the variation in accumulated charge density with respect to the increase in V_{DS} (near the drain terminal, charge density becomes zero) for a fixed gate voltage $V_{GS} > V_T$. Figures (f-g) show corresponding variations in drain current.

interface play a major role. Interface traps are formed because of unsatisfied dangling bonds and lattice mismatch between materials at an interface. Depending upon the position of Fermi level, these traps may act as donor like or acceptor like. Dielectrics with high dielectric constant (κ) are preferred in TFTs, since it allows the use of thicker dielectrics without decreasing the gate capacitance with better pin hole free layer, without increasing the on voltage and reducing the leakage current. Up to now, most of the TFTs have been produced using an engineered multilayered structure of aluminium oxide and titanium oxide (ATO), deposited by atomic layer deposition (ALD). This material has a high resistivity (10^{15}), high break down voltage (>4 MV/cm), and high dielectric constant ($\kappa \sim 16$) [153]. However, the ALD is not low temperature compatible. So the production of high quality high κ dielectrics at low temperatures are very important. Low temperature deposition generally gives amorphous dielectrics which reduces the leakage current due to the absence of leakage paths through grain boundaries [154]. Evaporated films are reported to show better interfaces with lower oxide charge density and interface trapped charge, than sputtered films [153]. Compared to HfO_2 , Ta_2O_5 shows better electrical and interfacial properties [153]. However, Ta_2O_5 has a low band offset with most of the channel layer materials used in TFTs. Hence a thicker layer is required to obtain an effective gate dielectric. Hence the use of multilayer dielectric, taking advantage of the good interface properties of one dielectric and high band offset of second one, provide better dielectric properties.

The mobility in MOS devices with high κ insulators is significantly smaller than devices with SiO_2 insulators [155]. The main reasons attributed to this mobility degradation is: (a) scattering by trapped charge and interfacial charge [155–157] and (b) remote optical phonon scattering

[158–160]. According to Fischetti *et al.* [161], high dielectric constant materials are easily polarizable and the frequency of relevant optical phonon is small. This leads to high occupation probability of these phonons at low temperatures and subsequent channel electron scattering and mobility degradation. Based on remote phonon scattering theory, Laikhtman *et al.* [162] has found that the channel mobility depends on the channel carrier concentration and insulator layer thickness.

2.3.5 Amorphous oxide channel TFTs

High resolution and large area flat panel displays (FPDs) require TFTs based active matrix (AM) driving schemes to suppress image blinking and to reduce the power dissipation. In displays, the use of opaque a-Si:H based TFTs severely restrict the amount of light transmitted to the observer and hence causing a large portion of the energy of the display to be lost. In organic light-emitting diode (OLED) displays, the light emitting pixels may be controlled by a thin-film transistor array for much better brightness and efficiency. The low field effect mobility results complex OLED driving circuitry when a-Si:H TFTs are used. a-Si:H TFTs also suffers from photo/bias induced instability, and generation of photo-excited carriers because of the small bandgap (~ 1.7 eV). To avoid this, TFTs are usually kept light blind by incorporating it into a metal shadow mask in AM circuits. TFTs using transparent oxide semiconductors (TOSs) as the channel layer have several merits compared with the conventional Si-TFTs when applied to flat panel displays and OLED driving circuits. These include the insensitivity of device performance to visible light illumination and efficient use of back light in LCDs or emitted light in OLEDs [109]. The use of transparent TFTs significantly lower the voltage and drive current

required by the OLEDs for sunlight readability, with an extended device lifetime. In addition, oxide TFTs have potential advantages over the covalent semiconductor-based TFTs in terms of their high voltage, temperature, and radiation tolerances.

Eventhough organic semiconductors and a-Si:H have been extensively investigated for flexible electronics, the device performance is limited by the low mobilities of the channel materials. In addition, Si-based devices are of less interest for transparent circuits because they are not transparent, owing to the small bandgap. Polycrystalline oxides like ZnO have columnar grain structures even on deposition at room temperature. TFTs with polycrystalline oxide channel suffer from problems associated with the grain boundaries [51, 52] such as the instability to the atmosphere by the gas absorption/desorption into the grain boundaries; higher film surface roughness because of facet formation etc. Amorphous oxides have uniform structures and smoother surfaces which could yield smooth channel interfaces to the gate insulators. Hence amorphous semiconductors are preferred over polycrystalline ones for channel layers from the viewpoints of processing temperature and uniformity of device characteristics.

However in the amorphous semiconductors like a-Si:H, the intrinsic nature of the chemical bonding (consist of sp^3 orbitals with strong directivity and, therefore, the bond angle fluctuation significantly alters the electronic levels, leading to high density deep tail-states) fundamentally limits the carrier mobility. Compared to its crystalline counterparts, these materials show carrier mobility lower by two or three orders of magnitude. As carrier transport is controlled by hopping between localized tail-states and band conduction is not achieved, the mobility of a-Si:H is limited to $\sim 1 \text{ cm}^2/Vs$.

In contrast, degenerate band conduction and large mobility ($\sim 10 \text{ cm}^2/\text{Vs}$) are possible in TAOSs containing post-transition-metal cations [59].

Identification of suitable transparent materials as channel layer in TFT structures has utmost importance. Controllability of carrier densities and carrier mobilities are two important parameters to be addressed. For the channel, significant modulation of the channel conductance is needed to achieve FET switching. For this, only moderate carrier densities are needed. For interconnects, TSOs with high conductivity are needed. Each of these materials is required to have significant transparency to visible light. Materials with marginal bandgaps for visible light transparency affects the efficiency of the devices, particular at the blue end of the spectrum where luminescence is weakest. In addition, the optical absorption by the channel region can lead to band-to-band excitations of carriers and subsequent shifting of transistor characteristics. This demands the use of wide bandgap materials for channel layer with bandgaps well above the visible absorption limit.

2.3.6 Influence of channel layer thickness

The active channel layer semiconductor thickness in TFTs can be controlled by adjusting the deposition parameters. Several works have been reported regarding the optimization of this thickness in a-Si:H TFTs. According to Martin *et al.* [163], channel layer thickness has little effect on TFT off current, but impacts several other aspects of transistor performance, including threshold voltage, sub-threshold slope, and channel mobility. The decrease in threshold voltage with increasing a-Si:H thickness is attributed to a weaker influence of the back interface. The sub-threshold slope increases for increasing a-Si:H thickness; this is attributed to an improve-

ment in the electronic quality of the amorphous silicon. Channel mobility increases initially, then decreases for increasing thickness; the decrease is attributed to the increasing influence of parasitic resistances with thickness.

2.3.7 Comparison of MOSFET and TFT

The primary difference between a MOSFET and TFT is that, TFT is fabricated on an insulating substrate and employs a thin film as the channel region while the MOSFET is fabricated on a single crystal semiconductor substrate that also serves as the channel. In a MOSFET, the carrier path between the source and drain is formed by the development of an inversion layer of minority carriers at the semiconductor-insulator interface, by the application of a gate voltage. While in a TFT, channel formation is achieved by the accumulation of majority carriers in the semiconductor-insulator interface. Source and drain contacts to the semiconducting channel material are injecting contacts to the channel in a TFT structure, rather than ohmic contacts to a p-n junction as in a MOSFET.

2.3.8 Thin film transistor characterisation

Static characterisation of a-Si:H TFTs

Following discussion is mainly based on the text book by Y. Kuo [42]. Depending on the terminal voltages, three main regimes of operation can be identified in a TFT (see figure 2.12) (Figure 2.13 shows a plot of drain current as a function of gate voltage for an a-ZITO TFT, which is explained in section 6.4.2. Since the device structure did not use any passivation layer, the effect of back channel conduction is not observable here). They are above threshold, subthreshold and Pool-Frenkel regime. In case of a-Si:H

TFTs used in commercial products, there are two interface regions between channel layer material and insulator. One from the usual semiconductor-insulator interface (front channel) and the other from semiconductor-passivation insulator interface (back channel). Hence the subthreshold region consists of forward subthreshold and reverse subthreshold regions. The localized states in the amorphous silicon can be divided into two types, tail states and deep states [164]. The tail states are the Si conduction band states broadened and localized by the disorder to form a “tail” of localized states just below the conduction band mobility edge. The deep states originate from defects (mostly consist of Si dangling bonds, which have a wide range of energies because of the variations in local environments) in the amorphous silicon network.

For positive gate voltages greater than the threshold voltage ($V_{GS} > V_T$), the Fermi level goes into the conduction band tail (it cannot be brought closer than ~ 0.1 eV to the conduction band mobility edge and hence Fermi level never enters into the conduction band) and the number of free electrons that participate in the conduction increases (Figures 2.10 and 2.14). This gives a high *above-threshold* current. Due to the exponential increase in the density of conduction band tail states, the density of tail state electrons becomes much higher than the density of electrons trapped in deep states and interface states. Hence the conduction band tail and its associated parameters like trap density and acceptor-like tail states determine the characteristics of the TFT in the above threshold region.

In the subthreshold region of operation, TFT switches from its off state to on state and current increases exponentially from its low off current value to a high on current value. Depending on the applied gate voltage, the

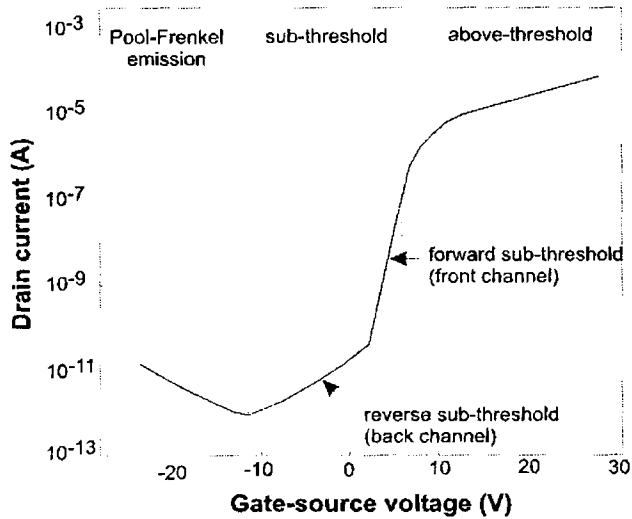


Figure 2.12: Typical transfer characteristics of an a-Si:H TFT showing the different regimes of operation.

subthreshold region can be identified as forward subthreshold and reverse subthreshold regions.

In this region, the transfer characteristics of TFT strongly depends on the quality of the gate insulator, a-Si:H bulk and passivation layer. As the gate voltage changes, the Fermi level moves in the middle of the bandgap. At zero gate volts the energy bands are close to the flatband condition. For positive gate voltages (forward subthreshold), the effect of the front interface and deep state defects of a-Si:H layer close to interface play major role. In this region, most of the induced electrons go into deep localized states in the a-Si:H bandgap and into the interface states at the a-Si:H-insulator interface. The increase in source-drain current is due to the small fraction of the band-tail electrons above the conduction band

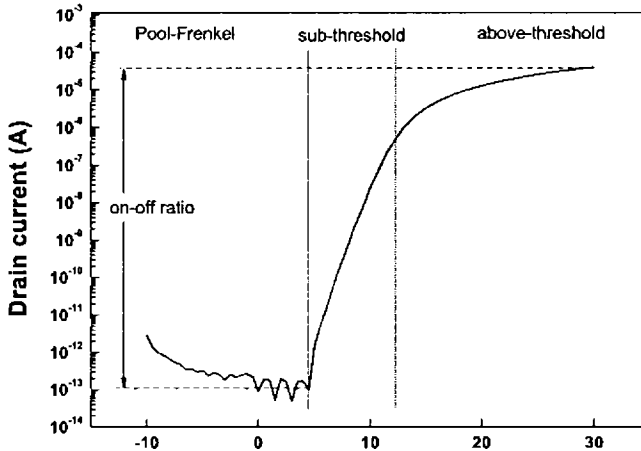


Figure 2.13: Typical drain-source current as a function of gate voltage at a constant V_{DS} for a-ZITO TFT showing the different regimes of operation. Since there was no passivation layer in the device, there is no back channel conduction process in this TFT.

mobility edge. As the positive gate voltage increases the density of electrons increases, which leads to an exponential growth of current which leads to the transition into above threshold region. For negative gate voltages (reverse subthreshold), most of the accumulated electrons from the interface are depleted. However, a high density of states at the back interface creates a weak electron channel (back channel) for conduction. This causes a band bending at back interface and an extended band bending in the bulk a-Si:H (Figure 2.15). As the gate voltage becomes more and more negative, the electron density at the back interface becomes lesser and lesser and hence the subthreshold current decreases and results in a subsequent transition into the Pool-Frenkel emission regime of operation.

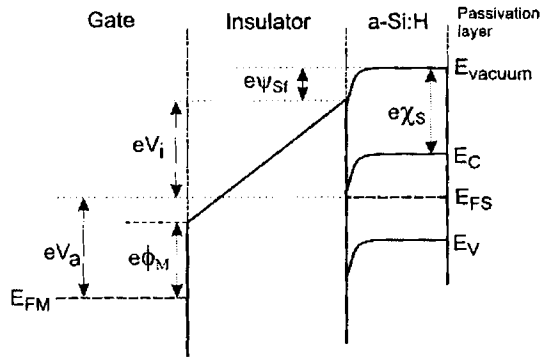


Figure 2.14: Band diagram for an arbitrary cross section of TFT in the middle of the channel in the above threshold regime. Symbols: ϕ_M is the metal work function, V_a is the applied gate voltage, ψ_{sf} is the band bending at the front interface, χ_S is the electron affinity of the semiconductor, E_{FM} is the metal Fermi level, E_{FS} is the semiconductor Fermi level, E_C is the conduction band mobility edge and E_V is the valence band mobility edge.

In a condition where gate biased negatively, major mechanisms responsible for the leakage current is the back channel (reverse subthreshold) and front channel (Pool-Frenkel emission) conduction. The TFT is off for high values of negative voltages at the gate terminal. However, the drain-source leakage current increases exponentially with the increase in negative gate potential. The front channel conduction via holes is responsible for this. At the front interface, holes are generated at the gate-drain overlap region by the Pool-Frenkel field enhanced thermionic emission process from the neutral deep trap states in the bandgap.

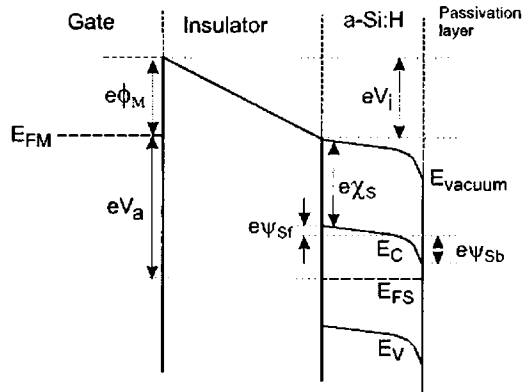


Figure 2.15: Band diagram for an arbitrary cross section of TFT in the middle of the channel showing the accumulation of electrons at the back interface and band bending at the front interface. Symbols: ϕ_M is the metal work function, V_a is the applied gate voltage, ψ_{sf} is the band bending at the front interface, ψ_{sb} is the band bending at the back interface, χ_s is the electron affinity of the semiconductor, E_{FM} is the metal Fermi level, E_{FS} is the semiconductor Fermi level, E_C is the conduction band mobility edge and E_V is the valence band mobility edge.

Oxide Channel TFT

Unlike crystalline silicon transistors, a-Si TFTs exhibit a bias induced metastability. This causes both the threshold voltage and subthreshold slope to change over time in the presence of a gate bias. The charge trapping in the insulator and defect state creation in the semiconductor are the main reasons attributed to this phenomenon. In contrast to traditional applications (e.g. LCDs) where TFT is used as a switch, analog applications (e.g. AMOLEDs, active pixel sensor etc) require the device to withstand prolonged voltages on both drain and gate terminals. Hence wide bandgap oxide based TFTs are expected to be a better substitute for a-Si:H TFTs.

Mobility and threshold voltage

The optical characterisation of the TFT typically consists of a transparency measurement as described in section 2.2.5 for individual thin films. Present work include the study of amorphous oxide channel TFTs without passivation layer. The electrical characterisation of TFT include the measurement of transistor output characteristics and transfer characteristics as in the case of a MOSFET. Various parameters like threshold voltage (V_T), sub-threshold voltage swing (S), field effect mobility (μ_{fe}), saturation mobility (μ_{sat}) etc are then derived from these characteristics. The ideal TFT drain current characteristics are identical to those of the MOSFET. Hence the drain current can be expressed by the relations:

$$I_D = \mu C_i \frac{W}{L} \left[(V_{GS} - V_T) V_{DS} - \frac{V_{DS}^2}{2} \right], \text{ for } V_{DS} \leq V_{GS} - V_T \quad (2.14)$$

and

$$I_D = \frac{1}{2} \mu C_i \frac{W}{L} (V_{GS} - V_T)^2, \text{ for } V_{DS} \geq V_{GS} - V_T \quad (2.15)$$

where μ is the average mobility of the carriers in the channel, C_i is the insulator capacitance, W is the channel width, L is the channel length, V_{GS} is the gate-source voltage, V_{DS} is the drain-source voltage and V_T is the threshold voltage.

The mobility and threshold voltage are the most important device performance parameters and can be estimated in three different ways. For TFTs, operating in the linear region ($V_{DS} \ll V_{GS} - V_T$), equation 2.14 can be written as:

$$I_D \approx \mu C_i \frac{W}{L} (V_{GS} - V_T) V_{DS} \quad (2.16)$$

The mobility and threshold voltage can be estimated from this expression using either the linear region drain conductance

$$g_d \equiv \frac{dI_D}{dV_{DS}} \Big|_{V_{GS}=\text{constant}} = \mu C_i \frac{W}{L} (V_{GS} - V_T) \quad (2.17)$$

or the linear region transconductance

$$g_m \equiv \frac{dI_D}{dV_{GS}} \Big|_{V_{DS}=\text{constant}} = \mu C_i \frac{W}{L} V_{DS} \quad (2.18)$$

The mobility estimated from the linear region drain conductance is referred to as the effective mobility, μ_{eff} . The effective mobility and threshold voltage is then graphically estimated by plotting linear region drain conductance versus V_{GS} . For $V_{GS} - V_T \gg V_{DS}$, this should become linear; the slope of which gives the effective mobility and the x-intercept gives the threshold voltage V_T . The μ_{eff} and V_T can also be estimated numerically from the equation 2.17.

The mobility estimated from the linear region drain transconductance is referred to as the field effect mobility, μ_{fe} . For a small constant value of V_{DS} , a plot of I_D as a function of V_{GS} would yield a straight line, the slope of which is proportional to μ_{fe} and the x-intercept gives V_T (Figure 2.16). That is,

$$\mu_{fe} = \frac{\text{slope}}{C_i(W/L)V_{DS}} \quad (2.19)$$

By numerical method, the μ_{fe} and V_T is calculated from equation 2.18 as:

$$\mu_{fe} = \frac{g_m}{C_i(W/L)V_{DS}} \quad (2.20)$$

and

$$V_T = V_{GS} - \frac{I_D}{\mu_{fe} C_i(W/L)V_{DS}} \quad (2.21)$$

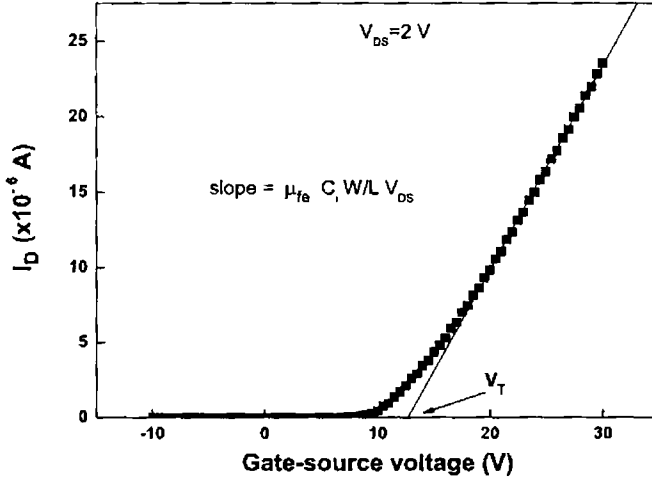


Figure 2.16: Determination of field-effect mobility and threshold voltage from the linear region of device operation. (Data: a-ZITO TFT for $V_{DS} = 2$ V.)

The mobility and threshold voltage can also be estimated from the saturation region ($V_{DS} > V_{GS} - V_T$) of transistor characteristics. Corresponding mobility is referred to as saturation mobility μ_{sat} . The expression for I_D , in this region is given by equation 2.15. μ_{sat} and V_T are obtained by plotting $\sqrt{I_D}$ as a function of V_{GS} . For $V_{GS} > V_T$, this plot would become linear and the slope of the linear part is proportional to μ_{sat} and the x-intercept gives V_T (Figure 2.17). That is,

$$\mu_{sat} = \frac{slope^2}{1/2C_i(W/L)} \quad (2.22)$$

Numerically,

$$\mu_{sat} = \frac{(d\sqrt{I_D}/dV_{GS})^2}{1/2C_i(W/L)} \quad (2.23)$$

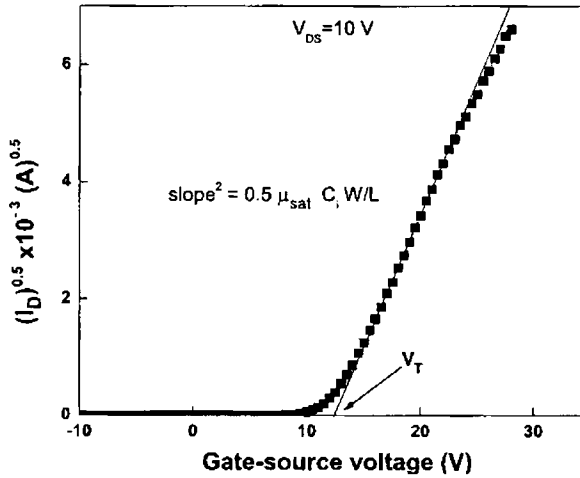


Figure 2.17: Determination of saturation mobility and threshold voltage from the saturation region of device operation. (Data: a-ZITO TFT for $V_{DS} = 10$ V.)

and

$$V_T = V_{GS} - \sqrt{\frac{I_D}{1/2C_i(W/L)}} \quad (2.24)$$

which is valid for $V_{GS} > V_T$ such that the assumption of saturation region operation is satisfied.

On-off current ratio

On-off ratio is another important TFT performance parameter. It is the ratio of the maximum drain current at above threshold region to the drain current when the device is in off condition (see figure 2.13). For higher resolution displays, TFTs are required to have a sufficiently large on current

to drive imaging pixels and a small off current to minimise power consumption, which consequently requires large on-off current ratio.

Subthreshold slope analysis

Subthreshold conduction is typically characterised by the inverse subthreshold slope (S) given by the equation:

$$S = \left(\frac{d \log(I_D)}{dV_{GS}} \right)^{-1} \quad (2.25)$$

S characterises the effectiveness of the gate voltage in reducing the drain current to zero. A small value of S is desirable since this corresponds to a very sharp transition from on to off state (Figure 2.18). The large S values indicates a larger density of tail states (D_{it}) because the S value is related to D_{it} by the equation [152]

$$S = \frac{2.3k_B T}{e} \left(1 + \frac{eD_{it}}{C_i} \right) \quad (2.26)$$

where k_B is Boltzmann's constant and C_i is the gate insulator capacitance).

In the present work, electrical characterisations of the TFTs were performed using a completely automated Keithley 4200 semiconductor characterisation system. In the case of TFTs fabricated by using shadow masks, the analysis were performed using two Keithly 236 SMUs which were controlled by LabVIEW program.

2.4 Conclusion

Thin film deposition techniques and thin film characterisation methods that were used in the present investigation was briefed in this chapter. Working

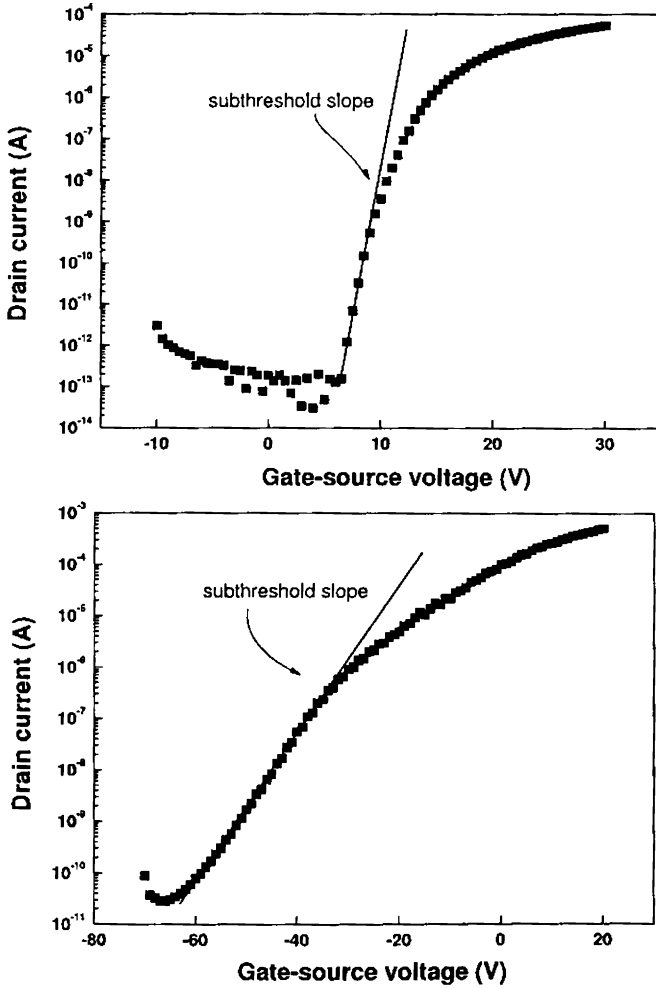


Figure 2.18: $\log(I_D) - V_{GS}$ characteristics for subthreshold slope analysis. Device with fast switching speed shows maximum slope (i.e., minimum S) compared to device with slow switching speed. Data: a-ZITO TFTs at $V_{DS} = 10$ V

principle of amorphous thin film transistors and methods of deriving the various device performance parameters were also discussed.

Chapter 3

Characterisation of Zinc Tin Oxide Thin Films Prepared by Pulsed Laser Deposition

This chapter describes the preparation of zinc tin oxide (ZTO) thin films by pulsed laser deposition (PLD) technique and their optical and electrical characterisations.

3.1 Introduction

Demands for visibly transparent and electrically conductive materials are rapidly growing in technological applications in optoelectronic devices like solar cells, liquid crystal displays, energy efficient windows and 'invisible electronic circuits' etc. A few crystalline materials like tin doped indium oxide (ITO), aluminium doped zinc oxide (ZnO:Al) and antimony doped tin oxide ($\text{SnO}_2\text{:Sb}$) in thin film form are presently being used for such

applications. Zinc tin oxide films have the advantages of both ZnO (higher transparency and more stability in activated hydrogen environments than ITO and SnO₂) and SnO₂ (high stability in acidic and basic solutions and in oxidizing environments at higher temperatures) [165–170]. Zinc tin oxide films have been grown by radio frequency and direct current magnetron sputtering, filtered vacuum arc deposition etc [171–175]. Most of these works were devoted to understand the optical and electrical properties of polycrystalline films deposited either by substrate heating or by high temperature post deposition annealing .

Amorphous transparent conductors are much attractive because they need a low processing temperature and can be grown on plastic substrates to form high-quality films suitable for practical devices. Since the mobility of conduction electrons is proportional to the width of the conduction bands and a narrow band tends to localize carriers, a large overlap between relevant orbitals is required to achieve a large mobility degenerate conduction in amorphous semiconductors. In addition, the magnitude of the orbital overlap needs to be insensitive to the structural randomness, which is intrinsic to the amorphous state, to reduce the formation of shallow localized states (often referred to as tail states). Metal oxides composed of heavy metal cations (HMCs) with an electronic configuration $(n-1)d^{10}ns^0$ (with $n \geq 4$) satisfy these requirements. A large band gap in oxides is attained by the low energy of oxygen 2p orbitals, which constitute the valence band maximum region. The bottom part of the conduction band in these oxides is primarily composed of ns orbitals of HMCs [59, 60].

3.2 Experimental conditions

Polycrystalline ceramic targets were prepared from a mixture of ZnO (99.999% pure) and SnO₂ (99.999% pure) powders (Zn:Sn = 1:1, 2:1, 4:1 and 8:1). The mixed powders were initially calcined at 1000°C for 4 hours and then hydrostatically pressed at a pressure of 1000 *Kgcm*⁻² to form a pellet of 1 *cm* diameter. The pellets were then sintered at 1450 °C for 6 hours. As discussed later in this session, the target with composition Zn:Sn = 2:1 formed a single phase compound of Zn₂SnO₄, and the other composition target lead to a mixture of ZnO, SnO₂, and Zn₂SnO₄, which were confirmed by XRD measurements (Figure 3.2). Thin films were deposited at RT by PLD from ceramics targets of ZTO with a KrF excimer laser (248 *nm* wavelength, 10 *Hz* repetition frequency). Laser ablation was carried out at a laser energy density of 35 *mJcm*⁻²*pulse*⁻¹. Films were deposited on glass substrates placed at a distance of 30 *mm* from the target. The depositions were carried out for 30 minutes by varying oxygen pressure (*P*_{O₂}) from 0 to 9 *Pa*. The resulting film thicknesses varied from 110 - 200 *nm*. To study the effects of post-deposition annealing on film properties, some films were annealed at temperatures up to 800°C in air.

3.3 Chemical composition

Chemical composition of the targets and thin films were determined from the XRF analysis. Figure 3.1 shows the compositional variation in the films with *P*_{O₂} during deposition. It was confirmed that the Zn/Sn ratios of the sintered targets were the same as those of the corresponding starting compositions (Inset of figure 3.1). Film composition shows some variation

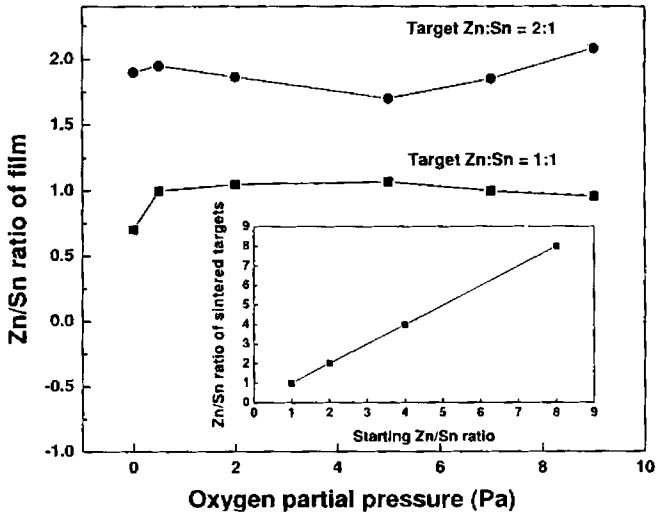


Figure 3.1: Zn/Sn compositional variations with respect to oxygen partial pressure for the PLD films deposited using different targets with the Zn:Sn ratios of 1:1 and 2:1. Inset shows the Zn/Sn composition in the sintered target.

with P_{O_2} , but is more or less the same as that of the PLD target, indicating that the PLD process can reproduce the chemical composition of the target in the films if an appropriate deposition condition is chosen.

3.4 Structural characterisation

ZnO-SnO₂ systems are reported to have two phases: Zn₂SnO₄ and ZnSnO₃ [176]. The Zn₂SnO₄ has a spinal type structure and has high thermal stability. The ZnSnO₃ exists in a stable crystalline form at temperatures < 600 °C and shows an ilmenite like structure. XRD patterns of the sintered targets are shown in figure 3.2. The target with composition Zn:Sn = 2:1 forms

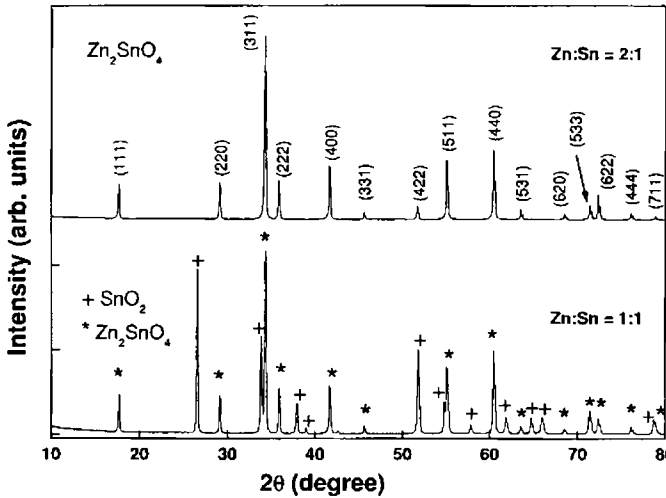


Figure 3.2: XRD pattern of PLD targets with the Zn:Sn ratios of 1:1 and 2:1. The Zn:Sn = 2:1 target forms a single phase compound of Zn_2SnO_4 . In the lower figure, * denotes Zn_2SnO_4 and + denotes SnO_2 .

a single phase compound of Zn_2SnO_4 , and the other composition lead to a mixture of ZnO, SnO_2 , and Zn_2SnO_4 . It has been reported that crystalline ZnSnO_3 cannot be prepared under calcination temperature $> 700\text{ }^\circ\text{C}$ [177]. The only stable phases at high temperature ($> 1000\text{ }^\circ\text{C}$) in the ZnO- SnO_2 system are Zn_2SnO_4 , ZnO and SnO_2 [176]. As the Zn content in the target is increased, the ZnO phase in the target becomes more and more prominent as observed from the increased intensity of diffraction peaks from ZnO planes. For films, glancing angle XRD analysis were performed at an incident angle of 0.5° . As evident from the GXRD pattern of films, all films were amorphous irrespective of the variations in oxygen partial pressure (Figure 3.3). Figure 3.4 show GXRD patterns of the films deposited using

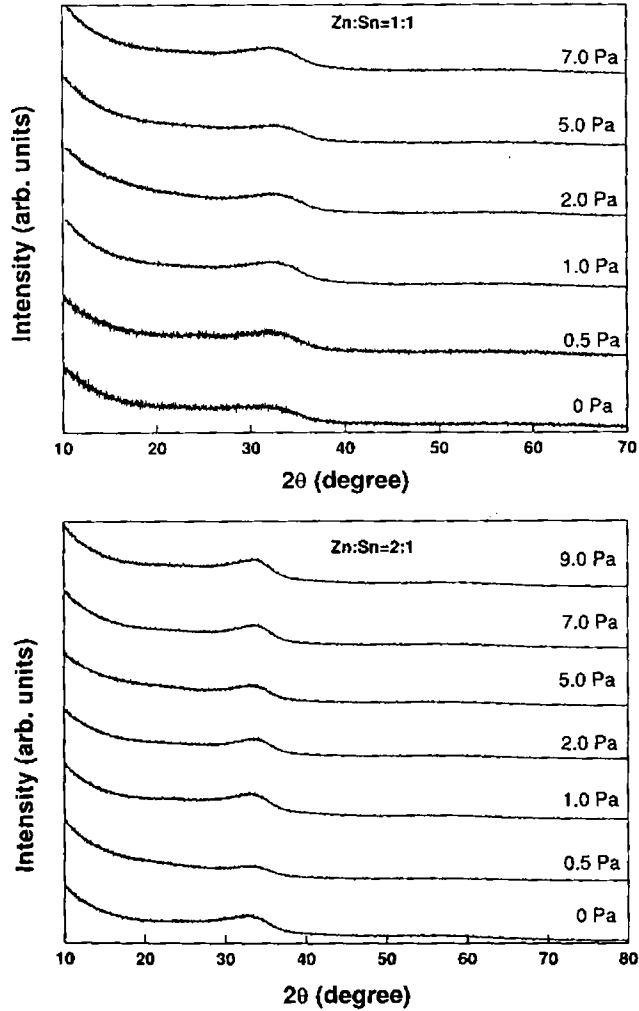


Figure 3.3: GXR D pattern of ZTO thin films prepared from targets with Zn:Sn ratios of 1:1 and 2:1 at different oxygen partial pressures.

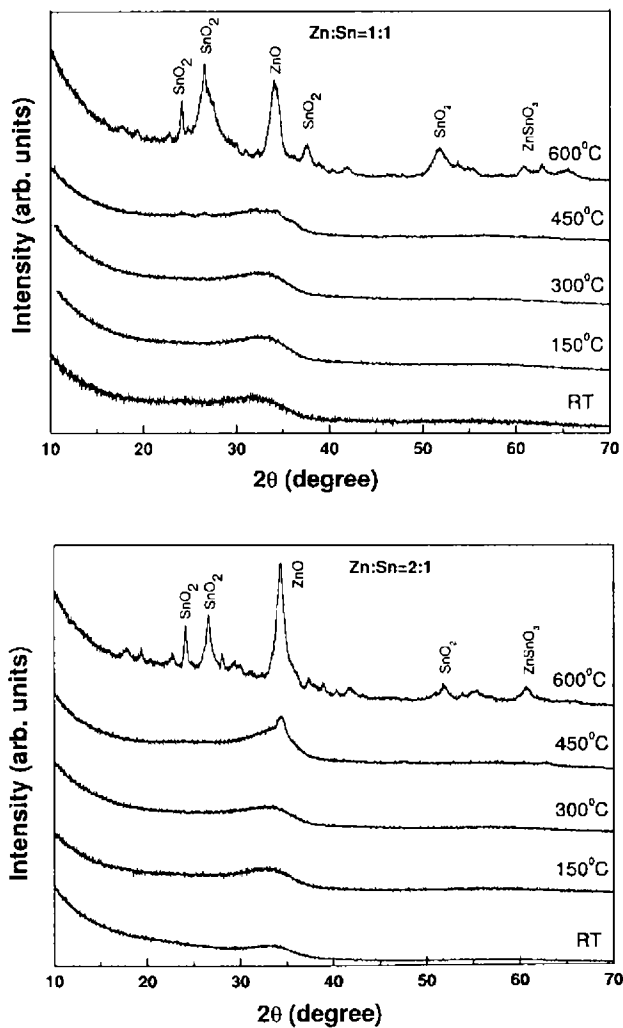


Figure 3.4: GXR D patterns of the films deposited using targets having Zn:Sn compositions 1:1 and 2:1 as a function of annealing temperature. Zn:Sn ratio and annealing temperature are shown above the corresponding GXR D pattern.

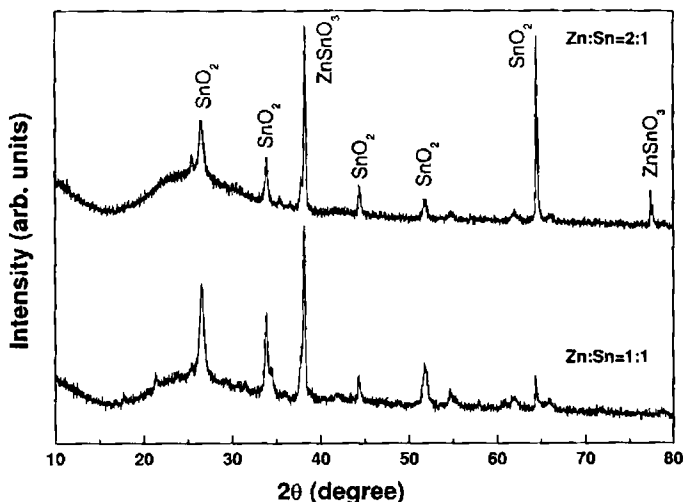


Figure 3.5: GXR D patterns of the films deposited from targets having Zn:Sn compositions 1:1 and 2:1 after annealing at 800 °C.

PLD targets with the Zn:Sn ratios of 1:1 and 2:1 as a function of post annealing temperature. It shows that the deposited films are amorphous, but 450 °C annealing crystallizes the films partially to give crystalline phases of the simple oxides, ZnO and SnO₂. The halos around $2\theta = 33^\circ$ indicate that some or large portion of the amorphous phases still remain. This result should be compared with the results on films grown by sputtering in references [110] and [173], in which the former reported no crystallization up to 600 °C while the latter reported the crystallization temperature as ~ 600 °C. The low crystallisation temperature in the present PLD grown films would be attributed to the different growth kinetics of the films between PLD and sputtering, where in general, deposition precursors have larger ki-

netic energies for PLD owing to the excitation by high energy laser pulses and few collisions of the deposition precursors with gaseous molecules due to a lower P_{O_2} deposition condition. That is, it is speculated that higher energy precursors in PLD deposition form a more relaxed amorphous structure that is more easily crystallized. Further higher temperature annealing at 600 - 800 °C (Figure 3.5) eliminates the remaining amorphous phases, producing a new crystalline phase $ZnSnO_3$ as a consequence of solid state reactions between the ZnO and SnO_2 phases segregated at 450 - 600 °C and the remained amorphous ZTO film [176, 178].

Figure 3.6 shows the AFM images and root-mean-squares (rms) surface roughness of the as-deposited films as a function of the chemical composition and P_{O_2} . It shows that the surface roughness depends on both the chemical composition and P_{O_2} and ranges up to 11 nm. The films with the Zn:Sn composition 1:1 have larger roughness compared to the 2:1 composition films, and its roughness decreases with the increase of P_{O_2} . The films deposited from the Zn:Sn = 2:1 target have atomically flat surfaces with surface roughness less than 0.3 nm at low $P_{O_2} \leq 2 Pa$. For TFT applications, an applied gate bias modulates the conductance of the semiconductor layer and form an accumulated channel of carriers in a narrow region confined at the semiconductor-insulator interface. Hence the surface flatness of an active layer is an important parameter because carrier transport in TFT channels is significantly affected by the carrier scattering due to roughness at the channel - gate insulator interface [179]. Smoother the interface, better will be the mobility of the carriers in the channel.

Figure 3.7 shows the AFM images of the film deposited from Zn:Sn = 2:1 target at an oxygen partial pressure of 0.5 Pa as a function of annealing temperature. The roughness of the film increases as the films are

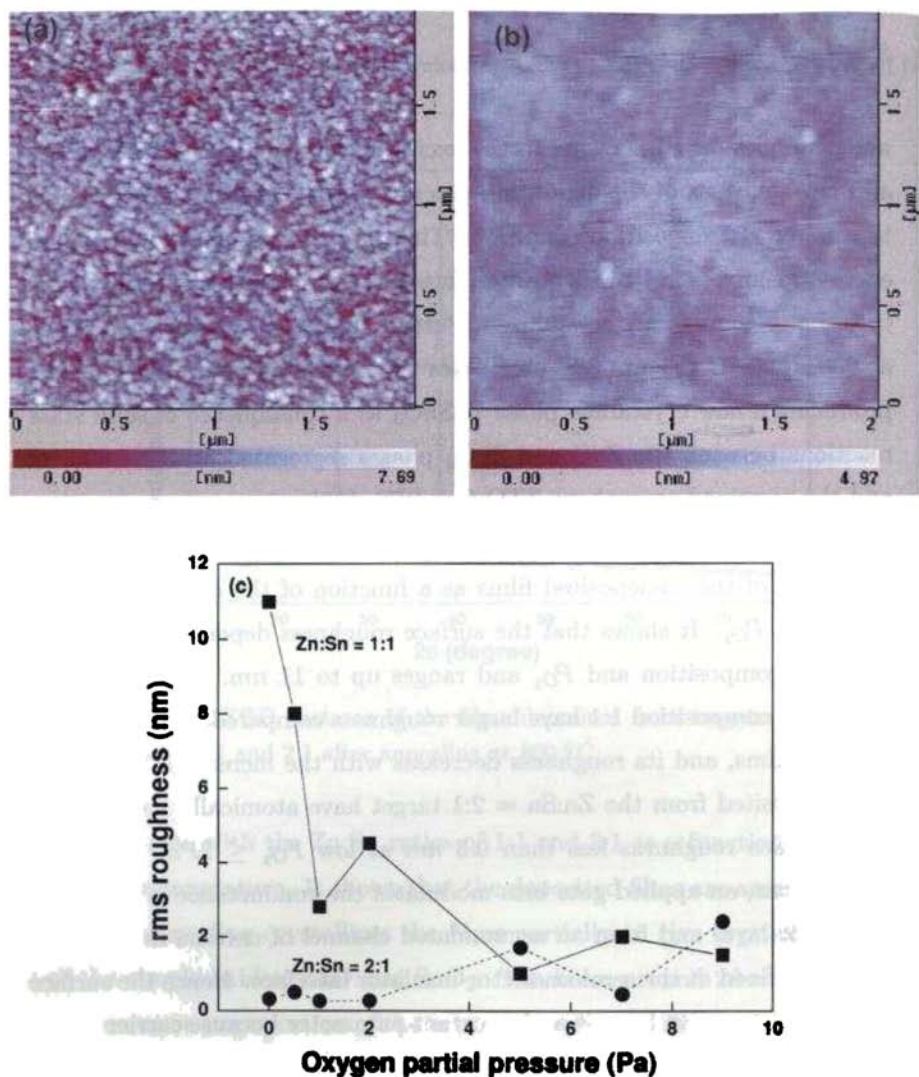


Figure 3.6: AFM images of ZTO films prepared from target composition (a) Zn:Sn=1:1 and (b) Zn:Sn=2:1. Both films are deposited at room temperature at an oxygen pressure of 0.5 Pa. (c) Dependence of surface roughness on oxygen partial pressure for the films deposited from targets having Zn:Sn compositions 1:1 and 2:1.

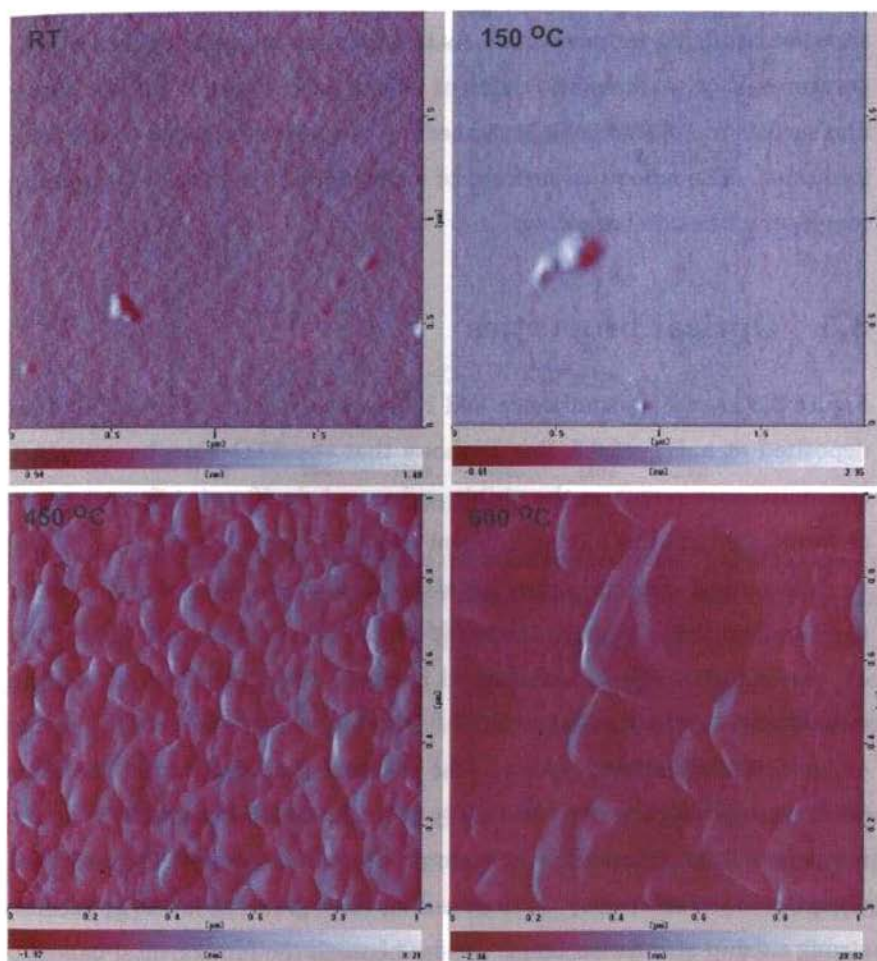


Figure 3.7: AFM images of ZTO films deposited from Zn:Sn = 2:1 target at an oxygen partial pressure of 0.5 Pa and then annealed at different temperatures.

annealed at higher temperatures. As the films are annealed at higher temperatures, it crystallizes into different phases (refer figure 3.4). The higher film surface roughness at higher annealing temperatures is due to the facet formation. The smoother surfaces of amorphous films change to granular rough structures on annealing.

3.5 Optical properties

Figure 3.8 shows transmittance and reflectance spectra of the ZTO films deposited at a P_{O_2} of 0.5 Pa. It shows that the ZTO films have average transmittances $> 85\%$ in the visible region and significant difference is not observed for the films having different chemical compositions.

The optical data in figure 3.8 were used in the Tauc plot to obtain the bandgap value [Figures 3.9(a,b)], which derived E_g values 2.37 - 2.86 eV varying with P_{O_2} as summarised in figure 3.9(c) (Method of bandgap evaluation is given in section 2.2.5). There was some uncertainty in the estimation of E_g at low P_{O_2} due to the presence of subgap states. The value of E_g is insensitive to P_{O_2} at $P_{O_2} \geq 2Pa$. It should be noticed that the fundamental band gap is an intrinsic property of a material: however, the exceptionally small values are obtained for films grown at low P_{O_2} , because strong subgap absorption bands appear beneath the fundamental bandgap and superimpose with the fundamental band absorption as observed in figure 3.10. These results should also be compared with previously reported results. As summarized in introduction of reference [110] and reported in reference [173], the Tauc gaps of ZTO films are 3.35 - 3.89 eV. But those films were crystallized, and therefore they should not be compared with the

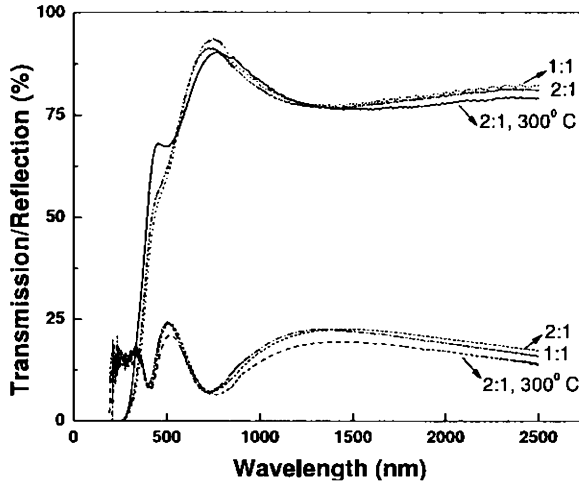


Figure 3.8: Optical transmission and reflection spectra of the ZTO films prepared at $P_{O_2} = 0.5 \text{ Pa}$ from targets having Zn:Sn compositions 1:1 and 2:1. The films are highly transparent across the visible region.

present data for amorphous ZTO. It indicates that the fundamental optical gaps of ZTO films are reduced to 2.8 - 2.86 eV on amorphization.

Figures in 3.10 are $\log(\alpha) - h\nu$ plots that show subgap absorption more clearly. It is observed that the as-deposited films $P_{O_2} \leq 2 \text{ Pa}$ have absorption larger by many orders of magnitude just below the fundamental bandgap ($\sim 2.8 \text{ eV}$) compared to films deposited at $P_{O_2} > 2 \text{ Pa}$ [Figures 3.10(a,b)]. This is the reason for the exceptionally small apparent E_g values obtained for amorphous ZTO films. At higher P_{O_2} , even though some subgap absorptions remain, they are more distinguishable from the fundamental band absorptions and give larger Tauc gaps $> 2.8 \text{ eV}$. It is also found that thermal annealing at 150°C reduces the strong subgap absorp-

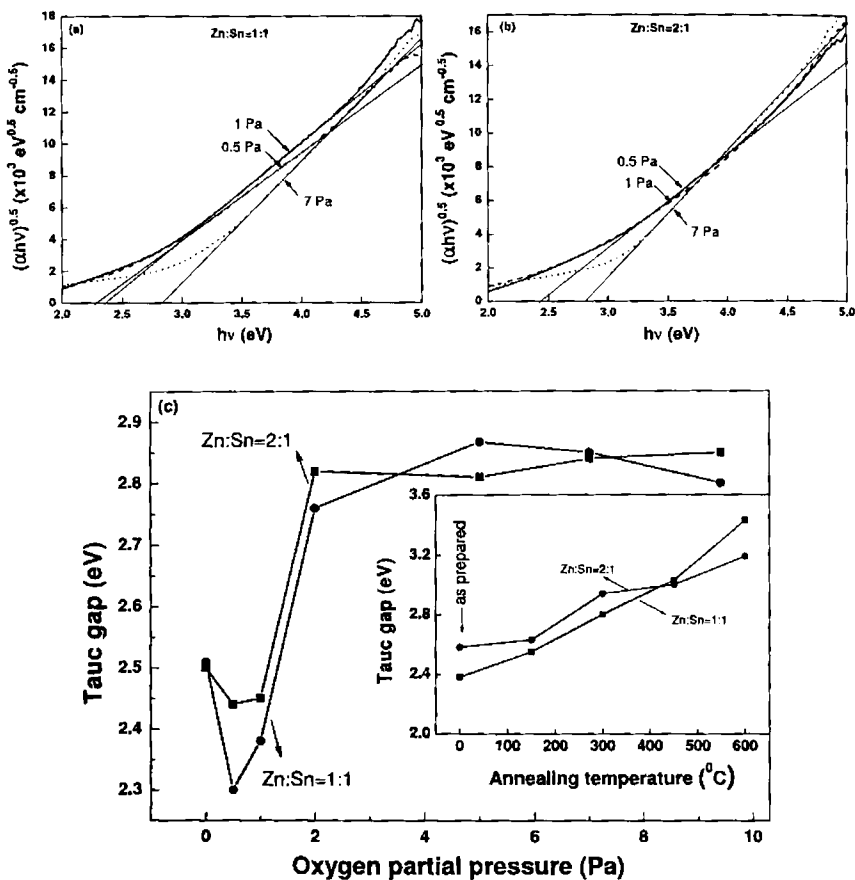


Figure 3.9: (a) Tauc plots for the films prepared from the Zn:Sn=1:1 target at different P_{O_2} . (b) Tauc plots for the films prepared from the Zn:Sn=2:1 target at different P_{O_2} . (c) Dependence of Tauc gap of the a-ZTO films on P_{O_2} during the growth. Inset shows the effect of annealing in air on Tauc gap of the films prepared at $P_{O_2} = 0.5$ Pa.

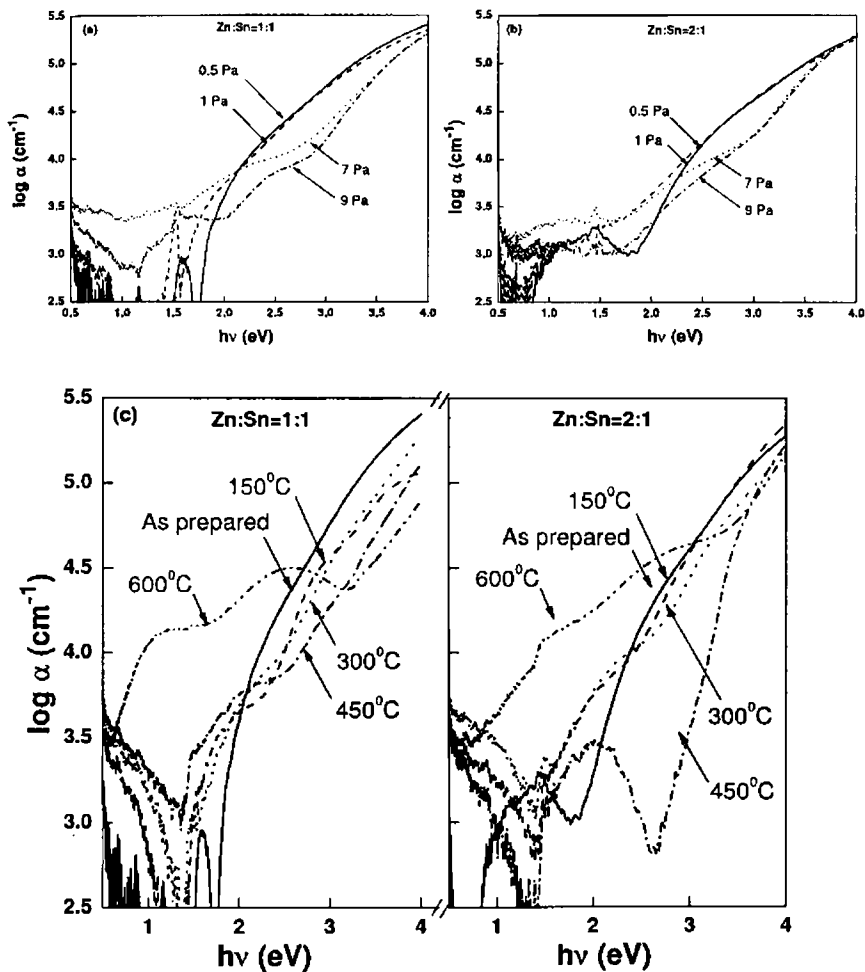


Figure 3.10: $\log \alpha - h\nu$ plots for ZTO films. (a) As-prepared films deposited from the target of Zn:Sn composition 1:1. (b) As-prepared films deposited from the target of Zn:Sn composition 2:1. (c) Annealed films (deposited at $P_{O_2} = 0.5$ Pa) as a function of annealing temperatures.

tions observed in the films deposited at low P_{O_2} [Figure 3.10(c)], and 300 °C annealing increases the Tauc gaps to > 2.8 eV as shown in the inset to figure 3.9c. The large increase in the subgap absorption for the 600 °C annealed films would be attributed to a strong reduction condition prevailing at high temperatures leading to high oxygen deficiency.

3.6 Electrical properties

Electrical properties of the as-deposited a-ZTO films are summarized in figures 3.11-3.13. Previous works on a disordered crystalline oxide semiconductor [180] and amorphous oxide semiconductors [126, 179, 181] indicate that carrier concentration should exceed a threshold value to obtain a large mobility needed for semiconductor devices with active layers having structural randomness. Similar to them, Hall mobilities comparable to or greater than 10 cm²/Vs were obtained in the a-ZTO films when the carrier concentrations exceeded 10^{16} cm⁻³ for the Zn:Sn = 2:1 films and 10^{18} cm⁻³ for the Zn:Sn = 1:1 films.

Figure 3.12 shows the controllability of the carrier concentration for as-deposited ZTO films. Carrier concentration can be controlled from 10^{12} to 10^{19} cm⁻³ by varying P_{O_2} from 0 to 5 Pa. The large carrier concentrations and mobilities are obtained for the films grown at P_{O_2} in the range of 2 - 7 Pa. The decrease of carrier concentration at higher P_{O_2} is due to the suppression of the oxygen vacancies that may contribute to the formation of donor states. However, the low carrier concentrations at low P_{O_2} are not common in PLD deposited transparent conducting oxides. It could be explained for the ZTO films by the large subgap states below 3 eV observed

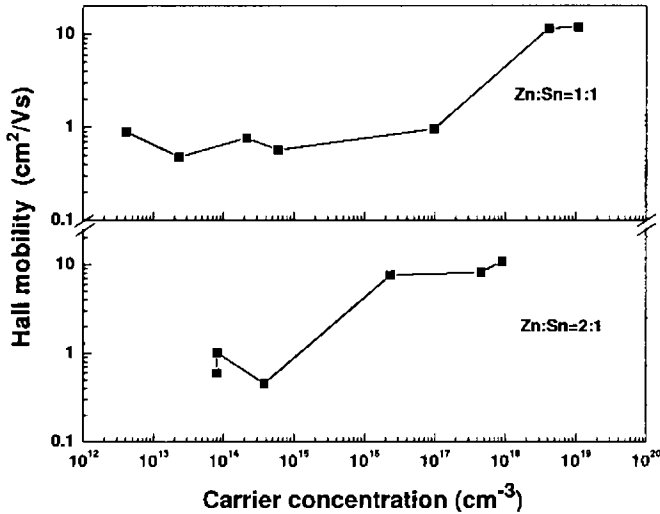


Figure 3.11: Relationship between Hall mobility and carrier concentration in a-ZTO as-deposited films using targets with Zn:Sn ratio 1:1 and 2:1.

in figure 3.10. These subgap states act as electron traps which limit number of electrons available to the conduction band. Effects of post thermal annealing on the electrical properties of the films prepared at 0.5 Pa are shown in figure 3.13. Figure 3.10(c) has shown that the post thermal annealing decreases the total subgap states. Up to the annealing temperature of 450 °C, there is a reduction of total subgap states which enhances the carrier concentration and hence the mobility. In the case of the 600 °C annealed films, it again produces a large number of subgap states although the films become polycrystalline as observed in the GXRD (Figure 3.4). This high subgap absorption at high annealing temperature suggests some reducing effect on the film properties. It suggests that the contribution of reducing atmosphere at the high temperature increases defects (e.g. oxy-

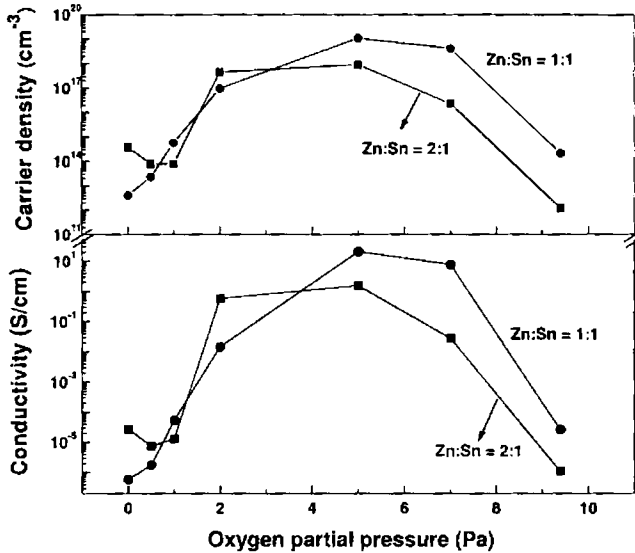


Figure 3.12: Dependence of carrier transport properties of ZTO films on oxygen partial pressure for the as-deposited films.

gen deficiencies) and localized states, which increases the film resistivity. This leads to a reduction in carrier concentration and hence the mobility (subsequently a higher resistivity) in the case of films annealed at 600 °C.

3.7 Conclusion

The structural, electrical and optical properties of amorphous zinc tin oxide films deposited by pulsed laser deposition were investigated for two Zn/Sn compositions as a function of oxygen partial pressure (P_{O_2}) and annealing temperature. The effects of post deposition annealing on the optical and electrical properties of ZTO films were also examined. It was found that

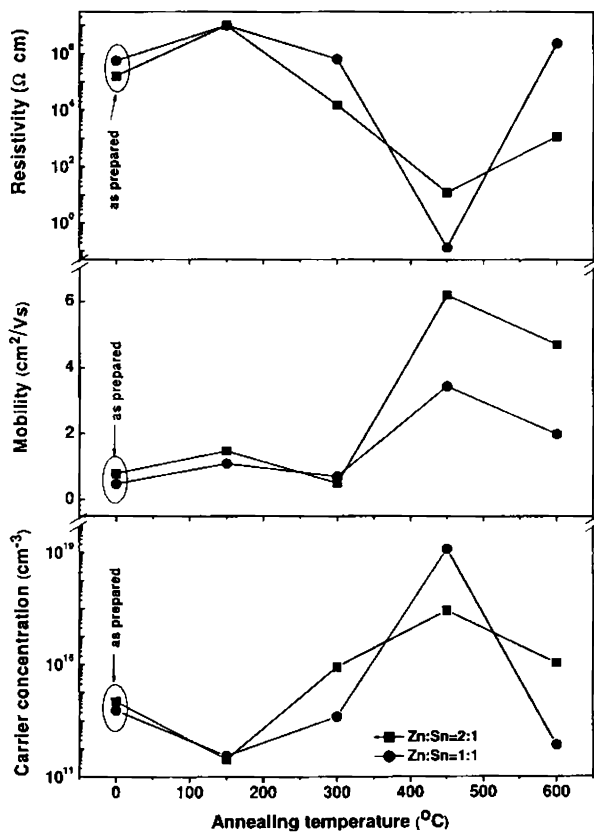


Figure 3.13: Dependence of carrier transport properties of ZTO films on post annealing temperature for the films deposited at $P_{O_2} = 0.5 Pa$.

optical absorption spectra showed strong subgap absorptions for the films deposited at $P_{O_2} < 2 \text{ Pa}$. Tauc gaps of the ZTO films were increased to 2.85 eV on deposition at high P_{O_2} or post thermal annealing, which resulted from the reduction of the subgap states. The carrier concentration - P_{O_2} relations showed broad peaks, which is explained by the existence of the electron traps in the subgap states for the films grown at low P_{O_2} and by the reduction of the oxygen vacancies on deposition of films at high P_{O_2} . The high electron concentration films were shown large Hall mobilities greater than $10 \text{ cm}^2/\text{Vs}$.

Chapter 4

Characterisation of Zinc Tin Oxide Thin Films Prepared by Co-sputtering

4.1 Introduction

This chapter describes the preparation of amorphous zinc tin oxide thin films by co-sputtering technique and their optical and electrical characterisations.

4.2 Experimental setup

The zinc tin oxide (ZTO) thin films were deposited via a DC-RF co-sputtering technique. High purity ZnO (99.99%, Alfa Aesar) powder was used as the DC target and SnO₂ (99.99%, Alfa Aesar) powder as RF target in a sputter up configuration (schematically shown in figure 4.1). Powders

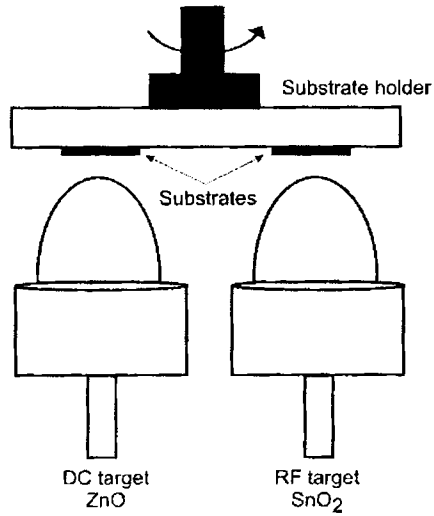


Figure 4.1: Schematic diagram of co-sputtering technique employed for the present study.

were taken in copper plates and fixed to magnetron guns. Both targets were kept in a plane.

Initially the deposition chamber was evacuated to a base pressure of 5×10^{-4} Pa using an oil diffusion pump and rotary pump. Working gas (argon) was then admitted to the chamber through a mass flow controller and the working pressure was maintained at 1 Pa by throttling the baffle valve. A circular substrate holder was attached to the shaft of a stepper motor and the substrates were rotated at a speed of 50 rotations per minute (rpm) at 4 cm distance above the targets. Deposition was carried out for 10 minutes at a DC current of 200 mA (600 V) and 10 W RF power. The experiment was repeated in similar experimental conditions by varying only the RF power up to 100 W.

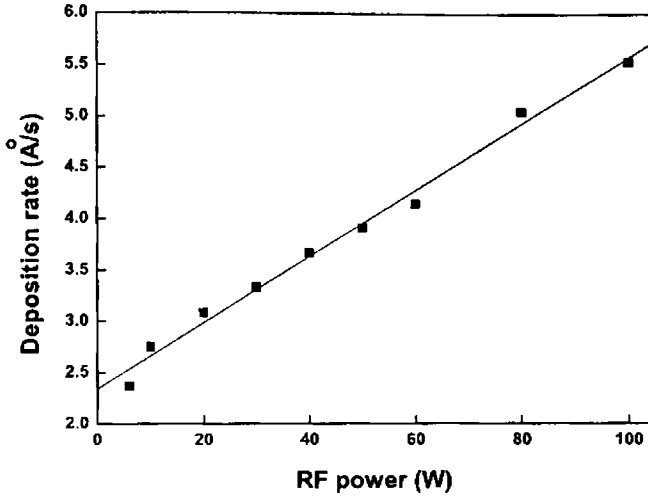


Figure 4.2: Deposition rate of ZTO thin films versus RF power to SnO₂ target.

4.3 Deposition rate

Figure 4.2 shows the deposition rate of co-sputtered ZTO thin films with respect to the variations in RF power applied to SnO₂ target. Film thickness was measured using a stylus profiler (Dektak 6M). The sputtering rate of SnO₂ target increases on increasing the RF power. As mentioned above, sputtering rate from ZnO target was maintained constant throughout this set of experiment. Hence the overall deposition rate of the compound film was increased linearly with RF power.

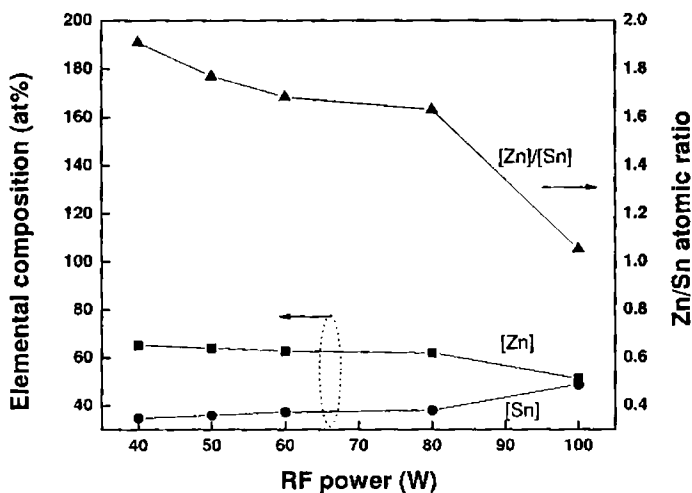


Figure 4.3: Compositional variation of co-sputtered ZTO thin films versus RF power to SnO_2 target.

4.4 Chemical composition

Chemical composition of the films was examined by XRF analysis. For the films grown up to 40 W RF power to SnO_2 target, the tin content in the film was not detectable from the XRF signal. Above that, the tin content in the film slightly increased with the increase of RF power. Hence the $[\text{Zn}]/[\text{Sn}]$ atomic ratio in the film decreases with the increase in RF power (Figure 4.3).

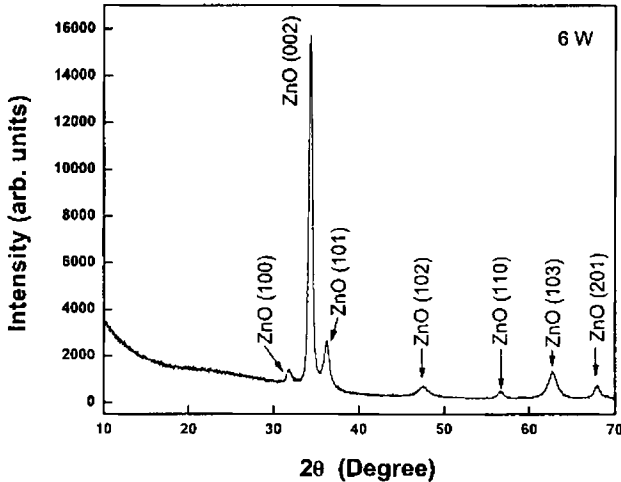


Figure 4.4: GXR D pattern of the film deposited at 6 W RF power supplied to SnO₂ target.

4.5 Structural characterisation

Structural characterisation of the films was carried out by GXR D analysis (RIGAKU RINT-2000 with Cu K α radiation) at the incident angle of 0.5°. The films deposited were polycrystalline when low RF powers (up to 40 W) was used for SnO₂ sputtering. Peaks were identified as the diffraction patterns from different planes of ZnO (Figure 4.4). ZnO generally shows an orientated growth preferred along [002] plane. However, here in co-sputtering, the growth is not along any preferred direction. In this polycrystalline films, the tin content was very small and was not detectable from the XRF analysis and there was no diffraction peaks characteristics of SnO₂. Hence tin may have a prominent role in obstructing the ZnO growth

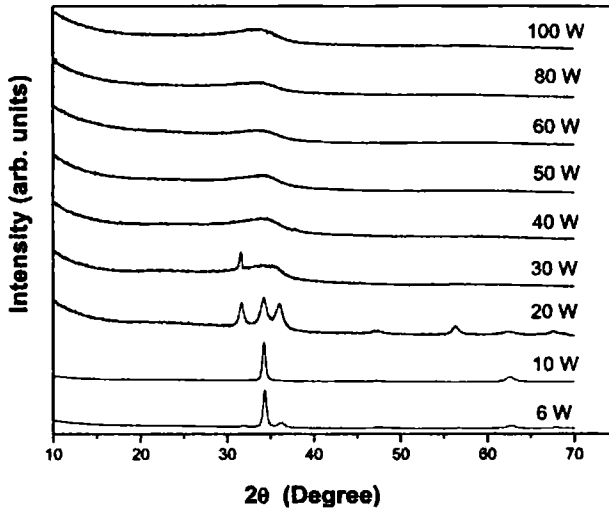


Figure 4.5: GXR D patterns of the co-sputtered ZTO films deposited at different RF powers keeping the DC power constant at 120 W. Films show only the diffraction peaks of ZnO at large RF powers.

along any preferred direction. This is further supported by the observation that with the increase of sputtering power to the SnO₂ target, the compound film becomes less crystalline and finally complete amorphous films were obtained for RF power above 30 W (Figure 4.5). Films deposited at RF powers greater than 30 W has shown only some halos around $2\theta = 33^\circ$ which indicated the absence of long range ordering in the co-sputtered ZTO films.

Roughness of the films were estimated from the AFM images. Figure 4.7 shows the variation of rms roughness of the co-sputtered films. The films which were polycrystalline have a more rough surface compared to the amorphous films. Smoothest film was observed for film grown at 60 W

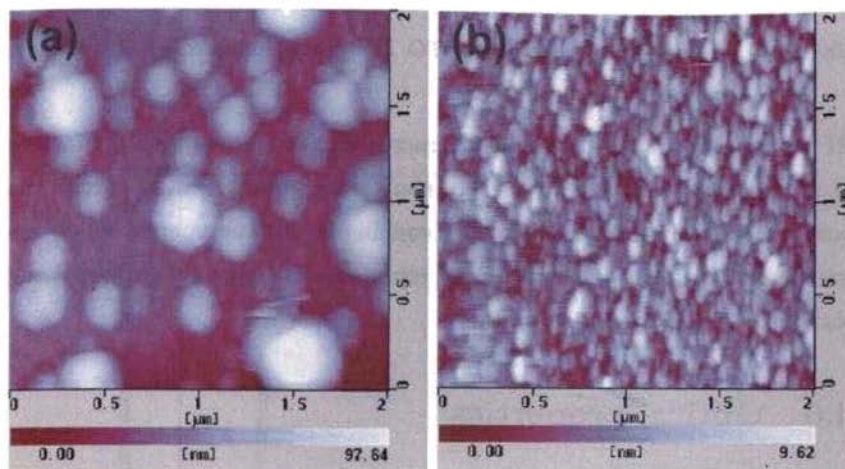


Figure 4.6: AFM images of co-sputtered ZTO films (a) polycrystalline film grown at RF power 6 W and (b) amorphous film grown at RF power 60 W. DC power fixed at 120 W.

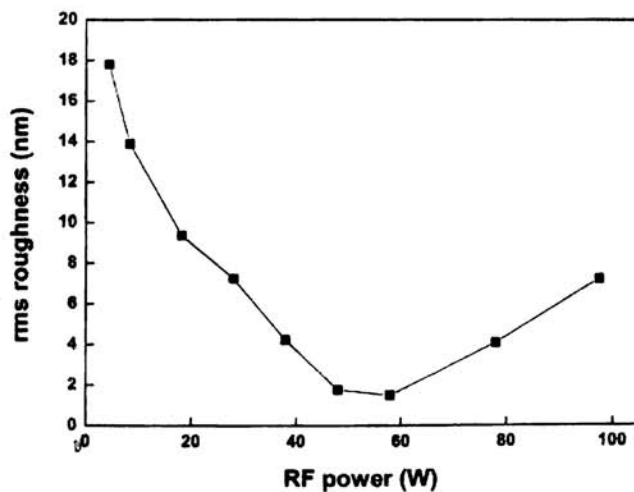


Figure 4.7: Variation of rms roughness of the co-sputtered ZTO films with respect to RF powers.

RF power and then it showed slight increase in roughness with the increase of RF power. With the increase of sputtering power, ejected species may land on the substrate with higher and higher kinetic energy which may eventually cause the surface to become more and more rough eventhough the films are amorphous in nature.

4.6 Optical properties

Figure 4.8 shows optical transmission and reflection spectra of ZTO thin films recorded using a UV-Vis-NIR spectrophotometer. The ZTO films have an average transmission (after correcting for reflection loss) $> 90\%$ across the visible spectrum. An abrupt decrease in transmission at lower wavelength is due to fundamental band to band absorption.

The absorption coefficient and bandgap of the films were calculated as mentioned in section 2.2.5. For polycrystalline films (up to 30 W), the bandgap was calculated from the plot of $(\alpha h\nu)^2$ versus $h\nu$ (Figure 4.9). These films were clearly shown a strong absorption band around 4 eV and a sub band around 3.3 eV. In case of amorphous films, the bandgap (i.e., Tauc gap) was estimated from $(\alpha h\nu)^{0.5}$ versus $h\nu$ plots (refer section 2.2.5). Those films were shown absorption from a single band around 3.3 eV. Figure 4.11 shows the bandgap variations with respect to the change in RF power. Effect of sub band is not observable in amorphous films. This becomes more clear in figure 4.10 which is a $\log(\alpha) - h\nu$ plot. As seen from the figure, the effect of sub band decreases with the increase of RF power.

Figure 4.11 shows the variation in bandgap with respect to the applied RF power to SnO₂ target. In case of polycrystalline films, the main absorption band shifts to higher energy and the sub band shifts to lower energy

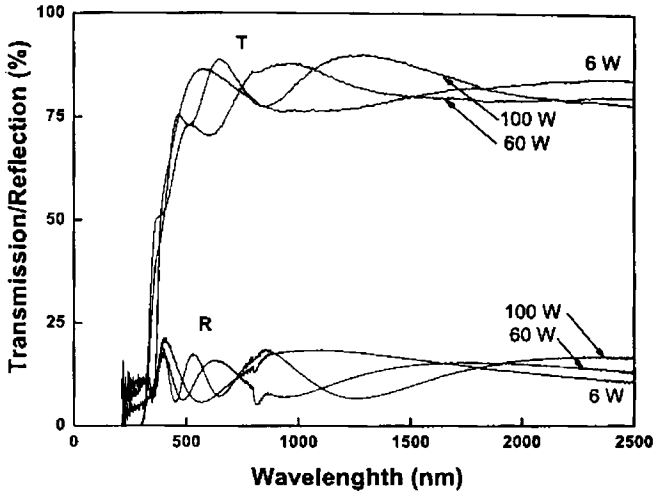


Figure 4.8: Optical transmission and reflection spectra of co-sputtered ZTO thin films.

side with the increase in power to SnO_2 target.

A direct bandgap of 4.1-4.2 eV for SnO_2 thin films, 3.2 eV for ZnO thin films [182], and 3.6 eV for zinc tin oxide thin films has been reported. This suggests that, in the present case, there exists both SnO_2 and ZnO phases in the ZTO films even though GXR D data did not show any indication of the SnO_2 phase. Sn may be acting as a catalyst to amorphosize the films and hence with the increase of sputtering power to SnO_2 target, ZTO films become amorphous. Hence amorphous co-sputtered films show a single Tauc gap value around 3.3 eV.

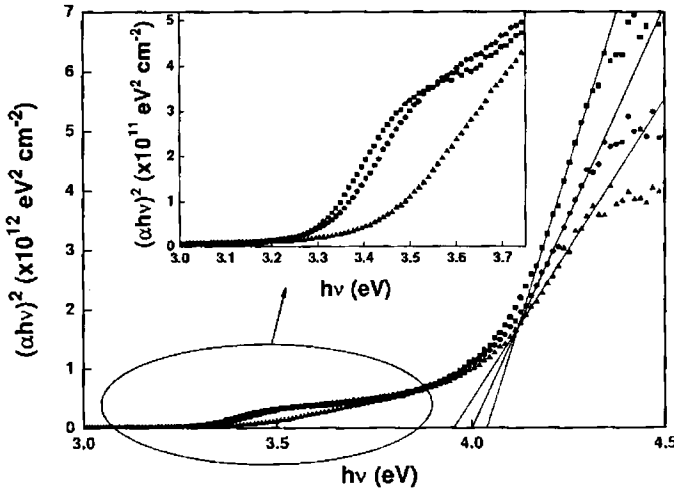


Figure 4.9: Bandgap estimation for polycrystalline films. The encircled portion is shown in the inset.

4.7 Electrical properties

From the Hall effect measurement, the type of carriers in co-sputtered ZTO thin films were identified as electrons. Eventhough the carrier density of the polycrystalline films were about three orders greater than that of the amorphous films, the mobility of the former was found lower than the latter (Figure 4.12). In polycrystalline films, the mobility is influenced by the carrier scattering at grain boundaries. Grain boundaries constitute the interface between two single-crystal grains of different crystallographic orientation. The normal atomic bonding in grains terminates at the grain boundary where more loosely bound atoms prevail. Like atoms on surfaces,

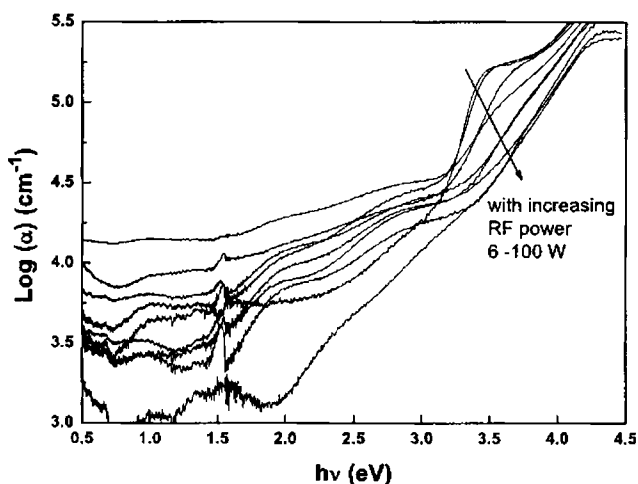


Figure 4.10: $\text{Log}(\alpha) - h\nu$ plot for ZTO films.

they are more energetic than those within the grain interior. This causes the grain boundary to be a heterogeneous region where various atomic reactions and processes favored. In addition, electronic transport is impeded through increased scattering at grain boundaries, which also serve as charge recombination centers in semiconductors. Amorphous films, being devoid of such scattering centres, have relatively higher mobility value compared to polycrystalline films. The carrier density do not show large variations with the increase of tin content in the amorphous ZTO films, whereas the mobility decreases steadily. Conductivity of the films decreased as film changed from polycrystalline to amorphous phase. In amorphous films, the conductivity was found to increase with the increase of tin content in the film (Figure 4.13).

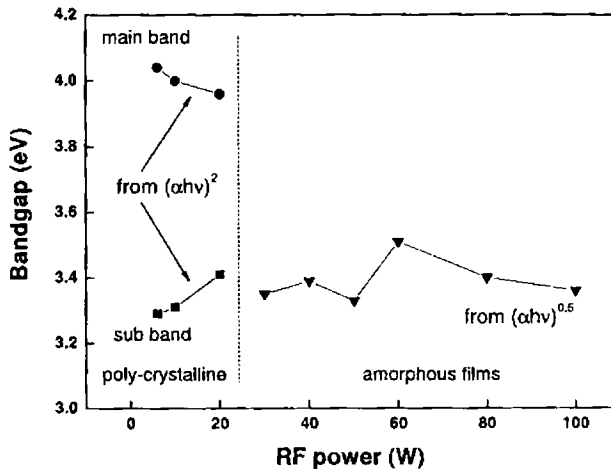


Figure 4.11: Tauc gap variation of co-sputtered ZTO films as a function of sputtering power to SnO_2 target. Poly-crystalline films show a main absorption band around 4 eV and a sub band around 3.3 eV.

4.8 Conclusion

ZTO thin films were prepared by the simultaneous sputtering of ZnO and SnO_2 powder targets via a DC-RF combination. Chemical composition of the films were shown systematic variation with proper control of sputtering power to the targets. Eventhough the optical properties were not much affected by the compositional changes, the structural and electrical properties were affected. The films were polycrystalline for low RF sputtering powers to SnO_2 target and became amorphous at high RF powers. All films were highly transparent in visible region. Amorphous films were shown better mobility compared to polycrystalline films which were explained as a consequence of grain boundaries.

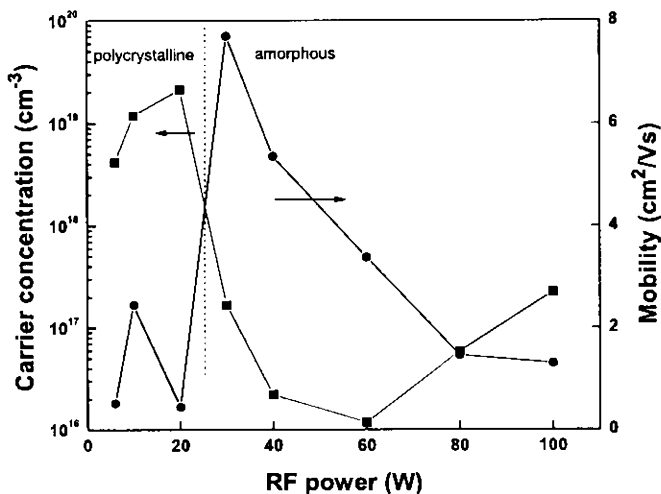


Figure 4.12: Variations in carrier concentration and Hall mobility of ZTO films with respect to RF power to SnO_2 target.

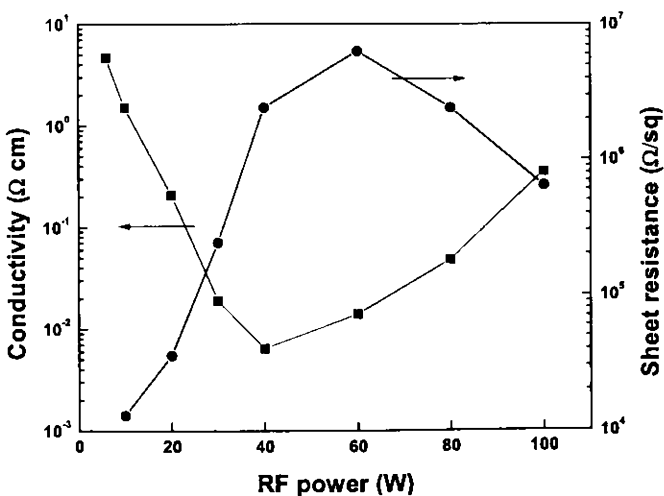


Figure 4.13: Variation of conductivity of ZTO films with RF power.

4.9 Comparison of ZTO films prepared by PLD and co-sputtering

In PLD, the films were deposited from targets having Zn/Sn compositions 1:1 and 2:1; whereas in co-sputtering, the films were prepared from separate ZnO and SnO₂ targets and film Zn/Sn composition varied approximately from 1:1 (corresponding to 100 W RF power) to 2:1 (corresponding to 40 W RF power). Films prepared at RF powers less than 40 W were polycrystalline and had shown only ZnO phases. Hence those films are not considered for the comparison here. Profound difference is observed in the case of bandgap values. The PLD a-ZTO films show an optical Tauc gap around 2.8 eV, while the same is around 3.3 eV for the co-sputtered films. The effect of subgap states, just below the fundamental band, are more prominent in the case of PLD films. In co-sputtered films, the carrier concentration increased from 2.2×10^{16} to $2.2 \times 10^{17} \text{ cm}^{-3}$ and the mobility decreased from 5.4 to $1.3 \text{ cm}^2/\text{Vs}$ as the Zn/Sn composition varied from 2:1 to 1:1. In case of PLD films deposited at zero oxygen pressure, these variations were $10^{14} - 10^{12} \text{ cm}^{-3}$ and 0.45 - $0.9 \text{ cm}^2/\text{Vs}$ respectively. At very low oxygen pressure, the PLD films are expected to show a high carrier concentration because of the increased oxygen deficiencies. However, because of the profound effects of carrier trapping subgap states, the density was at least two orders less compared to co-sputtered films. Above 2 Pa, the effect of subgap states was not very serious, and films show almost comparable carrier density and mobility with co-sputtered films.

Another noticeable effect between the films are in the roughness. The sputtered films show higher roughness, while possibility of higher working pressure ensures smoother films in PLD. In sputtering, it is common that

the O^- anions produced near the target surface are accelerated by the electric field in the cathode dark space region and adversely affect the film surface by colliding the substrate during film growth.

Chapter 5

Characterisation of Amorphous Zinc Indium Tin Oxide Thin Films Prepared by Co-sputtering

This chapter gives the details of preparation of zinc indium tin oxide (ZITO) thin films by co-sputtering technique. Films were then analysed by GXR, XRF, UV-Vis-NIR spectrophotometer and Hall effect measurements. All films grown at room temperature (RT) were amorphous and had shown sufficient conductivity and mobility. The effect of oxygen partial pressure during deposition on the optical and electrical properties of co-sputtered ZITO films are also discussed.

5.1 Introduction

Several crystalline transparent semiconducting oxides (TSOs), like $\text{In}_2\text{O}_3:\text{Sn}$, $\text{ZnO}:\text{Al}$ [170], MgIn_2O_4 [183], ZnGa_2O_4 [184], $\text{Cd}_{1-x}\text{Y}_x\text{Sb}_2\text{O}_6$ [185], AgSbO_3 [186], and InGaZnO_4 [187], in thin film form have widely been used in technical applications such as transparent electrode materials for liquid crystal displays, solar cells, smart windows etc. Amorphous TSOs have recently been got much attention owing to its capability for use in applications like large area flexible displays, invisible electronic circuits and amorphous solar cells etc. Electrically conducting and visibly transparent amorphous thin film materials have unique advantage of low temperature processing over crystalline materials. This enables the deposition of thin films of these amorphous materials on plastic substrates. Several amorphous TSOs such as indium oxide [188, 189], indium gallium zinc oxide [190], cadmium germanate [191, 192], zinc tin oxide and zinc indium oxide and their use in electronic circuits have been reported [110, 118, 126, 193, 194]. These materials exhibit excellent optical transmission, high electrical conductivity and high chemical stability [195–198]. Detailed description of working hypothesis of amorphous TSOs were given in section 1.8.

This chapter is divided into two parts. First part gives the deposition and analysis of a-ZITO thin films as a function of chemical composition. Second part gives the effect of oxygen partial pressure on the deposited films.

5.2 Effect of zinc content on the optical and electrical properties of ZITO thin films

5.2.1 Experimental details

ZITO thin films were prepared by co-sputtering method using powders of ZnO (99.99% pure, Alfa Aeser) and pre-sintered $\text{In}_2\text{Sn}_2\text{O}_7$ (ITO) (99.99% pure) targets. Powders were taken in Cu plates having two inch diameter. Schematic diagram of the deposition configuration has been shown in figure 4.1. ZnO target was powered by a radio frequency (RF) power supply and ITO target by a direct current (DC) power supply. DC target (ITO) current was fixed at 200 mA (600 V) and films were grown at various powers to RF target (ZnO) which varied from 25 to 200 W in steps of 25 W. Sputtering was carried out for 10 minutes in pure argon atmosphere. Glass substrates were placed parallel to the targets at a distance of 4 cm from its surface and were not intentionally heated during the deposition. Substrates were rotated over the targets at a speed of 50 rpm using a stepper motor assembly. Composition of deposited films were controlled by adjusting the power to the sputtering targets.

5.2.2 Deposition rate

Thicknesses of the films were measured by Veeco Dektak 6M stylus profiler. Thickness of the films varied from 295 nm to 430 nm on increasing the RF power from 25 W to 200 W for the fixed sputtering duration of ten minutes. Figure 5.1 shows the deposition rate estimated from the measured thickness with respect to the variations in RF power. Deposition rate increases almost linearly with the increase in RF power.

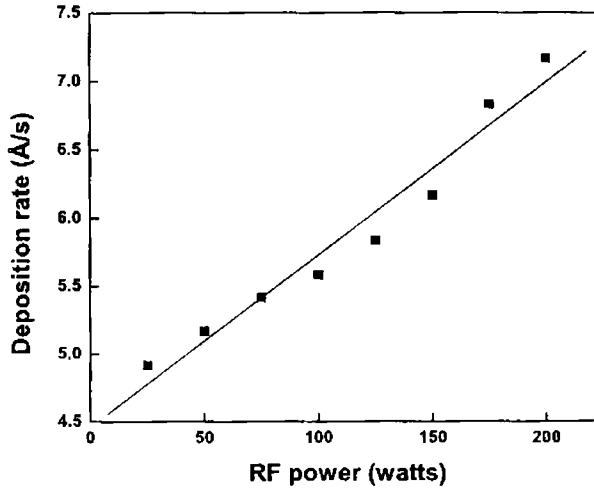


Figure 5.1: The deposition rate of ZITO films for various RF powers to the ZnO target keeping the ITO target at a constant DC current of 200 mA.

5.2.3 Compositional analysis

Chemical composition of the films were analysed by XRF (Rigaku ZSX100E) measurements. With the increase of RF power, the zinc content in the film increased linearly while the tin and indium content remained almost constant (Figure 5.2). The Zn:In:Sn atomic ratios varied from 0.05:0.56:0.39 to 0.5:0.27:0.23 in the co-sputtered films on varying the RF power. Since the films have shown gradual variation in chemical composition, the various properties of the films are discussed in terms of the zinc content $[Zn/(Zn+In+Sn)]$ in the film.

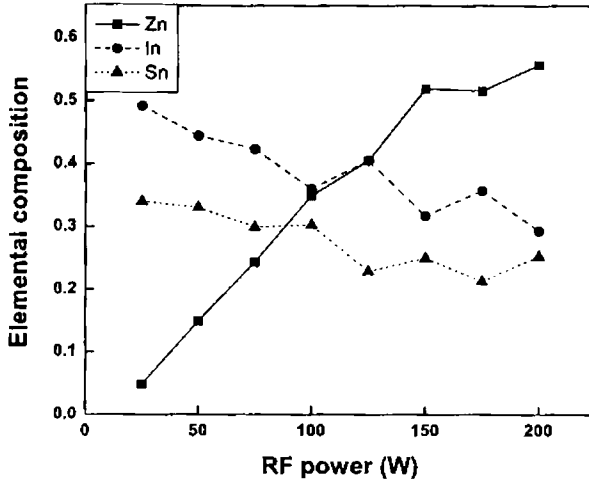


Figure 5.2: Variations in chemical composition of the cosputtered ZITO thin films with respect to the RF power variation at the ZnO target for a constant DC current of 200 mA for ITO target.

5.2.4 Structural characterisation

The film structures were characterised by GXR D at an incident angle of 0.5° using Rigaku RINT-2000 with $Cu K_\alpha$ radiation. GXR D profiles of as deposited films shown in figure 5.3 have only a halo peak around 34° . The absence of sharp peaks indicate that all films are amorphous irrespective of variations in RF power and composition. Film roughness was estimated using AFM (SPI - 3800N, S.I.I). Except for the film with very low Zn content, all films were found to have an rms roughness of approximately 3 nm (Figure 5.4).

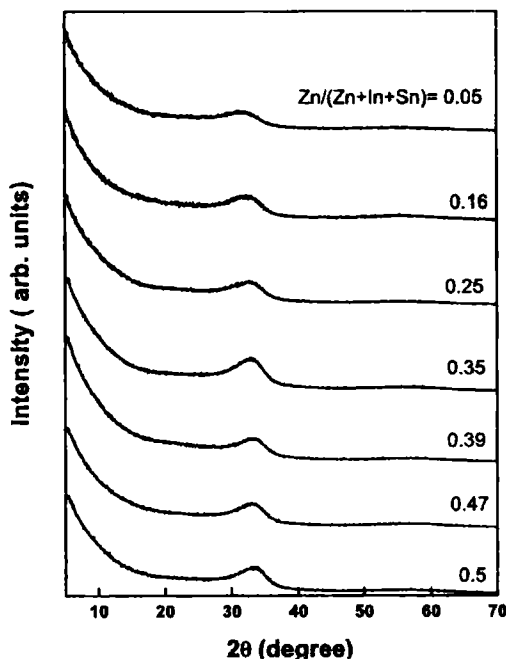


Figure 5.3: Glancing angle x-ray diffraction pattern of ZITO films for various Zn content showing the amorphous nature of the deposited films.

5.2.5 Optical characterisation

Optical transmittance and reflectance spectra were recorded using a UV-Vis-NIR spectrophotometer (Hitachi U-4000). Optical transmission spectra showed an average transmission greater than 90% for all films in the visible region of electromagnetic spectrum (Figure 5.5). An abrupt decrease in transmission at lower wavelength is due to fundamental band to band absorption and loss of transmission at higher wavelength is attributed to the absorption by free carrier electrons.

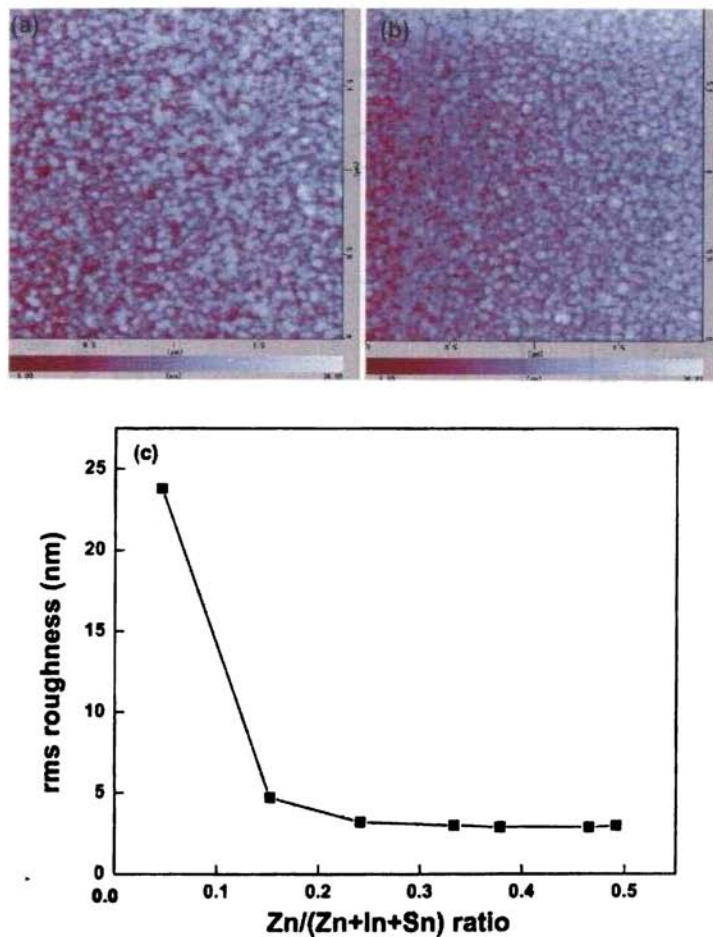


Figure 5.4: AFM images of co-sputtered amorphous ZITO films (a) $Zn/(Zn+In+Sn)=0.35$ and (b) $Zn/(Zn+In+Sn)=0.5$. (c) Variation of rms roughness of the films with Zn content.

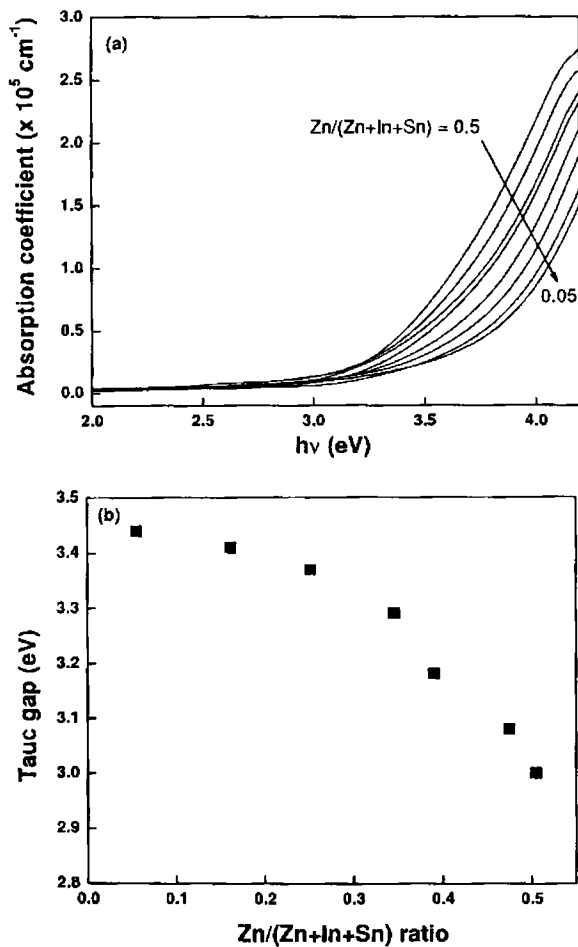


Figure 5.7: (a) Plot of absorption coefficient (α) Vs photon energy ($h\nu$) for different zinc concentrations. The downward arrow indicates the variation of zinc content from $\text{Zn}/(\text{Zn}+\text{In}+\text{Sn}) = 0.5$ to $\text{Zn}/(\text{Zn}+\text{In}+\text{Sn}) = 0.05$. (b) Band gap variation with the variation of zinc content in the film.

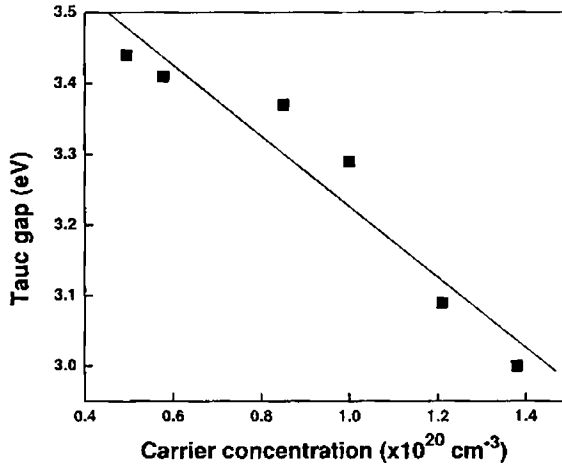


Figure 5.8: Dependence of band gap on carrier concentration of the film.

enhanced by the increase of zinc content. This causes the band gap to decrease with the increase of carrier density in the film (Figure 5.8).

Effective mass and momentum relaxation time (τ) of free electrons were analysed from free carrier absorption spectra observed in highly conductive as-deposited film by fitting an optical model to the observed R and T spectra. This optical model includes a film/glass substrate structure and a Cauchy type dispersion with a Drude-type free carrier absorption (details were reported in reference [203]). Large optical absorptions observed in the near infrared (IR) region (1500 - 2500 nm) comes from reflection and absorption due to the free electrons (free carrier absorption: FCA) and consistent with the high electron concentrations obtained by the Hall effect measurements (discussed later). Optical analysis were performed for these data on the as-deposited films to extract an effective mass and a momen-

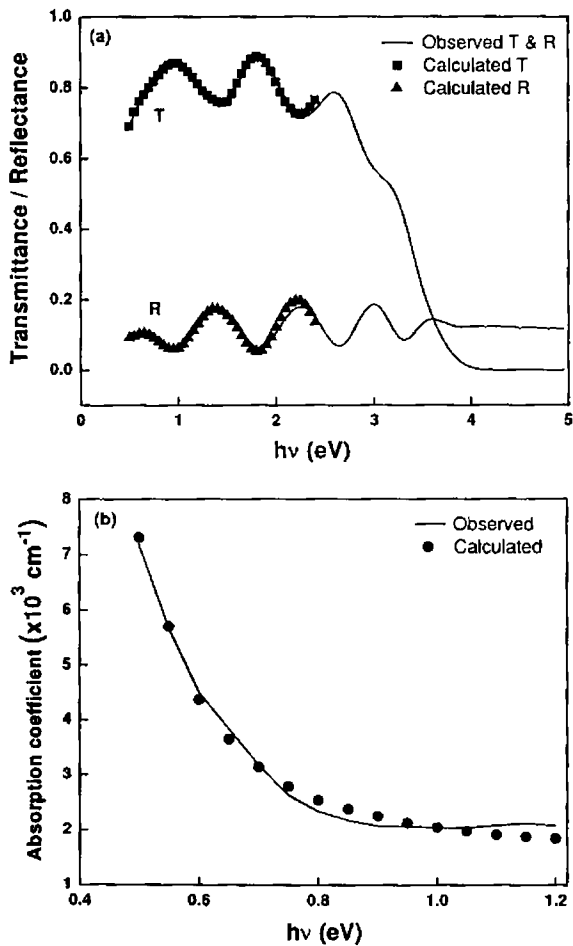


Figure 5.9: (a) Fitting result of FCA analysis presented in transmittance (T) and reflectance (R) spectra for the Zn:In:Sn=0.35:0.35:0.3 film. Solid lines: Observed R and T spectra. Symbols: Fitted results. (b) Observed and fitted results in optical absorption coefficients for various photon energies for the same film.

tum relaxation time from FCA, but a reasonable fitting agreement to both the T and R spectra was obtained only for the Zn:In:Sn = 0.35:0.35:0.3 film. Figure 5.9 shows that the simulated T and R spectra agree well with the observed spectra, giving the plasma frequency of 0.51 eV and τ of 3.9 fs. Using the electron density obtained by the Hall measurement ($1 \times 10^{20} \text{ cm}^{-3}$), an effective mass of $0.53 m_e$ (m_e is the rest mass of electron) was obtained for the conduction electrons. It would be of interest to compare these results with another amorphous oxide semiconductor (AOS), a-InGaZnO₄. An effective mass of $0.34 m_e$ and τ of 3.4 fs has been reported for an as-deposited a-InGaZnO₄ film by simply fitting to only an optical absorption spectrum [181]. In this study, the measurement was repeated by employing a more reliable approach to use both the T and R spectra for the fitting procedures, and obtained the effective mass of $0.36 m_e$ and τ of 4.4 fs for the as deposited InGaZnO₄. Comparing these results indicates that the smaller mobility of the Zn:In:Sn = 0.35:0.35:0.3 film ($9.1 \text{ cm}^2/\text{Vs}$) than that of the a-InGaZnO₄ film ($17 \text{ cm}^2/\text{Vs}$) is primarily attributed to the heavier effective mass because the difference in relaxation time is smaller than the difference in the effective masses.

5.2.6 Electrical characterisation

Electrical resistivity and Hall coefficient were measured by four probe van der Pauw configuration with AC modulation of magnetic field at room temperature (RESITEST 8300, Toyo Cor.). To ensure the low resistive ohmic contacts, sputtered Au electrodes were used for the electrical measurements. Conductivity, carrier concentration and hall mobility of the co-sputtered ZITO films are shown in figures 5.10 and 5.11. Mobility and carrier concentration increased with Zn content in the film. Hence conductivity shows

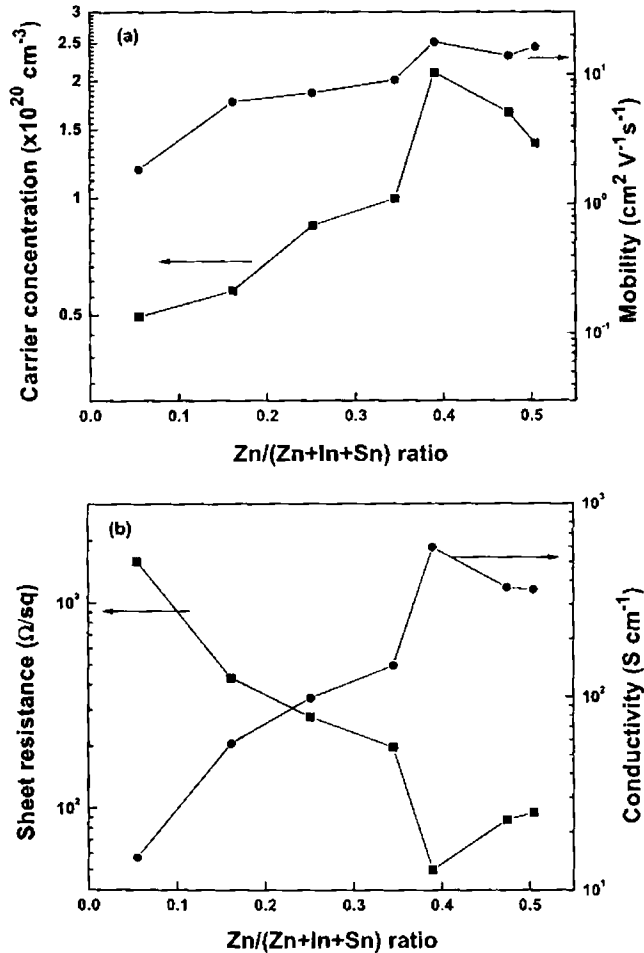


Figure 5.10: (a) Variation of Hall mobility and carrier concentration with the increase of zinc content in amorphous ZITO films. (b) Sheet resistance and conductivity variation in a-ZITO films with zinc content.

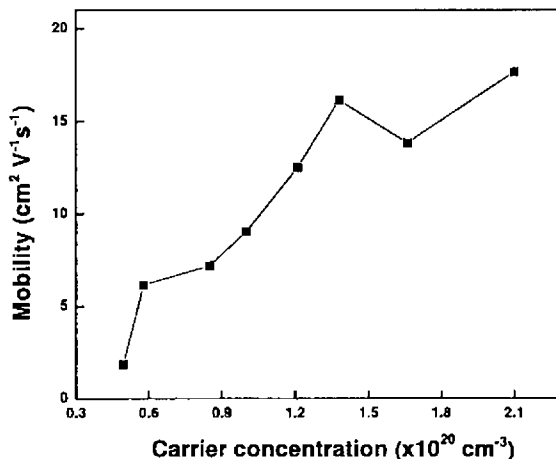


Figure 5.11: Dependence of Hall mobility on carrier concentrations.

an increasing behaviour with the increase of Zn content. Maximum conductivity of $6 \times 10^2 \text{ S cm}^{-1}$ was obtained for Zn:In:Sn atomic ratio 0.4:0.4:0.2 in the film. Hall mobility strongly depends on carrier concentration and steeply increases from ~ 2 to $12.5 \text{ cm}^2/\text{Vs}$ as the carrier concentration slightly increases from 4×10^{19} to $1.2 \times 10^{20} \text{ cm}^{-3}$. Maximum mobility obtained was $18 \text{ cm}^2/\text{Vs}$ at a carrier concentration of $2.1 \times 10^{20} \text{ cm}^{-3}$ (Figure 5.11). The mean free path length l is calculated using the equation [190],

$$l = \frac{(3\pi^2)^{1/3} \hbar n^{1/3} \mu}{2\pi e} \quad (5.1)$$

where h , n , e and μ denote the Planck constant, carrier density, elementary electric charge and mobility respectively. Estimated mean free path length varies from 1.4 \AA to 2 nm as the carrier concentration varied from 5×10^{19} to $2.1 \times 10^{20} \text{ cm}^{-3}$. Variation of Hall mobility with respect to the increase

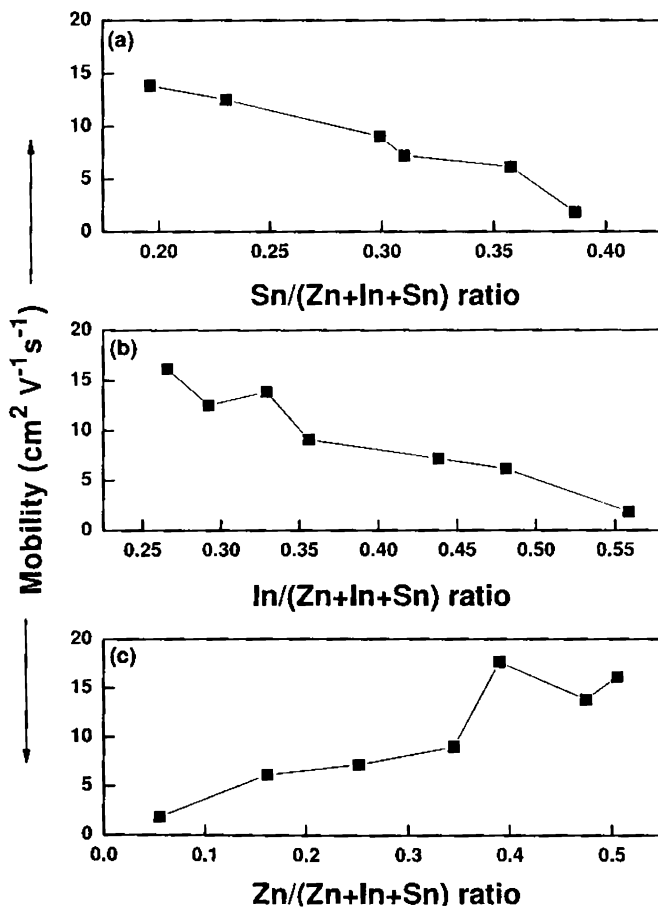


Figure 5.12: Hall mobility variation with (a) tin (b) indium and (c) zinc cationic contents in amorphous ZITO films.

of different cationic content in the film is shown in figure 5.12. As tin and indium content increases, the mobility shows a gradual decrease, while it increases with the increase of zinc content.

5.2.7 Discussion

Observed characteristics of amorphous ZITO films can be explained on the basis of working hypothesis of wide band gap electrically conducting amorphous oxides (refer section 1.8). Inverse photoelectron spectroscopic and molecular orbital studies carried out on similar amorphous TSOs had shown the similarity in density of states of conduction band bottom between the amorphous material and the crystalline material [72, 190]. Eventhough the topological sequence of the ion arrangement in heavy metal-oxide systems is metal-oxygen-metal, the conduction band bottom is primarily composed of vacant *s* orbitals of the heavy metal cations and the contribution of the intervening oxygen is rather small.

For complex amorphous systems containing several metal ions, the percolation theory should be taken into consideration [72]. The site percolation threshold decreases as the site density increases, and reaches the value of 0.20 for close packed fcc systems [204]. Hence the metal ions that play the dominant role in providing conductivity should occupy more than 20% of all ion sites in an amorphous phase. In our case the Zn (which forms conduction band bottom) content varies from 5% to 50% of total cation content. The carrier transport in a-ZITO may be governed by percolation conduction over the distribution of potential barriers around the conduction band edge. Non-localized tail states may form in the vicinity of conduction band bottom with potential barriers due to the random distribution of Zn, In and Sn ions in amorphous structures. As carrier concentration increases

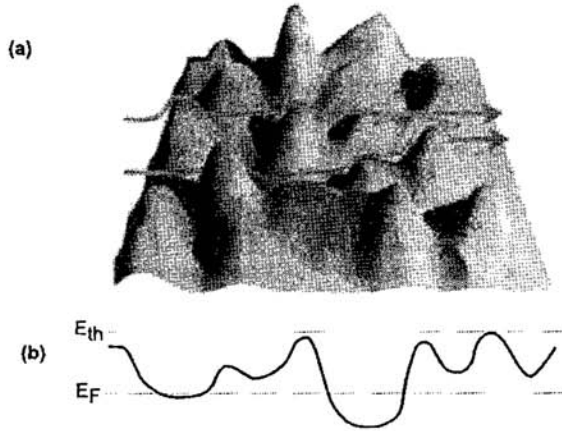


Figure 5.13: (a) The schematic diagram of carrier conduction around conduction band edge. Arrows show electronic conduction path. (b) Schematic energy diagram around conduction band edge. The position of the Fermi energy (E_F) determines the carrier transport through such a system. For low density of carriers, conduction takes place by percolation through available paths. When there are sufficient number of electrons in the conduction band, to overcome the threshold energy (E_{th}), the conduction mechanism changes to degenerate conduction.

the potential barriers are overcome, and therefore the Hall mobility increases with the increase of carrier concentration, and large Hall mobilities ($> 15 \text{ cm}^2/\text{Vs}$) are obtained at carrier concentrations $\sim 10^{20} \text{ cm}^{-3}$ (Figure 5.13).

Eventhough the long range order is lost in present amorphous films, the Sn 5s, In 5s and/or Zn 4s orbitals can form conduction path, since the content of these ions are greater than the percolation threshold of 20%. The condition for the formation of conduction path in amorphous oxides has been explained by Orita *et al.* [190] by the evaluation of an overlap

integral S , between ns orbital functions of various metal ions. This overlap integral strongly depends on the principal quantum number n and the core charge Z . They suggested a threshold value of 0.4 for overlap integral as a criterion for the formation of extended wave functions which are responsible for good conductivity. The overlap integrals between ns wave functions for Zn 4s, In 5s and Sn 5s orbitals are 0.6045, 0.5613, and 0.4523 respectively [190]. These values, originally derived for crystalline metal oxides, are also applicable to the amorphous phase since the overlap integrals of s orbitals simply depends on the metal-metal distance for a fixed metal ion.

In amorphous semiconductors, the valence and conduction bands have tails of localized states, and the energy that separates the localized states from the delocalized state is called the mobility edge. A sharp drop in the mobility by a factor of about 10^2 has been generally observed at the mobility edge in amorphous materials [205]. High carrier densities and mobilities in co-sputtered ZITO films indicate that the Fermi level in these amorphous films exceeds the mobility edge of the conduction band. In the present study, the Hall mobility was found to increase with the increase of Zn content in the film. As the zinc content increases, the Zn-Zn average distance becomes shorter, and direct overlap between 4s orbitals of neighboring zinc cations is possible in the films. On the other hand, the Hall mobility decreases with the increase of In and Sn content. This observation, along with the fact that In 5s and Sn 5s orbitals have a low overlap integral value compared to Zn 4s orbitals, suggests that the conduction path in amorphous ZITO films are primarily formed by 4s orbital of Zn ions.

5.2.8 Effect of thermal annealing

The optical and electrical analysis of a-ZITO films suggest that the a-ZITO films have large mobilities ($\sim 10 \text{ cm}^2/\text{Vs}$) and may produce high mobility TFTs, but their carrier concentrations would be too high to effectively modulate the channel conductance by a gate bias voltage. Therefore we examined the effects of post thermal annealing at $300 \text{ }^\circ\text{C}$ in air. Figures 5.14 a and b compares the optical transmittance (after reflection correction) before and after annealing. It is clear that, eventhough the transmittance has not changed in the visible region by thermal annealing, the large IR absorption by free carriers observed in as-prepared films are very small in annealed films. Figure 5.15 compares the optical absorption spectra before and after the thermal annealing plotted in terms of the Tauc' plot. It shows that the Tauc gaps of the as-prepared films decreases from 3.3 to 3.0 eV with increasing the Zn content from 0.35 to 0.50. The thermal annealing changed the Tauc gap from 3.30 to 3.20 eV for the Zn content of 0.35, for example. It should be noted that the slopes of the Tauc' plots become sharper and the subgap absorptions beneath the Tauc' gaps become smaller after the thermal annealing. It is more clear in the logarithmic plot (Figures 5.15c and d). Thermal annealing caused the reduction of the extra absorptions in the vicinity of Tauc' gap.

In the energy range $E < E_g$, the optical absorption coefficient shows a tail (Urbach tail) of the form $\alpha(h\nu) \propto e^{(h\nu - E_g)/E_U}$, where E_U is the Urbach energy. The Urbach energies were estimated as 0.20, 0.19 and 0.17 eV for the annealed films with Zn contents 0.35, 0.48 and 0.5 respectively. The total area of subgap absorption decreased by thermal annealing.

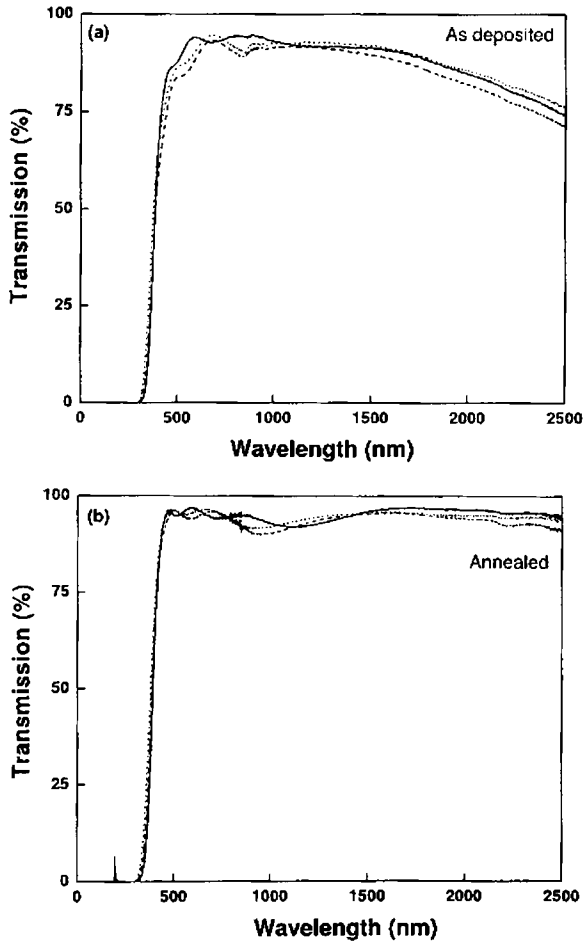


Figure 5.14: Optical transmission spectra of a-ZITO thin films (a) as-deposited and (b) annealed at 300 °C having different Zn:In:Sn atomic ratios. The compositions Zn:In:Sn are: (Solid lines) 0.50:0.27:0.23, (dashed lines) 0.48:0.30:0.22, and (dotted lines) 0.35:0.35:0.30. Spectra are corrected for reflection. As-prepared films show large optical absorption in the IR region.

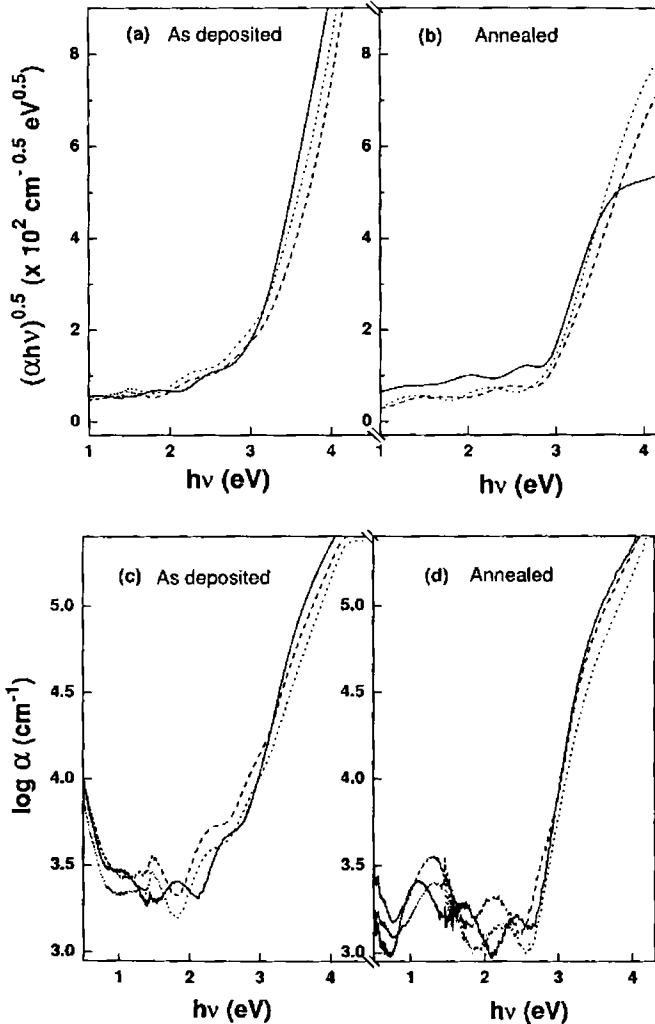


Figure 5.15: Tauc' plots of as-deposited (a) and annealed (b) films as a function of Zn content. (c) and (d) show the plots of $\log \alpha - h\nu$. The compositions Zn:In:Sn are: (Solid lines) 0.50:0.27:0.23, (dashed lines) 0.48:0.30:0.22, and (dotted lines) 0.35:0.35:0.30.

Table 5.1: Chemical composition and transport properties of a-ZITO films

RF power (W)	[Zn]	[In]	[Sn]	As prepared films		Annealed films	
				N_e $10^{20} cm^{-3}$	μ cm^2/Vs	N_e $10^{18} cm^{-3}$	μ cm^2/Vs
200	0.50	0.27	0.23	1.38	16.2	5.33	10.7
150	0.48	0.29	0.23	1.21	12.5	4.87	7.6
100	0.35	0.35	0.30	1.0	9.05	2.1	5.43

Hall measurement data given in Table 5.1 shows that the thermal annealing decreased the carrier concentrations drastically by two orders of magnitude to the order of $10^{18} cm^{-3}$. Hall mobilities also decreased simultaneously since amorphous oxide semiconductors have a potential fluctuation around the conduction band minimum (refer figure 5.13), and consequently a large mobility is obtained at somewhat large carrier density which is enough to fill these potential valleys [181]. These results indicate that the thermal annealing in air causes oxidation of the films, and reduce the carrier concentration and the subgap states.

5.3 Effect of oxygen partial pressure

Amorphous ZITO is a potential candidate for channel layer material in thin film transistors (TFTs) [118]. In the preceding section, the optical and electrical properties of amorphous ZITO thin films prepared by co-sputtering method was studied as a function of chemical composition of the films. In that case, all films were highly conductive with carrier density greater than $10^{19} cm^{-3}$. It is known that the performance of a TFT

strongly depends on the quality and transport mechanism of active channel materials [62, 90, 126, 206]. The carrier density and mobility are two important factors which affect the performance of a TFT. High carrier density in the channel material causes large OFF current and the normally ON characteristics of a TFT [127]. Hence it is more important to control the carrier density less than 10^{17} cm^{-3} to get proper transistor action. Therefore, to control the carrier density in the amorphous ZITO films, thin film depositions were carried out by varying the oxygen partial pressure in the deposition chamber. In this section the effect of oxygen partial pressure on the optical and electrical properties of amorphous ZITO thin films are discussed.

5.3.1 Experimental setup

ZnO (99.99% pure) powder and $\text{In}_2\text{Sn}_2\text{O}_7$ (ITO) (99.99% pure) target were used in an RF-DC co-sputtering method to prepare ZITO thin films. Sputtering was carried out for 10 minutes in pure argon and argon + oxygen atmosphere. Oxygen partial pressure in the chamber was varied from 0.1 Pa to 0.9 Pa keeping the total gas pressure at 1 Pa. ZnO was sputtered at an RF power of 75 W and ITO at 200 mA (600 V) DC current (targets were of 2 inch diameter). Glass substrates were placed parallel to the targets at a distance of 4 cm from target surfaces and were not intentionally heated during the deposition. Substrate was rotated over the targets at a speed of 50 rpm using a stepper motor assembly. Schematic diagram of the setup is shown in figure 4.1 in chapter 4.

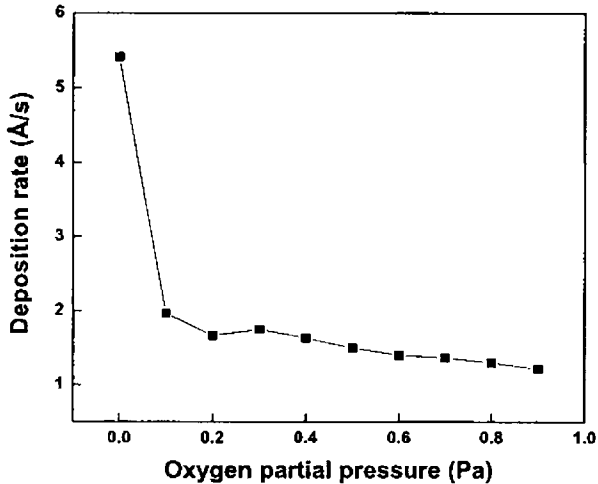


Figure 5.16: Variation of ZITO deposition rate with oxygen partial pressure for a fixed DC power of 120 W and RF power of 75 W.

5.3.2 Deposition rate

Deposition rate of ZITO thin films on glass substrates for different oxygen partial pressure is shown in figure 5.16. The total gas pressure (argon + oxygen) in the vacuum chamber was maintained at 1 Pa during deposition. The deposition rate was drastically reduced by the introduction of oxygen gas in the sputtering chamber. The reduction of deposition rate with oxygen pressure in the sputtering of metal oxides is a generally observed phenomenon and it is attributed to the re-sputtering of atoms from the film surface by the energetic O^- ions [207–209]. Since more O^- ions are available at high oxygen partial pressure, re-sputtering gets more enhanced and a reduction in deposition rate is henceforth observed.

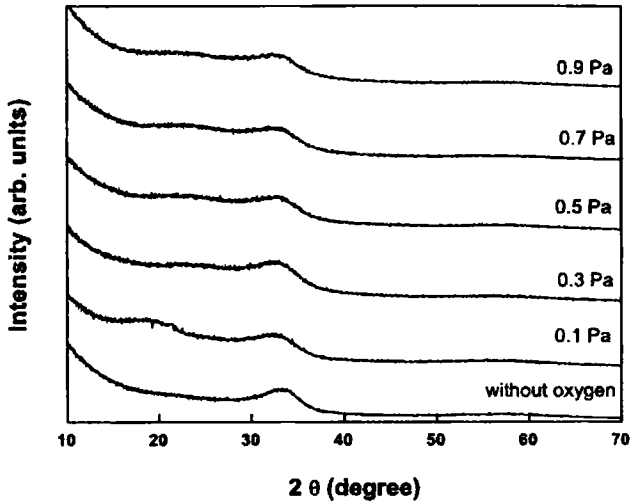


Figure 5.17: Glancing angle x-ray diffraction patterns of co-sputtered ZITO thin films grown at different oxygen partial pressures keeping the DC and RF powers constant.

5.3.3 Structural characterisation

GXRD profiles of ZITO films (Figure 5.17) show only a halo peak around 34° and there are no sharp diffraction peaks. This indicates that all films are amorphous irrespective of oxygen partial pressure. Films deposited at very low and very high oxygen partial pressure shows surface roughness less than 5 nm . Films showed higher roughness in the oxygen partial pressure range of $0.2\text{--}0.7\text{ Pa}$ (Figure 5.18). As the oxygen partial pressure is increased, the film surface gets bombarded by the energetic O^- ions and becomes rough. Chemical composition of the films, analysed by XRF, showed Zn:In:Sn atomic ratio $0.48:0.29:0.23$ and there was not much variation in this atomic

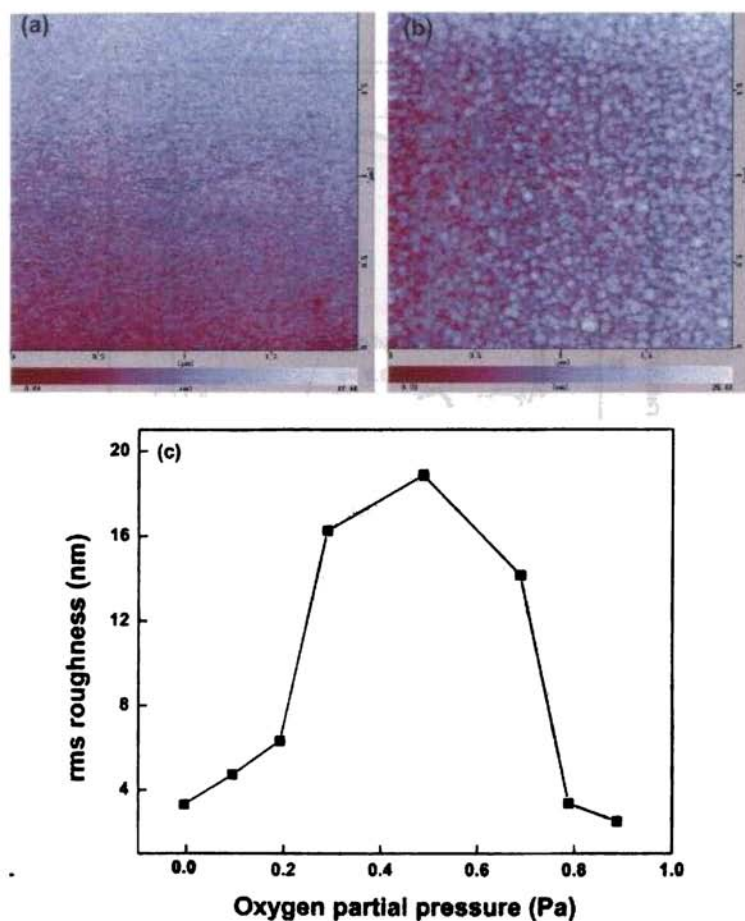


Figure 5.18: AFM images of ZITO films deposited at oxygen partial pressure (a) 0 Pa and (b) 0.9 Pa. (c) rms roughness of the ZITO films grown at different oxygen partial pressures.

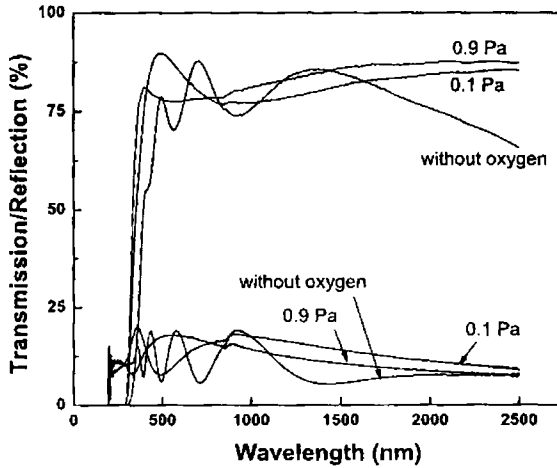


Figure 5.19: Optical transmission and reflection spectra of amorphous ZITO films prepared at various oxygen partial pressures keeping the DC and RF powers constant.

ratio with respect to the variation in oxygen partial pressure.

5.3.4 Optical characterisation

Optical transmission and reflection spectra of the amorphous ZITO films are shown in figure 5.19. These films have an average transmittance $> 85\%$ across the visible region irrespective of the oxygen partial pressure. An abrupt drop in transmission at lower wavelength is due to the band to band absorption in the film. Film prepared in pure argon atmosphere shows a loss of transmission at higher wavelength which is attributed to the free carrier reflection and absorption. There is a sudden change in band gap (Tauc gap) between the films deposited in pure argon atmosphere and 0.1

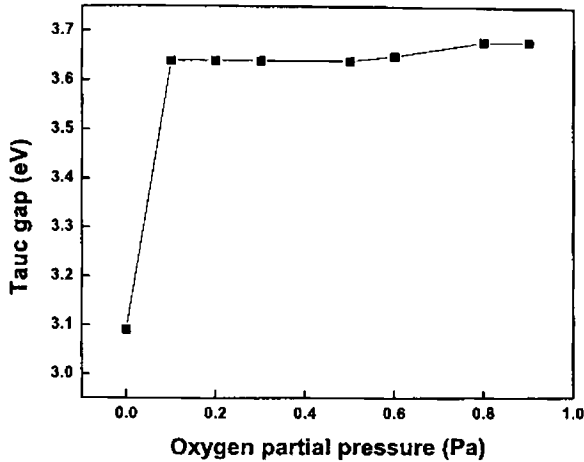


Figure 5.20: Dependence of optical band gap of amorphous ZITO films on oxygen partial pressure.

Pa oxygen partial pressure from 3.1 eV to 3.64 eV (Figure 5.20). After that the band gap of the films remains almost insensitive to the variations of oxygen partial pressure. The change in band gap, in case of films deposited with and without oxygen pressure, is the effect of subgap states. Figure 5.21 shows that the film prepared without oxygen partial pressure has large subgap states just below the fundamental band gap. This reduces apparent band gap value compared to the films deposited in oxygen ambience.

5.3.5 Electrical characterisation

Electrical properties of the amorphous ZITO films shows a strong dependence on oxygen partial pressure. Conductivity of the film prepared in pure argon was $2 \times 10^2 \text{ Scm}^{-1}$, which dropped to $4 \times 10^{-3} \text{ Scm}^{-1}$ with the

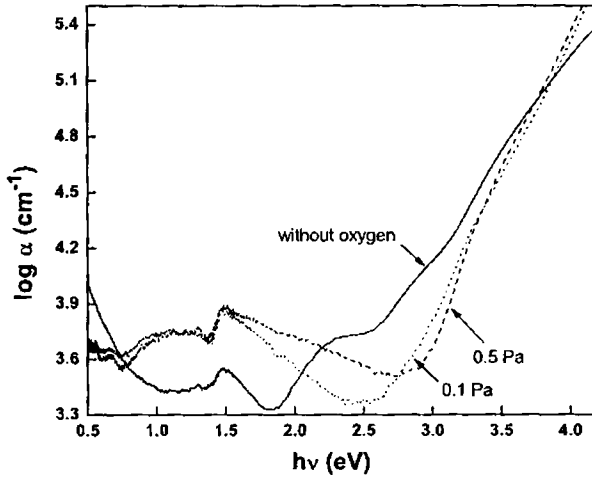


Figure 5.21: $\text{Log}(\alpha) - h\nu$ plots of a-ZITO films deposited with and without oxygen partial pressure.

introduction of oxygen gas to the sputtering chamber during sputtering (Figures 5.22 and 5.23). The value further decreased on increasing oxygen partial pressure and it reduced even to $3 \times 10^{-7} \text{ Scm}^{-1}$ at the oxygen partial pressure of 0.9 Pa . Carrier concentration and Hall mobility also decreased with increase in oxygen partial pressure. Carrier concentration dropped from $1 \times 10^{20} \text{ cm}^{-3}$ to $1 \times 10^{12} \text{ cm}^{-3}$ and Hall mobility from 12.5 to $0.4 \text{ cm}^2/\text{Vs}$ on increasing the oxygen pressure from 0.1 to 0.9 Pa (Figure 5.22 a,b).

Origin of conductivity in transparent oxide semiconductors is still controversial. It has been postulated for a long time that transparent conductivity is related to the existence of shallow donor levels near the conduction

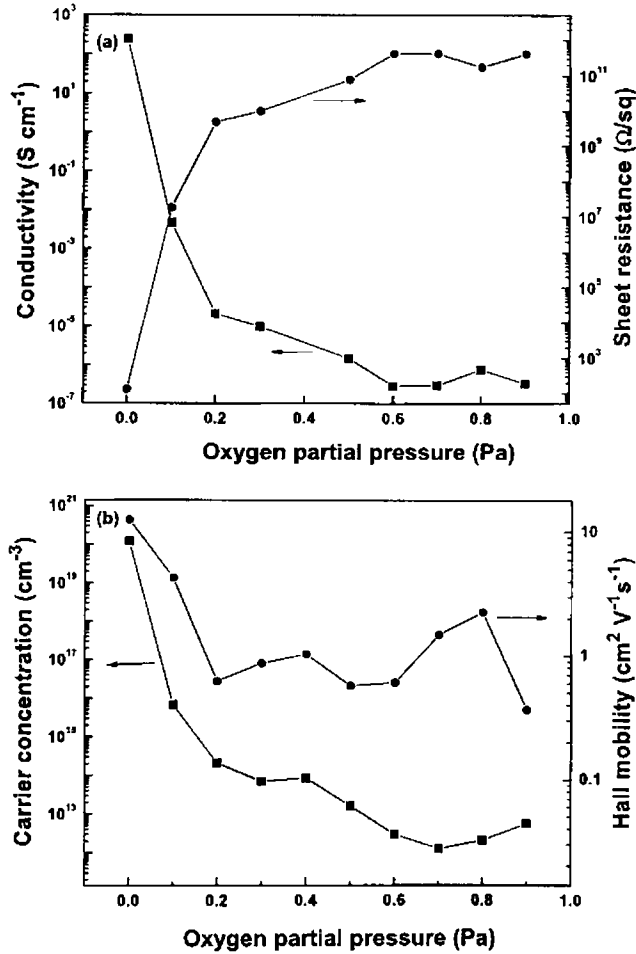


Figure 5.22: (a) Variation of conductivity and sheet resistance of amorphous ZITO thin films with the increase of oxygen partial pressure during sputtering. (b) Carrier concentration and Hall mobility are reduced with the increase of oxygen partial pressure.

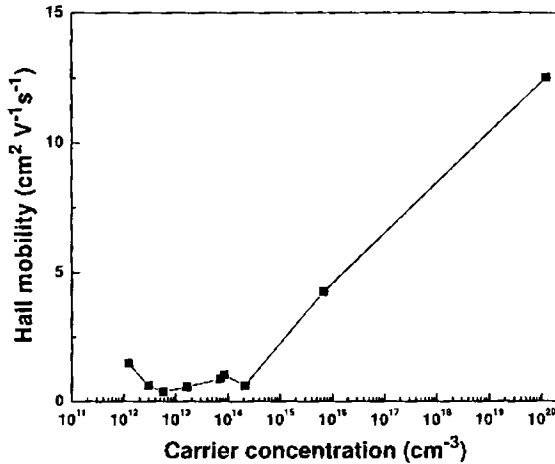


Figure 5.23: Dependence of Hall mobility on carrier concentration.

band, formed by oxygen vacancies [53]. In contrast, there are reports which show that oxygen vacancies form deep levels [55, 56]. Even in amorphous oxide films, oxygen vacancies are believed to be responsible for controlling the carrier concentration [60, 188]. Present study also support this argument, that the carrier generation in amorphous ZITO films are mainly controlled by the oxygen vacancies ($\text{O}^{2-} = 1/2 \text{O}_2 + 2\text{e}^{-1}$) in the film. High oxygen partial pressure reduces the density of oxygen vacancies and thereby lower the carrier concentration. As mentioned in the previous session, carrier concentration should exceed a threshold value to obtain a large mobility [126, 179, 181]. High mobility was obtained in ZITO films when the carrier concentrations exceeded 10^{16} cm^{-3} (Figure 5.23).

5.4 Analysis of carrier transport mechanism

To understand the carrier transport mechanism in amorphous ZITO films, temperature dependence of DC electrical conductivity of selected samples were studied. For resistivity measurements at low temperature, samples were kept in a cryostat equipped with helium refrigerator and the measurements were carried out over the temperature range between 80 K and 300 K in vacuum. Figure 5.24 shows the conductivity variations for three carrier concentrations. The samples were chosen such that their carrier concentrations span from a lower value (below the threshold concentration required to show the degenerate band conduction) to some higher value above which the degenerate band conduction is expected. Film with carrier density $6.86 \times 10^{15} \text{ cm}^{-3}$ was prepared at 0.1 Pa oxygen partial pressure at an RF power of 75 W . The film with carrier concentration $4.95 \times 10^{19} \text{ cm}^{-3}$ was prepared at 25 W RF power and $1.21 \times 10^{20} \text{ cm}^{-3}$ was deposited at 150 W RF power to ZnO target in pure argon atmosphere keeping the DC power to SnO₂ target constant at 120 W . All these films have shown a definite Hall voltage with a minimum mobility of 4.25 cm^2/Vs for the film deposited at 0.1 Pa oxygen partial pressure.

Measured data points of the film deposited at 0.1 Pa oxygen fit to a straight line in the $\log(\sigma)$ versus $T^{-1/4}$ plot in the whole temperature region. This can be explained on the basis of percolation conduction model which yields a $T^{-1/4}$ behaviour in randomly oriented systems with potential fluctuations at the bottom of the conduction band (refer figure 5.13). This potential variation arises from the random distribution of the various different cations in the film that in turn modulates the electronic structure around the conduction band edge. There is a threshold energy that

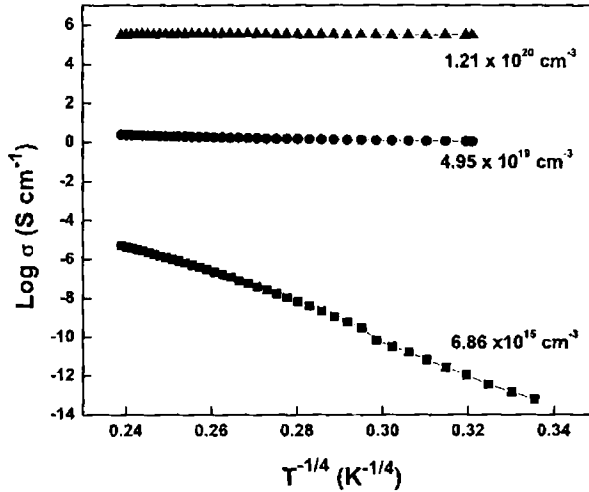


Figure 5.24: Temperature dependence of DC electrical conductivity of amorphous ZITO films with different carrier concentrations. Film with low carrier density shows activated type conduction which changes to degenerate type conduction at higher carrier densities.

separates the carrier conduction mechanism from percolation to degenerate conduction. At sufficiently high values of carrier densities (Figure 5.23), the carriers may overcome the potential fluctuations and the conduction mechanisms changes from percolation to degenerate conduction [53, 55, 126]. This behaviour is very clear in the case of high electron density film shown in figure 5.24 where the conductivity does not show any activated type behaviour as the Fermi level exceeds the potential fluctuations.

5.5 Conclusion

Conductive transparent thin films of amorphous zinc indium tin oxide were prepared at room temperature by co-sputtering of zinc oxide and indium tin oxide. Film compositions could be varied by adjusting the power to the sputtering targets. Hall mobility was found to be strongly depend on the type of cationic contents in the films. The conduction band bottom, controlling electron transport properties in amorphous ZITO films, were primarily composed of Zn 4s orbitals and the magnitude of overlap between neighboring orbitals is large and insensitive to the structural randomness. The electronic structure is dominated by local atomic structures, which, in amorphous oxides, is close to the situation in a crystal. Hence the electron mobility of these materials is comparable with that in the crystalline state. This behaviour is in contrast with the low mobility situation in tetrahedral amorphous semiconductors like hydrogenated amorphous silicon (a-Si:H) where the electron conduction paths are composed of s-p hybrid orbitals and carrier transport is controlled by nearest neighbor hopping or variable range hopping.

The optical and electrical properties of co-sputtered amorphous ZITO films were also investigated as a function of oxygen partial pressure in the deposition chamber during sputtering. There was a sharp change in optical band gap values between the films prepared with and without oxygen partial pressure owing to the effect of subgap states. Conductivity of the amorphous ZITO film reduced from 2×10^2 to $4 \times 10^{-3} \text{ Scm}^{-1}$ with the introduction of oxygen gas (0.1 Pa) to the sputtering chamber. Further increase of oxygen partial pressure decreased the conductivity and it reached $3 \times 10^{-7} \text{ Scm}^{-1}$ at 0.9 Pa oxygen partial pressure. Carrier concentration

and Hall mobility also decreased with the increases of oxygen partial pressure. Carrier concentration varied from 1×10^{20} to $1 \times 10^{12} \text{ cm}^{-3}$ and Hall mobility from 12.5 to $0.4 \text{ cm}^2/\text{Vs}$ on increasing the oxygen pressure from 0.1 to 0.9 Pa.

Temperature dependent conductivity shows the existence of non-localized tail states around conduction band bottom with potential barriers due to the random distributions of various cations.

Chapter 6

Fabrication and Characterisation of Amorphous Zinc Tin Oxide and Amorphous Zinc Indium Tin Oxide Thin Film Transistors

This chapter describes the fabrication and characterisation of thin film transistors (TFTs) fabricated on silicon substrates using amorphous channels of zinc tin oxide (a-ZTO) and zinc indium tin oxide (a-ZITO). This chapter has four main sections. Section 6.2 gives the a-ZTO TFT fabrication by PLD and device performance analysis. Section 6.3 deals with co-sputtered

a-ZTO channel TFTs. Section 6.4 gives detailed analysis of co-sputtered a-ZITO channel TFTs. Last section (section 6.5) gives the details of fabrication of all oxide transparent TFTs on glass substrates with co-sputtered a-ZITO as channel layer.

6.1 Introduction

High resolution and large area flat panel displays (FPDs) require thin film transistor (TFT) based active matrix (AM) driving schemes to suppress image blinking and to reduce the power dissipation. TFT technology has been receiving more attention because it is also a promising mean for achieving three dimensional (3D) integration [210]. Amorphous semiconductors are preferred over polycrystalline ones for active layers in TFTs because of low processing temperature and high uniformity of device characteristics. As we have seen in chapter 1, in contrast to low mobility in covalent bonded amorphous materials (where carrier transport is controlled by hopping between localized tail states), degenerate band conduction and thereby high mobilities are possible in amorphous oxide semiconductors containing post transition metal cations. The bottom of the conduction band in these oxide semiconductors having a high ionicity is primarily composed of spatially spread metal ns orbitals with isotropic shapes (n is the principal quantum number), and direct overlap among neighbouring metal ns orbitals is possible [59, 60].

Several amorphous semiconductor materials like zinc oxide [98], indium gallium zinc oxide [119–121, 123, 125, 126], zinc tin oxide [110, 132], gallium nitride [193], and zinc indium oxide [62, 194, 211, 212] have been employed as TFT n-channel layers in recent years. Grover *et al.* [118] have reported

the use of amorphous zinc indium tin oxide as channel ($\text{ZnO}:\text{In}_2\text{O}_3:\text{SnO}_2$ molar ratio 5:20:75) layers in depletion mode TFTs. These channel layer materials have excellent optical transmission in the visible region and the electrical conductivity can be controlled by adjusting the processing conditions [195–198, 213]. As such, amorphous oxide semiconductors are promising materials for TFT technology and there are plenty of works remaining to be surveyed to improve active layer materials with new chemical compositions. It is not easy to vary the film chemical composition by a conventional sputtering technique because one needs to prepare a ceramic target for each chemical composition [120, 213].

SiO_2 films made by thermal oxidation of single crystal Si wafers have the smoothest surface among the commercially available materials [214]. TFTs formed on Si/ SiO_2 are useful for evaluating the channel materials in a wide range of the gate voltage, regardless of the roughness of the channel interface and the gate leakage current. High breakdown voltage strength and low leakage current of SiO_2 enable to observe the transistor characteristics up to several tens of V_{GS} .

In the following discussion, the chemical composition, Hall parameters and optical parameters of the channel layer was estimated from corresponding measurements performed on thin film samples prepared under similar experimental conditions as that used for the channel layer deposition.

6.2 Fabrication of amorphous zinc tin oxide thin film transistors by PLD

6.2.1 Experimental details

Bottom gate zinc tin oxide TFTs were fabricated on silicon substrates by standard photolithography and lift-off technique. Thermally oxidized Si substrates with an SiO₂ layer thickness of 100 nm, was patterned for channel deposition. For this, the photoresist was coated on the substrate by spin coating at 1000 rpm for 10 s. After that, the substrate was dried in an oven at 100 °C for 20 s. Then the channel mask is aligned over the substrate and whole system is exposed to UV light for 20 seconds. Substrates are then developed and washed and then dried by putting it in an oven again at 100 °C for 3 minutes. Such substrates are placed at 3 cm distance from the target. Channel layer is deposited by PLD from a sintered target at an oxygen partial pressure of 0.5 Pa using a KrF excimer laser (248 nm wavelength, 10 Hz repetition frequency). Laser ablation was carried out at a laser energy density of 35 mJcm⁻²pulse⁻¹. Thermally oxidized layer of Si serves as gate oxide. After channel layer deposition, the photoresist was removed by dipping the substrates in acetone for 10 minutes followed by ultrasonic agitation for one minute. Channel deposited substrates are then again patterned for source/drain deposition. Electron beam evaporation was used to deposit Ti/Au (7/40 nm) stack as the source and drain electrodes while Si substrate itself acts as gate electrode. Ideally, the source and drain should form ohmic contact with semiconducting channel layer. Ti forms ohmic contact with ZTO and ZITO semiconductors while Au serves as a probing terminal for measurements. About 100 devices were fabricated on a 10 × 10 mm Si substrate with width/length of the channel

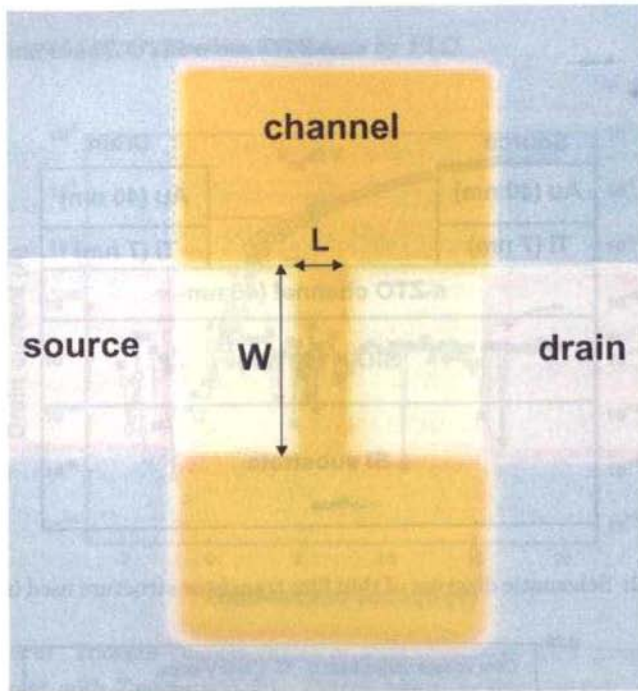


Figure 6.1: Details of a patterned thin film transistor structure used in this study. Figure shows the various layers and W and L parameters.

$= 300 \mu\text{m}/50 \mu\text{m}$. Figure 6.1 shows the image of a single TFT showing the various layers and W and L parameters and 6.2 shows the schematic diagram of TFT structure using a-ZTO channel layer.

6.2.2 Transistor performance

Room temperature fabricated TFTs did not show any transistor characteristics without annealing. After annealing the same device at 300°C for one hour in air, transistor characteristics were observed. The channel layer was deposited at an oxygen pressure of 0.5 Pa using target with Zn:Sn

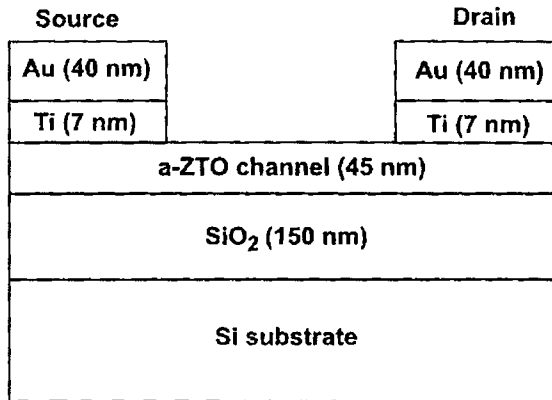


Figure 6.2: Schematic diagram of thin film transistor structure used in this study.

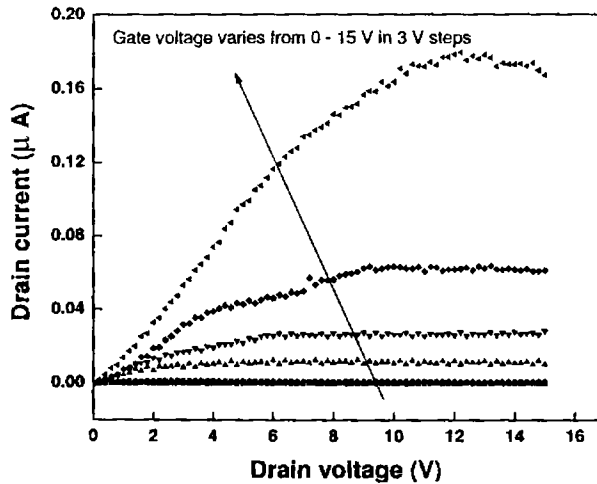


Figure 6.3: Output characteristics of 300 °C post-annealed thin film transistor with a-ZTO as active channel layer prepared by PLD using target with Zn:Sn ratio 2:1. Device operates in enhancement mode as there is no drain current at zero gate voltage.

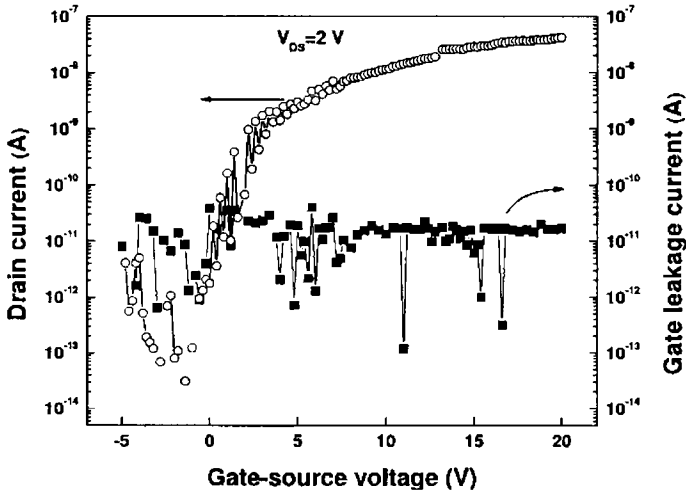


Figure 6.4: Transfer characteristics of a-ZTO channel TFT prepared by PLD using target with Zn:Sn ratio 2:1. Device has a leakage current of the order of 10^{-11} A and an on-off ratio $\sim 10^5$. The results are of the device annealed at 300°C in air.

ratio 2:1 and the resulting film had Zn:Sn ratio 41:59. This is very close to the ratio (36:64) where an extremely stable device with minimum shift in threshold voltage was reported [132]. Figure 6.3 shows a typical output characteristic of TFT for various gate biases after annealing. The device exhibits typical n-channel transistor behavior operating in enhancement mode. Maximum field effect mobility obtained was $0.015\text{ cm}^2/\text{Vs}$. Figure 3.13 (chapter 3) has shown that there was not much difference in the electrical parameters of room temperature deposited films and annealed (at 300°C) films. Similarly a clear impact of processing temperature was not observed in the stability of ZTO thin film transistors [132]. However the TFT functionality was achieved only after annealing the device at 300°C .

Hence the device functionality may be attributed to the modification of semiconductor-insulator interface or improved local atomic rearrangements with annealing. The transfer characteristic (Figure 6.4) shows a very small leakage current of the order of 10^{-11} A and an on-off ratio $\sim 10^5$. The threshold voltage by extrapolating the $I_D - V_{GS}$ curve in the linear region was ~ 6 V. Method of estimating the threshold voltage, mobility, on-off ratio etc are described in section 2.3.8.

TFTs were also prepared using targets having Zn:Sn ratio 4:1 and 8:1. The channel layer was grown at 0.5 Pa oxygen pressure and the devices were annealed at 300 °C. All devices in this series were operating in depletion mode. A field effect mobility of $0.32 \text{ cm}^2/Vs$ was obtained for the device fabricated from Zn: Sn ratio 8:1 target and annealed at 300 °C with a threshold voltage -4.5 V. Because of the large off currents, these devices had shown an on-off ratio less than 10^2 . TFTs fabricated from 4:1 target worked in depletion mode even without annealing.

6.3 Amorphous zinc tin oxide thin film transistors by co-sputtering

6.3.1 Experimental details

TFT structures, similar to those mentioned in previous section, were also fabricated from co-sputtered amorphous ZTO channel layer. Device structure was similar to that shown in figure 6.2. Here the ZTO channel layer is deposited via DC-RF co-sputtering technique. As described in chapter 4, high purity ZnO and SnO₂ powder was used as the sputtering targets in a sputter up configuration. The Si/SiO₂ substrate, patterned for channel

layer, was placed at 4 cm distance above the targets and was rotated at a speed of 50 rpm. TFT channel layer was deposited at a DC current of 200 mA (power 130 W, for SnO₂) and 100 W RF powers (for ZnO) so that the resulting film has Zn/Sn atomic ratio 0.51/0.49 in the channel layer. Chemical composition of the channel was determined by XRF spectroscopy using films prepared under similar conditions as that of channel layer. Co-sputtering was carried out for about one minute time so that a channel layer of about 45 nm thickness was formed. Argon pressure of 1 Pa was maintained in the chamber and there was no intentional heating of the substrate during the deposition.

As in previous case, as prepared TFTs did not show any transistor behaviour. The devices were, then, furnace annealed in air for 1 hour at 300 °C. About 100 devices were fabricated on a 10 × 10 mm Si substrate with channel width/length = 300/50 μm using standard lithographic and lift off technique. Ti/Au (7/40 nm) stack deposited by electron beam evaporation was used as source and drain electrodes while Si substrate itself was used as gate electrode.

From the analysis of films deposited under similar conditions, a-ZTO channel layer has the following properties (See chapter 4).

6.3.2 Transistor performance

The device exhibited typical n-channel transistor behaviour operating in enhancement mode. A sufficient positive gate voltage was required to enhance the conductivity in the channel layer. The flatness of output characteristics, shown in figure 6.5, for large drain source voltages (V_{DS}) indicates that the device exhibits ‘hard saturation’ (i.e. complete pinch-off of the channel).

Table 6.1: Properties of a-ZTO thin films used for TFT fabrication by Co-sputtering.

Property	Value
Zn:Sn ratio	0.51:49
Optical bandgap	3.43 eV
rms roughness	0.72 nm
Resistivity	21.14 $\Omega \text{ cm}^{-1}$
Mobility	1.31 cm^2/Vs
Carrier density	$2.25 \times 10^{17} \text{ cm}^{-3}$

Transfer characteristics of the device shown in figure 6.6 shows that, the device has a leakage current of the order of 10^{-11} A and an on-off ratio of 10^6 . The field effect mobility (μ_{fe}) of the device, extracted from the slope of linear portion of I_D - V_{GS} plot, was $\sim 0.0043 \text{ cm}^2/\text{Vs}$ (Figure 6.7). The threshold voltage V_T , estimated by extrapolating the straight line to the V_{GS} axis, was $\sim 4.8 \text{ V}$. The positive threshold voltage indicates the enhancement mode operation of the device.

6.4 Amorphous zinc indium tin oxide thin film transistors

Co-sputtering is an effective technique to control the chemical composition of a multicomponent film in a systematic and easy way. Especially, as our apparatus had both RF sputtering and DC sputtering systems, we can choose a process appropriate for the sputtering target. For the ZITO system, DC sputtering was employed for the conducting indium tin oxide

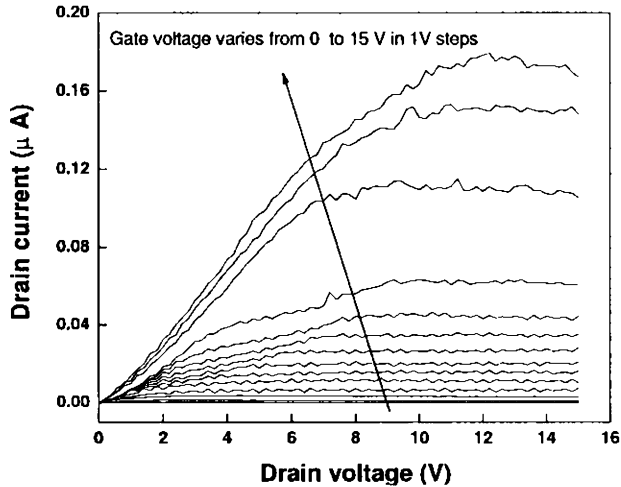


Figure 6.5: Output characteristics of thin film transistor with co-sputtered a-ZTO as active channel layer with Zn/Sn atomic ratio 0.51/0.49.

(ITO) target as it is a mass production compatible method widely used in the flat panel display (FPD) manufacturing and a faster growth method for a conducting target. RF sputtering was used for zinc oxide because of the ease of working with a high resistivity powder target without any troublesome sintering process. The characteristics of TFTs using amorphous transparent ZITO films were examined as a function of the chemical composition. Due to the high electron concentrations, TFTs fabricated using the as-deposited films for the channels did not show source-to-drain current modulation. Thermal annealing of the TFTs at 300 °C in air resulted in TFT operations for all the chemical compositions.

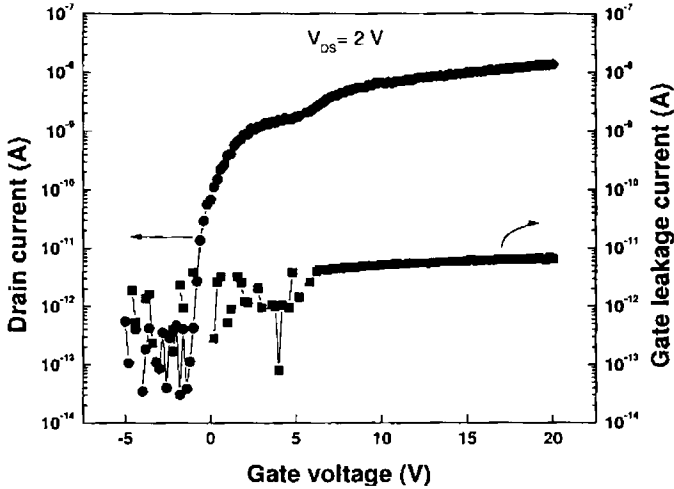


Figure 6.6: Transfer characteristics of co-sputtered a-ZTO TFT with Zn/Sn atomic ratio 0.51/0.49 in the channel layer.

6.4.1 Experimental details

The procedure adopted for a-ZITO TFT fabrication was same as described for ZTO TFTs (see section 6.2.1). Bottom gate, top contact TFTs were fabricated using the a-ZITO films with five different channel compositions on thermally-oxidized n-type Si wafers. The thickness of the thermal oxide was 100 nm and that of the channels were ~ 45 nm. About 100 devices were fabricated on a 10×10 mm² area with a channel width and length of 300 and 50 μ m, respectively, using lithography and lift off. Ti/Au (7 nm/40 nm) stacks deposited by electron beam evaporation were used as source and drain electrodes while the thermal oxide and the Si substrate themselves act as a gate insulator and a gate electrode, respectively (device structure was same as shown in figure 6.2 except for an a-ZITO channel).

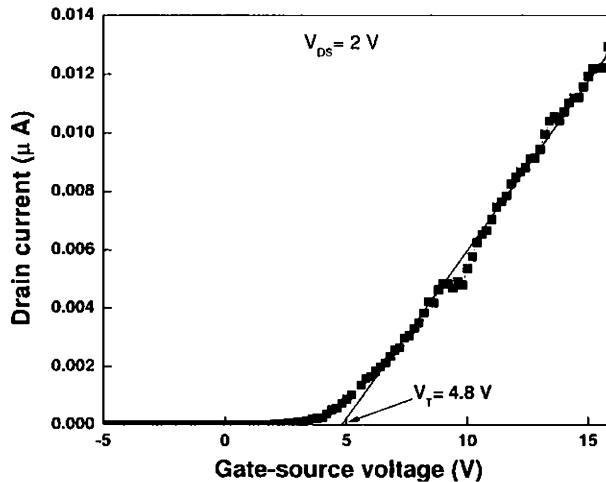


Figure 6.7: Plot of drain current against gate voltage for $V_{DS} = 2$ V for co-sputtered ZTO TFT with Zn/Sn atomic ratio 0.51/0.49 in the channel layer.

For channel layer deposition, co-sputtering was carried out in pure argon ambience at a pressure of 1 Pa. Effects of post-thermal annealing were also examined for the TFTs. Some TFT chips were annealed at 300 °C in air for 1 hour after finishing the TFT fabrication process (i.e. annealed after depositing the Ti/Au electrodes). In addition, some TFTs were fabricated using channels annealed at the same condition before the Ti/Au deposition (i.e. the Ti/Au electrodes were deposited after the thermal annealing of the channels). Electrical characterisations of the TFTs were performed using a Keithley 4200 semiconductor characterisation system.

6.4.2 Transistor performance

TFTs fabricated with ~ 45 nm thick as-deposited a-ZITO channels did not show any modulation in a source-to-drain current (I_D) by a gate bias (V_{GS}). This would be due to the large carrier concentrations in the channels. Figure 5.10 and table 5.1 in chapter 5 shows high carrier density (of the order of 10^{20} cm^{-3}) for as-prepared a-ZITO films. The carrier density in the channel material should not be very high for gate voltage to effectively modulate the channel conduction. Hence we cannot expect transistor action in such devices. In order to reduce the carrier density in the channel material, the TFTs (i.e. with the Ti/Au electrodes) were air annealed at 300°C for 1 hour. Measurements are taken on annealed devices and corresponding output characteristics and transfer curves are shown in figure 6.8.

The μ_{fe} , extracted from the slope of the linear region of the I_D - V_{GS} plot, was greater than $1 \text{ cm}^2/\text{Vs}$ for the TFT with the Zn:In:Sn atomic ratio 0.35:0.35:0.3. The threshold voltage V_T , estimated by extrapolating the straight line to the V_{GS} axis, was $\sim 9 \text{ V}$. The positive threshold voltage indicates the enhancement mode operation of the device. The value of μ_{fe} was much smaller for other two compositions. The device with channel composition Zn:In:Sn atomic ratio 0.5:0.27:0.23 operated in depletion mode. Figure 6.8 shows that these TFTs have an on-off current ratios of the order of $10^4 - 10^5$. The output characteristics (Figure 6.8) also exhibits hard saturation at large V_{DS} , which is similar to pinch off in usual field-effect transistors. However, the I_D first steeply increased in the small V_{DS} region up to $\sim 0.5 \text{ V}$ and then the slopes become much gentler and finally showed the saturation. This behaviour is not usual in the TFT theory.

As the field effect mobility ($1 \text{ cm}^2/\text{Vs}$) is almost one order of magnitude

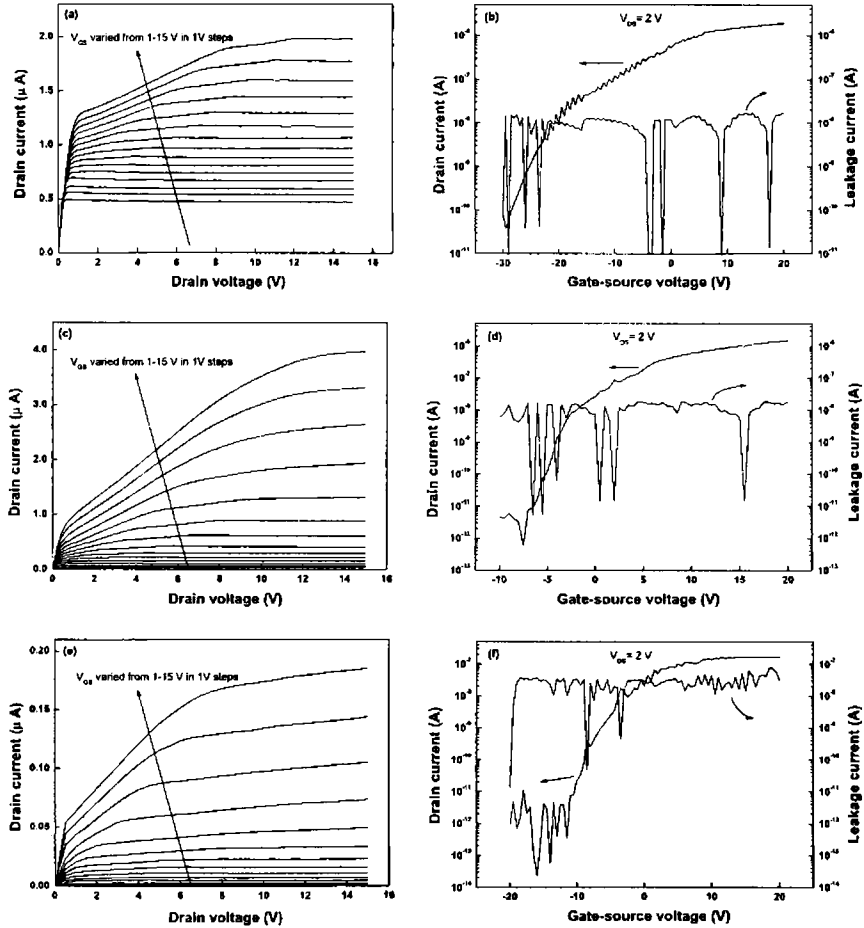


Figure 6.8: Output and transfer characteristics of a-ZITO TFTs with different chemical compositions in the channel layer (Annealed devices). (a), (c) and (e) show the output characteristics of a-ZITO channel TFTs with Zn : In : Sn atomic ratios 0.5 : 0.27 : 0.23, 0.48 : 0.3 : 0.22 and 0.35 : 0.35 : 0.30 respectively, and (b), (d) and (f) show corresponding transfer characteristics at $V_{DS} = 2\text{ V}$.

smaller than the Hall mobility ($9 \text{ cm}^2/\text{Vs}$) and the subthreshold voltage swing is large $\sim 4 \text{ V/decade}$, it is speculated that the channel - insulator interface has somewhat large density of subgap states, which would form inhomogeneous field distribution in the channel and cause the unusual output characteristics. This is analogous to the situation considering discrete trap modeling of TFTs [215]. As per this model, the acceptor-like traps anywhere in the device (particularly in the insulator-semiconductor interface formed by unsatisfied bonds and lattice mismatch) causes kinks in the drain current characteristics. Simulation studies predict the increase in inverse subthreshold voltage swing and degradation in channel mobility with the increase of trap density. In the present case, air annealing might have definitely reduced the carrier density in the channel by compensating the oxygen vacancies. This leads to some field effect behaviour in the devices as the channel can now be controlled by the gate bias. At the same time, the annealing after depositing the source/drain terminals might have caused diffusion and/or oxidation of the Ti electrodes which might have significantly contributed trap states in the semiconducting channel material.

Due to the speculation that these non-ideal behaviors were caused by diffusion and/or oxidation of the Ti electrodes, the a-ZITO channel/thermal oxide/Si samples were annealed before depositing Ti/Au electrodes, and then formed the source and drain contacts to finish the TFT structures. As observed in Table 5.1 in chapter 5, the channel annealing must have reduced the carrier density in the channel by two orders. Most of the TFTs operated with field effect mobilities varying from 3.4 to $12.4 \text{ cm}^2/\text{Vs}$ as the Zn content decreased from 48 at% to 5 at% in the channel layer. Figure 6.9 summarises the output and transfer characteristics of the TFTs. The I_D were very low $< 0.1 \text{ nA}$ in the off regions and increased up to few

mA by increasing V_{GS} , indicating that the TFTs operated as a n-channel transistor. Transfer characteristics of the TFTs in figure 6.9 show on-off ratios of $10^7 - 10^8$.

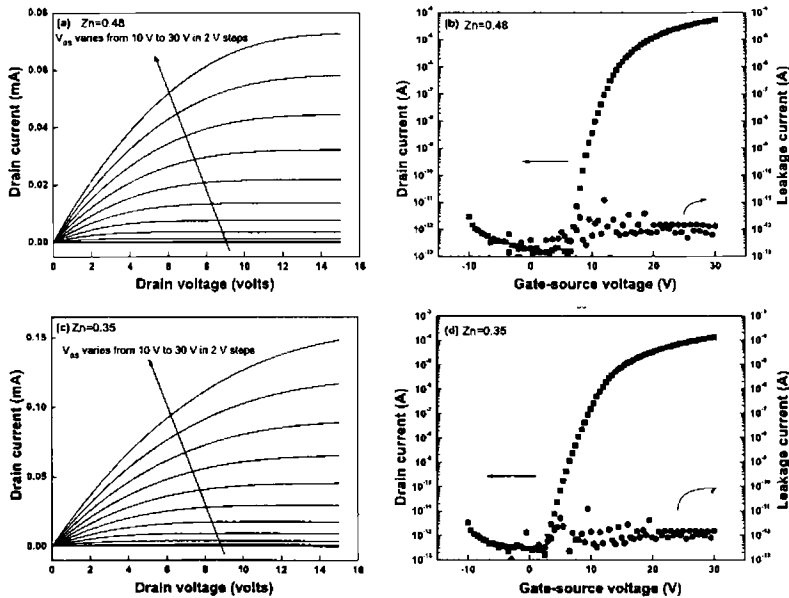
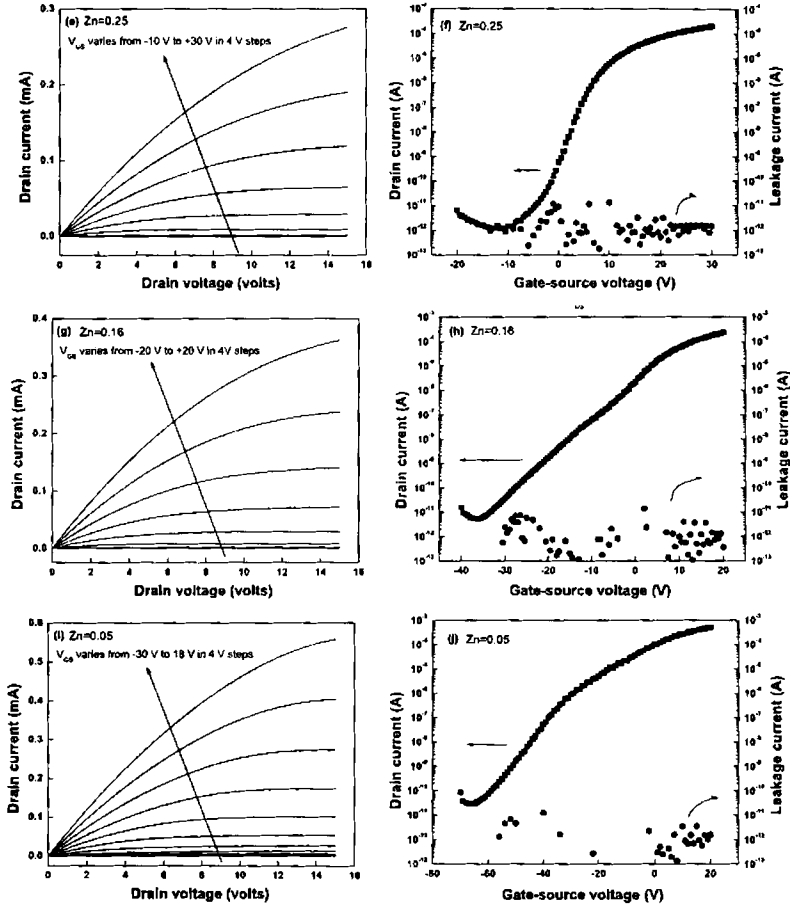


Figure 6.9: Output and transfer characteristics of a-ZITO TFTs with different chemical compositions in the channel layer. Here the channel layer was annealed before the completion of the device with source and drain electrodes. (a, c) show the output characteristics of a-ZITO channel TFTs with Zn : In : Sn atomic ratios 0.48 : 0.29 : 0.23 and 0.35 : 0.35 : 0.30 respectively, and (b, d) show corresponding transfer characteristics at $V_{DS} = 10 \text{ V}$ (figure continues in the next page).



(Figures continued from the previous page) Output and transfer characteristics of a-ZITO TFTs with different chemical compositions in the channel layer. (e, g, i) show the output characteristics of a-ZITO channel TFTs with Zn : In : Sn atomic ratios 0.25 : 0.44 : 0.31, 0.16 : 0.48 : 0.36, and 0.05 : 0.56 : 0.39, respectively, and (f, h, j) show corresponding transfer characteristics at $V_{DS} = 10$ V.

Since TFTs in figure 6.9 show ideal MOSFET behaviour, we can analyse the device performance using the standard MOSFET theory.

In the non-saturation region of the transistor operation, for a small constant value of V_{DS} , a plot of I_D as a function of V_{GS} would yield a straight line, the slope of which is proportional to μ_{fe} . By contrast, drain current in the saturation region (i.e. at V_{DS} greater than pinch-off voltage) is proportional to the square of V_{GS} which provides the saturation mobility and the threshold voltage V_T from a plot of $I_D^{0.5}$ as a function of V_{GS} (details of analysis are given in section 2.3.8 in chapter 2). Figure 6.10 shows a plot of $I_D^{0.5}$ versus V_{GS} for different channel composition. The μ_{sat} was obtained from the slopes of the straight lines drawn to each plot and the V_T from its intersection values at x-axis.

For the TFT with the highest Zn content of 48 at% (Figures 6.9(a,b)), the μ_{fe} , extracted from the slope of the linear region of the I_D - V_{GS} plot, was $3.4 \text{ cm}^2/Vs$. Threshold voltage obtained by extrapolating a $I_D^{0.5}$ - V_{GS} plot at $V_{DS}=10 \text{ V}$ to the V_{GS} axis was 12.1 V . The positive threshold voltage indicates the enhancement mode operation of the device. Figure 6.9(a) exhibits hard saturation at large V_{DS} , which is similar to pinch off in usual field-effect transistors. The TFTs using the other composition channels (Figures 6.9 (c-j)) showed similar output characteristics. The TFT with the smallest channel Zn content of 5 at% showed significant current flow even at zero gate voltage. The soft saturation of drain current in the output characteristic indicates that the channel is not fully depleted even if a large V_{DS} of 15 V was applied for $V_{GS} \leq 20 \text{ V}$.

Systematic variations were observed in the field effect mobilities and the V_T , where the V_T increases with increasing the Zn content in the channel layer. Variations in field effect mobility, saturation mobility, threshold

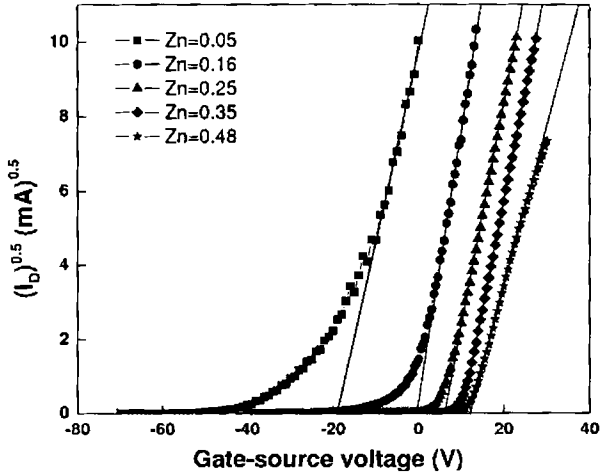


Figure 6.10: $(I_D)^{0.5}$ versus V_{GS} plot for a-ZITO channel TFTs with different Zn:In:Sn atomic ratios at $V_{DS} = 10$ V. The channel Zn contents are shown in the figure. The slopes in the linear regions were used for extracting the saturation mobilities. Extrapolation of the linear region to the abscissa gives the threshold voltage.

voltage, subthreshold voltage swing (S) and current on-off ratio with RF power (Zn content) has been summarised in table 6.2. The TFT with the Zn content of 48 at% operated in an enhanced mode with a V_T of 12.1 V, and that with 5 at% operated in a depletion mode with a large negative V_T of -19 V. Subthreshold swing increased with decreasing the Zn content, indicating that the subgap trap densities increased with decreasing Zn content.

Table 6.2: Variations in TFT parameters with Zn content $[Zn/(Zn+In+Sn)]$ in the channel

RF power (W)	Zn content (at%)	TFT parameters				
		μ_{fe} (cm^2/Vs)	μ_{sat} (cm^2/Vs)	V_T (V)	S (V/dec)	on-off ratio
150	48	3.40	1.82	12.1	0.35	10^8
100	35	6.01	3.32	10.3	0.52	10^8
75	25	7.30	3.50	6.20	0.86	10^7
50	16	10.5	5.00	-0.6	2.65	10^7
25	5	12.4	2.90	-19	3.05	10^7

6.4.3 Role of zinc in a-ZITO TFTs

Since we do not have enough experimental evidence, these are highly speculative, but it would be informative to try to understand the carrier transport properties obtained in chapter 5 to understand the role of Zn ions in the a-ZITO films. It was observed that the threshold voltage largely decreased and the S value increased with decreasing Zn content. This trend is not specific to the a-ZITO system but also observed in the a-In-Ga-Zn-O system [120]. The larger S value indicates a larger density of subgap states (D_{it}) because the S value is related to D_{it} by the equation,

$$S = \frac{2.3k_B T}{e} \left(1 + \frac{eD_{it}}{C_i} \right) \quad (6.1)$$

where k_B is Boltzmann's constant and C_i is the gate insulator capacitance [152]. Therefore, these experimental results suggest that the Zn poor films have larger D_{it} and more donor states. This idea appears to contradict with the variation of the carrier density because Table 5.1 in chapter 5

shows the free carrier density measured by the Hall measurements tends to decrease with decreasing Zn content. However, as it is also observed that the room-temperature Hall mobility largely decreases with decreasing Zn content, it is suggested that the Zn poor films have larger amounts of trap states, which decreases the free carrier concentration. This speculation is consistent with the TFT mobilities because larger D_{it} decreases free carrier concentrations and channel conductance in the saturation regime of the TFTs, and consequently the apparent μ_{sat} value is lower than drift mobility. The μ_{fe} value are larger for the Zn poor films, probably because the μ_{fe} value is estimated above the subthreshold region from a differential of the I_D with respect to V_{GS} and less affected by D_{it} . Therefore, the μ_{fe} value more reflects drift mobility and carrier scattering in the channel. That means, the Zn poor (i.e., In-rich) a-ZITO films have larger D_{it} , but extended drift mobilities would be larger, which is supported by Hall measurement on the a-In-Zn-O system in reference [179]. The larger D_{it} in the Zn poor films would be related to the local structure of multicomponent amorphous oxides. It is known that the structure of crystalline In_2O_3 is composed of an edge-sharing network of (InO_6) octahedra. This structure is remained partly in amorphous InGaZnO_4 [216], and In-Zn-O [217], and the portion of the edge-sharing structures decreases with decreasing the In content and the edge-sharing structures are converted to corner-sharing ones. As reported in amorphous Zn-Rh-O system [218], an edge-sharing structure has a much stronger geometrical constraint to form an amorphous structure, and the increase in corner-sharing structures would form a more stable amorphous structure. Therefore the increase in the Zn content in a-ZITO films and probably also in other AOSs may cause an increase in corner-sharing structures, forms a more stable amorphous structure, and reduces

Di. That is to say, Zn ions work as an effective stabilizer of an amorphous structure in In_2O_3 -based AOSs [59].

6.5 Amorphous zinc indium tin oxide transparent thin film transistors

6.5.1 Introduction

There is an emerging interest in the field of transparent electronics, wherein electrical devices comprises of optically transparent materials [140]. Among these, transparent thin film transistors (TTFTs) are getting more attention since it is a key device in realising transparent circuits. TTFTs have potential applications in invisible sensors, interactive media, transparent active matrix liquid crystal displays, organic light emitting diode displays etc [126, 219–222]. Room temperature depositions of TAOSs allow the fabrication of transparent electronic circuits on flexible substrates like polyethylene naphthalate (PEN), polyethylene terephthalate (PET) etc. Such flexible see-through structures may find wide use in military, biosensing and consumer goods [126, 140, 219, 220].

Even though several transparent amorphous semiconductor materials like indium gallium zinc oxide [119–121, 123–126], zinc tin oxide [110], gallium nitride [193], zinc indium oxide [194], zinc oxide [98], and zinc tin oxide [118] have been employed in recent years as thin film transistor (TFT) channel layers, most of these reports were based on the fabrication of TFT on silicon substrates with metallic source and drain electrodes which limits its application in transparent electronic circuits. In addition to this, in most of those cases, the devices were subjected to high temperature

treatment to obtain the transistor action. This section describe the room temperature fabrication of fully transparent transistors on glass substrates where the channel layers were deposited by co-sputtering method. Most of the TAOSs are multicomponent materials and have large flexibility to tune their chemical compositions for TFT applications. It is not easy to vary the film chemical composition by a conventional pulsed laser deposition or sputtering technique since we have to prepare a ceramic target for each different chemical composition. Co-sputtering from different targets allow fine control of the chemical composition of the deposited films by simply adjusting the power of individual targets (see chapter 5). Hence we can tune the optical and electrical properties of the multicomponent TAOSs according to the requirements of the application. Only a few reports have been published in the development of TFTs using this combinatorial approach [120, 125].

6.5.2 Experimental details

Co-sputtering method was employed for depositing the channel layer. As we have seen in the earlier sections, this is an effective technique for a multicomponent channel layer deposition and to control the film chemical composition in a systematic and easy way. Zinc indium tin oxide (ZITO) films were deposited via a DC-RF co-sputtering technique to control the film chemical composition (Figure 6.11 a). High purity ZnO powder was used as the RF target and sintered target of 10 wt% tin doped indium oxide ($\text{In}_2\text{O}_3\text{:Sn}$, ITO) was used as the DC target in a sputter up configuration. Compared to the deposition condition employed in section 6.4, here a highly conducting ITO target with very small tin content was used as one of the target. Such a selection was based on the observation that zinc indium

oxide TFTs [62, 113] exhibit higher mobility than zinc tin oxide TFTs [110]. Present investigation also showed such trend. Optical and electrical analysis of zinc tin oxide thin films have shown profound effect of subgap states and hence very poor TFT performance. Whereas, we got high performing TFTs with zinc indium tin oxide channel layer with less tin content than the indium and zinc concentration. Additionally, a high temperature annealing or high substrate temperature was essential in achieving TFT action in zinc tin oxide TFTs. All these reports points towards some negative effects of tin content in the film, eventhough the exact nature of this is not known. So we tried TFT fabrication with very small tin content in the channel.

RF power was kept at 25 W while the DC power was maintained at 60 W. The substrate was kept at 16 cm from the targets as shown in figure 6.11 a. This was the approximate distance at which the plasma from two targets were focussed. In this case, the substrate was rotated in the focal plane of plasmas. In chapter 5, the setup was in such a way that the plasma evolved from the target were exactly vertical in the upward direction and substrate was rotated in between two plasma regions. So the deposition was sequential. Here, as the substrate is exactly at the focal plane, simultaneous deposition from two targets were possible. In addition, adatoms reaching at such larger distances might not have enough energy to migrate over the substrates to occupy an energetically suitable position. Hence the films are expected to be amorphous. Argon pressure of 1 Pa was maintained in the chamber and there was no intentional heating of the substrate during the deposition. Aluminium metallic masks were used during the deposition to realise channel and source/drain parts of the TTFT.

The chemical composition of the channel was measured by energy dispersive xray spectroscopic (EDAX) analysis of films deposited under simi-

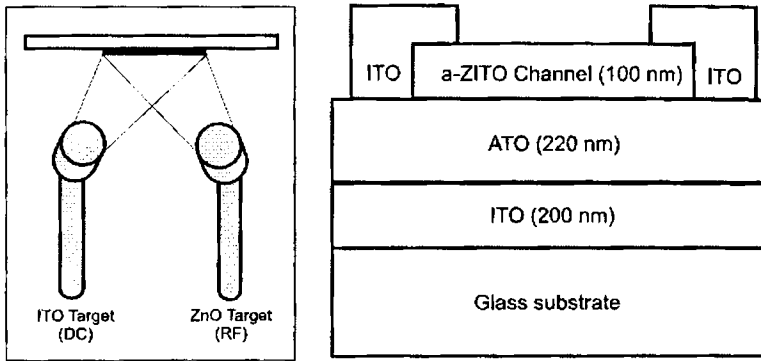


Figure 6.11: Schematics setup of co-sputtering method (a) and device structure (b) used in the study.

lar conditions. The film structures were characterised by x-ray diffraction (XRD) analysis using Rigaku powder x-ray diffractometer with $\text{Cu K}\alpha$ radiation. Thickness of various layers was measured using Dektak 6M stylus profiler. Optical reflectance and transmission spectra were measured using a near infrared to ultraviolet double-beam spectrophotometer (Jasco V570). Electrical measurements of the devices were done using two Keithley source measure units.

TTFT structure used in this study is shown in figure 6.11 b. A glass substrate coated with 200 nm thick layer of sputtered ITO and a 220 nm thick layer of aluminium-titanium oxide (ATO), provided by Planar Systems Inc., was used for TTFT fabrication. ITO is a highly transparent n-type conductor (sheet resistance $20 \Omega/\text{sq}$) which acts as the TTFT gate. ATO is an engineered insulator consisting of a superlattice of alternating layers of Al_2O_3 and TiO_2 , which serves as gate insulator. A 100 nm thick amorphous ZITO channel layer was deposited by co-sputtering method.

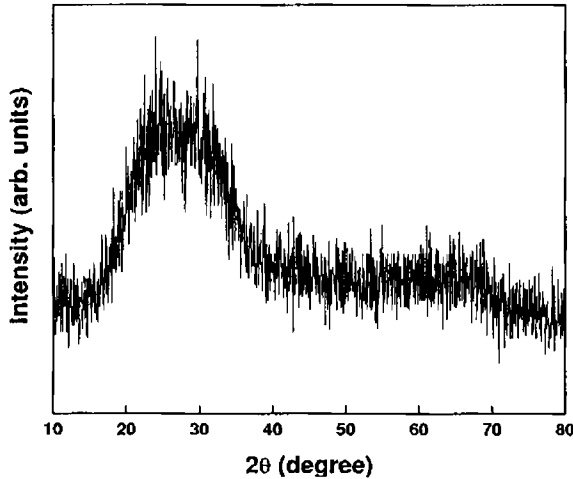


Figure 6.12: X-ray diffraction pattern of a 200 nm thick ZITO thin film prepared under similar condition as that used for channel layer deposition in a-ZITO TTFT fabrication.

For source and drain contacts, RF sputtered ITO layer was deposited over channel layer using a shadow mask. The channel width and length were 1200 and 1000 μm , respectively.

6.5.3 Channel properties

XRD profiles of as deposited films shown in figure 6.12 have only a halo peak. The absence of sharp peak indicates the amorphous nature of the channel layer. EDAX analysis of the same film shows that the channel layer has a chemical composition of Zn:In:Sn ratios 0.37:0.57:0.06. Figure 6.13 shows the optical transmission spectra through a 200 nm thick ZITO thin film and also through complete device. The average optical transmission of

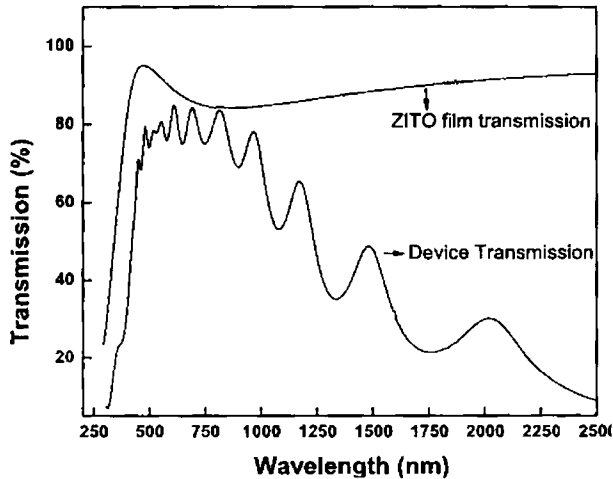


Figure 6.13: Optical transmission spectra of a-ZITO thin film and thin film transistor using amorphous ZITO channel layer.

the device in the visible region was $> 70\%$ (Figure 6.13). This is an admissible condition for clear vision in automobiles. The loss of transmission at higher wavelength is due to the reflection and absorption by free carriers in the ITO layers.

6.5.4 Transistor performance

As prepared devices showed good transistor action without any kind of thermal treatment. The drain current - drain voltage (I_D - V_{DS}) characteristics of the transistor, given in figure 6.14, shows typical enhancement mode operation of an n-channel transistor. A positive gate voltage was required to induce the channel conduction, and the channel conductivity

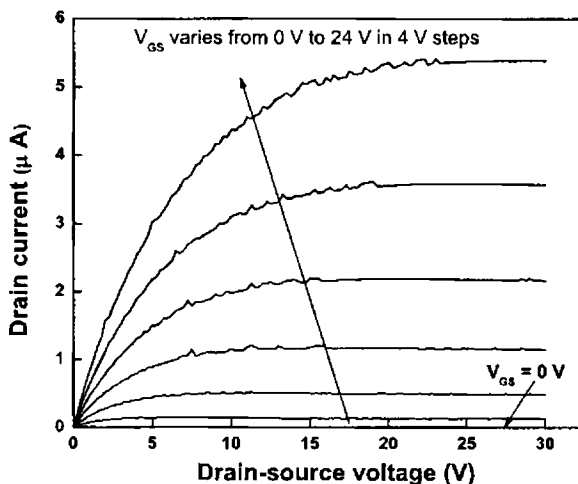


Figure 6.14: Output characteristics of transparent thin film transistor using amorphous ZITO channel layer. Device shows typical n-channel transistor behaviour.

increased with increase of positive gate voltage. The device exhibited 'hard saturation' as evident from the flatness of I_D curves at large V_{DS} . This indicates that the entire channel thickness have been depleted of carriers. Figure 6.15 shows the transfer characteristics ($\log(I_D) - V_{GS}$) of the fabricated transistors which give an on-off ratio of 10^5 (right hand side y-axis is the same drain current plot on a linear scale, the slope of which is used for field effect mobility calculation). The field effect mobility extracted from the linear region slope of I_D - V_{GS} plot was $5.7 \text{ cm}^2/\text{Vs}$. The threshold voltage V_T , estimated by extrapolating the straight line to the V_{GS} axis, was 6 V . The positive threshold voltage indicates the enhancement mode operation of the device. A maximum subthreshold voltage swing of 0.3

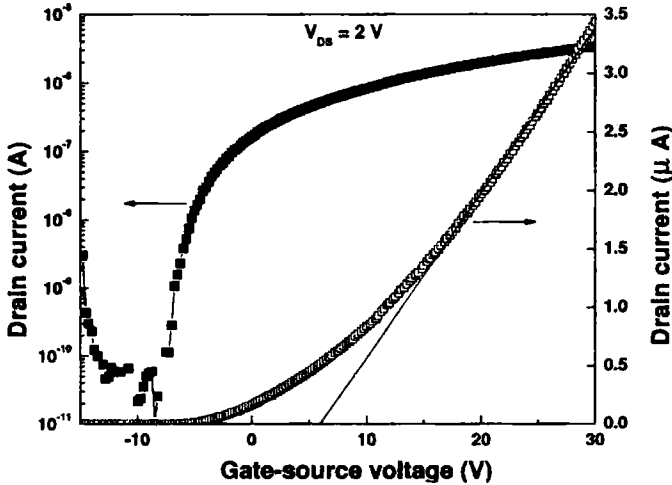


Figure 6.15: Transfer characteristics of transparent thin film transistor using amorphous ZITO channel layer. The field effect mobility was estimated from the slope of linear part of drain current- V_{GS} curve (right side).

V/dec , and on-off ratio 10^5 were obtained from the transfer curve of the devices. Figure 6.16 shows a picture of a-ZITO TTFTs fabricated on glass substrate. The background colour is easily visible through the complete device structure. This shows that the devices are completely transparent to visible light and invisible to an observer.

6.6 Conclusion

Eventhough amorphous channel ZTO TFTs fabricated on silicon substrates showed typical transistor behaviour, its performance was very poor due to the presence of high density of subgap states. This caused very low mobility



Figure 6.16: Photograph of all oxide transparent thin film transistors on glass substrates. This 1"×1" glass substrates have six transistors in two row.

values and moderately high leakage currents. Amorphous ZITO TFTs with different chemical compositions were deposited on silicon substrates by co-sputtering from ZnO and $\text{In}_2\text{Sn}_2\text{O}_7$ targets. Effects of post annealing on ZITO TFT characteristics were analysed. The as-deposited films had high electron densities $\sim 10^{20} \text{ cm}^{-3}$ and did not produce operating TFTs. The thermal annealing at 300 °C reduced the electron densities and produced operating TFTs. The TFT characteristics showed systematic variation with the chemical composition of the channels. The TFT having the largest Zn content 48 at% showed a field effect mobility of $\sim 3.4 \text{ cm}^2/\text{Vs}$, a current on off ratio of $\sim 10^8$, and a positive threshold voltage of $\sim 12.1 \text{ V}$. The TFT having lowest Zn content 5 at% showed a negative threshold voltage -19 V

and a depletion mode operation. Co-sputtering has been demonstrated as an effective technique for multicomponent oxide channel layer deposition.

Enhancement mode operation of an all oxide transparent thin film transistors with amorphous ZITO as active channel layer has also been demonstrated. Channel layer was deposited by a DC-RF co-sputtering method from ITO and ZnO targets. Resulting film was amorphous with Zn:In:Sn atomic ratio 0.37:0.57:0.06. Fabricated transistors showed $> 70\%$ transmission in the visible region. Room temperature fabricated transistor showed typical n-channel enhancement mode operation with a threshold voltage of 6 V and field effect mobility of $5.7\text{ cm}^2/\text{Vs}$ and on-off ratio of 10^5 without any kind of thermal treatment. Since device performance was obtained without any kind of thermal process, electronic devices can be realised on plastic substrates, provided with a low temperature insulator deposition. Hence co-sputtering can be used as an effective technique for developing multicomponent amorphous material based transparent electronic circuits on flexible substrates.

Although the present study demonstrated that ZITO channel TFTs operate even if the channels were deposited from powder ZnO target, the use of the powder target may limit the quality of the channels and the TFT characteristics would be improved by using a higher-quality target and further optimising deposition condition and channel chemical composition.

Chapter 7

Summary and Scope for further study

7.1 Summary of present study

Transistor was one of the greatest invention of the twentieth century. Transistors found enormous applications in almost every items that dealt with human being. Invention of integrated chips (ICs) enabled this technology to fabricated billions of transistors in a single silicon chip. This made the electronic equipments cheaper and more efficient. ICs contain billions of metal oxide semiconductor field effect transistors (MOSFETs) made on single crystalline silicon. However, the prize reduction in ICs is inseparable from the ever reducing size of the MOSFETs. There are situations where the device dimensions becomes larger as in the case of active matrix liquid crystal displays (AMLCD). In such cases, the use of conventional transistors made from single crystalline silicon to control individual pixel elements are not economic. Hence, thin film transistor (TFT) technology

were developed to handle this situation.

Today, AMLCD technology is widely used in display applications and all commercially available products uses a-Si:H TFTs to control the pixels. However, extremely low mobility of electrons, inherent from its amorphous structure, limits its application. Due to this, complicated circuits have to be used to use it in high current applications like in the case of active matrix organic light emitting diodes (AMOLED). In addition to this, due to very low bandgap value, silicon based devices are opaque to visible light. Light absorption by silicon channel causes shift in operating parameters of the TFT. This necessitate the use of metal masks to protect the channel from light absorption. Opacity of TFT further causes power loss in the applications. Most of the display panels use a background light source to illuminate the display volume. This light is effectively modulated by the liquid crystals (LC) to perceive the image visionary. Use of opaque TFTs limits the amount of light reaching the observers eyes. Because of these problems, scientists were looking for alternative materials for TFT fabrication. Modern TFT concept is based on the properties transparent electronic materials.

Transparent electronics is the latest technology in the field of display and other applications. Transparent semiconducting oxide were integral components in flat panel displays, solar cells, and smart windows. However, all these applications utilises the metallic behaviour of these transparent materials as a passive component in the circuitry. The development of p-type transparent conductors led to the applications where the transparent conductors function as active components in the circuitry. This directs to the development of transparent diodes, photodetectors, transparent transistors etc and blossomed the 'transparent electronics' or 'invisible

electronics'. The backbone in this technology is the transparent thin film transistors. These are the transistors fabricated on a transparent substrate like glass or plastic with wide band gap oxide semiconductors. Different layers like source, drain, channel, gate electrode, gate insulator, all are fabricated from transparent materials. This makes the circuits invisible from an observer. Transparent electronic circuits can be embedded into large areas like windows, walls, desktops and other locations. While a pane of glass might look like an ordinary window, it could actually incorporate a new type of electronics with a range of functions. With the advent of this technology, displaying video imagery when required on windows, automobile windshields, or eyeglass lenses all these are soon becoming a reality. Transparent transistors will also make an impact in liquid crystal display (LCD) panels, organic light-emitting diode (OLED) panels and other displays. They can provide larger screens with finer definition, high aperture ratio and less power consumption with simpler manufacturing technology.

The aim of this work was the development of thin film transistors based on wide bandgap amorphous semiconductor channel. Use of an amorphous channel ensures uniformity in transistor performance parameters and avoid the necessity of substrate heating during deposition. This helps to realise the device on temperature sensitive substrates like plastics and glass. As in the case of any technology, deposition parameters had to be optimised before starting the device fabrication. Work presented in this thesis utilised pulsed laser deposition (PLD) and co-sputtering techniques for depositing the channel layer. PLD is employed in this study as it is relatively a new technique in thin film deposition and it allows deposition at high oxygen pressures compared to sputtering. Use of high oxygen pressure enables to control the carrier density by controlling the oxygen vacancies in the film.

Proper transistor action will be obtained only if the channel carrier density is properly controlled. However, sputtering is a well known and widely used technique in thin film deposition technology.

The choice of co-sputtering arose from the multicomponent nature of the amorphous film used here. Most of the amorphous oxide semiconductors are multicomponent and as such there are possibilities for wide compositional variations. The device performance should obviously be a function of the channel chemical composition. In order to optimise the device performance, studies have to be done over large compositional variations. For this, separate targets must be prepared for each of the composition if we adopt conventional techniques like PLD and sputtering. In co-sputtering, two or more targets can be sputtered simultaneously and power to each targets can be separately controlled. In the present work, two targets were sputtered simultaneously and power was individually controlled by two separate power sources. This helped to control the chemical composition of the deposited film over a wide range. Both silicon and glass were used as substrate for TFT fabrication. SiO₂ films made by thermal oxidation of single crystal Si wafers have the smoothest surface among the commercially available materials [214]. High breakdown voltage strength and low leakage current of SiO₂ enabled to observe the transistor characteristics up to several tens of V_{GS} . Hence, the use of opaque silicon substrate can be justified in the sense that they allow us to look into the channel property without bothering about the leakage or interface roughness. More than that, study of TFTs using wide bandgap materials on silicon substrate is worthy in the sense of integration of new functions to the existing silicon technology. Even if the substrate is opaque, oxide TFTs on silicon shows much better performance (high on-off ratio, high mobility, blindness to visible light

etc) than a-Si:H TFTs. Use of glass substrate led to the development of complete transparent TFTs.

Amorphous zinc tin oxide (a-ZTO) and amorphous zinc indium tin oxide (a-ZITO) were used in the present study. In an economic point of view, indium free devices are more suitable than indium containing devices. Hence the study of a-ZTO devices are meaningful. However, films deposited, both by PLD and co-sputtering were found to had large amount of subgap states. This subgap states acted as electron traps and caused poor transistor performance despite of its smooth surface, moderate conductivity and carrier density.

Co-sputtered a-ZITO films have given smooth films with high electron density and moderate Hall mobility. Eventhough the reactive co-sputtering in oxygen ambience helped to control the electron density in the films, this adversely affected the carrier mobility and surface smoothness of the film. Hence TFTs were fabricated by depositing the channel in oxygen free atmosphere and subsequent transistor action was achieved by annealing the channel in air for one hour. Eventhough the air annealing after completing the device fabrication resulted transistor action, it had shown some unusual transistor behaviour due to the diffusion of source/drain metals into the semiconductor and thereby creating traps in the channel. TFT performance has analysed as a function of channel chemical composition. The TFT having the largest Zn content showed better performance. The TFT having lowest Zn content showed a negative threshold voltage and depletion mode operation.

Present study shows that co-sputtering can be used as an effective technique for multicomponent oxide semiconductor thin film deposition and also for channel layer deposition in TFT fabrication.

7.2 Scope for further study

Although the present study demonstrated that amorphous oxide channel TFTs operate even if the channels were deposited from powder targets, the use of the powder target may limit the quality of the channels and the TFT characteristics would be improved by using a higher-quality target and further optimising deposition condition and channel chemical composition.

Instead of using two sputtering guns, if zinc, indium and tin metallic targets are reactively sputtered from three individual targets, the chemical composition can be further optimised for better device performance.

Eventhough channel layers were deposited at RT, the attempts to fabricate TFTs on plastic substrates were not quite successful. High leakage current, due to immature dielectric deposition, was the main problem in achieving high performance TFTs on plastics. High κ dielectrics Y_2O_3 and Ta_2O_5 were deposited by RF magnetron sputtering and electron beam evaporation. This was not successful as the films seemed much porous in nature. Hence the proper optimisation of insulator deposition conditions are essential to deposit insulators on plastic substrates. This itself requires further detailed study.

Several issues like the stability in device performance in extreme conditions, effect of bias stress and light induced changes on threshold voltage and mobility etc have to be studied in detail.

Appendix A

Symbols used in the thesis

Table A.1: Symbols used in the thesis

Symbol	Description
a	Primitive cell size
α	Absorption coefficient, inverse localisation length
B	Conduction band width, Magnetic flux density
C_i	Insulator Capacitance
d	Sample thickness
D_{it}	Density of tail states
χ_S	Electron affinity of the semiconductor
e	Elementary electronic charge
E	Energy, Electric field
E_0	Optical gap (Tauc gap)
E_A	Valence band tail edge
E_B	Conduction band tail edge
E_C	Conduction band mobility edge
E_d	Defect state energy
E_F	Fermi energy
E_t	Threshold energy
E_V	Valence band mobility edge
E_U	Urbach energy

Table A.1:continued

Symbol	Description
ϵ_0	Permittivity of free space
g_d	Drain conductance
g_m	Drain transconductance
h	Plank's constant
H	Hamiltonian
I	Current
I_D	Drain current
\vec{k}	Wave vector
k	Magnitude of wave vector
Δk	Uncertainty in wave vector magnitude
k_B	Boltzmann's constant
k_{BZ}	Maximum crystal momentum in first Brillouin zone
k_1	Extinction coefficient
l	Mean free path length
L	Channel length, Grain size
λ	Screening length
m	Rest mass of electron
m_e^*	Electron effective mass
M	Mass of nucleus
μ	Conduction electron mobility, Chemical potential
μ_{eff}	Effective mobility
μ_{fe}	Field effect mobility
μ_H	Hall mobility
μ_n	Electron mobility (conductivity measurements)
μ_p	Hole mobility (conductivity measurements)
μ_{sat}	Saturation mobility
n	Electron density, Principal quantum number, Refractive index
$N(E)$	Electronic density of states
N_F	Electron density at Fermi level
$N_v(\nu)$	Vibrational density of states
ν	Photon frequency
ν_{ph}	Phonon frequency

Table A.1:continued

Symbol	Description
r	Scattering factor
R	Reflectance, Magnitude of position vector
R_H	Hall coefficient
p	Hole density
P	Momentum operator, Probability function
P_{O_2}	Oxygen partial pressure
q	Electronic charge
ϕ_M	Metal work function
ϕ_S	Semiconductor work function
ψ_{Sb}	Band bending at back interface
ψ_{Sf}	Band bending at front interface
S	Subthreshold voltage swing, Sputtering yield
σ	DC electrical conductivity
t	Thin film thickness
T	Absolute temperature, Transmittance
τ	Relaxation time, Collision time
U	Electron correlation energy
U_s	Surface binding energy of atoms
v	Velocity
V	Sample volume
V_1	Matrix element involving intra-atomic interactions in Weaire and Thorpe model
V_2	Matrix element involving interatomic interactions in Weaire and Thorpe model
V_a	Applied voltage
V_{DS}	Drain-Source voltage
V_{GS}	Gate-Source voltage
V_H	Hall voltage
V_P	Pinch-off voltage
V_{sat}	Saturation drain voltage
V_T	Threshold voltage
W	Channel width

Appendix B

Abbreviations used in the thesis

Table B.1: Abbreviations used in the thesis

Abbreviation	Expansion
3D	Three Dimension
a-Si:H	Hydrogenated Amorphous Silicon
AFM	Atomic Force Microscope
AM	Active Matrix
AMLCD	Active Matrix Liquid Crystal Display
AOS	Amorphous oxide semiconductor
ATO	Aluminium Titanium Oxide
BCC	Body centered Cubic
BM	Balanced Magnetron
CBM	Conduction Band Minimum
C-V	Capacitance-Voltage
CVD	Chemical Vapour Deposition
CRT	Cathode Ray Tube
DC	Direct Current
DOS	Density of States

Table B.1:continued

Abbreviation	Expansion
EDAX	Energy Dispersive X-ray spectroscopy
EXAFS	Extended X-ray Absorption Fine Structure
FCC	Face Centered Cubic
GXRD	Glancing Angle X-ray Diffraction
HMC	Heavy Metal Cation
IC	Integrated Circuit
IGZO	Indium Gallium Zinc Oxide
IPE	Inverse Photoelectron
ITO	Indium Tin Oxide
JFET	Junction Filed Effect Transistor
LCD	Liquid Crystal Display
LVDT	Linear Variable Differential Transformer
MOSFET	Metal Oxide Semiconductor Filed Effect Transistor
OLED	Organic Light Emitting Diode
OTFT	Organic Thin Film Transistor
PE	Photoelectron
PECVD	Plasma Enhanced Chemical Vapour Deposition
PEN	Poly Ethylene Naphthalate
PET	Poly Ethylene Terephthalate
PLD	Pulsed Laser Deposition
PVD	Physical Vapour Deposition
RF	Radio Frequency
rpm	Rotations Per Minute
RT	Room Temperature
RTA	Rapid Thermal Annealing
SCL	Space Charge Limited
SPM	Scanning Probe Microscope
TAOS	Transparent Amorphous Oxide Semiconductor
TFT	Thin Film Transistor
TSO	Transparent Semiconducting Oxide
TTFT	Transparent Thin Film Transistor
UBM	Unbalanced Magnetron
UV	Ultraviolet

Table B.1:continued

Abbreviation	Expansion
VBM	Valence Band Maximum
XPS	X-ray Photoelectron Spectroscopy
XRD	X-ray Diffraction
XRF	X-ray Fluorescence Spectroscopy
ZITO	Zinc Indium Tin Oxide
ZTO	Zinc Tin Oxide

Bibliography

- [1] Y. Yonezawa (Ed). *Fundamental Physics of Amorphous Semiconductors*. Springer-Verlag, New York, 1981.
- [2] S. R. Elliot. *Physics of Amorphous Materials*. Longman Group Limited, New York, 1984.
- [3] S. R. Ovshinsky D. Adler, H. Fritzsche. *Physics of Disordered Materials*. Plenum Press, London, 1985.
- [4] J. Singh and K. Shimakawa. *Advances in Amorphous Semiconductors*. Taylor & Francis, London, 2003.
- [5] S. R. Elliot. *The Physics and Chemistry of Solids*. John Wiley & Sons, Sussex, 1998.
- [6] M. H. Brodsky (Ed). *Amorphous Semiconductors*. Springer Verlag, New York, 1979.
- [7] M. H. Cohen, H. Fritzsche, and S. R. Ovshinsky. Simple band model for amorphous semiconducting alloys. *Phys. Rev. Lett.*, 22:1065, 1969.
- [8] N. F. Mott. States in the gap in non-crystalline semiconductors. *J. Phys. C: Solid State Phys.*, 13:5433, 1980.

- [9] N. Mott. The mobility edge since 1967. *J. Phys. C: Solid State Phys.*, 20:3075, 1987.
- [10] M. H. Cohen. Electronic structure and transport in covalent amorphous semiconducting alloys. *J. Non-Cryst. Solids*, 2:432, 1970.
- [11] D. Emin in: P. G. Le Comber (ed). *Electronic and Structural Properties of Amorphous Semiconductors*. Academic Press, London, 1973.
- [12] J. M. Marshall and A. E. Owen. Drift mobility studies in vitreous arsenic triselenide. *Philos. Mag.*, 24:1281, 1971.
- [13] D. Weaire. Existence of a gap in the electronic density of states of a tetrahedrally bonded solid of arbitrary structure. *Phys. Rev. Lett.*, 26:1541, 1971.
- [14] D. Weaire and M. F. Thorpe. Electronic properties of an amorphous solid - A simple tight binding theory. *Phys. Rev. B*, 4:2508, 1971.
- [15] M. F. Thorpe and D. Weaire. Electronic properties of an amorphous solid - Further aspects of the theory. *Phys. Rev. B*, 4:3518, 1971.
- [16] E. A. Davis. Studies of amorphous semiconductors under pressure. *Jpn. J. Appl. Phys.*, 32:178, 1993.
- [17] D. L. Wood and J. Tauc. Weak absorption tails in amorphous semiconductors. *Phys. Rev. B*, 5:3144, 1972.
- [18] G. D. Cody, B. G. Brooks, and B. Abels. Optical absorption above the optical gap of amorphous silicon hydride. *Sol. Energy Mat.*, 8:231, 1982.

- [19] H. Fritzsche. Characterization of glow-discharge deposited a-Si:H. *Sol. Energy Mat.*, 3:447, 1980.
- [20] N. F. Mott and E. A. Davis. *Electronic Processes in Non-Crystalline Materials*. Clarendon Press, Oxford, 1979.
- [21] F. Demichellis, E. M. Mezzetti, A. Tagliaferro, E. Tresso, P. Rava, and N. M. Ravindra. Optical properties of hydrogenated amorphous silicon. *J. Appl. Phys.*, 59:611, 1986.
- [22] E. A. Fagen and H. J. Fritzsche. Photoconductivity of amorphous chalcogenide alloy films. *J. Non-Cryst. Solids*, 4:480, 1970.
- [23] G. D. Cody in : J. I. Pankove (ed.). *Hydrogenated Amorphous Silicon*. Academic Press, New York, 1984.
- [24] S. Abe and Y. Toyozawa. Interband absorption spectra of disordered semiconductors in the coherent potential approximation. *J. Phys. Soc. Jpn.*, 50:2185, 1981.
- [25] R. Zallen. *The Physics of Amorphous Solids*. John Wiley and Sons, New York, 1983.
- [26] N. F. Mott. Conduction in non-crystalline systems IV. Anderson localization in a disordered lattice. *Philos. Mag.*, 22:7, 1970.
- [27] T. Kasuya. A theory of impurity conduction I. *J. Phys. Soc. Jpn.*, 13:1096, 1958.
- [28] A. Miller and E. Abrahams. Impurity conduction at low concentrations. *Phys. Rev.*, 120:745, 1960.

- [29] N. F. Mott. Conduction in non-crystalline materials. *Philos. Mag.*, 19:835, 1969.
- [30] I. P. Zvyagin. On the theory of hopping transport in disordered semiconductors. *Physica Stat. Solidi (b)*, 58:443, 1973.
- [31] H. Overhof. Thermopower calculation for variable range hopping - application to α -Si. *Physica Stat. Solidi (b)*, 67:709, 1975.
- [32] M. H. Brodsky and R. J. Gambino. Electrical conduction in evaporated amorphous silicon films. *J. Non-Cryst. Solids*, 8:739, 1972.
- [33] K. Shimakawa, T. Kato, K. Hayashi, A. Masuda, M. Kumeda, and T. Shimizu. *Philos. Mag. B*, 70:1035, 1994.
- [34] D. K. Schroder. *Semiconductor material and device characterization*. Wiley-Interscience, New Jersey, 1998.
- [35] L. Friedman and T. Holstein. Studies of polaron motion : Part III: The hall mobility of the small polaron. *Ann. Phys.*, 21:494, 1963.
- [36] L. Friedman. Hall conductivity of amorphous semiconductors in the random phase model. *J. Non-Cryst. Solids*, 6:329, 1971.
- [37] D. Emin. The sign of the hall effect in hopping conduction. *Philos. Mag.*, 35:1189, 1977.
- [38] N. F. Mott. The sign of the Hall effect in amorphous silicon. *Philos. Mag. B*, 63:3, 1991.
- [39] H. Okamoto, K. Hattori, and Y. Hamakawa. Hall effect near the mobility edge. *J. Non-Cryst. Solids*, 164:445, 1993.

- [40] H. Hosono, Y. Yamashita, N. Ueda, H. Kawazoe, and K. Shimidzu. New amorphous semiconductor: 2CdO.PbO_x . *Appl. Phys. Lett.*, 68:661, 1996.
- [41] P. W. Anderson. Absence of diffusion in certain random lattices. *Phys. Rev.*, 109:1492, 1958.
- [42] Y. Kuo. *Thin Film Transistors: Materials and Processes Vol. 1*. Kluwer Academic Publishers, Massachusetts, 2004.
- [43] W. E. Spear and P. G. LeComber. Substitutional doping of amorphous silicon. *Solid State Comm.*, 17:1193, 1975.
- [44] A. Ohtomo, M. Kawasaki, T. Koida, K. Masubuchi, H. Koinuma, Y. Sakurai, Y. Yoshida, T. Yasuda, and Y. Segawa. $\text{Mg}_x\text{Zn}_{1-x}\text{O}$ as a II-VI widegap semiconductor alloy. *Appl. Phys. Lett.*, 72:2466, 1998.
- [45] S. Choopun, R. D. Vispute, W. Yang, R. P. Sharma, T. Venkatesan, and H. Shen. Realization of band gap above 5.0 eV in metastable cubic-phase $\text{Mg}_x\text{Zn}_{1-x}\text{O}$ alloy films. *Appl. Phys. Lett.*, 80:1529, 2002.
- [46] O. Madelung. *Semiconductors: Data Handbook, 3rd ed.* Springer, New York, 2003.
- [47] Y. R. Ryu, T. S. Lee, J. A. Lubguban, A. B. Corman, H. W. White, J. H. Leem, M. S. Han, and Y. S. Park. Wide-band gap oxide alloy: BeZnO . *Appl. Phys. Lett.*, 88:052103, 2006.
- [48] S. F. Ding, G. H. Fan, S. T. Li, K. Chen, and B. Xiao. Theoretical study of $\text{Be}_x\text{Zn}_{1-x}\text{O}$ alloys. *Physica B*, 394:127, 2007.

- [49] J. M. Khoshman, A. Khan, and M. E. Kordesch. Optical properties of sputtered amorphous beryllium nitride thin films. *J. Appl. Phys.*, 101:103532, 2007.
- [50] J. M. Khoshman, D. C. Ingram, and M. E. Kordesch. Bandgap engineering in amorphous $\text{Be}_x\text{Zn}_y\text{O}$ thin films. *Appl. Phys. Lett.*, 92:091902, 2008.
- [51] F. M. Hossain, J. Nishii, S. Takagi, A. Ohtomo, T. Fukumura, H. Fujioka, H. Ohno, H. Koinuma, and M. Kawasaki. Modeling and simulation of polycrystalline ZnO thin-film transistors. *J. Appl. Phys.*, 94:7768, 2003.
- [52] R. L. Hoffman. ZnO-channel thin-film transistors: channel mobility. *J. Appl. Phys.*, 95:5813, 2004.
- [53] S. Samson and C. G. Fonstad. Defect structure and electronic donor levels in stannic oxide crystals. *J. Appl. Phys.*, 44:4618, 1973.
- [54] J. E. Medvedeva and A. J. Freeman. Combining high conductivity with complete optical transparency: A band structure approach. *Europhys. Lett.*, 69:583, 2005.
- [55] S. Lany and A. Zunger. Dopability, intrinsic conductivity, and non-stoichiometry of transparent conducting oxides. *Phys. Rev. Lett.*, 98:045501, 2007.
- [56] S. B. Zhang and S. H. Wei. Self-doping of cadmium stannate in the inverse spinel structure. *Appl. Phys. Lett.*, 80:1376, 2002.

- [57] S. B. Zhang, S. H. Wei, and A. Zunger. Intrinsic n-type versus p-type doping asymmetry and the defect physics of ZnO. *Phy. Rev. B*, 63:075205, 2001.
- [58] H. Hosono, M. Yasukawa, and H. Kawazoe. Novel oxide amorphous semiconductors: transparent conducting amorphous oxides. *J. Non-Cryst. Solids*, 203:334, 1996.
- [59] H. Hosono, N. Kikuchi, N. Ueda, and H. Kawazoe. Working hypothesis to explore novel wide band gap electrically conducting amorphous oxides and examples. *J. Non-Cryst. Solids*, 198-200:165, 1996.
- [60] H. Hosono. Ionic amorphous oxide semiconductors: Material design, carrier transport, and device application. *J. Non-Cryst. Solids*, 352:851, 2006.
- [61] R. Martins, P. Barquinha, L. Pereira, I. Ferreira, and E. Fortunato. Role of order and disorder in covalent semiconductors and ionic oxides used to produce thin film transistors. *Appl. Phys. A*, 89:37, 2007.
- [62] R. Martins, P. Barquinha, I. Ferreira, L. Pereira, G. Goncalves, and E. Fortunato. Role of order and disorder on the electronic performances of oxide semiconductor thin film transistors. *J. Appl. Phys.*, 101:44505, 2007.
- [63] T. Kamiya and H. Hosono. Electronic structures and device applications of transparent oxide semiconductors: What is the real merit of oxide semiconductors. *Int. J. Appl. Ceram. Technol.*, 2:285, 2005.
- [64] W. A. Harrison. *Electronic Structure and Properties of Solids*. W. A. Freeman, San Francisco, 1980.

- [65] R. Robertson. Defect levels of SnO_2 . *Phys. Rev. B*, 30:3520, 1984.
- [66] R. Martins, P. Barquinha, A. Pimentel, L. Pereira, E. Fortunato, D. Kang, I. Song, C. Kim, J. Park, and Y. Park. Electron transport in single and multicomponent n-type oxide semiconductors. *Thin Solid Films*, 516:1322, 2008.
- [67] R. A. Street and K. Winer. Defect equilibria in undoped a-Si:H. *Phys. Rev. B*, 40:6236, 1989.
- [68] W. B. Jackson. Role of band-tail carriers in metastable defect formation and annealing in hydrogenated amorphous silicon. *Phys. Rev. B*, 41:1059, 1990.
- [69] M. J. Powell and S. C. Deane. Improved defect-pool model for charged defects in amorphous silicon. *Phys. Rev. B*, 48:10815, 1993.
- [70] R. A. Street. Current-induced defect creation and recovery in hydrogenated amorphous silicon. *Appl. Phys. Lett.*, 59:1084, 1991.
- [71] P. W. Peacock and J. Robertson. Behavior of hydrogen in high dielectric constant oxide gate insulators. *Appl. Phys. Lett.*, 83:2025, 2003.
- [72] S. Narushima, M. Orita, M. Hirano, and H. Hosono. Electronic structure and transport properties in the transparent amorphous oxide semiconductor $2\text{CdO} \cdot \text{GeO}_2$. *Phys. Rev. B*, 66:035203, 2002.
- [73] L. L. Kazmerski (Ed). *Polycrystalline and Amorphous Thin Films and Devices*. Academic Press, New York, 1980.

- [74] L. Mei and J. E. Greene. RF-sputtered amorphous Si/crystalline Si junctions. *J. Vac. Sci. Technol.*, 11:145, 1974.
- [75] G. W. Neudeck and A. K. Malhotra. An amorphous silicon thin film transistor: Theory and experiment. *Appl. Phys. Lett.*, 19:721, 1976.
- [76] R. C. Chittik, J. H. Alexander, and H. F. Sterling. The preparation and properties of amorphous silicon. *J. Electrochem. Soc.*, 116:77, 1969.
- [77] W. E. Spear, P. G. Le Comber, S. Kinmond, and M. H. Brodsky. Amorphous silicon p-n junction. *Appl. Phys. Lett.*, 28:105, 1976.
- [78] D. E. Carlson and C. R. Wronski. Amorphous silicon solar cell. *Appl. Phys. Lett.*, 28:671, 1976.
- [79] P. J. Zanzucchi, C. R. Wronski, and D. E. Carlson. Optical and photoconductive properties of discharge-produced amorphous silicon. *J. Appl. Phys.*, 48:5227, 1977.
- [80] J. I. Pankove and D. E. Carlson. Electroluminescence in amorphous silicon. *Appl. Phys. Lett.*, 29:620, 1976.
- [81] D. L. Staebler and C. R. Wronski. Reversible conductivity changes in discharge-produced amorphous Si. *Appl. Phys. Lett.*, 31:292, 1977.
- [82] D. L. Staebler. Laser-beam annealing of discharge-produced amorphous silicon. *J. Appl. Phys.*, 50:3648, 1979.
- [83] P. G. Le Comber, A. Madan, and W. E. Spear. Electronic transport and state distribution in amorphous Si films. *J. Non-Cryst. Solids*, 11:219, 1972.

- [84] A. Madan, P. G. Le Comber, and W. E. Spear. Investigation of the density of localized states in a-Si using the field effect technique. *Appl. Phys. Lett.*, 20:239, 1976.
- [85] M. W. J. Prins, K. O. G. Holz, G. Muller, J. F. M. Cillessen, J. B. Giesbers, R. P. Wenning, and R. M. Wolf. A ferroelectric transparent thin-film transistor. *Appl. Phys. Lett.*, 68:3650, 1996.
- [86] J. B. Giesbers, M. W. J. Prins, J. F. M. Cillessen, and H. A. V. Esch. Dry etching of all oxide transparent thin film memory transistors. *Microelectronic Engineering*, 35:71, 1997.
- [87] H. Takatsuji, T. Hiromori, K. Tsujimoto, S. Tsuji, K. Kuroda, and H. Saka. Characterization of transparent conductors in indium zinc oxide and their application to thin-film-transistor liquid-crystal displays. *Proc. Materials Research Society Symposium*.
- [88] J. Nishii, F. M. Hossain, S. Takagi, T. Aita, K. Saikusa, Y. Ohmaki, I. Ohkubo, S. Kishimoto, A. Ohtomo, T. Fukumura, F. Matsukura, Y. Ohno, H. Koinuma, H. Ohno, and M. Kawasaki. High mobility thin-film transistors with transparent ZnO channels. *Jpn. J. Appl. Phys.*, 42:347, 2003.
- [89] E. Fortunato, P. Barquinha, A. Pimental, A. Goncalves, A. Marques, R. Martins, and L. Pereira. Wide-bandgap high-mobility ZnO thin-film transistors produced at room temperature. *Appl. Phys. Lett.*, 85:2541, 2004.
- [90] R. L. Hoffman, B. J. Norris, and J.F. Wager. ZnO-based transparent thin-film transistors. *Appl. Phys. Lett.*, 82:733, 2003.

- [91] P. F. Carcia, R. S. McLean, M. H. Reilly, G. Nunes, and Jr. Transparent ZnO thin-film transistor fabricated by rf magnetron sputtering. *Appl. Phys. Lett.*, 82:1117, 2003.
- [92] S. Masuda, K. Kitamura, Y. Okumura, S. Miyatake, H. Tabata, and T. Kawai. Transparent thin film transistors using ZnO as an active channel layer and their electrical properties. *J. Appl. Phys.*, 93:1624, 2003.
- [93] E. Fortunato, A. Pimental, L. Pereira, A. Goncalves, G. Lavareda, H. Aguas, I. Ferreira, C. N. Carvalho, and R. Martins. High field-effect mobility zinc oxide thin film transistors produced at room temperature. *J. Non-Cryst. Solids*, 338:806, 2004.
- [94] E. Bellingeri, D. Marré, L. Pellegrino, I. Pallecchi, G. Canu, M. Vignolo, C. Bernini, and A. S. Siri. High mobility ZnO thin film deposition on SrTiO₃ and transparent field effect transistor fabrication. *Superlattices and Microstructures*, 38:446, 2005.
- [95] Q. J. Yao and D. J. Li. Fabrication and property study of thin film transistor using rf sputtered ZnO as channel layer. *J. Non-Cryst. Solids*, 351:3191, 2005.
- [96] I. D. Kim, M. H. Lim, K. T. Kang, H. G. Kim, and S. Y. Choi. Room temperature fabricated ZnO thin film transistor using high-*K* Bi_{1.5}Zn_{1.0}Nb_{1.5}O₇ gate insulator prepared by sputtering. *Appl. Phys. Lett.*, 89:022905, 2006.

- [97] H. C. Cheng, C. F. Chen, and C. C. Lee. Thin-film transistors with active layers of zinc oxide (ZnO) fabricated by low-temperature chemical bath method. *Thin Solid Films*, 498:142, 2006.
- [98] H. H. Hung and C. C. Wu. Amorphous ZnO transparent thin-film transistors fabricated by fully lithographic and etching processes. *Appl. Phys. Lett.*, 91:013502, 2007.
- [99] S. J. Lim, S. J. Kwon, H. Kim, and J. S. Park. High performance thin film transistor with low temperature atomic layer deposition nitrogen doped ZnO. *Appl. Phys. Lett.*, 91:183517, 2007.
- [100] K. Remashen, J. H. Jang, D. K. Hwang, and S. J. Park. ZnO-based thin film transistors having high refractive index silicon nitride gate. *Appl. Phys. Lett.*, 91:182101, 2007.
- [101] S. M. Yoon, S. H. Ko Park, C. S. Hwang, H. Y. Chu, and K. I. Cho. Fabrication of oxide TFTs with Al₂O₃/ZnO gate stacks patterned using a dry etching method. *Electrochem. Solid State Lett.*, 11:J15, 2008.
- [102] Dhananjay and S. B. Krupanidhi. Low threshold voltage ZnO transistor with a Zn_{0.7}Mg_{0.3}O gate dielectric for transparent electronics. *J. Appl. Phys.*, 101:123717, 2007.
- [103] M. G. McDowell, R. J. Sanderson, and I. G. Hill. Combinatorial study of zinc tin oxide thin film transistors. *Appl. Phys. Lett.*, 92:013502, 2008.
- [104] J. H. Kim, B. D. Ahn, C. H. Lee, K. A. Jeon, H. S. Kang, and S. Y. Lee. Characteristics of transparent ZnO based thin film transistors

- with amorphous HfO_2 gate insulators and Ga doped ZnO electrodes. *Thin Solid Films*, 516:1529, 2008.
- [105] G. Lavareda, C. N. Carvalho, E. Fortunato, A. R. Ramos, E. Alves, O. Conde, and A. Amaral. Transparent thin film transistors based on indium oxide semiconductor. *J. Non-Cryst. Solids*, 352:2311, 2006.
- [106] H. Tetsuka, Y. J. Shan, K. Tezuka, and H. Imoto. Transparent amorphous conductive Cd-In-Sb-O thin films for flexible devices. *Vacuum*, 80:1038, 2006.
- [107] Dhananjay and C. W. Chu. Realization of In_2O_3 thin film transistors through reactive evaporation process. *Appl. Phys. Lett.*, 91:132111, 2007.
- [108] D. Hong, H. Q. Chiang, R. E. Presley, N. L. Dehuff, J. P. Bender, C. H. Park, J. F. Wager, and D. A. Keszler. Transparent thin film transistor exploratory development via sequential layer deposition and thermal annealing. *Thin Solid Films*, 515:2717, 2006.
- [109] P. Görrn, M. Sander, J. Meyer, M. Kröger, E. Becker, H. H. Johannes, W. Kowalsky, and T. Riedl. Towards see-through displays: Fully transparent thin-film transistors driving transparent organic light emitting diodes. *Adv. Mater.*, 18:738, 2006.
- [110] H. Q. Chiang, J. F. Wager, R. L. Hoffman, J. Jeong, and D. A. Keszler. High mobility transparent thin-film transistors with amorphous zinc tin oxide channel layer. *Appl. Phys. Lett.*, 86:013503, 2005.

- [111] W. B. Jackson, R. L. Hoffman, and G. S. Herman. High-performance flexible zinc tin oxide field-effect transistors. *Appl. Phys. Lett.*, 87:193503, 2005.
- [112] Y. J. Chang, D. H. Lee, G. S. Herman, and C. H. Chang. High-performance, spin-coated zinc tin oxide thin-film transistors. *Electrochem. Solid-State. Lett.*, 10:H135, 2008.
- [113] N. L. Dehuff, E. S. Kettenring, D. Hong, H. Q. Chiang, J. F. Wager, R. L. Hoffman, C. H. Park, and D. A. Keszler. Transparent thin-film transistors with zinc indium oxide channel layer. *J. Appl. Phys.*, 97:064505, 2005.
- [114] C. G. Choi, S. J. Seo, and B. S. Bae. Solution-processed indium-zinc oxide transparent thin-film transistors. *Electrochem. Solid-State. Lett.*, 11:H7, 2008.
- [115] R. E. Presley, C. L. Munsee, C. H. Park, D. Hong, J. F. Wager, and D. A. Keszler. Tin oxide transparent thin film transistors. *J. Phys. D: Appl. phys.*, 37:2810, 2004.
- [116] Y. Kwon, Y. Li, Y. W. Heo, M. Jones, P. H. Holloway, D. P. Norton, Z. V. Park, and S. Li. Enhancement-mode thin-film field-effect transistor using phosphorus-doped (Zn,Mg)O channel. *Appl. Phys. Lett.*, 84:2685, 2004.
- [117] K. Matsuzaki, H. Hiramatsu, K. Nomura, H. Yanagi, T. Kamiya, M. Hirano, and H. Hosono. Growth, structure and carrier transport properties of Ga₂O₃ epitaxial film examined for transparent field-effect transistor. *Thin Solid Films*, 496:37, 2006.

- [118] M. S. Grover, P. A. Hersh, H. Q. Chiang, E. S. Kettenring, J. F. Wager, and D. A. Keszler. Thin-film transistors with transparent amorphous zinc indium tin oxide channel layer. *J. Phys. D: Appl. Phys.*, 40:1335, 2007.
- [119] H. Yabuta, M. Sano, K. Abe, T. Aiba, T. Den, H. Kumomi, K. Nomura, T. Kamiya, , and H. Hosono. High-mobility thin-film transistor with amorphous InGaZnO_4 channel fabricated by room temperature rf-magnetron sputtering. *Appl. Phys. Lett.*, 89:112123, 2006.
- [120] T. Iwasaki, N. Itagaki, T. Den, H. Kumomi, K. Nomura, T. Kamiya, and H. Hosono. Combinatorial approach to thin film transistors using multicomponent semiconductor channels: An application to amorphous oxide semiconductors in In-Ga-Zn-O system. *Appl. Phys. Lett.*, 90:242114, 2007.
- [121] D. Kang, H. Lim, C. Kim, I. Song, J. Park, Y. Park, and J. G. Chung. Amorphous gallium indium zinc oxide thin film transistors: Sensitive to oxygen molecules. *Appl. Phys. Lett.*, 90:192101, 2007.
- [122] R. Hayashi, M. Ofuji, N. Kaji, K. Takahashi, K. Abe, H. Yabuta, M. Sano, H. Kumomi, K. Nomura, T. Kamiya, M. Hirano, and H. Hosono. Circuits using uniform tfts based on amorphous In-Ga-Zn-O. *J. SID*, 15:915, 2007.
- [123] M. Kim, J. H. Jeong, H. J. Lee, T. K. Ahn, H. S. Shin, J. S. Park, J. K. Jeong, Y. G. Mo, and H. D. Kim. High mobility bottom gate InGaZnO thin film transistors with SiO_x etch stopper. *Appl. Phys. Lett.*, 90:212114, 2007.

- [124] J. S. Park, J. K. Jeong, Y. G. Mo, H. D. Kim, and S. Kim. Improvements in the device characteristics of amorphous indium gallium zinc oxide thin film transistors by Ar plasma treatment. *Appl. Phys. Lett.*, 90:262106, 2007.
- [125] J. K. Jeong, J. H. Jeong, H. W. Yang, J. S. Park, Y. G. Mo, and H. D. Kim. High performance thin film transistors with cosputtered amorphous indium gallium zinc oxide channel. *Appl. Phys. Lett.*, 91:113505, 2007.
- [126] K. Nomura, H. Ohta, A. Takagi, T. Kamiya, M. Hirano, and H. Hosono. Room-temperature fabrication of transparent flexible thin-film transistors using amorphous oxide semiconductors. *Nature*, 435:488, 2004.
- [127] K. Nomura, H. Ohta, K. Ueda, T. Kamiya, M. Hirano, and H. Hosono. Thin-film transistor fabricated in single-crystalline transparent oxide semiconductor. *Science*, 300:1269, 2003.
- [128] W. Lim, S. Kim, Y. Wang, J. W. Lee, D. P. Norton, S. J. Pearton, F. Ren, and I. I. Kravchenko. High-performance indium gallium zinc oxide transparent thin-film transistors fabricated by radio-frequency sputtering. *J. Electrochem. Soc.*, 155:H383, 2008.
- [129] R. B. Wehrspohn, S. C. Deane, I. D. French, I. Gale, J. Hewett, M. J. Powell, and J. Robertson. Relative importance of the SiSi bond and SiH bond for the stability of amorphous silicon thin film transistors. *J. Appl. Phys.*, 87:144, 2000.

- [130] M. J. Powell. The physics of amorphous-silicon thin-film transistors. *IEEE Trans. Electron Devices*, 36:2753, 1989.
- [131] R. B. M. Cross and M. M. De Souza. Investigating the stability of zinc oxide thin film transistors. *Appl. Phys. Lett.*, 89:263513, 2006.
- [132] P. Görrn, P. Hölzer, T. Riedl, W. Kowalsky, J. Wang, T. Weimann, P. Hinze, and S. Kipp. Stability of transparent zinc tin oxide transistors under bias stress. *Appl. Phys. Lett.*, 90:063502, 2007.
- [133] A. Suresh and J. F. Muth. Bias stress stability of indium gallium zinc oxide channel based transparent thin film transistors. *Appl. Phys. Lett.*, 92:033502, 2008.
- [134] P. Görrn, M. Lehnhardt, T. Riedl, and W. Kowalsky. The influence of visible light on transparent zinc tin oxide thin film transistors. *Appl. Phys. Lett.*, 91:193504, 2007.
- [135] J. S. Park, J. K. Jeong, H. J. Chung, Y. G. Mo, and H. D. Kim. Electronic transport properties of amorphous indium gallium zinc oxide semiconductor upon exposure to water. *Appl. Phys. Lett.*, 92:072104, 2008.
- [136] Y. Vygranenko, K. Wang, and A. Nathan. Stable indium oxide thin-film transistors with fast threshold voltage recovery. *Appl. Phys. Lett.*, 91:263508, 2007.
- [137] K. Remashan, D. K. Hwang, S. D. Park, J. W. Bae, G. Y. Yeom, S. J. Park, and J. H. Jang. Effect of N_2O plasma treatment on the performance of ZnO TFTs. *Electrochem. Solid State Lett.*, 11:H55, 2008.

- [138] H. J. Chung, J. H. Jeong, T. K. Ahn, H. J. Lee, M. Kim, K. Jun, J. S. Park, J. K. Jeong, Y. G. Mo, and H. D. Kim. Bulk limited current conduction in amorphous InGaZnO thin films. *Electrochem. Soild State Lett.*, 11:H51, 2008.
- [139] Y. L. Wang, L. N. Covert, T. J. Anderson, W. Lim, J. Lin, S. J. Pearton, D. P. Norton, J. M. Zavada, and F. Ren. RF characteristics of room temperature deposited small gate dimation indium zinc oxide TFTs. *Electrochem. Soild State Lett.*, 11:H60, 2008.
- [140] G. Thomas. Invisible circuits. *Nature*, 389:907, 1997.
- [141] T. Nozawa. *Transparent Electronic Products Soon a Reality*. Nikkei Electronics Asia, 2007.
- [142] K. Wasa, M. Kitabatake, and H. Adachi. *Thin Film Materials Technology*. Springer-Verlag GmbH & Co. KG, Germany, 2004.
- [143] L. I. Maissel and R. Glang (Eds). *Handbook of Thin Film Technology*. McGraw-Hill, New York, 1970.
- [144] M. Ohring. *Materials Science of Thin Films: Deposition and Structure*. Academic Press, New York, 2001.
- [145] P. Sigmund. Theory of sputtering. I. Sputtering yield of amorphous and polycrystalline targets. *Phys. Rev.*, 184:383, 1969.
- [146] R. A. Powell and S. M. Rossnagel. *PVD for Microelectronics: Sputter Deposition Applied to Semiconductor Manufacturing*. Academic Press, San Diego, 1999.

- [147] D. B. Chrisey and G. K. Hubler. *Pulsed Laser Deposition of Thin Films*. John Wiley and Sons, New York, 1994.
- [148] Veeco Dektak 6M stylus profiler. *Manual*, 2004.
- [149] P. Dutta. Grazing incidence x-ray diffraction. *Current Science*, 78:1478, 2000.
- [150] P. E. J. Flewitt and R. K. Wild. *Physical methods for materials characterisation*. IOP Publishing Ltd, London, 2003.
- [151] C. R. Brundle, C. K. Evans Jr., and S. Wilson. *Encyclopedia of Material Characterization*. Butxetworch-Heinemann, Massatussites, 1992.
- [152] C. R. Kagan and P. Andry. *Thin Film Transistors*. Marcel Dekker, New York, 2003.
- [153] L. Pereira, P. Barquinha, E. Fortunato, R. Martins, D. Kang, C. J. Kim, H. Lim, I. Song, and Y. Park. High κ dielectrics for low temperature electronics. *Thin Solid Films*, 516:1544, 2008.
- [154] R. M. Wallace and G. Wilk. Alternative gate dielectrics for microelectronics. *Appl. Phys. Lett.*, 27:192, 2002.
- [155] E. P. Gusev, D. A. Buchanan, E. Cartier, A. Kumar, D. DiMaria, S. Guha, A. Callegari, S. Zafar, P. C. Jamison, D. A. Neumayer, M. Copel, M. A. Gribelyuk, H. O. Schmidt, C. Demic, P. Kozlowski, K. Chan, N. Bojarczuk, L. A. Ragnarsson, P. Ronsheim, K. Rim, R. J. Fleming, A. Mocuta, and A. Ajmera. Ultrathin high- κ gate stacks for advanced CMOS devices. *Tech. Dig.-Int. Electron Devices Meet*, page 451, 2001.

- [156] L. A. Ragnarsson, S. Guha, M. Copel, E. Cartier, N. A. Bojarczuk, and J. Karasinski. Molecular beam deposited yttrium oxide dielectrics in aluminum gated metal oxide semiconductor field effect transistors: Effective electron mobility. *Appl. Phys. Lett.*, 78:4169, 2001.
- [157] R. W. Murto, M. I. Gardner, G. A. Brown, P. M. Zeitzoff, and H. R. Huff. An analytical look at vertical transistor structures. *Solid State Technol.*, 46:43, 2003.
- [158] S. Q. Wang and G. D. Mahan. Electron scattering from surface excitations. *Phys. Rev. B*, 6:4517, 1972.
- [159] K. Hess and P. Vogl. Remote polar phonon scattering in silicon inversion layers. *Solid State Commun.*, 30:797, 1979.
- [160] B. T. Moore and D. K. Ferry. Remote polar phonon scattering in Si inversion layers. *J. Appl. Phys.*, 51:2603, 1980.
- [161] M. V. Fischetti, D. A. Neumayer, and E. A. Cartier. Effective electron mobility in Si inversion layers in metal oxide semiconductor systems with a high κ insulator: The role of remote phonon scattering. *J. Appl. Phys.*, 90:4587, 2001.
- [162] B. Laikhtman and P. M. Solomon. Remote phonon scattering in field effect transistors with a high κ insulating layer. *J. Appl. Phys.*, 103:014501, 2008.
- [163] S. Martin, C. S. Chiang, J. Y. Nahm, T. Li, J. Kanicki, and Y. Ugai. Influence of the amorphous silicon thickness on top-gate thin film transistor electrical performance. *Jpn.J. Appl. Phys.*, 40:530, 2001.

- [164] M. Shur and M. Hack. Physics of amorphous silicon based alloy field-effect transistors. *J. Appl. Phys.*, 55:3831, 1984.
- [165] S. Major, S. Kumar, M. Bhatnager, and K. L. Chopra. Effect of hydrogen plasma treatment on transparent conducting oxides. *Appl. Phys. Lett.*, 49:394, 1986.
- [166] T. Minami, H. Sato, H. Nanto, and S. Takata. Heat treatment in hydrogen gas and plasma for transparent conducting oxide films such as ZnO, SnO₂ and indium tin oxide. *Thin Solid Films*, 176:277, 1989.
- [167] Z. C. Jin, I. Hamberg, and C. G. Granqvist. Optical properties of sputter-deposited ZnO:Al thin films. *J. Appl. Phys.*, 64:5117, 1988.
- [168] J. Hu and R. G. Gordon. Atmospheric pressure chemical vapor deposition of gallium doped zinc oxide thin films from diethyl zinc, water, and triethyl gallium. *J. Appl. Phys.*, 71:880, 1992.
- [169] R. J. Cava, J. M. Phillips, J. Kwo, G. A. Thomas, R. B. van Dover, S. A. Carter, J. J. Krajewski, W. F. Peck, Jr., J. H. Marshall, and D. H. Rapkine. GaInO₃: A new transparent conducting oxide. *Appl. Phys. Lett.*, 64:2071, 1994.
- [170] K. L. Chopra, S. Major, and D. K. Pandra. Transparent conductors: A status review. *Thin Solid Films*, 102:1, 1983.
- [171] T. Minami, S. Takata, H. Sato, and H. Sonohara. Properties of transparent zinc-stannate conducting films prepared by radio frequency magnetron sputtering. *J. Vac. Sci. Technol. A*, 13:1095, 1995.

- [172] D. L. Young, D. L. Williamson, and T. J. Coutts. Structural characterization of zinc stannate thin films. *J. Appl. Phys.*, 91:1464, 2002.
- [173] D. L. Young, H. Moutinho, Y. Yan, and T. J. Coutts. Growth and characterization of radio frequency magnetron sputter-deposited zinc stannate, Zn_2SnO_4 , thin films. *J. Appl. Phys.*, 92:310, 2002.
- [174] T. Moriga, Y. Hayashi, K. Kondo, Y. Nishimura, K. Murai, I. Nakabayashi, H. Fukumoto, and K. Tominaga. Transparent conducting amorphous Zn-Sn-O films deposited by simultaneous dc sputtering. *J. Vac. Sci. Technol. A*, 22:1705, 2004.
- [175] E. Cetinörgü, S. Goldsmith, and R. L. Boxman. Effect of deposition conditions on the characteristics of ZnO-SnO₂ thin films deposited by filtered vacuum arc. *Thin Solid Films*, 515:880, 2006.
- [176] D. Kovacheva and K. Petrov. Preparation of crystalline ZnSnO₃ from Li₂SnO₃ by low-temperature ion exchange. *Solid State Ionics*, 109:327, 1998.
- [177] Y. S. Shen and Z. T. Zhang. *Sensors Actuators B*, 12:5, 1993.
- [178] *Joint Committee on Powder Diffraction Standards, Powder Diffraction File Card No. 21-1250*. ASTM, Philadelphia, 1967.
- [179] K. Nomura, A. Takagi, T. Kamiya, H. Ohta, M. Hirano, and H. Hosono. Amorphous oxide semiconductors for high-performance flexible thin-film transistors. *Jpn. J. Appl. Phys.*, 45:4303, 2006.
- [180] K. Nomura, T. Kamiya, M. Ohta, K. Ueda, M. Hirano, and H. Hosono. Carrier transport in transparent oxide semiconductor

- with intrinsic structural randomness probed using single-crystalline $\text{InGaO}_3(\text{ZnO})_5$ films. *Appl. Phys. Lett.*, 85:1993, 2004.
- [181] A. Takagi, K. Nomura, H. Ohta, H. Yanagi, T. Kamiya, M. Hirano, and H. Hosono. Carrier transport and electronic structure in amorphous oxide semiconductor, a-InGaZnO_4 . *Thin Solid Films*, 486:38, 2005.
- [182] H. L. Hartnagal, A. L. Dawar, A. K. Jain, and C. Jagadish. *Semiconducting Transparent Thin Films*. Institute of Physics, London, 1995.
- [183] H. Asahi, T. Hisaka, S. G. Kim, T. Kaneko, S. J. Yu, Y. Okuno, and S. Gonda. Influence of hydrogen on the step flow growth of GaAs on vicinal surfaces by gas-source migration enhanced epitaxy. *Appl. Phys. Lett.*, 61:1054, 1992.
- [184] T. Omata, N. Ueda, K. Ueda, and H. Kawazoe. New ultraviolet-transport electroconductive oxide, ZnGa_2O_4 spinel. *Appl. Phys. Lett.*, 64:1077, 1994.
- [185] K. Yanagawa, Y. Ohki, T. Omata, H. Hosono, N. Ueda, and H. Kawazoe. Preparation of $\text{Cd}_{1-x}\text{Y}_x\text{Sb}_2\text{O}_6$ thin film on glass substrate by radio frequency sputtering. *Appl. Phys. Lett.*, 65:406, 1994.
- [186] M. Yasukawa, H. Hosono, N. Ueda, and H. Kawazoe. Photoemission studies on valence band structure of AgSbO_3 . *J. Ceram. Soc. Jpn.*, 103:455, 1995.

- [187] M. Orita, H. Tanji, M. Mizuno, H. Adachi, and I. Tanaka. Mechanism of electrical conductivity of transparent InGaZnO_4 . *Phys. Rev. B*, 61:1811, 2001.
- [188] J. R. Bellingham, W. A. Philips, and C. J. Adkins. Electrical and optical properties of amorphous indium oxide. *J. Phys.: Condens. Matter*, 2:6207, 1990.
- [189] H. Nakazawa, Y. Ito, E. Matsumoto, K. Adachi, N. Aoki, and Y. Ochiai. The electronic properties of amorphous and crystallized In_2O_3 films. *J. Appl. Phys.*, 100:093706, 2006.
- [190] M. Orita, H. Ohta, M. Hirano, S. Narushima, and H. Hosono. Amorphous transparent conductive oxide $\text{InGaO}_3(\text{ZnO})_{m(m \leq 4)}$: a Zn 4s conductor. *Philos. Mag. B*, 81:501, 2001.
- [191] S. Narushima, H. Hosono, J. Jisun, T. Yoko, and K. Shimakawa. Electronic transport and optical properties of proton-implanted amorphous $2\text{CdO} \cdot \text{GeO}_2$ films. *J. Non-Cryst. Solids*, 274:313, 2000.
- [192] N. Kikuchi, H. Hosono, H. Kawazoe, K. Oyoshi, and S. Hishita. Transparent, conducting, amorphous oxides: Effect of chemical composition on electrical and optical properties of cadmium germanates. *J. Am. Ceram. Soc.*, 80:22, 1997.
- [193] S. Kobayashi, S. Nonomura, T. Ohmori, K. Abe, S. Hirata, T. Uno, T. Gotoh, S. Nitta, and S. Kobayashi. Optical and electrical properties of amorphous and microcrystalline GaN films and their application to transparent TFT. *Appl. Surf. Sci.*, 113/114:480, 1997.

- [194] N. L. Dehuff, E. S. Kettenring, D. Hong, H. Q. Chiang, J. F. Wager, R. L. Hoffman, C. H. Park, and D. A. Kezler. Transparent thin-film transistors with zinc indium oxide channel layer. *J. Appl. Phys.*, 97:064505, 2005.
- [195] T. Minami, H. Sonohara, T. Kakumu, and S. Takata. Highly transparent and conductive $Zn_2In_2O_5$ thin films prepared by rf magnetron sputtering. *Jpn. J. Appl. Phys.*, 34:L971, 1995.
- [196] Y. S. Jung, Y. J. Seo, D. W. Lee, and D. Y. Jeon. Influence of dc magnetron sputtering parameters on the properties of amorphous indium zinc oxide thin film. *Thin Solid Films*, 445:63, 2003.
- [197] J. M. Phillips, R. J. Cava, G. A. Thomas, S. A. Carter, J. Kwo, T. Siegrist, J. J. Krajewski, J. H. Marshall, W. F. Peck Jr., and D. H. Rapkine. Zinc-indium-oxide: A high conductivity transparent conducting oxide. *Appl. Phys. Lett.*, 67:2246, 1995.
- [198] T. Sasabayashi, N. Ito, E. Nishimura, M. Kon, P. K. Song, K. Utsumi, A. Kaijo, and Y. Shigesato. Comparative study on structure and internal stress in tin-doped indium oxide and indium-zinc oxide films deposited by rf magnetron sputtering. *Thin Solid Films*, 445:219, 2003.
- [199] R. Swanepoel. Determination of the thickness and optical constants of amorphous silicon. *J. Phys. E: Sci. Instrum.*, 16:1214, 1983.
- [200] K. F. Berggren and B. E. Sernelius. Band-gap narrowing in heavily doped many-valley semiconductors. *Phys. Rev. B*, 24:1971, 1981.

- [201] P. B. Allen. Solids with thermal or static disorder. I. One-electron properties. *Phys. Rev. B*, 18:5217, 1978.
- [202] B. Chakraborty and P. B. Allen. Solids with thermal or static disorder. II. Optical properties. *Phys. Rev. B*, 18:5225, 1978.
- [203] H. Hiramatsu, K. Ueda, H. Ohta, M. Hirano, M. Kikuchi, H. Yanagi, T. Kamiya, and H. Hosono. Heavy hole doping of epitaxial thin films of a wide gap *p*-type semiconductor, LaCuOSe, and analysis of the effective mass. *Appl. Phys. Lett.*, 91:012104, 2007.
- [204] D. Stauffer and A. Aharony. *Introduction to percolation Theory 2nd Ed.* Taylor & Francis, London, 1992.
- [205] E. A. Davis and N. F. Mott. Conduction in non-crystalline systems V. conductivity, optical absorption and photoconductivity in amorphous semiconductors. *Philos. Mag.*, 22:903, 1970.
- [206] P. Barquinha, G. Goncalves, L. Pereira, R. Martins, and E. Fortunato. Effect of annealing temperature on the properties of IZO films and IZO based transparent TFTs. *Thin Solid Films*, 515:8450, 2007.
- [207] J. M. Ngaruiya, O. Kappertz, S. H. Mohamed, and M. Wuttig. Structure formation upon reactive direct current magnetron sputtering of transition metal oxide films. *Appl. Phys. Lett.*, 85:748, 2004.
- [208] S. Mráz and J. M. Schneider. Energy distribution of O ions during reactive magnetron sputtering. *Appl. Phys. Lett.*, 89:051502, 2006.
- [209] S. Mráz and J. M. Schneider. Influence of the negative oxygen ions on the structure evolution of transition metal oxide thin films. *J. Appl. Phys.*, 100:023503, 2006.

- [210] D. J. Radack. Advanced microelectronics: The role of SOI. *Proc. IEEE Int. SOI Conf.*, page 5, 1999.
- [211] P. Barquinha, P. Pimentel, A. Marques, L. Pereira, R. Martins, and E. Fortunato. Effect of UV and visible light radiation on the electrical performances of transparent TFTs based on amorphous indium zinc oxide. *J. Non-Cryst. Solids*, 352:1756, 2006.
- [212] B. Yagliglu, H. Y. Yeom, R. Bereshford, and D. C. Paine. High-mobility amorphous In_2O_3 10 wt ZnO thin film transistors. *Appl. Phys. Lett.*, 89:062103, 2006.
- [213] J. D. Perkins, J. A. del Cueto, J. L. Alleman, C. Warmsingh, B. M. Keyes, L. M. Gedvilas, P. A. Parilla, B. To, D. W. Readey, and D. S. Ginley. Combinatorial studies of Zn-Al-O and Zn-Sn-O transparent conducting oxide thin films. *Thin Solid Films*, 411:152, 2002.
- [214] H. Kumomi, K. Nomura, T. Kamiya, and H. Hosono. Amorphous oxide channel TFTs. *Thin Solid Films*, 516:1516, 2008.
- [215] J. F. Wager, D. A. Keszler, and R. E. Presley. *Transparent Electronics*. Springer-Verlag, New York, 2007.
- [216] K. Nomura, T. Kamiya, H. Ohta, T. Uruga, M. Hirano, and H. Hosono. Local coordination structure and electronic structure of the large electron mobility amorphous oxide semiconductor In-Ga-Zn-O: Experiment and *ab initio* calculations. *Phys. Rev. B*, 75:035212, 2007.
- [217] F. Utsuno, H. Inoue, Y. Shimane, T. Shibuya, K. Yano, K. Inoue, I. Hirohara, M. Sato, and T. Honma. A structural study of amorphous

- In₂O₃ZnO films by grazing incidence x-ray scattering (GIXS) with synchrotron radiation. *Thin Solid Films*, 516:5818, 2008.
- [218] T. Kamiya, S. Narushima, H. Mizoguchi, K. Shimizu, K. Ueda, H. Ohta, M. Hirano, and H. Hosono. Electrical properties and structure of p-type amorphous oxide semiconductor xZnO.Rh₂O₃. *Adv. Funct. Mater.*, 15:968, 2005.
- [219] J. F. Wager. Transparent electronics. *Science*, 300:1245, 2003.
- [220] S. R. Forrest. The path to ubiquitous and low-cost organic electronic appliances on plastic. *Nature*, 428:911, 2004.
- [221] H. C. Lim, B. Schulkin, M. J. Pulickal, S. Liu, R. Petrova, G. Thomas, S. Wagner, and K. J. Feerici. Flexible membrane pressure sensor. *Sensors Actuators A: Physical*, 119:332, 2005.
- [222] H. Ohta and H. Hosono. Transparent oxide optoelectronics. *Mat. Today*, June:42, 2004.